

**DOE-ER-0313/61
Distribution
Categories
UC-423, -424**

**FUSION MATERIALS
SEMIANNUAL PROGRESS REPORT
FOR THE PERIOD ENDING**

December 31, 2016

**Prepared for
DOE Office of Fusion Energy Sciences
(AT 60 20 10 0)**

DATE PUBLISHED: February 2017

**Prepared by
OAK RIDGE NATIONAL LABORATORY
Oak Ridge, Tennessee 37831
Managed by
UT-Battelle, LLC
For the
U.S. DEPARTMENT OF ENERGY**

FOREWORD

This is the sixty-first in a series of semiannual technical progress reports on fusion materials science activity supported by the Fusion Energy Sciences Program of the U.S. Department of Energy. It covers the period ending December 31, 2016. This report focuses on research addressing the effects on materials properties and performance of exposure to the neutronic, thermal and chemical environments anticipated in the chambers of fusion experiments and energy systems. This research is a major element of the national effort to establish the materials knowledge base for an economically and environmentally attractive fusion energy source. Research activities on issues related to the interaction of materials with plasmas are reported separately.

The results reported are the products of a national effort involving a number of national laboratories and universities. A large fraction of this work, particularly in relation to fission reactor irradiations, is carried out collaboratively with partners in Japan, Russia, and the European Union. The purpose of this series of reports is to provide a working technical record for the use of program participants, and to provide a means of communicating the efforts of fusion materials scientists to the broader fusion community, both nationally and worldwide.

This report has been compiled under the guidance of F. W. (Bill) Wiffen and Stephanie Melton, Oak Ridge National Laboratory. Their efforts, and the efforts of the many persons who made technical contributions, are gratefully acknowledged.

Daniel Clark
Research Division
Office of Fusion Energy Sciences

TABLE OF CONTENTS

1	FERRITIC/MARTENSITIC STEEL DEVELOPMENT	
1.1	DEVELOPMENT OF CASTABLE NANOSTRUCTURED ALLOYS AS ADVANCED RAFM STEELS—L. Tan (Oak Ridge National Laboratory)	1
1.2	MODIFIED 3Cr-3WVTa BAINITIC STEEL PLATE PRODUCTION FOR PROPERTY EVALUATION—Y. Yamamoto (Oak Ridge National Laboratory)	4
1.3	IMPACT OF NEUTRON IRRADIATION ON THERMAL HELIUM DESORPTION FROM IRON—X. Hu, K.G. Field (Oak Ridge National Laboratory), S. Taller (University of Michigan, Ann Arbor), Y. Kath (Oak Ridge National Laboratory), B.D. Wirth (University of Tennessee, Knoxville, Oak Ridge National Laboratory)	9
2	ODS AND NANOCOMPOSITED ALLOY DEVELOPMENT	
2.1	ALLOY YTTRIUM AND TITANIUM VARIATION EFFECTS ON NANO-OXIDES IN NANOSTRUCTURED FERRITIC ALLOYS—N.J. Cunningham, G.R. Odette (University of California, Santa Barbara)	10
2.2	A NUMERICAL INVESTIGATION OF DELAMINATION EFFECTS ON THE FRACTURE BEHAVIOR OF A 14YWT NANOSTRUCTURED FERRITIC ALLOYS (NFA-1)—C. Ruggieri, M. E. Alam, G. R. Odette, (UCSB)	19
2.3	STRUCTURAL AND CHEMICAL EVOLUTION IN NEUTRON IRRADIATED AND HELIUM-INJECTED FERRITIC ODS PM2000 ALLOY—Hee Joon Jung, Dan J Edwards, Richard J Kurtz (Pacific Northwest National Laboratory), Takuya Yamamoto, Yuan Wu and G. Robert Odette (University of California, Santa Barbara)	30
2.4	HIGH TEMPERATURE HELIUM IMPLANTATION OF NI/FE – Y₂Ti₂O₇ BILAYERS—T. Stan, Y. Wu, G.R. Odette, T. Yamamoto (University of California Santa Barbara), and Y. Wang (Los Alamos National Laboratory)	32
2.5	HELIUM SEQUESTRATION AT NANOPARTICLE-MATRIX IN HELIUM+HEAVY ION IRRADIATED NANOSTRUCTURED FERRITIC ALLOYS—C. M. Parish, K.A. Unocic, L. Tan, D.T. Hoelzer, Y. Katoh (Oak Ridge National Laboratory), S.J. Zinkle (ORNL and University of Tennessee), S. Kondo (Kyoto University), L.L. Snead (Massachusetts Institute of Technology)	43
2.6	ON THE ASSOCIATION BETWEEN BUBBLES AND NANO-OXIDES IN ANNEALED AND HELIUM IMPLANTED 14YWT—Y. Wu, T. Stan, T. Yamamoto, G. R. Odette (University of California Santa Barbara), and J. Ciston (Lawrence Berkeley National Laboratory)	50
3	CERAMIC COMPOSITE STRUCTURAL MATERIAL DEVELOPMENT	
3.1	LOW TEMPERATURE AIR BRAZE PROCESS FOR JOINING SILICON CARBIDE COMPONENTS USED IN HEAT EXCHANGERS, FUSION AND FISSION REACTORS, AND OTHER ENERGY PRODUCTION AND CHEMICAL SYNTHESIS SYSTEMS—J.R. Fellows, C.A. Lewinsohn (Ceramatec, Inc.), Y. Katoh, T. Koyanagi (Oak Ridge National Laboratory)	57

TABLE OF CONTENTS

3.2	LOW ACTIVATION JOINING OF SiC/SiC COMPOSITES FOR FUSION APPLICATIONS: MODELING THERMAL AND IRRADIATION-INDUCED SWELLING EFFECTS ON INTEGRITY OF Ti₃SiC₂/SiC JOINT —B.N. Nguyen, C.H. Henager, Jr., and R.J. Kurtz (Pacific Northwest National Laboratory) M. Ferraris (Politecnico di Torino, Italy) Y. Katoh (Oak Ridge National Laboratory)	58
3.3	POSITRON ANNIHILATION SPECTROSCOPY INVESTIGATION OF VACANCY DEFECTS IN NEUTRON-IRRADIATED 3C-SiC —Xunxiang Hu ¹ , Takaaki Koyanagi ¹ , Yutai Katoh ¹ , Brian D. Wirth ^{1, 2} (¹ Oak Ridge National Laboratory, ² University of Tennessee, Knoxville)	66
3.4	VACANCY EFFECTS ON THE FORMATION OF HELIUM AND KRYPTON CAVITIES IN 3C-SiC IRRADIATED AND ANNEALED AT ELEVATED TEMPERATURES* —Hang Zang, Wenbo Liu, Tao Li, Chaohui He, Di Yun (Department of Nuclear Science and Technology, Xi'an Jiaotong University, China) Weilin Jiang, Arun Devaraj, Danny J. Edwards, Charles H. Henager Jr., Richard J. Kurtz (Pacific Northwest National Laboratory) and Zhiguang Wang (Institute of Modern Physics, Lanzhou, China)	67
4	HIGH HEAT FLUX MATERIALS AND COMPONENT TESTING	
4.1	DESIGN AND DEVELOPMENT OF NOVEL Cu ALLOYS FOR FUSION ENERGY APPLICATIONS —Ying Yang (Oak Ridge National Laboratory), Steven J. Zinkle (University of Tennessee at Knoxville and Oak Ridge National Lab), and Lance Snead (Massachusetts Institute of Technology)	69
4.2	MECHANICAL PROPERTIES CHARACTERIZATION OF 90-97wt% WNiFe HEAVY ALLOYS —M.E. Alam, S. Pal, K. Fields, G. R. Odette (University of California, Santa Barbara)	73
4.3	EXPERIMENTAL MEASUREMENTS OF SURFACE DAMAGE AND RESIDUAL STRESSES IN MICRO-ENGINEERED PLASMA-FACING MATERIALS- David Rivera, Richard Wirz, Nasr M. Ghoniem (University of California, Los Angeles)	83
4.4	NEUTRON IRRADIATION EFFECTS IN TUNGSTEN —L.M. Garrison, Y. Katoh, M. McAlister (Oak Ridge National Laboratory), L. L. Snead (MIT), T. S. Byun (PNNL)	102
4.5	PROGRESS IN THE STUDY OF ION IRRADIATION IN TUNGSTEN —Weilin Jiang, Karen Kruska, Charles H. Henager Jr., and Richard J. Kurtz (Pacific Northwest National Laboratory)	115
4.6	INTERACTION OF INTERSTITIAL CLUSTERS WITH RHENIUM, OSMIUM, AND TANTALUM IN TUNGSTEN —W. Setyawan, G. Nandipati, and R. J. Kurtz (Pacific Northwest National Laboratory)	120
4.7	NEUTRON IRRADIATION EFFECTS IN TUNGSTEN-COPPER COMPOSITES —L.M. Garrison, Yutai Katoh (Oak Ridge National Laboratory)	122
4.8	HIGH-HEAT FLUX TESTING OF LOW-LEVEL IRRADIATED MATERIALS USING PLASMA ARC LAMPS —A.S. Sabau, S. Gorti, C. Schaich, J. Kiggans, Y. Katoh (Oak Ridge National Laboratory)	129

TABLE OF CONTENTS

5	MAGNETIC AND DIAGNOSTIC SYSTEM MATERIALS <i>No contributions this reporting period.</i>	
6	FUSION CORROSION AND COMPATIBILITY SCIENCE	
6.1	CHARACTERIZATION OF FeCrAlMo AFTER EXPOSURE TO FLOWING Pb-LI AT 500°-600°C —B. A. Pint and J. Jun (Oak Ridge National Laboratory, USA)	133
7	MECHANISMS AND ANALYSIS	
7.1	THERMAL AND ELECTRICAL PROPERTIES OF MAX PHASES AFTER NEUTRON IRRADIATION —C. Ang*, C. Shih, S.J. Zinkle, C. Silva, C. Parish, N. Cetiner, P. Edmondson, Q. Smith and Y. Katoh (Oak Ridge National Laboratory)	137
7.2	DAMAGE MECHANISM INTERACTIONS AT THE PLASMA-MATERIALS INTERFACE (Early Career Award) —C. M. Parish, K. Wang (Oak Ridge National Laboratory)	141
8	MODELING PROCESSES IN FUSION SYSTEM MATERIALS	
8.1	STRENGTHENING DUE TO RADIATION INDUCED OBSTACLES IN Fe AND FERRITIC ALLOYS —Yu. N. Osetskiy (Oak Ridge National Laboratory)	148
8.2	DEVELOPMENT OF INTERATOMIC POTENTIALS IN TUNGSTEN-RHENIUM SYSTEMS —W. Setyawan and R. J. Kurtz (Pacific Northwest National Laboratory)	151
8.3	STRUCTURES AND TRANSITIONS IN TUNGSTEN GRAIN BOUNDARIES —Timofey Frolov (Lawrence Livermore National Laboratory), Qiang Zhu (University of Nevada Las Vegas), Jaime Marian (University of California Los Angeles) and Robert E. Rudd (Lawrence Livermore National Laboratory)	159
8.4	MODELING DUCTILE-PHASE TOUGHENED TUNGSTEN FOR PLASMA-FACING MATERIALS: PROGRESS IN DAMAGE FINITE ELEMENT ANALYSIS OF THE TUNGSTEN-COPPER BEND BAR TESTS —B. N. Nguyen, C. H. Henager, Jr., R. J. Kurtz (Pacific Northwest National Laboratory)	171
8.5	OKMC STUDY OF COMPARISON OF CASCADE ANNEALING IN TUNGSTEN, MOLYBDENUM AND CHROMIUM —G. Nandipati, A. Pattanayak, W. Setyawan, R. J. Kurtz (Pacific Northwest National Laboratory) A. Shelby and B. D. Wirth (University of Tennessee)	178
9	FUSION SYSTEM DESIGN	
9.1	PREPARATION FOR MATERIAL STANDARDIZATION OF ALLOY F82H —H. Sakasegawa, H. Tanigawa, T. Miyazawa, T. Hirose (National Institutes for Quantum and Radiological Science and Technology, Japan), R.K. Nanstad and Y. Katoh (Oak Ridge National Laboratory)	182
10	IRRADIATION METHODS, EXPERIMENTS AND SCHEDULES	
10.1	THE MFE-RB-19J HFIR IRRADIATION EXPERIMENT —J.L. McDuffee, J.W. Geringer (Oak Ridge National Laboratory)	188

TABLE OF CONTENTS

10.2	NEUTRON FLUENCE MEASUREMENTS AND RADIATION DAMAGE CALCULATIONS FOR THE JP30 AND JP31 EXPERIMENTS IN HFIR—L. R. Greenwood, B. D. Pierson, M. G. Cantaloub and T. Trang-Le (Pacific Northwest National Laboratory)	190
10.3	HFIR IRRADIATION EXPERIMENTS—J.P. Robertson (Oak Ridge National Laboratory)	198

TABLE OF CONTENTS

1	FERRITIC/MARTENSITIC STEEL DEVELOPMENT	
1.1	DEVELOPMENT OF CASTABLE NANOSTRUCTURED ALLOYS AS ADVANCED RAFM STEELS—L. Tan (Oak Ridge National Laboratory)	1
	<p>Two new heats of CNAs designed using computational thermodynamics were fabricated by vacuum induction melting. The two alloys are intended to have different amounts of MX and $M_{23}C_6$ precipitates to study the effect of the precipitates on mechanical properties. Microstructural characterization of the alloys in the normalized and tempered condition showed much finer Ta-rich precipitates with higher densities than literature-reported values for F82H-BA07. However, clusters of Ta/Ti-rich coarse particles were observed in the alloys, which is likely to reduce the amount of Ta/Ti-rich fine particles and may consequently diminish the difference in mechanical properties between the alloys that are being studied.</p>	
1.2	MODIFIED 3Cr-3WVTa BAINITIC STEEL PLATE PRODUCTION FOR PROPERTY EVALUATION—Y. Yamamoto (Oak Ridge National Laboratory)	4
	<p>A new alloy design strategy for PWHT-free 3Cr-3WVTa bainitic steel has been proposed; reducing the as-normalized hardness without losing high hardenability, in order to reduce potential property inhomogeneity across weldments. The steel with 2Mn-0.5Si-0.05C was down-selected for scale-up, based on the study of lab-scale heats. A vacuum induction melted heat with low carbon combined with high Mn and Si has been fabricated by a commercial manufacturer and delivered to ORNL. A hot-forged and rolled plate, 16 mm thick, was prepared for various property evaluations including weld studies. Tensile, creep, and Charpy impact testing is planned.</p>	
1.3	IMPACT OF NEUTRON IRRADIATION ON THERMAL HELIUM DESORPTION FROM IRON—X. Hu, K.G. Field (Oak Ridge National Laboratory), S. Taller (University of Michigan, Ann Arbor), Y. Kath (Oak Ridge National Laboratory), B.D. Wirth (University of Tennessee, Knoxville, Oak Ridge National Laboratory)	9
	<p><i>Abstract of a manuscript submitted to Journal of Nuclear Materials (in revision).</i></p>	
2	ODS AND NANOCOMPOSITED ALLOY DEVELOPMENT	
2.1	ALLOY YTTRIUM AND TITANIUM VARIATION EFFECTS ON NANO-OXIDES IN NANOSTRUCTURED FERRITIC ALLOYS—N.J. Cunningham, G.R. Odette (University of California, Santa Barbara)	10
	<p>Twelve nanostructured ferritic alloys were produced, varying Y_2O_3 from 0.2 to 0.5 wt.% and Ti to maintain atom Ti:Y ratios of 1.6, 2.4, and 3.1. Small angle neutron scattering measured systematic increases in number density and volume fraction with increased Y_2O_3 and alloy Ti:Y, with greater variation occurring at either 0.2 or 0.5 wt.% Y_2O_3. Oxide size was similar except for the 0.2 wt.% Y_2O_3. Atom probe tomography measured slight decreases in oxide Y/Ti and Cr for the 3.1 Ti:Y ratio alloy. Minimizing Ti in the 1.6 Ti:Y alloy, were still able to produce high number densities of oxides.</p>	

TABLE OF CONTENTS

- 2.2 A NUMERICAL INVESTIGATION OF DELAMINATION EFFECTS ON THE FRACTURE BEHAVIOR OF A 14YWT NANOSTRUCTURED FERRITIC ALLOYS (NFA-1)—C. Ruggieri, M. E. Alam, G. R. Odette, (UCSB) 19**

This investigation addresses a numerical investigation of the crack front fields and effects of crack-tip constraint in subsized SE(B) specimens with transverse delamination. Nonlinear numerical analyses of very detailed 3-D finite element models of SE(B) fracture specimens for a 14 YWT nanostructured ferritic alloy (NFA) enable assessing the effects of prescribed delamination cracks on the crack front fields with increased loading levels. Further, the work addresses the potential coupled effects of geometry and delamination size on crack-tip constraint, thereby providing valuable insight into the effect of delamination cracks on macroscopic fracture behavior in conventional fracture specimens. Overall, the present exploratory analyses reveal important features of 3-D crack front fields in fracture specimens with transverse delamination that have a direct bearing on the often observed toughness increase in fracture testing of materials with through-thickness anisotropy in mechanical properties.

- 2.3 STRUCTURAL AND CHEMICAL EVOLUTION IN NEUTRON IRRADIATED AND HELIUM-INJECTED FERRITIC ODS PM2000 ALLOY—Hee Joon Jung, Dan J Edwards, Richard J Kurtz (Pacific Northwest National Laboratory), Takuya Yamamoto, Yuan Wu and G. Robert Odette (University of California, Santa Barbara) 30**

This extended abstract reports on some of the major results in a paper recently published in the Journal of Nuclear Materials
<http://dx.doi.org/10.1016/j.jnucmat.2016.11.022>.

- 2.4 HIGH TEMPERATURE HELIUM IMPLANTATION OF NI/FE – Y₂Ti₂O₇ BILAYERS—T. Stan, Y. Wu, G.R. Odette, T. Yamamoto (University of California Santa Barbara), and Y. Wang (Los Alamos National Laboratory) 32**

The 2.5 nm average diameter Y-Ti-O nano-oxides (NOs) in Nanostructured Ferritic Alloys (NFAs), help impede dislocation climb and glide, stabilize dislocation and grain structures, and trap He in harmless nm-scale bubbles. To complement other studies of the NOs themselves, mesoscopic-scale bilayer interfaces were fabricated by electron beam deposition of Fe films on {100}, {110}, and {111} Y₂Ti₂O₇ (YTO) bulk single crystal substrates. Four Fe-YTO orientation relationships were observed, and reported here. After encapsulating the bilayers with Ni, the Fe side was high temperature (700 °C) ion implanted using 1.6 MeV He⁺ to a dose of 2.26x10¹⁶ He/cm². Radiation enhanced diffusion led to the intermixing of Ni and Fe, and to the formation of Kirkendall 1µm voids at the Ni/Fe-YTO interfaces. Further, He bubbles were seen in all of the Ni/Fe films, as well as inside of some YTO substrates. No bubbles were observed at the metal-oxide interfaces.

TABLE OF CONTENTS

2.5	HELIUM SEQUESTRATION AT NANOPARTICLE-MATRIX IN HELIUM+HEAVY ION IRRADIATED NANOSTRUCTURED FERRITIC ALLOYS —C. M. Parish, K.A. Unocic, L. Tan, D.T. Hoelzer, Y. Katoh (Oak Ridge National Laboratory), S.J. Zinkle (ORNL and University of Tennessee), S. Kondo (Kyoto University), L.L. Snead (Massachusetts Institute of Technology)	43
	<p>The disposition of He in three classes of materials – FeCr-based NFA, FeCrAl NFA and castable nanostructured alloy (CNA) – have been explored by means of scanning/transmission electron microscopy (STEM) combined with multivariate statistical analysis (MVSA) data mining. In particular, this report focuses on directly relating bubbles/cavities to engineered precipitates at high resolution.</p>	
2.6	ON THE ASSOCIATION BETWEEN BUBBLES AND NANO-OXIDES IN ANNEALED AND HELIUM IMPLANTED 14YWT —Y. Wu, T. Stan, T. Yamamoto, G. R. Odette (University of California Santa Barbara), and J. Ciston (Lawrence Berkeley National Laboratory)	50
	<p>To further the understanding of the interaction between helium and nano-oxides (NOs) in nanostructured ferritic alloys (NFAs), a 14YWT alloy was annealed to coarsen the NOs, and He implanted to produce He bubbles. High resolution transmission electron microscopy shows that smaller NOs are associated with smaller bubbles, while some of the largest NOs (>6 nm) have two bubbles. Most bubbles nucleate near dislocation cores at {111} NO facets.</p>	
3	CERAMIC COMPOSITE STRUCTURAL MATERIAL DEVELOPMENT	
3.1	LOW TEMPERATURE AIR BRAZE PROCESS FOR JOINING SILICON CARBIDE COMPONENTS USED IN HEAT EXCHANGERS, FUSION AND FISSION REACTORS, AND OTHER ENERGY PRODUCTION AND CHEMICAL SYNTHESIS SYSTEMS —J.R. Fellows, C.A. Lewinsohn (Ceramatec, Inc.), Y. Katoh, T. Koyanagi (Oak Ridge National Laboratory)	57
	<p><i>Abstract of a paper in press for Ceramic Engineering and Science Proceedings</i></p>	
3.2	LOW ACTIVATION JOINING OF SiC/SiC COMPOSITES FOR FUSION APPLICATIONS: MODELING THERMAL AND IRRADIATION-INDUCED SWELLING EFFECTS ON INTEGRITY OF Ti₃SiC₂/SiC JOINT —B.N. Nguyen, C.H. Henager, Jr., and R.J. Kurtz (Pacific Northwest National Laboratory) M. Ferraris (Politecnico di Torino, Italy) Y. Katoh (Oak Ridge National Laboratory)	58
	<p>Referring to the studies on the miniature THG specimen with the fully bonded joint [1-2], we have investigated the same THG specimen made of CVD-SiC substrates joined by a 10-to-15-micron Ti₃SiC₂/SiC bonding layer. Such a specimen was tested in the High Flux Isotope Reactor (HFIR) at Oak Ridge National Laboratory at 800°C and 5 dpa. Before testing, SEM examination indicated no transverse cracks or microcracks in the bonding layer or at the interfaces. After the irradiation experiment, limited crack propagation along the interface between the bonding layer and the CVD substrate was observed, however, the interface bonding appeared mainly intact. Microcracks were also found in the Ti₃SiC₂/SiC joint layer, but no extensive crack propagation was observed. No irradiation experiments were reported at temperatures lower than 800°C for the Ti₃SiC₂/SiC-joined CVD-SiC specimens although Ref. [1] reports experiments at 500°C and 3 dpa for similar specimens containing a bonding layer made of a different material.</p>	

TABLE OF CONTENTS

- 3.3 POSITRON ANNIHILATION SPECTROSCOPY INVESTIGATION OF VACANCY DEFECTS IN NEUTRON-IRRADIATED 3C-SiC**—Xunxiang Hu ¹, Takaaki Koyanagi ¹, Yutai Katoh ¹, Brian D. Wirth ^{1, 2} (¹ Oak Ridge National Laboratory, ² University of Tennessee, Knoxville) **66**

Abstract of a manuscript submitted to Physical Review B

- 3.4 VACANCY EFFECTS ON THE FORMATION OF HELIUM AND KRYPTON CAVITIES IN 3C-SiC IRRADIATED AND ANNEALED AT ELEVATED TEMPERATURES***—Hang Zang, Wenbo Liu, Tao Li, Chaohui He, Di Yun (Department of Nuclear Science and Technology, Xi'an Jiaotong University, China) Weilin Jiang, Arun Devaraj, Danny J. Edwards, Charles H. Henager Jr., Richard J. Kurtz (Pacific Northwest National Laboratory) and Zhiguang Wang (Institute of Modern Physics, Lanzhou, China) **67**

Extended abstract of a paper in Nuclear Instruments and Methods in Physics Research B <http://dx.doi.org/10.1016/j.nimb.2016.11.017> [1]

4 HIGH HEAT FLUX MATERIALS AND COMPONENT TESTING

- 4.1 DESIGN AND DEVELOPMENT OF NOVEL Cu ALLOYS FOR FUSION ENERGY APPLICATIONS**—Ying Yang (Oak Ridge National Laboratory), Steven J. Zinkle (University of Tennessee at Knoxville and Oak Ridge National Lab), and Lance Snead (Massachusetts Institute of Technology) **69**

During the six months from June to December 2016, we have completed the electrical conductivity measurements on previously developed Cu-Cr-Nb-Zr alloys, developed a thermodynamic database for the Cu-Cr-Ta-Zr alloy systems, and designed and fabricated one new Cu-Cr-Nb-Zr plus two new Cu-Cr-Ta-Zr alloys.

- 4.2 MECHANICAL PROPERTIES CHARACTERIZATION OF 90-97wt% WNiFe HEAVY ALLOYS**—M.E. Alam, S. Pal, K. Fields, G. R. Odette (University of California, Santa Barbara) **73**

Ductile phase toughening (DPT) is a promising approach to improve toughness of brittle materials like tungsten (W). Four commercial liquid phase sintered W-based alloy composites, containing 90, 92.5, 95 and 97 wt.% W, with the balance of a 7:3 wt. % Ni:Fe ductile solid solution phase, was characterized. Microhardness increases with increasing W% slowly at room temperature (RT), but more rapidly at liquid nitrogen temperature (LN₂). Tensile strength increases and ductility decreases with decreasing temperature up to 95W, and remains relatively unchanged at 97W. Pre-cracked single edge notch bend bar fracture toughness tests at RT shows stable crack growth with average maximum load initiation toughness, K_{Jc} , $\approx 102 \pm 7 \text{ MPa}\sqrt{\text{m}}$, relatively independent of the W fraction up to 95 wt.%, but decreasing to $\approx 73 \pm 13 \text{ MPa}\sqrt{\text{m}}$ for the 97W alloy. Low temperatures toughness tests show the brittle-to-ductile transition temperature (BDTT) increases with increasing W fraction from $\approx -150^\circ\text{C}$ for 90W to $\approx -50^\circ\text{C}$ for 97W alloy.

TABLE OF CONTENTS

- 4.3 EXPERIMENTAL MEASUREMENTS OF SURFACE DAMAGE AND RESIDUAL STRESSES IN MICRO-ENGINEERED PLASMA-FACING MATERIALS-** David Rivera, Richard Wirz, Nasr M. Ghoniem (University of California, Los Angeles) **83**

The thermomechanical damage and residual stresses in plasma-facing materials operating at high heat flux are experimentally investigated. Materials with micro-surfaces are found to be more resilient, when exposed to cyclic high heat flux generated by arc-jet plasma. We demonstrate that W surfaces with micro-pillar type surface architecture have significantly reduced residual thermal stresses after plasma exposure, as compared to those with flat surfaces. X-ray diffraction (XRD) spectra of the W-(110) peak reveal that broadening of the FWHM for micro-engineered samples is substantially smaller than corresponding flat surfaces. Cyclic plasma heat loading is shown to anneal out most of the residual stresses in micro-engineered surfaces, consistent with relaxation of residual thermal. The initial residual stress state of flat W samples is compressive (-1.3 GPa), and after 50 plasma cycles, it relaxes to -1.0 GPa. Micro-engineered samples show that the initial residual stress state is compressive at (-250 MPa), and remains largely unchanged after plasma exposure.

- 4.4 NEUTRON IRRADIATION EFFECTS IN TUNGSTEN**—L.M. Garrison, Y. Katoch, M. McAlister (Oak Ridge National Laboratory), L. L. Snead (MIT), T. S. Byun (PNNL) **102**

Approximately 440 TITAN program samples were irradiated in HFIR at temperatures from 70 to 900°C and fast neutron fluences of 0.01 to 20 $\times 10^{25}$ n/m² (E>0.1 MeV). Single crystal tungsten samples irradiated up to 9 $\times 10^{25}$ n/m² (E>0.1 MeV) have been tensile tested. All samples tensile tested at 22°C had brittle failures. Before irradiation, ductility is observed starting at 300°C test temperature. For material irradiated to 0.55 dpa at 430°C the ductile to brittle transition temperature (DBTT) seen in tensile tests shifted above 300°C, and for material irradiated to 0.4 dpa at 700°C the DBTT shifted above 500°C.

- 4.5 PROGRESS IN THE STUDY OF ION IRRADIATION IN TUNGSTEN**—Weilin Jiang, Karen Kruska, Charles H. Henager Jr., and Richard J. Kurtz (Pacific Northwest National Laboratory) **115**

This progress report describes experimental preparations and presents initial characterization results from x-ray diffraction (XRD) and scanning electron microscopy (SEM) for poly- and mono-crystalline tungsten (W). The XRD data suggest that the polycrystalline sample is single-phase body-centered cubic tungsten with an average crystallite size of ~40 nm. The SEM results indicate that the polycrystalline tungsten has a grain size ranging from 1 to 5 μ m without visible large cavities. The high-resolution XRD from a symmetric $2\theta-\omega$ scan shows that the monocrystalline tungsten has only one strong, sharp W (222) diffraction peak, confirming that the sample is a (111)-oriented tungsten single crystal. Asymmetric ω scan exhibits multiple peaks around the primary (222) peak, indicating that the single crystal has a mosaic structure. Pole figures from XRD measurements exhibit distinctive (110) and (111) poles, which match the simulation poles for (111) oriented tungsten. Diffraction rings from polycrystalline tungsten are not observed.

TABLE OF CONTENTS

- 4.6 INTERACTION OF INTERSTITIAL CLUSTERS WITH RHENIUM, OSMIUM, AND TANTALUM IN TUNGSTEN**—W. Setyawan, G. Nandipati, and R. J. Kurtz (Pacific Northwest National Laboratory) **120**

Extended Abstract of a recently published paper: W. Setyawan, G. Nandipati, R. J. Kurtz, "Ab Initio Study of Interstitial Cluster Interaction with Re, Os, and Ta in W", Journal of Nuclear Materials 484 (2017) 30-41, doi: 10.1016/j.jnucmat.2016.11.002

- 4.7 NEUTRON IRRADIATION EFFECTS IN TUNGSTEN-COPPER COMPOSITES**—L.M. Garrison, Yutai Katoh (Oak Ridge National Laboratory) **122**

As part of the TITAN program, two types of tungsten-copper composites were irradiated in HFIR at temperatures from 300 to 900°C and fast neutron fluences of 0.01 to 20 $\times 10^{25}$ n/m² at E>0.1 MeV. One material was a tungsten-copper laminate composite composed of 0.1 mm alternating layers of tungsten and copper. The other material was a tungsten-copper powder sintered composite, with 75% W and 25% Cu. Tensile tests of unirradiated and irradiated tungsten-copper sintered composite have been completed.

- 4.8 HIGH-HEAT FLUX TESTING OF LOW-LEVEL IRRADIATED MATERIALS USING PLASMA ARC LAMPS**—A.S. Sabau, S. Gorti, C. Schaich, J. Kiggans, Y. Katoh (Oak Ridge National Laboratory) **129**

Thermo-mechanical model simulations of the high-heat flux testing (HHFT) of W/SiC specimens were completed. Preliminary results indicated that stresses experienced by the specimens during HHFT are relatively small compared to those for the W/F82H specimens. A new line-focus reflector for the Plasma Arc Lamp was designed to increase the heat flux to its maximum achievable for the maximum arc temperature. The fabrication of the reflector is imminent.

- 5 MAGNETIC AND DIAGNOSTIC SYSTEM MATERIALS**

No contributions this reporting period.

- 6 FUSION CORROSION AND COMPATIBILITY SCIENCE**

- 6.1 CHARACTERIZATION OF FeCrAlMo AFTER EXPOSURE TO FLOWING Pb-LI AT 500°-600°C**—B. A. Pint and J. Jun (Oak Ridge National Laboratory, USA) **133**

The second monometallic thermal convection loop (TCL) using Kathal FeCrAlMo alloy APMT tubing and specimens completed 1000 h using commercial purity eutectic Pb-Li with a peak temperature of 600°C. Characterization of the oxide surface morphologies after exposure based on the pre-oxidation conditions suggest that the oxide formed in PbLi is the most adherent. The tensile properties of selected hot and cold leg specimens have been measured at room temperature and no significant degradation occurred between 515°-600°C in the second loop.

TABLE OF CONTENTS

7	MECHANISMS AND ANALYSIS	
7.1	THERMAL AND ELECTRICAL PROPERTIES OF MAX PHASES AFTER NEUTRON IRRADIATION —C. Ang*, C. Shih, S.J. Zinkle, C. Silva, C. Parish, N. Cetiner, P. Edmondson, Q. Smith and Y. Katoh (Oak Ridge National Laboratory)	137
	<p>$M_{n+1}AX_n$ (MAX) phases of “Ti_3SiC_2” and “Ti_2AlC” composition were neutron irradiated in HFIR to 2×10^{25} n/m² ($E > 0.1$ MeV) or ~ 2 dpa based on the SiC displacement cross-section (see DOE/ER-0313/58). Compositions were determined to be ~80% MAX phase. During irradiation at ~400°C, 5-10 wt% or less decomposed to MX. Swelling was higher in the Al-variant, with a c-axis swelling ($\Delta c/c$) of 3.1% compared to 1.6% for the Si-variant. After irradiation at ~630-700°C, unit cell swelling was not observed, and equibiaxial flexural strength values were within 80-95% of unirradiated values. The prior program under the Unique Materials FOA was able to obtain thermal diffusivity and dilatometry annealing data, but the quantitative determination of activation energies was improved by electrical resistivity annealing. This was obtained in a Nuclear Science User Facilities Rapid Turnaround Experiment in October 2016. Preliminary data suggested differences in defect configurations, and/or concentrations of defects in Ti_3SiC_2 and Ti_3AlC_2.</p>	
7.2	DAMAGE MECHANISM INTERACTIONS AT THE PLASMA-MATERIALS INTERFACE (Early Career Award) —C. M. Parish, K. Wang (Oak Ridge National Laboratory)	141
	<p>Effort this reporting period emphasized exploration of effects of starting microstructures (hot rolled state vs recrystallized state) on the plasma materials interaction in tungsten using multi-types of electron microscopy characterization. This has included performing tKD analysis on isolated tungsten nanotendrils to understand the growth mechanism of the nanotendrils in low energy helium ions exposure environments.</p>	
8	MODELING PROCESSES IN FUSION SYSTEM MATERIALS	
8.1	STRENGTHENING DUE TO RADIATION INDUCED OBSTACLES IN Fe AND FERRITIC ALLOYS —Yu. N. Osetskiy (Oak Ridge National Laboratory)	148
	<p>Irradiation of structural alloys by neutrons and ions lead to formation of a high density of nanoscale features such as second phase precipitates, voids and gas-filled bubbles. These objects are obstacles to dislocation motion and cause wanted or unwanted changes in mechanical properties. In order to predict materials behavior these obstacles must be characterized as well as their individual strength estimated. The only technique that allows this at the scale of nanometers is classical molecular dynamics (MD). In this work we modeled vacancy voids, He-filled bubbles, Cu precipitates and rigid inclusions in a bcc-Fe matrix. At the current stage of the research we investigated $\frac{1}{2}\langle 111 \rangle\{110\}$ edge dislocations. During its motion this dislocation cannot change its glide plane (cannot cross-slip) to avoid interaction with obstacles and therefore produces maximum effect on strengthening. The results obtained in this research will be used to improve theoretical prediction of mechanical property changes.</p>	

TABLE OF CONTENTS

8.2 DEVELOPMENT OF INTERATOMIC POTENTIALS IN TUNGSTEN-RHENIUM SYSTEMS—W. Setyawan and R. J. Kurtz (Pacific Northwest National Laboratory) 151

Reference data are generated using ab initio methods to fit interatomic potentials for W-Re system. The reference data include single phases of W and Re, strained structures, slabs, systems containing several concentrations of point defects, melt structures, structures in the σ and χ phases, and structures containing several concentrations of solid solutions of Re in bcc W and W in hcp Re. The initial fit of the angular-dependent potential for pure W has been completed. The potential is capable of reproducing the cohesive energy of single phases of W and the equation of states of bcc W. Melting behavior and defect formation energies will be explored in the future.

8.3 STRUCTURES AND TRANSITIONS IN TUNGSTEN GRAIN BOUNDARIES—Timofey Frolov (Lawrence Livermore National Laboratory), Qiang Zhu (University of Nevada Las Vegas), Jaime Marian (University of California Los Angeles) and Robert E. Rudd (Lawrence Livermore National Laboratory) 159

Recrystallization determines the upper extent of the operating temperature of tungsten as a divertor or first-wall material. At temperatures above the onset of recrystallization, migrating grain boundaries sweep out defects that contribute to hardening, making the material brittle. Thermomechanical models to predict recrystallization and its effect on mechanical properties have to be informed of the mechanisms of grain boundary migration, their structure and kinetic properties at tokamak operating temperatures. In this work grain boundary structures and energies as a function of misorientation and inclination were generated using atomistic simulations with several empirical potentials and compared with the available DFT calculations. We find new ground states of previously studied boundaries by performing grand canonical optimization of the structure. The finding of the true ground states of grain boundaries at temperatures relevant to tokamak operation has important consequences for recrystallization and embrittlement.

8.4 MODELING DUCTILE-PHASE TOUGHENED TUNGSTEN FOR PLASMA-FACING MATERIALS: PROGRESS IN DAMAGE FINITE ELEMENT ANALYSIS OF THE TUNGSTEN-COPPER BEND BAR TESTS—B. N. Nguyen, C. H. Henager, Jr., R. J. Kurtz (Pacific Northwest National Laboratory) 171

A promising approach to increasing fracture toughness and decreasing the ductile-brittle transition temperature (DBTT) of a W-alloy is by ductile-phase toughening (DPT) [1-3]. In this method, a ductile phase is included in a brittle matrix to prevent fracture propagation by crack bridging or crack deflection. Liquid-phase sintered W-Ni-Fe alloys and hot-pressed and sintered W-Cu composites are two examples of such materials that PNNL and University of California at Santa Barbara are investigating. However, there is a need for improved mechanical property models of such composite systems in order to begin to optimize these structural materials with regard to strength and fracture toughness. This report describes such a model that has recently been developed at PNNL.

TABLE OF CONTENTS

8.5	OKMC STUDY OF COMPARISON OF CASCADE ANNEALING IN TUNGSTEN, MOLYBDENUM AND CHROMIUM —G. Nandipati, A. Pattanayak, W. Setyawan, R. J. Kurtz (Pacific Northwest National Laboratory) A. Shelby and B. D. Wirth (University of Tennessee)	178
	<p>Results are obtained and discussed using the object kinetic Monte Carlo (OKMC) code KSOME [1] to simulate annealing of primary cascade damage in bulk tungsten (W), molybdenum (Mo) and chromium (Cr) for primary knock-on atom (PKA) energies of 7.5 keV and 15 keV at 300 K. Differences in defect mobility and, perhaps, cascade defect structures appear to be able to account for the observed annealing differences, but more work is required to fully understand the observations.</p>	
9	FUSION SYSTEM DESIGN	
9.1	PREPARATION FOR MATERIAL STANDARDIZATION OF ALLOY F82H —H. Sakasegawa, H. Tanigawa, T. Miyazawa, T. Hirose (National Institutes for Quantum and Radiological Science and Technology, Japan), R.K. Nanstad and Y. Katoh (Oak Ridge National Laboratory)	182
	<p>Existing codes such as RCC-MR and ASME define the required material data for the qualification of a new material. The result of gap analyses referring to these codes indicated that we now have adequate F82H material data to meet most requirements, but there are still some missing material data. It is necessary to continue some tests to comply with the requirements. We plan to integrate the material databases, to qualify F82H within the ASTM system.</p>	
10	IRRADIATION METHODS, EXPERIMENTS AND SCHEDULES	
10.1	THE MFE-RB-19J HFIR IRRADIATION EXPERIMENT —J.L. McDuffee, J.W. Geringer (Oak Ridge National Laboratory)	188
	<p>The HFIR RB-19J experiment used a new design with a gadolinium metal cylinder thermal neutron shield to modify the fast/thermal neutron ratio over the life of the experiment. The experiment contains six cylindrical holders (four temperature zones) which houses ~1300 tungsten and steel specimens. Assembly of the RB19J capsule was completed in May 2016 and installed in HFIR in June 2016. The first irradiation cycle, number 466, started June 14 2016. Starting temperatures stabilized within design ranges for the 500°C and the 800°C holders. The 1200°C and the 300°C were lower and higher than designed by about 50°C and 100°C respectively. The fourth and last irradiation cycle was completed in December 2016. It was decided to complete at four cycles instead of six due to concerns with possible gadolinium burn-out and risk of excessive tungsten to rhenium and osmium transmutation.</p>	

TABLE OF CONTENTS

10.2	NEUTRON FLUENCE MEASUREMENTS AND RADIATION DAMAGE CALCULATIONS FOR THE JP30 AND JP31 EXPERIMENTS IN HFIR— L. R. Greenwood, B. D. Pierson, M. G. Cantaloub and T. Trang-Le (Pacific Northwest National Laboratory)	190
-------------	--	------------

The JP30 and JP31 experiments were irradiated in target positions E2 and B4, respectively, of HFIR in cycles 439 starting November 21, 2011 through cycle 449 ending August 24, 2013 for a total exposure of 276.13 EFPD (effective full power days) at a nominal power level of 85 MW for a total exposure of 23471.28 MWD (megawatt days). Neutron dosimetry monitors fabricated by PNNL were inserted in the JP30 and JP31 experimental assemblies at various elevations. After the irradiation, the neutron fluence monitors were recovered and sent to PNNL for analysis. The activated monitor wires were analyzed to determine activation rates that were used to adjust the neutron fluence spectrum at each irradiation position. The adjusted neutron fluence spectra were then used to calculate radiation damage parameters.

10.3	HFIR IRRADIATION EXPERIMENTS— J.P. Robertson (Oak Ridge National Laboratory)	198
-------------	---	------------

The HFIR completed 3.3 cycles during the second half of 2016. Cycle 466 ended on July 7, 2016, accumulating 1970.95 MWD. Cycle 467 began on July 26 and ended on August 18, 2016 (2003.84 MWD), Cycle 468 began on September 6 and ended on September 30, 2016 (2036.29 MWD), and Cycle 469 began on November 15 and ended on December 8, 2016 (1990.19 MWD).

1. FERRITIC/MARTENSITIC STEEL DEVELOPMENT

1.1 DEVELOPMENT OF CASTABLE NANOSTRUCTURED ALLOYS AS ADVANCED RAFM STEELS—L. Tan (Oak Ridge National Laboratory)

OBJECTIVE

Castable nanostructured alloys (CNAs) are being developed at ORNL to favor the formation of a larger amount of ultrafine precipitates in reduced-activation ferritic-martensitic steels. The high density of fine precipitates will improve high temperature strength and radiation resistance. The goal is to design two alloys with different amounts of MX (M=metal, X=C/N) and $M_{23}C_6$ precipitates, and analyze the effect of the precipitates on mechanical properties. This will lead to specification of appropriate amounts of the precipitates to obtain superior properties.

SUMMARY

Two new heats of CNAs designed using computational thermodynamics were fabricated by vacuum induction melting. The two alloys are intended to have different amounts of MX and $M_{23}C_6$ precipitates to study the effect of the precipitates on mechanical properties. Microstructural characterization of the alloys in the normalized and tempered condition showed much finer Ta-rich precipitates with higher densities than literature-reported values for F82H-BA07. However, clusters of Ta/Ti-rich coarse particles were observed in the alloys, which is likely to reduce the amount of Ta/Ti-rich fine particles and may consequently diminish the difference in mechanical properties between the alloys that are being studied.

PROGRESS AND STATUS

Introduction

The concept of developing CNAs was based on oxide-dispersion-strengthened (ODS) alloys that have super high strength providing superior radiation resistance and strength. Unlike mechanically alloyed ODS alloys, however, introducing and increasing the amount of MX precipitates in conventional RAFM steels is restricted by the high-temperature solubility of the elements forming the desired precipitates. Furthermore, excessively high content of the precipitate-forming elements can result in the formation of blocky precipitates and/or deteriorated ductility induced by too much dispersed-barrier-hardening. Therefore, the effects of the dominant precipitates on mechanical properties need to be investigated to obtain an optimum amount of the precipitates for superior properties.

Experimental Procedure

Two alloys were designed using the Calphad approach of computational thermodynamics. Figure 1a shows the two alloys (05 and 06) having C/(Ti+Ta) in atomic ratio of 2.26 and 2.64, respectively, which lead to less MX and $M_{23}C_6$ in alloy-05 compared to that in alloy-06. The designed mole fractions of MX precipitate in the two alloys are more than double of that in F82H or Eurofer97. The alloys were fabricated by vacuum induction melting at Carpenter Technology. The product compositions deviated somewhat from the design values. Figure 1b shows the temperature-dependent phase fraction in the two alloys using the as fabricated compositions, which have C/(Ti+Ta) in atomic ratio of 3.83 and 2.16 for alloy-05 and -06, respectively. Alloy-05 has less MX, but more $M_{23}C_6$, than alloy-06 according to the product compositions. The fabricated alloys provide opportunities to understand if a larger amount (1% or more in mole fraction) of MX can compensate for the reduced amount (~1% mole fraction) of $M_{23}C_6$ in terms of strength and other properties. Scanning electron microscopy was used to characterize the alloys in the normalized and tempered condition.

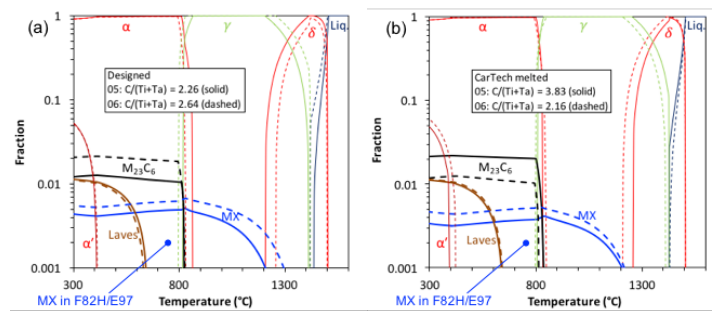


Figure 1. Calculated temperature-dependent phase fractions in (a) designed and (b) fabricated CNAs.

Results

Figure 2 shows backscattered electron images (BEIs) of the two alloys (bottom row), illustrating significantly finer Ta-rich particle distributions (in white) with higher densities than the literature data of F82H-BA07 (top row). The overall microstructure of alloy-06 is shown in Figure 3 (left), indicating the presence of a blocky TiN at lower left and many coarse Ta-rich particles at center. The center area is shown at higher magnification in Figure 3 (right), which exhibits the coarse Ta-rich particles on the order of 1 μm , similar to the sizes of the Ta-rich particles in Fig. 2 Ta-EDS of F82H-BA07. Additionally, some dark particles of sub-micrometer size, likely to be Ti-rich particles, are shown in Figure 3 (right). The presence of the clusters of Ta/Ti-rich coarse particles reduces the available Ta/Ti content available to form ultrafine MX precipitates, which may diminish the difference in mechanical properties between the two alloys.

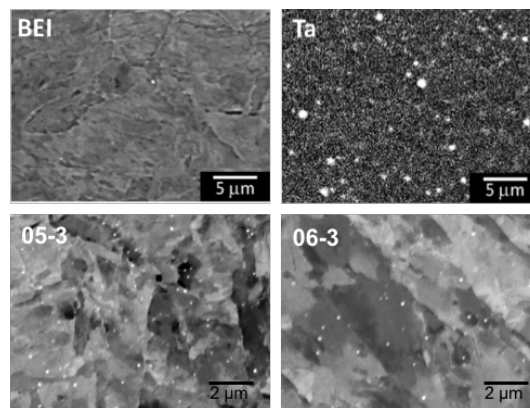


Figure 2. BEIs of the two new CNAs (alloy-05 and -06) compared to the BEI and Ta-EDS of F82H-BA07.

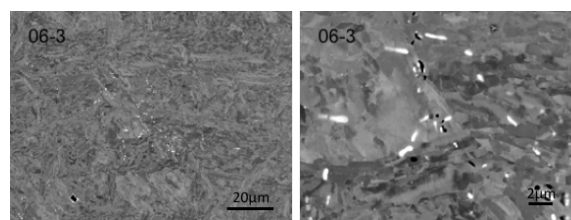


Figure 3. BEIs of alloy-06 at two magnifications.

Thermomechanical treatments at different temperatures are being explored to examine the effect of processing temperature on microstructure and mechanical properties of the alloys. Mechanical properties, including Vickers hardness, tensile, and Charpy impact toughness will be evaluated for the alloys in different conditions.

1.2 MODIFIED 3Cr-3WVTa BAINITIC STEEL PLATE PRODUCTION FOR PROPERTY EVALUATION—Y. Yamamoto (Oak Ridge National Laboratory)

OBJECTIVE

This work aims to develop new bainitic steels, based on 3Cr-3WV(Ta) steels originally developed at ORNL. The goal is mechanical properties of both base metal and weldments superior to those of existing commercial bainitic steels or ferritic-martensitic (F-M) steels, together with no requirement for post-weld heat treatment (PWHT). The target applications are high temperature structural components in fusion reactors such as vacuum vessel, structural ring which supports the blanket modules, and magnet shields, to be used at or above the 400-500°C range. Improvement of long-term creep properties by introducing additional fine, stable second-phase dispersions, as well as maintaining good weldability, is targeted via optimization of alloy composition and thermo-mechanical heat treatment.

SUMMARY

A new alloy design strategy for PWHT-free 3Cr-3WVTa bainitic steel has been proposed; reducing the as-normalized hardness without losing high hardenability, in order to reduce potential property inhomogeneity across weldments. The steel with 2Mn-0.5Si-0.05C was down-selected for scale-up, based on the study of lab-scale heats. A vacuum induction melted heat with low carbon combined with high Mn and Si has been fabricated by a commercial manufacturer and delivered to ORNL. A hot-forged and rolled plate, 16 mm thick, was prepared for various property evaluations including weld studies. Tensile, creep, and Charpy impact testing is planned.

PROGRESS AND STATUS

Introduction

Developmental of new bainitic steels was initiated under Fusion Energy Materials Program in FY2014, as a modification of the original 3Cr-3WV(Ta) steels developed at ORNL [1, 2, 3]. The alloy design strategy is to improve creep performance through minor alloying additions of Mn, Si, and N (“Gen. I” steels). Computational thermodynamics tools were used to predict optimized minor alloying additions to promote the formation of stable MN precipitates (M: mainly V) in a wide temperature range below ~1100°C and increase the stability of $M_{23}C_6$ (M: mainly Cr) relative to M_7C_3 (M: mainly Cr). Improved oxidation resistance was also expected through the Si addition [4]. Although the creep-rupture properties have been successfully improved, the alloy modification also resulted in the hardness of the as-normalized materials being extremely high compared to than that of the original 3Cr-3WV(Ta) steels, whereas the hardness after tempering was lower than the original, indicating that the variation of the properties across the welded material (in as-weld condition) could be significant compared to the original 3Cr-3WVa(Ta) steels [5]. This suggests that the alloy design strategy of the Gen. I steels failed to meet the PWHT-free requirement.

Based on the results for Gen. I steels, it was suggested that relatively lowered hardness in the normalized conditions could be a key for the PWHT-free material design strategy since it could reduce the cross-weld property inhomogeneity compared to that of the base steels. In order to decrease the hardness in the normalized condition without losing the high “hardenability” to promote the carbide-free acicular bainite ferrite formation, a new alloy strategy with lower carbon and higher Mn, together with Si for improved oxidation resistance, was proposed, as “Gen II” steels. Evaluation of the lab-scale heats with this new alloy design strategy indicated that the steel with 2 wt.% Mn combined with 0.05% C (ID: MSLC2) successfully showed less hardness in the normalized condition compared to that of the original steel, whereas the hardness after tempering was not lower than the original. The cross-weld hardness distribution of the steels also indicated a successful reduction of the hardness inhomogeneity across the weld in the modified steel as shown in Figure 1, suggesting that the new design strategy would potentially be suitable for PWHT-free behavior. The MSLC2 steel was down-selected for the scale-up effort in order

to prepare various samples for property evaluation. In this report, the recent procurement of a large size ingot and preparation of the hot-rolled plate are summarized.

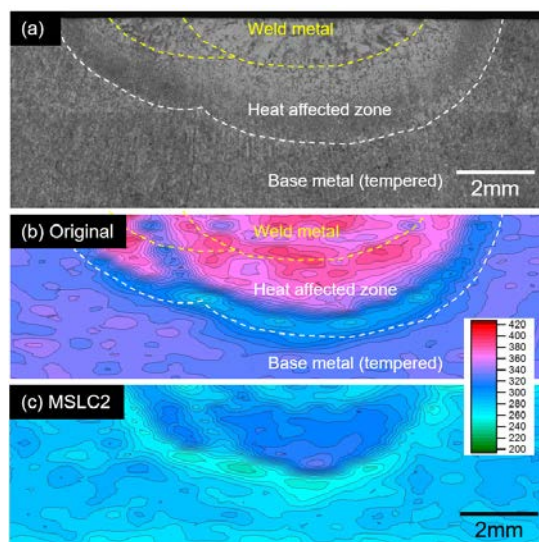


Figure 1. Microstructure and hardness maps for two bainitic steel weldments. Insert shows the Vickers hardness scale for the color code used.

Experimental Procedure

The alloy compositions of the original (“Original”) and modified (“MSLC2”) steels are listed in Table 1. The MSLC2 steel ingot was prepared by Sophisticated Alloys, Inc. (Butler, PA) using vacuum induction melting (VIM). Nearly ~25 kg of the melt was poured into a columnar shaped graphite mold 100 mm diameter and ~300 mm long. The ingot was sectioned into four pieces; hot-top, 100 mm length, 12 mm length, and ~190 mm length, and the 12 mm thick disc piece was further sectioned into small pieces for microstructure characterization of as-cast and normalized conditions. The 100 mm diameter x 100 mm length piece was homogenized at 1200°C for 4 h, forged in the radial direction to make a 50 mm thick plate, and then air-cooled to room temperature. The plate was soaked at 1100°C and hot-rolled with ~10% thickness reduction per pass with inter-pass annealing at 1100°C, to yield a 16 mm thick plate. The rolled plate was subsequently annealed at 1100°C for 30 min, and then air-cooled to room temperature. Several small pieces were sectioned from the rolled plate, and tempered at 700°C in laboratory air for various periods of time from 15 min to 4 h, followed by air cooling. Some of the small pieces were also tempered for 1 h in the temperature range 660 to 840°C, followed by air cooling. Vickers hardness tests were conducted on all heat treated specimens. The specimens were mounted in epoxy resin, ground and polished with conventional metallographic preparation technique, and then hardness tested with 500 g load. A minimum of 25 indents were measured for each specimen.

Table 1. Nominal compositions in weight percent, balanced Fe

Heat	Composition, wt.%							Remarks
	C	Mn	Si	Cr	V	W	Ta	
Original	0.10	0.40	0.16	3.0	0.2	3	0.1	3WVTa
MSLC2	0.05	2.00	0.5	3.0	0.2	3	0.1	Low C + 2Mn

Results

The as received VIM ingot is shown in Figure 2. There was no cracking or defects seen in the outer surface during visual inspection. The heat ID is “16114943”, and the analyzed chemical composition is Fe-3.1Cr-2.9W-0.22V-0.12Ta-1.9Mn-0.5Si-0.05C in weight percent, with 20 wppm oxygen and less than 50 wppm nitrogen, sulfur, and phosphorus.

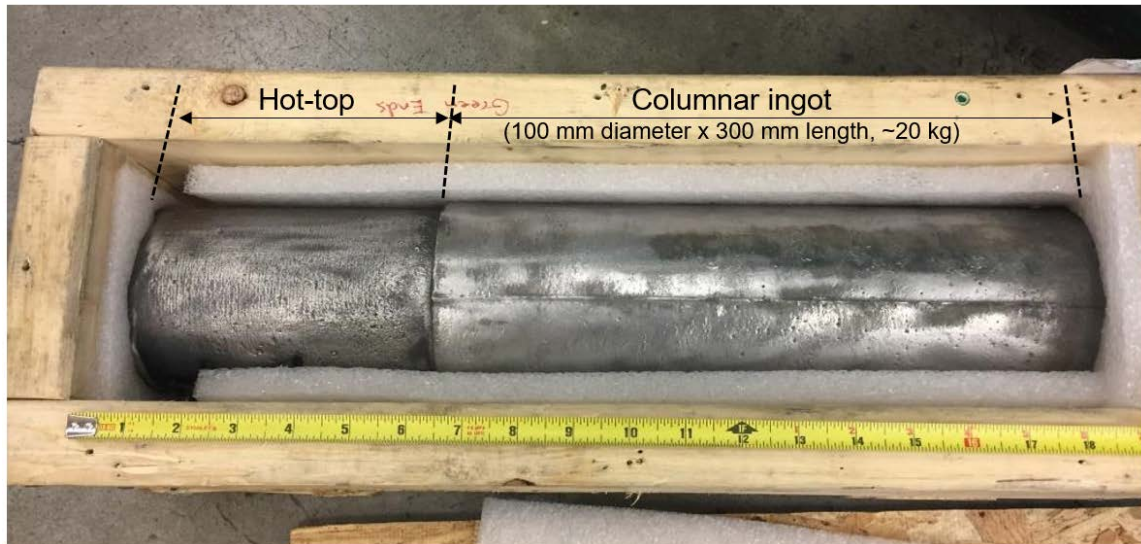


Figure 2. As-received VIM ingot of MSLC2 steel (the heat ID is “16114943”).

Figure 3 shows the optical micrographs of as-cast (3a) and normalized at 1100°C (3b) and 1200°C (3c, 3d), together with the Vickers hardness test results (3e). All microstructures show a typical bainitic microstructure. The as-cast microstructure consisted of irregular and coarse prior austenite grain (PAG) structure, whereas the normalized microstructure showed equiaxed PAGs. The PAG size became larger as the temperature or hold time increased. The hardness result showed a slightly wider variation of hardness in both as-cast and 1100°C normalized samples than that of the samples normalized at 1200°C. This indirectly indicates that annealing at 1200°C for more than 1 h would be required to break the solidification microstructure and homogenize the cast ingot.

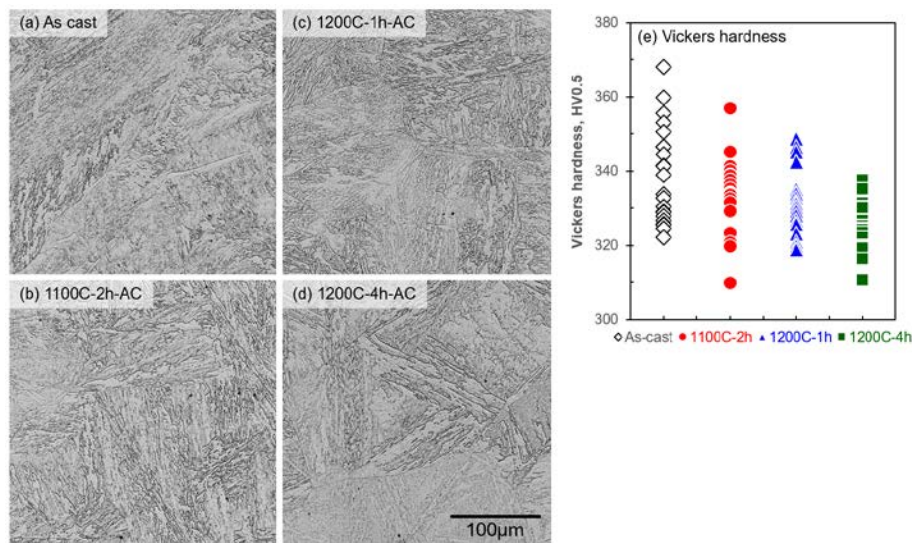


Figure 3. Optical micrographs of VIM-MSLC2 steel; (a) as-cast, (b) normalized at 1100°C for 2 h, (c) at 1200°C for 1 h, and (d) 1200°C for 4 h, together with (e) the Vickers hardness values.

Figure 4 illustrates the process sequence of the rolled plate preparation. The as cast ingot (4a) was successfully forged from 100 mm diameter to 50 mm thickness (4b) at 1200°C without any technical difficulties. The forged plate was hot-rolled and annealed at 1100°C (4c). There was no crack opening after forging and rolling. In the next step the rolled plate will be tempered, and it will be used for mechanical property evaluations including tensile, creep, and Charpy impact toughness testing of the base metal, as well as that of welded plate.

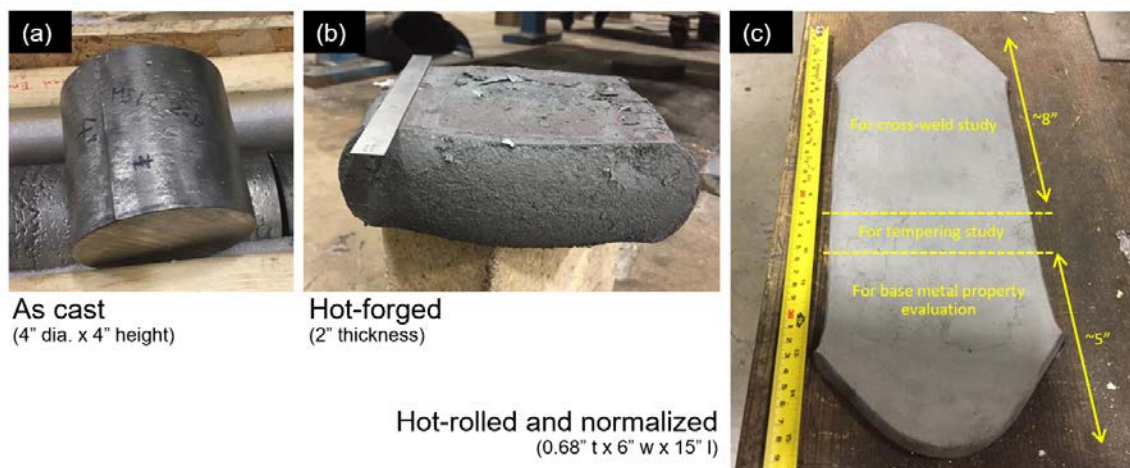


Figure 4. Process sequence of the rolled plate preparation; (a) as-cast ingot, (b) as-forged, and (c) rolled and annealed.

The hardness test results for tempered MSLC2 plate are summarized in Figure 5, showing the effect of the tempering time at 700°C (5a) and the tempering temperature (5b). The hardness of the as-normalized sample was ~350 HV, and it gradually decreased with increasing tempering time. The hardness also decreased with increasing tempering temperature up to 760-780°C, and then increased above that temperature range. The A_1 temperature (BCC \rightarrow BCC+FCC) calculated by computational thermodynamics was ~750°C, so that the transition of temperature dependence could be due to the

formation of austenite during tempering above the A_1 temperature (which transformed to un-tempered bainite or martensite during cooling to RT).

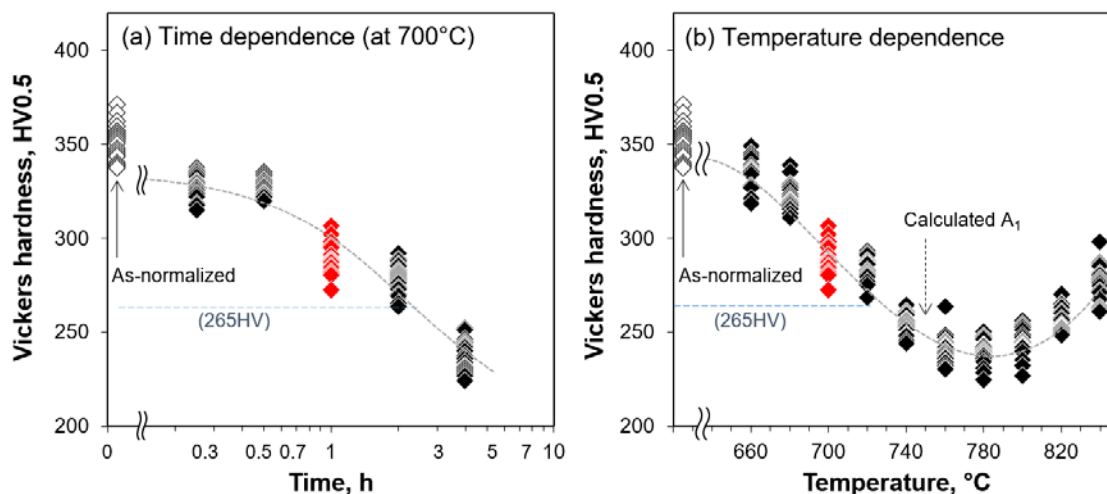


Figure 5. Effect of tempering time and temperature on the hardness. (a) Time dependence at 700°C, and (b) temperature dependence for 1 h tempering.

It should be emphasized that maximum hardness specified for Grade 91/92 ferritic martensitic steels after tempering is 265 HV (ASTM-A213), so that the tempering condition at 700°C for 1 h (the red symbols in Figure 5) used for previous work would result in relatively high hardness. It would potentially help improve tensile and creep properties, but could lead to a negative impact on room temperature toughness. Charpy impact testing is to be conducted, and the toughness improvement through optimization of tempering condition will be discussed.

References

- [1] R.L. Klueh, Elevated-Temperature Ferritic and Martensitic Steels and Their Application to Future Nuclear Reactors, ORNL/TM-2004/176, November 2004.
- [2] R.L. Klueh, N.D. Evans, P.J. Maziasz, V.K. Sikka, Creep-rupture behavior of 3Cr-3W-V bainitic steels, *International Journal of Pressure Vessels and Piping*, 84 (2007) 29-36.
- [3] M. Jawad, V.K. Sikka, Development of a New Class of Fe-3Cr-W(V) Ferritic Steels for Industrial Process Applications, ORNL/TM-2005/82, 2005, Oak Ridge National Laboratory.
- [4] T. Ishitsuka et al., Effect of Silicon on the Steam Oxidation Resistance of a 9%Cr Heat Resistant Steel, *Oxidation of Metals* 61(1-2) (2004)125.
- [5] Y. Yamamoto et al., Development of Advanced 3Cr-3WV(Ta) Bainitic Steels for Fusion Structural Applications, Presentation at ICFRM-17, Aachen, Germany, October 2015.

1.3 IMPACT OF NEUTRON IRRADIATION ON THERMAL HELIUM DESORPTION FROM IRON—X.
Hu, K.G. Field (Oak Ridge National Laboratory), S. Taller (University of Michigan, Ann Arbor), Y. Kath (Oak Ridge National Laboratory), B.D. Wirth (University of Tennessee, Knoxville, Oak Ridge National Laboratory)

Abstract of a manuscript submitted to Journal of Nuclear Materials (in revision).

The synergistic effect of neutron irradiation and transmutant helium production is an important concern for the application of iron-based alloys as structural materials in fission and fusion reactors. In this study, we investigated the impact of neutron irradiation on thermal helium desorption behavior in high purity iron. Single crystalline and polycrystalline iron samples were neutron irradiated in HFIR to 5 dpa at 300°C and in BOR-60 to 16.6 dpa at 386°C, respectively. Following neutron irradiation, 10 keV He ion implantation was performed on both samples to a fluence of 7×10^{18} He/m² at room temperature. Thermal desorption spectrometry (TDS) was conducted to assess the helium diffusion and clustering kinetics by analyzing the desorption spectra. The comparison of He desorption spectra between unirradiated and neutron irradiated samples showed that the major He desorption peaks shift to higher temperatures for the neutron-irradiated iron samples, implying that strong trapping sites for He were produced during neutron irradiation, which appeared to be nm-sized voids through TEM examination. The underlying mechanisms controlling the helium trapping and desorption behaviors were deduced by assessing changes in the microstructure, as characterized by TEM, of the neutron irradiated samples before and after TDS measurements.

2. ODS AND NANOCOMPOSITED ALLOY DEVELOPMENT

2.1 ALLOY YTTRIUM AND TITANIUM VARIATION EFFECTS ON NANO-OXIDES IN NANOSTRUCTURED FERRITIC ALLOYS—N.J. Cunningham, G.R. Odette (University of California, Santa Barbara)

OBJECTIVE

The objective of this work is to optimize the properties of Nanostructured Ferritic Alloys by studying the effects of Y and Ti on the nano-oxide (NO) character. The goals are to determine the Y and Ti content limits where NO number densities and sizes are negatively impacted, and to gain insight into how changes in alloy chemistry affect the NO composition.

SUMMARY

Twelve nanostructured ferritic alloys were produced, varying Y_2O_3 from 0.2 to 0.5 wt.% and Ti to maintain atom Ti:Y ratios of 1.6, 2.4, and 3.1. Small angle neutron scattering measured systematic increases in number density and volume fraction with increased Y_2O_3 and alloy Ti:Y, with greater variation occurring at either 0.2 or 0.5 wt.% Y_2O_3 . Oxide size was similar except for the 0.2 wt.% Y_2O_3 . Atom probe tomography measured slight decreases in oxide Y/Ti and Cr for the 3.1 Ti:Y ratio alloy. Minimizing Ti in the 1.6 Ti:Y alloy, were still able to produce high number densities of oxides.

PROGRESS AND STATUS

Introduction

Realizing the promise of fusion power requires the development of first-wall and blanket materials capable of withstanding high heat flux and the hostile fusion radiation environment. Nanostructured ferritic alloys (NFAs) are candidate fusion structural materials that have remarkable high temperature creep strength, exhibit excellent radiation damage resistance, and can effectively manage high levels of He [1,2]. These material properties stem from an ultra-high number density of stable Y-Ti-O nm-scale oxides (NOs) that impede dislocation motion, act as recombination sites for radiation induced defects, and trap He in small bubbles away from grain boundaries. The typical NO ranges from 2-4 nm in diameter with number densities of $\sim 5 \times 10^{23} \text{ m}^{-3}$ [1]. There is an emerging consensus that the NO are predominantly pyrochlore $Y_2Ti_2O_7$, but details on the exact stoichiometry and defect structures are still open questions, especially for the smallest NOs ~ 2 nm in size [3,4,5,6,7]. Atom probe tomography (APT) often measures NOs with Y/Ti atom ratios of 0.3 to 0.5, and the discrepancy between APT data and the $Y_2Ti_2O_7$ measured by TEM can potentially be explained by microscope artifacts [8,9,10,11,12].

Alloy MA957, a legacy NFA, nominally contains 14 wt.% Cr, 0.3 wt.% Mo, 1.0 wt.% Ti, and 0.25 wt.% Y_2O_3 [13]. Newer NFAs typically consist of 12-14 wt.% Cr, 3 wt.% W, 0.2-0.4 wt.% Ti, and additions of ~ 0.3 wt.% Y_2O_3 . In 14YWT alloys the W provides solid solution strengthening and replaces the Mo in MA957. Numerous studies have identified Ti as the key alloying component required to reduce the size and increase the number density of the Y-Ti rich NOs after high temperature processing [14,15,16,17,18]. Alternatively, the role of Ti can be filled using Zr and Hf, which may further reduce the NO size and increase number density [19,20]. However, the scope of this study is limited to Ti containing NFAs.

Past optimization of the Y and Ti content has primarily focused on mechanical property testing with few observations on how the composition affects the NOs directly. Ukai et al. showed that increasing Ti and Y_2O_3 from 0.13 to 0.31 and 0.08 to 0.24, respectively increased creep strength [17]. Oksiuta and Baluc produced six NFA materials to compare Ti additions of 0.1, 0.3, and 0.5 wt.% and 12 or 14 wt.% Cr with 0.3 wt.% Y_2O_3 [21]. Based on charpy impact properties and strength, the ideal Ti composition was 0.3 wt.%. Increasing Ti further reduced the toughness due to large TiO_2 precipitates. Reducing Ti to 0.1 wt.% gives a bulk Ti:Y atom ratio of ~ 0.6 and would not favor formation of the $Y_2Ti_2O_7$ NO typically found in NFA.

The NFA are expected to operate at temperatures in excess of 800°C for extended time periods. The NOs have been found to be remarkably resistant to coarsening after high temperature aging [22,23,24,25,26]. However, after long-term aging of MA957 at 950°C and 1000°C the excess Ti in the matrix and some Ti associated with the NOs migrates to form large Ti-rich oxides that may degrade mechanical properties [26]. After aging, APT measured a slight decrease in Ti and increase in Cr in the NOs. Avoiding the formation of larger Ti-rich oxides in service will require minimizing the Ti content while maintaining a quantity necessary to still form the high number density of NOs.

Recent APT studies by London et al. observing the NO in NFAs with low bulk Ti:Y atom ratios of ~1.6 also measured high Cr in the precipitates and attributed it to a Cr shell around the $Y_2Ti_2O_7$ NOs. In addition the NO Y/Ti ratios were ~1, which is in contrast to the 0.3-0.5 ratio found in most APT studies on alloys with higher bulk Ti/Y atom ratios [27].

This paper quantifies the changes in NO size, number density, volume fraction, and composition for a set of twelve powders produced with varying levels of Y and Ti. Many 14YWT NFAs have a Ti:Y atom ratio > 3:1 with excess Ti available in the matrix that may later form larger Ti-oxides detrimental to material properties. The formation of $Y_2Ti_2O_3$ requires a ratio ≥ 1 . Therefore, these ratios formed the bounds of the compositions studied in this paper. The goal of this research is to:

- Determine the Y and Ti content limits where NO number density and size are negatively impacted.
- Gain insight into how changes in alloy chemistry affect the NO composition.

Experimental Procedure

Conventional NFAs often have Y_2O_3 content of ~0.3 wt%. Using this value and modifying the Ti from 0.4 to 0.3 to 0.2 wt.% corresponds to alloy Ti:Y atom ratios of 3.1, 2.4, and 1.6, respectively. Maintaining these ratios while varying the Y_2O_3 from 0.2 to 0.5 in 0.1 wt.% increments results in the twelve alloy combinations analyzed in this study, as shown in Table 1. Mechanical alloying of Fe-14Cr-3W pre-alloyed powder with elemental Ti and 15 nm Y_2O_3 powder was carried out using an 8000M SPEX shaker mill for 10 h with a 50:50 mixture (by mass) of 6 and 8 mm diameter tool steel milling balls and a 10:1 ball-to-powder mass ratio. After milling, the powders were subsequently degassed under high-vacuum at 400 °C for up to twelve hours and annealed at 1150°C for 3 h in ½ atm dry He with a Nb oxygen getter foil.

Table 1. Milling matrix showing Ti wt.% for corresponding Y_2O_3 and Ti:Y ratios

		Ti:Y (atom ratio)		
		1.6:1	2.4:1	3.1:1
Y_2O_3 (wt.%)	0.2	0.13	0.20	0.27
	0.3	0.20	0.30	0.40
	0.4	0.27	0.40	0.53
	0.5	0.33	0.50	0.67

The SANS was used to characterize the average radius ($\langle r \rangle$), number density (N), and volume fraction (f_v) of the NOs for each milled and annealed condition. The SANS measurements were performed at the NIST Center for Neutron Research in Gaithersburg, MD [30] on the NG7 beam line, using a neutron wavelength (λ) of 0.5 ± 0.03 nm with a two-dimensional 3He detector located 1.55 m from the sample and offset by ≈ 20 cm to increase the useful scattering vector ($q = 4\pi \sin\theta / \lambda$ where θ is the scattering angle) range up to $\approx 3 \text{ nm}^{-1}$.

The powder was contained in hermetically sealed 1100 series Al holders with a 7.4 mm diameter pocket to contain the powder within the 8.01 mm diameter neutron beam so the probed mass was known. The effective thickness of the powder was determined using the beam diameter, the powder mass, and a theoretical density of 7.798 g/cm^3 . The samples were placed within a $\sim 1.7 \pm 0.1 \text{ T}$ magnetic field to saturate the magnetic Fe–Cr matrix and permit separation of the nuclear (n) and magnetic (m) differential scattering cross sections ($d\Sigma(q)/d\Omega$). After subtracting a control sample devoid of the NO, the magnetic scattering was fit to calculate the N , $\langle r \rangle$, and f_v . Further details on the SANS fitting procedure can be found elsewhere [8,14,31].

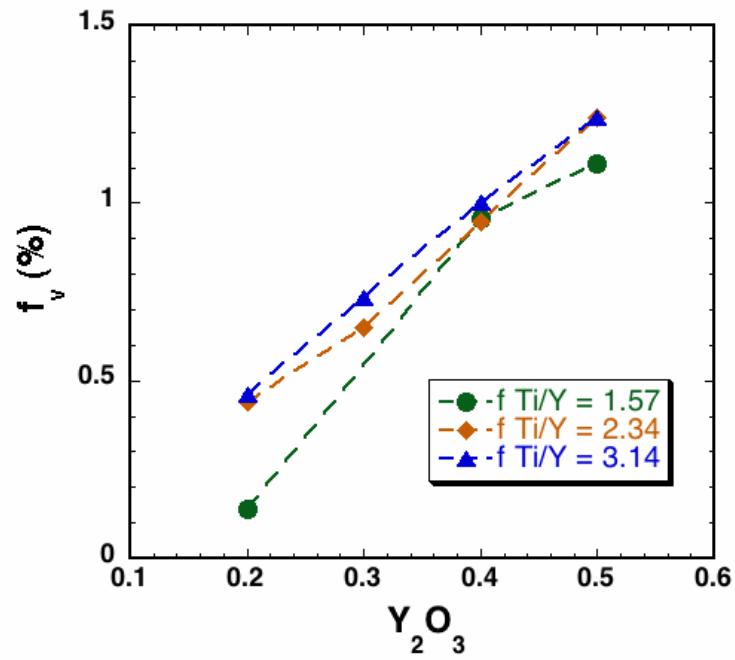
The APT was performed on three samples and conducted at the UCSB Microscopy and Microanalysis Facility using a Cameca 3000X HR laser assisted local electrode atom probe. Details on the APT reconstruction and cluster analysis can be found elsewhere [8]. In brief, the APT specimens were prepared using the trench method outlined by Thompson [32] with an FEI Helios 600 dual beam Scanning Electron Microscope/Focused Ion Beam (SEM/FIB) tool. Final milling included a 2kV low current cleanup to remove Ga damage. The APT analysis parameters included a 20% voltage pulse fraction, 1% evaporation rate, 200 kHz pulse rate, and a temperature of 40-50 K.

Feature sizes, compositions, and number densities were evaluated from 3-dimensional atom maps reconstructed by the commercial Cameca Integrated Visualization and Analysis Software (IVAS) package. The NOs were identified in the reconstructed data using both isoconcentration surfaces and the maximum separation distance methods for the solute ions of interest, namely Y, Ti and O, including their complex ionic forms like TiO and YO. The NO number density was calculated using the total number of ranged ions for the sample volume and counting the total number of complete NOs entirely within the tip volume plus one half the NOs on the edge of the data set. The size calculation also only counted NOs within the volume, ignoring edge clusters, except for those that were larger than the average size. Using this method a lower bound was established for the volume of solutes in the probed region. The volume fraction was estimated by measuring the total corrected cluster atom count divided by the total sample volume atom count (f_s). The NO corrected composition was found by subtracting all Fe and a corresponding amount of other matrix atoms from the NO that are artificially placed within the clusters due to trajectory aberrations as outlined by Williams et al. [11]. The cluster size was calculated using this same corrected NO atom count per cluster and an assumed atomic density equal to BCC Fe.

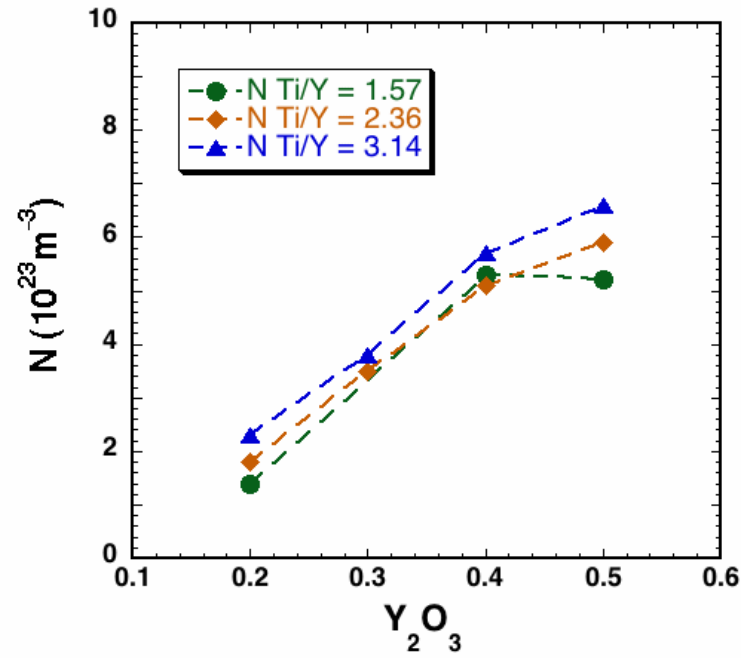
Results

SANS Characterization

The SANS data in Figure 1 show a systematic increase in f_v (Figure 1a) and N (Figure 1b) with increasing Y_2O_3 content. The effect on f_v with changing alloy Ti:Y ratio was greatest at 0.2 wt.% Y_2O_3 , where the f_v was reduced in the 1.6 Ti:Y ratio powder compared to the 2.3 and 3.1 ratio powders. A larger spread in N was also apparent in the 0.5 wt.% Y_2O_3 powders. The powder with 0.3 wt.% Y_2O_3 and a Ti:Y ratio of 1.6 is not shown because the results were highly inconsistent and this outlier may have been caused by a mechanical malfunction with the SPEX mill or incorrect milling chemistry. For clarity this sample was omitted from the analysis.



a)



b)

Figure 1. a) NO volume fraction (f_v) and b) Number density (N) versus Y_2O_3 content for each Ti:Y ratio.

As shown in Figure 2, despite the large variation in Ti and Y_2O_3 , the average size of the NOs was similar for all alloys except for the slightly smaller $\langle r \rangle$ in the 1.6 Ti:Y ratio powder with 0.2 wt.% Y_2O_3 that mirrored the f_v result. The magnetic to nuclear scattering ratio (M/N) measured by SANS will vary with the composition and atom density of the NO and can be used to gain insight into the NO composition. For the eleven NFA powders the M/N remained consistent with an average M/N of 1.27 ± 0.08 . These fairly uniform M/N values indicate a narrow NO composition range between all the powders. The expected M/N ratio for $Y_2Ti_2O_3$ NO in 14YWT is approximately 1.4. The lower measured M/N can indicate higher Ti content in the NO since Ti has a negative scattering length or it could indicate lower atomic density. The 1.6 ratio powder had the highest average M/N of 1.37 ± 0.1 with a maximum of 1.47 in the powder with 0.2 wt.% Y_2O_3 and only 0.13 wt.% Ti, potentially indicating lower NO Ti content compared to the other alloys.

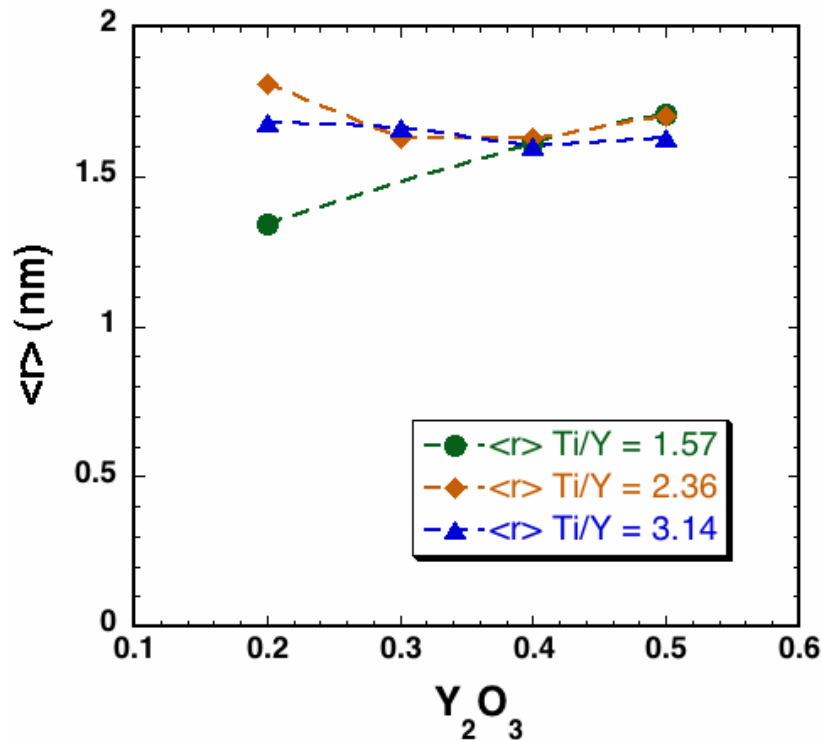


Figure 2. $\langle r \rangle$ versus Y_2O_3 for each Ti:Y ratio.

The APT was performed on 3 of the 12 milled and annealed powders. The 0.3 wt.% Y_2O_3 , Ti:Y = 1.6 powder that showed inconsistent SANS results also gave APT results with larger NO and lower number densities than expected, reinforcing the belief of a problem with the mechanical alloying. The other two measurements included the 0.3 wt.% Y_2O_3 , with Ti:Y = 2.4 and the 0.4 wt.% Y_2O_3 , Ti:Y = 1.6. These results were compared to APT results from a previously milled powder using an alternative alloying method with 0.3 wt.% Y_2O_3 , Ti:Y = 3.1, and this alloy is an equivalent replacement to the Ti:Y = 3.1 and 0.3 wt.% Y_2O_3 measured by SANS [33]. Table 2 shows the APT measured N, $\langle d \rangle$, and f_s for the three powders are relatively consistent with the SANS results. There is a slight increase in the volume fraction and number density of the Ti:Y = 1.6 powder due to the higher 0.4 wt.% Y_2O_3 content. For the three alloys in Table 2 there were between 2-4 samples analyzed from each powder and a total of 66 million ions collected.

Table 2. NO N, $\langle d \rangle$, and f_s comparison between powders with different Ti:Y ratios

Powder Composition	Ti-Y Ratio	N (10^{23} m^{-3})	$\langle d \rangle$ (nm)	f_s (%)
0.4 Y_2O_3 , 0.27 Ti	1.57	6.1	2.4±0.5	0.52
0.3 Y_2O_3 , 0.3 Ti	2.36	4.8	2.3±0.5	0.40
0.3 Y_2O_3 , 0.4 Ti	3.14	5.3	2.2±0.5	0.41

Figure 3 displays 20 nm thick atom maps of the 2.4 ratio powder. The atom maps show the clusters are composed of the typical Y, Ti, and O, while also containing CrO ions. The O atoms are more spread out around the TiO, Y, and YO ions, as is typical of this alloy class and that may be caused by O atom mobility along the tip surface before evaporation. The NOs appear to exhibit a TiO and smaller CrO tail below the precipitates in reference to the z direction. This TiO and CrO tail may indicate the remnants of a Ti and Cr shell surrounding the NO Y-Ti-O core [8,12].

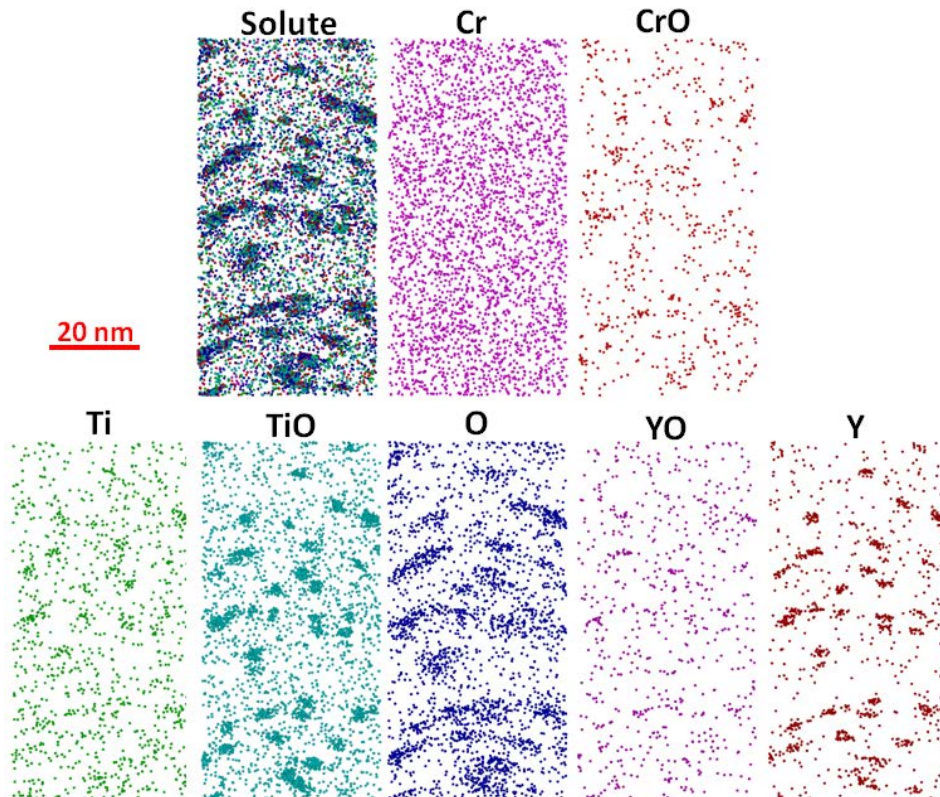


Figure 3. 20 nm X 40 nm X 80 nm atom maps from the 0.3 wt.% Y_2O_3 , Ti:Y = 2.4 powder.

Table 3 compares the APT measured matrix and NO compositions. The NOs typically contain a significant amount of matrix Fe and Cr due to trajectory aberrations in the microscope. The NO composition in Table 3 is adjusted by removing the Fe and a corresponding amount of matrix ions. The

residual Cr is significant in all three alloys with the lowest Cr content of ~20% occurring in the 3.1 ratio powder. The only significant difference in matrix content between the three powders is the Ti. The higher value in the 3.14 ratio powder is expected. The matrix Ti in the 2.4 ratio powder is lower than in the 1.6 ratio powder. One possible explanation is a higher level of O and N contamination in the 2.4 ratio powder. Contamination is often a problem when ball milling as the powders can quickly acquire any contaminants in the milling atmosphere. Improvements to the milling can seal were made between the 2.4 and 1.6 ratio powders and the N contamination dropped from ~0.2 wt.% to 0.05 wt.%. Although little N was observed in the APT data, previous analyses on other alloys with high N contamination have contained large Ti-nitride precipitates that can remove some Ti from the matrix.

As shown in Table 4 the NO Y/Ti ratio was ~0.4 for the 1.6 and 2.4 ratio powders alloys, while the 3.1 ratio powder had a Y/Ti ratio of ~0.3. A similar difference was observed in the (Y+Ti)/O ratios while the difference in M/O (M = Y+Ti+Cr) between the three powders was less significant.

Table 3. NO raw and adjusted composition for the Ti:Y 1.6, 2.4, and 3.1 powder with 0.3 wt.% Y₂O₃

Element	Ti:Y = 1.6		Ti:Y = 2.4		Ti:Y = 3.1	
	Matrix	Cluster*	Matrix	Cluster*	Matrix	Cluster*
Fe	84.35	0.0	84.50	0.0	84.01	0.0
Cr	14.14	24.56	14.12	28.92	14.45	19.93
Ti	0.036	25.28	0.020	22.91	0.270	30.68
W	0.925	0.67	0.840	0.68	0.960	0.18
Y	0.009	10.54	0.003	9.33	0.006	10.57
O	0.100	34.95	0.070	33.50	0.180	36.33
Mn, V, Si, P, C, Co, Ni, Al	0.217	3.66	0.436	4.16	0.117	1.57

*adjusted compositions with all Fe and corresponding matrix atoms removed

Table 4. NO composition comparison between powders with different Ti:Y ratios

Powder Composition	Ti:Y	Y/Ti/O	Y/Ti	(Y+Ti)/O	M/O
0.4 Y ₂ O ₃ , 0.27 Ti	1.57	15.1/36.0/48.9	0.43	1.03	1.73
0.3 Y ₂ O ₃ , 0.3 Ti	2.36	14.3/34.9/50.8	0.41	0.97	1.83
0.3 Y ₂ O ₃ , 0.4 Ti	3.14	13.8/40.2/46.0	0.34	1.18	1.70

Discussion and Summary

Despite the large range in alloy Y_2O_3 and Ti content, the NFAs produced here have remarkably similar size distributions with only the 1.6 ratio powder at 0.2 Y_2O_3 having a significantly smaller size. Changes in N and f_v were systematic and increased with increasing Y_2O_3 . Increasing the alloy Ti:Y ratio from 1.6 to 2.4 to 3.1 had minor increases on the N and f_v . Any significant variation only occurred at the lowest (0.2 wt.%) and highest (0.5 wt.%) Y_2O_3 content. A significant reduction in f_v occurred in the 1.6 ratio powder with 0.2 wt.% Y_2O_3 , and there was a greater spread in N values for the three powder ratios at 0.5 wt.% Y_2O_3 . The APT measured compositions showed a small decrease in the NO Y/Ti ratio when the alloy Ti content was increased. This increase in Ti was accompanied by a decrease in the NO Cr content giving a fairly stable NO metal/oxygen ratio (M/O).

The $\langle r \rangle$, N, f_s and APT compositions for the powder alloys produced in this study are consistent with many other previous 14YWT and alloy MA957 studies including the NO Y/Ti ratios of 0.3 to 0.4. However, several new 14YWT alloys described by London with low Ti content at 0.2 wt.% and a Ti:Y ratio of 1.6 have APT Y/Ti ratios of ~ 1 [34]. London describes several corrections performed on the data to explain part of this discrepancy including peak decomposition of overlapping TiO^{++} and O_2^+ ions at 32 da in the APT mass spectrum. These peak overlaps are not present for any of the three APT samples measured in this study, and this may be due to differences in APT run conditions including the use of voltage pulsing here compared to laser pulsing by London et al. London also describes an absence in elemental Ti peaks in the matrix mass spectrum, which indicates the excess Ti is tied up in larger features not probed by APT.

London et al. confirms the presence of $Y_2Ti_2O_7$ NOs and demonstrates the presence of a Cr shell where the shell thickness scaled linearly with the precipitate size [27,34]. Similar Cr shells on precipitates >2 nm in a 14YWT were also observed by Badjeck et al. using high resolution STEM-EELS analysis, but a metallic Ti or TiO layer also existed between the Cr shell and $Y_2Ti_2O_7$ core [4]. It is likely the alloy Ti content affects the interface chemistry, and how the Cr and/or Ti shell forms.

This experiment observed the effects of a wide range of Y and Ti alloy content on the NOs in 14YWT alloys. The ranges explored appear to all produce an acceptable alloy chemistry with respect to forming a high density of small NO capable of supplying high temperature creep strength and radiation damage resistance except for possibly the lowest 0.2 wt.% Y_2O_3 alloy composition that had a lower N and f_v with a wider variability in size between the three Ti:Y ratios. To avoid the formation of large Ti-oxides during high-temperature service, this study suggests it is preferable to use alloys with lower Ti content down to at least a Ti:Y ratio of 1.6. Therefore, the ideal Y_2O_3 and Ti composition ranges from 0.3-0.4 wt.% and 0.2-0.27 wt.%, respectively.

Acknowledgments

This work was supported by the DOE Office of Fusion Energy (DE-FG03-94ER54275). We acknowledge the support of the National Institute of Standards and Technology, US Department of Commerce, in providing the neutron research facilities used in this work.

References

- [1] G.R. Odette, M.J. Alinger, B.D. Wirth, Annual Review of Materials Research, 38, 2008.
- [2] G.R. Odette, JOM, 66, 12, 2014, 2427-2441.
- [3] Y. Wu, J. Ciston, S. Krämer, et al., Acta Materialia, 111, 2016, 108-115.
- [4] V. Badjeck, M.G. Walls, L. Chaffron, et al., Journal of Nuclear Materials, 456, 2015, 291-301.
- [5] A.J. London, B.K. Panigrahi, C.C. Tang, et al., Scripta Materialia, 110, 2016, 24-47.
- [6] K. Dawson and G.J. Tatlock, J. Nucl. Mater., 444, 2014, 252-260.
- [7] M. Klimiankou, R. Lindau, and A. Möslang, Journal of Nuclear Materials, 329-333, 2004, 347-351.
- [8] N.J. Cunningham, Ph.D. Dissertation, University of California Santa Barbara, 2012.
- [9] E.A. Marquis and J.M. Hyde, Materials Science and Engineering: R, 69, 2010, 37-62.

- [10] C.A. Williams, G.D.W. Smith, E.A. Marquis, *Ultramicroscopy*, 125, 2013, 10-17.
- [11] C.A. Williams, E.A. Marquis, A. Cerezo, et al., *Journal of Nuclear Materials*, 400, 2010, 37.
- [12] E.A. Marquis, *Appl Phys Lett*, 93, 2008, 181904.
- [13] M.I. Hamilton, D.S. Gelles, R.J. Lobsinger, et al, Technical Report PNL-13168, 1991, Richland, WA: Pacific Northwest Laboratory.
- [14] M.J. Alinger, G.R. Odette, D.T. Hoelzer, *Acta Materialia*, 57, 2009, 392-406.
- [15] M. Ratti, D. Leuvrey, M.H. Mathon, *Journal of Nuclear Materials*, 386-388, 2009, 540-543.
- [16] H. Kishimoto, M.J. Alinger, G.R. Odette, et al., *Journal of Nuclear Materials*, 329-333, 2004, 369-371.
- [17] S. Ukai, S. Mizuta, T. Yoshitake, et al., *Journal of Nuclear Materials*, 283-287, 2000, 702-706.
- [18] I. Kim, B. Choi, C. Kang, et al., *ISIJ International*, 43, 2003, 1640-1646.
- [19] Y. Uchida, S., Ohnuki, N., Hashimoto, et al., *Material Research Society Symposium Procedure Vol. 981*, 2007, Materials Research Society.
- [20] L. Zhang, S. Ukai, T. Hoshino, et al., *Acta Materialia*, 57, 2009, 3671-3682.
- [21] Z. Oksiuta, and N. Baluc, *Nuclear Fusion*, 49, 2009.
- [22] M.K. Miller, K.F. Russell, D.T. Hoelzer, *J. Nucl. Mater* 351, 2006, 261–268.
- [23] H. Sakasegawa, F. Legendre, L. Boulangeret al., *J. Nucl. Mater* 417, 2011, 229–232.
- [24] M.J. Alinger, G.R. Odette, D.T. Hoelzer, *J. Nucl. Mater.* 329–333, 2004, 382–386.
- [25] N. Cunningham, Y. Wu, D. Kingensmith, et al., *Mater. Sci. and Engr. A*, 613, 2014, 296-305.
- [26] N. Cunningham, M.J. Alinger, D. Kingensmith, *Mater. Sci. and Engr. A*, 655, 2016, 355-362.
- [27] A.J. London, S. Lozano-Perez, M.P. Moody, *Ultramicroscopy*, 159, 2015, 360-367.
- [28] S. Ohtsuka, S. Ukai, M. Fujiwara, et al., *Journal of Physics and Chemistry*, 66, 2005, 571-575.
- [29] P. Dou, A. Kimura, R., Kasada, et al., *J. of Nucl. Mater.*, 442, 2013, S95-S100.
- [30] C.J. Glinka, J.G. Barker, B. Hammouda, et al., *J. Appl. Cryst.* 31, 1998, 430.
- [31] E. Mader, Ph.D. Thesis, University of California, Santa Barbara, 1995.
- [32] K. Thompson, D. Lawrence, D.J. Larson, et al., *Ultramicroscopy*, 107, 2007, 131.
- [33] N.J. Cunningham, Y. Wu, G.R. Odette, et al., *Fusion Reactor Materials Program Semiannual Progress Report for the period ending June 30, 2013*, DOE/ER-0313/54.
- [34] A.J. London, S. Santra, S. Amirthapandian, et al., *Acta Materialia* 97, 2015, 223-233.

2.2 A NUMERICAL INVESTIGATION OF DELAMINATION EFFECTS ON THE FRACTURE BEHAVIOR OF A 14YWT NANOSTRUCTURED FERRITIC ALLOYS (NFA-1)—C. Ruggieri, M. E. Alam, G. R. Odette, (UCSB)

OBJECTIVE

Recent fracture toughness testing conducted on SE(B) specimens for a 14YWT NFA revealed high fracture toughness properties orientations. The objective of this study is to gain insight into the effects of delamination on crack front fields and crack-tip constraint, which mediate the observed toughness increase.

SUMMARY

This investigation addresses a numerical investigation of the crack front fields and effects of crack-tip constraint in subsized SE(B) specimens with transverse delamination. Nonlinear numerical analyses of very detailed 3-D finite element models of SE(B) fracture specimens for a 14 YWT nanostructured ferritic alloy (NFA) enable assessing the effects of prescribed delamination cracks on the crack front fields with increased loading levels. Further, the work addresses the potential coupled effects of geometry and delamination size on crack-tip constraint, thereby providing valuable insight into the effect of delamination cracks on macroscopic fracture behavior in conventional fracture specimens. Overall, the present exploratory analyses reveal important features of 3-D crack front fields in fracture specimens with transverse delamination that have a direct bearing on the often observed toughness increase in fracture testing of materials with through-thickness anisotropy in mechanical properties.

PROGRESS AND STATUS

Introduction

The demands of the fusion environment have prompted the development of nanostructured ferritic alloys (NFA) made of an ultrahigh density of nm-scale Y-Ti-O rich oxide nanofeatures (NFs) that provides outstanding combination of high strength, ductility and fracture toughness. Motivated by the experimental studies of Alam et al. [1], here, we explore the effects of delamination cracks on the macroscopic fracture behavior by changing the crack front (through thickness) constraint.

The phenomenon of delamination in structural alloys has received considerable attention in recent years. Early experimental studies on delamination effects in notch impact specimens for hot-rolled steels [2-4] revealed a marked influence of delamination cracking on the ductile-to-brittle transition (DBT) behavior for these materials as the ductile-brittle transition shifts towards lower temperatures with increased number of fracture surface delaminations. These effects arise from the strong interaction between anisotropic microstructural features of the material which govern the separation of transverse weak planes and the loss of stress triaxiality in the crack front region due to through-thickness splitting. Later, Rao et al. [5] and Rao and Ritchie [6-7] provided strong experimental evidence that the increased fracture toughness properties in L-T orientation at low temperature for Al-Li alloys is primarily associated with the development of delamination cracks.

While these previous studies advanced the understanding of delamination effects on the experimental fracture toughness behavior of structural materials, only little effort has been expended to quantify the rather complex interaction of transverse delamination cracks with the crack front of the macroscopic crack. The primary reason offered for the increased fracture toughness observed in fracture testing of specimens in the transverse (L-T or T-L) orientations is that the behavior is controlled by a mechanism of crack-divider delamination toughening in which the incidence of through-thickness splitting results in loss of through-thickness constraint [5]. Here, the influence of through-thickness splitting is viewed as effectively dividing the bulk of the specimen into smaller sections of reduced thickness thereby relaxing

the crack front stress triaxiality from predominantly plane-strain to nearer plane-stress conditions. Recent work of Kalyanam et al. [8] addressed a numerical investigation of delamination cracking effects in Al-Li alloys to characterize the crack front stress-strain fields for 3-D, small scale yielding (SSY) finite element models with and without a delamination crack. However, how the controlling mechanical features - delamination size and crack-tip constraint - are interconnected and their relative contributions to the macroscopic fracture behavior remain open issues.

Delamination Effects on Fracture Toughness of Nanostructured Ferritic Alloys (NFA)

Alam et al. [1] recently performed extensive fracture toughness tests on conventional, plane-sided three-point bend fracture specimens with a nominal $a/W=0.5$ in the L-T and T-L orientations. The geometry and dimensions of the tested fracture specimens follow ASTM E1820 [9] with $B=1.67$ mm, $W=3.33$ mm and $S=4W$. Here, a is the crack size, W denotes the specimen width, b represents the specimen thickness and S is the load span. Fracture toughness testing of this configuration was performed at different test temperatures ranging from $T= 23^{\circ}\text{C}$ to -196°C following the procedures given by ASTM E1921 [10] and ASTM E1820 [9]. Exceptionally high fracture toughness and low transition temperature were observed by Alam et al. [1]. The measured upper-shelf fracture toughness is in the range of $K_{Jc}= 100\text{MPa}\sqrt{\text{m}}$ with a remarkably low ductile-to-brittle transition (DBT) temperature at about -175°C .

Much of this fracture toughness behavior can be explained in terms of the connection between delamination cracking and increased toughness in the L-T orientation due to loss of through thickness constraint. Alam et al. [1] show typical fracture surfaces of the tested SE(B) specimens at 23°C and -150°C in which formation of delamination cracks (splits) is clearly seen at both test temperatures with delamination planes normal to both the extrusion and cross rolling directions. In these specimens, the delamination cracks extend over a large fraction of the remaining crack ligament as much as ~ 0.8 - 1.2mm from the crack tip. It is evident that the through-thickness splitting causes the bulk of the specimen to be divided into thinner ligaments defined by the delamination cracks thereby relaxing the near-tip stresses which drive the cleavage fracture process and, further, affecting strongly the crack-front size over which high levels of near-tip stress triaxiality (constraint) are maintained. These changes in the crack-tip stress fields following the onset and subsequent development of delamination cracks along the crack front are likely to enhance the fracture toughness of the specimen. The numerical results that follow provide valuable insight into the role of delamination cracking on the local crack driving forces to support interpretation of the cleavage fracture toughness behavior of the tested NFA material.

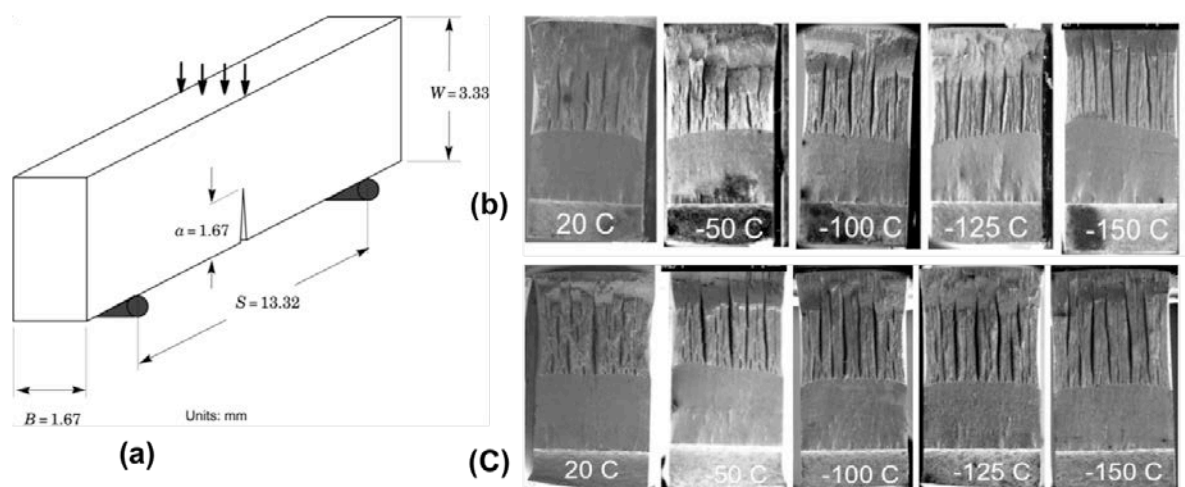


Figure 1. (a) Geometry of plane-sided, three-point bend fracture specimens with $a/W=0.5$ tested by Alam et al. [1]. (b-c) Typical SEM fractographs of the fracture surfaces for LT and T-L orientations, respectively, at varying test temperatures reported by Alam et al. [1]

Overview of Finite Element Procedures

Finite Element Models

Nonlinear numerical analyses are conducted on detailed 3-D finite element models for the plane-sided SE(B) specimen thickness, $B=1.67\text{mm}$, and $W=3.33$ utilized in the fracture testing. Alam et al. [1] provide the material flow properties utilized in the finite element computations. Figure 2(a-b) shows the finite element model constructed for analyses of the tested SE(B) specimen. Symmetry conditions enable analyses using one-quarter of the 3-D models with appropriate constraints imposed on the symmetry planes. The finite element mesh has 33 variable thickness layers defined over the half-thickness $B/2$ to accommodate strong Z variations in the stress distribution, and at the same time to resolve the steep stress gradients near the center-plane delamination crack as shown in Figure 2(b). The quarter-symmetric, 3-D model for this specimen has 98702 nodes and 92037 elements. As already noted before, transverse delamination cracking is associated with anisotropic microstructural features of the material that govern the separation of transverse weak planes. Under increased loading, the near-tip stresses acting along the through-thickness direction (Z) reach a critical value [4] thereby causing fracture of the weak planes (most often by a transgranular cleavage mechanism) and creating a macroscopically transverse planar crack. In this investigation, we idealize this process by introducing a delamination crack in the specimen center-plane region with a prescribed length, l_D , and height, h_D at the onset of loading as depicted in Figure 3(a). Within the present simplification, the delamination crack is viewed as a thin rectangular slab embedded into the specimen center plane and centered at the crack tip.

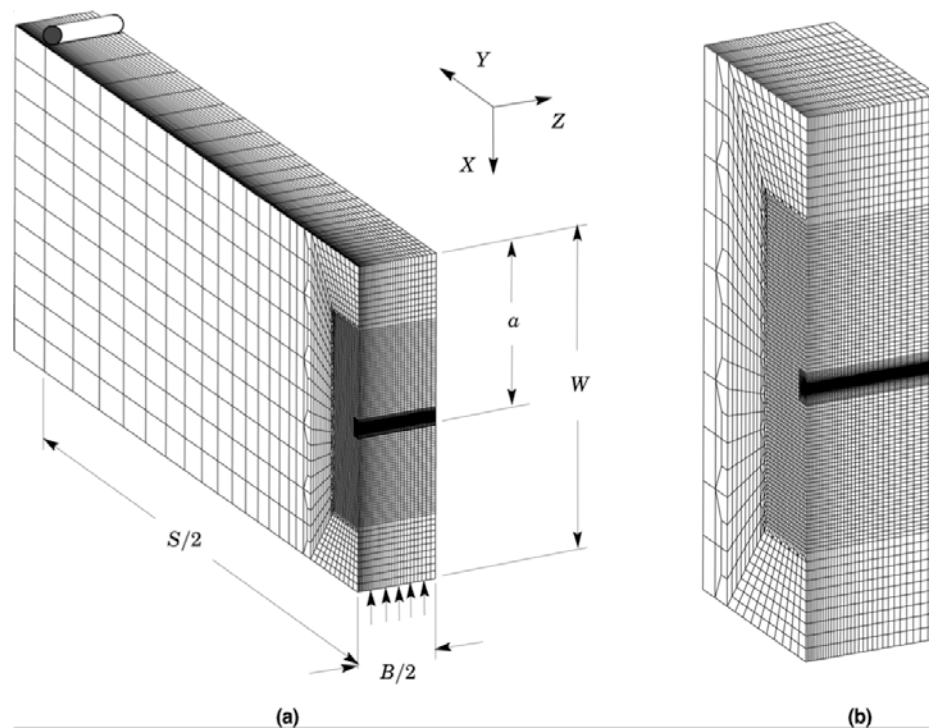


Figure 2. (a) Quarter-symmetric finite element model used in the 3-D analyses of the SE(B) specimen with $a/W=0.5$ tested by Alam et al. [1]; (b) Mesh detail of the crack-tip region.

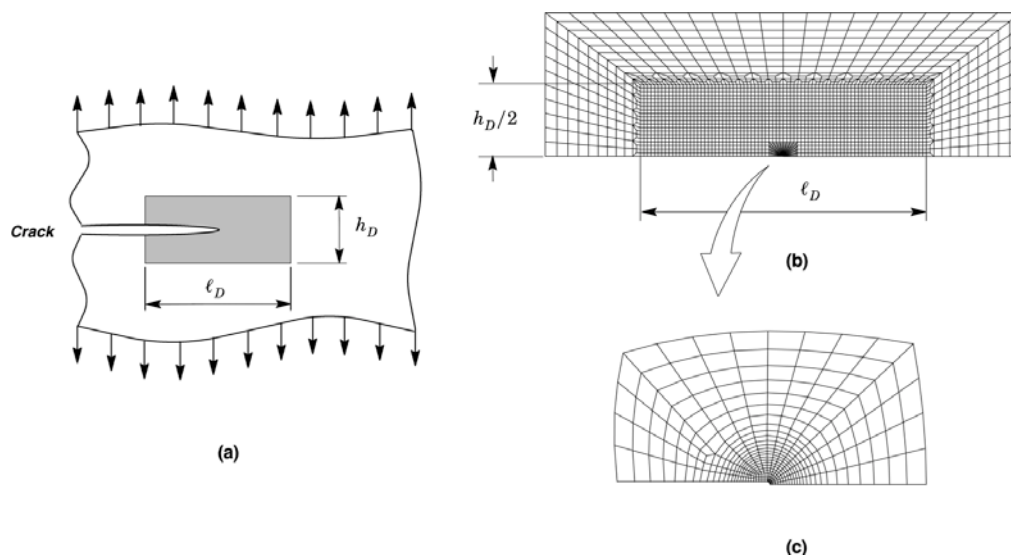


Figure 3. (a) Schematic for the adopted geometry of the transverse rectangular delamination; (b) Finite element model of the transverse rectangular delamination, and (c) the near-tip mesh detail.

Figure 3(b) shows the highly refined finite element mesh defining the delamination crack region in which the size of the square elements within the thin slab is 0.025mm. The innermost focused mesh configuration illustrated in Figure 3(c) provides the very high level of mesh refinement required to accurately resolve the near-tip stress and strain fields. As indicated in Figures 2(b) and 3(b), the physical delamination crack is introduced into the model by releasing the Z-constraints on the nodes defining the delamination crack region. Guided by experimental observations made by Alam et al. [1], the delamination sizes (as characterized by the length, l_D , and the height, h_D) adopted in the present study are taken as $0.5 \times 0.25 \text{ mm}^2$, $1 \times 0.5 \text{ mm}^2$ and $2 \times 1 \text{ mm}^2$. This range of sizes provides a close representation of the observed delamination crack sizes and shapes with increased load levels up to a maximum K_I -value of $100 \text{ MPa}\sqrt{\text{m}}$, which is in accord with the upper-shelf fracture toughness measured in the fracture testing. Moreover, while the adopted approach does not consider the growth of the delamination crack with increased loading, thereby not including history effects on the evolving crack front stress fields and crack front constraint, it is adequately descriptive of the local conditions affecting macroscopic fracture behavior in conventional fracture specimens with transverse delamination.

Material Models and Solution Procedures

The finite element code WARP3D [11] provides the numerical solutions for the 3-D analyses reported here. The analyses for delamination effects on crack front fields described next utilize an elastic-plastic constitutive model with conventional Mises plasticity in small geometry change (SGC) setting. The numerical solutions employ a simple power-hardening model to characterize the uniaxial true stress vs. logarithmic strain in the form

$$\frac{\bar{\varepsilon}}{\varepsilon_0} = \frac{\bar{\sigma}}{\sigma_0} \quad , \quad \bar{\varepsilon} \leq \varepsilon_0 \quad ; \quad \frac{\bar{\varepsilon}}{\varepsilon_0} = \left(\frac{\bar{\sigma}}{\sigma_0} \right)^n \quad , \quad \varepsilon > \varepsilon_0 \quad (9)$$

where σ_0 and ε_0 are the yield stress and yield strain, and n defines the strain hardening exponent. For the tested high strength nanostructured ferritic (14YWT) alloy, a curve fitting procedure to the true stress-logarithmic strain response (converted from the engineering stress-strain curve given in [1]) provides the strain hardening exponents at $T=23 \text{ }^\circ\text{C}$ as $n=20.1$.

Results and Discussion

Delamination Effects on 3-D Crack Front Stress Fields

Figures 3 and 4 show the development of near-tip opening stresses, σ_{yy} , and out-of-plane stresses, σ_{zz} , with increased levels of deformation, as characterized by K_J , for the analyzed SE(B) models with and without transverse delamination cracks. In these plots, the opening stresses are normalized by the material yield stress, σ_0 , and crack-tip distances are normalized by J/σ_0 . The opening stresses are extracted from the nearest layer to the specimen center plane which does not contain a delamination crack ($Z/(B/2) = 0.01$) whereas the transverse stresses are extracted at the normalized crack-tip distance, $r/(J/\sigma_0)=1$, which corresponds approximately to $3xCTOD$ (crack tip opening displacement). The macroscopic load levels range from $K_J = 100 \text{ MPa}\sqrt{\text{m}}$ to $K_J = 40 \text{ MPa}\sqrt{\text{m}}$, which is in accord with the toughness levels at fracture measured by Alam et al. [1]. Throughout this brief report, we employ the standard relationship between the J-integral and K_J given by $J = K_J^2/(1-\nu^2)$, where ν denotes the Poisson's ratio.

Consider first the numerical results for the model without a delamination crack displayed in Figures 4(a) and 5(a). The opening stress distributions shown in Figure 4(a) are entirely consistent with a J-dominated field with the opening stresses attaining a value of $\sim 3.2\sigma_0$ at $r/(J/\sigma_0) = 1$, which is characteristic of low hardening materials under well-contained yielding conditions. The distribution of σ_{zz} over the crack front shown in 5(a) reveals maximum values over a large fraction of the specimen thickness extending from midplane and then gradually decreasing as the stress-free surface is approached; observe, however, that the stress gradient over the crack front is more pronounced with increased K_J -values as large scale yielding develops in the specimen and interacts with the stress-free specimen surface.

Consider now the behavior of the normal and transverse components of stress for the models having a center-plane delamination crack with varying sizes shown in Figures 4(b-d) and 5(b-d). Clearly, the introduction of a delamination crack now creates a stress-free surface at the center plane thereby relaxing the through-thickness constraint and, at the same time, shifting the near-tip highly stressed region to the middle portion of the remaining thickness ligament (this corresponds approximately to $Z/(B/2) \approx 0.4\sim 5$). Here, the opening stresses at the nearest layer to the specimen center plane fall rapidly to values of $\sim 1.2\sigma_0$ for $r/(J/\sigma_0) \geq 1$ whereas the σ_{zz} -stresses vanish at $Z/(B/2) = 0$ and 1. Further, apart from minor differences in the stress levels, note that the distributions of normal stress, σ_{yy} , and transverse stress, σ_{zz} , are essentially unchanged with increased delamination sizes.

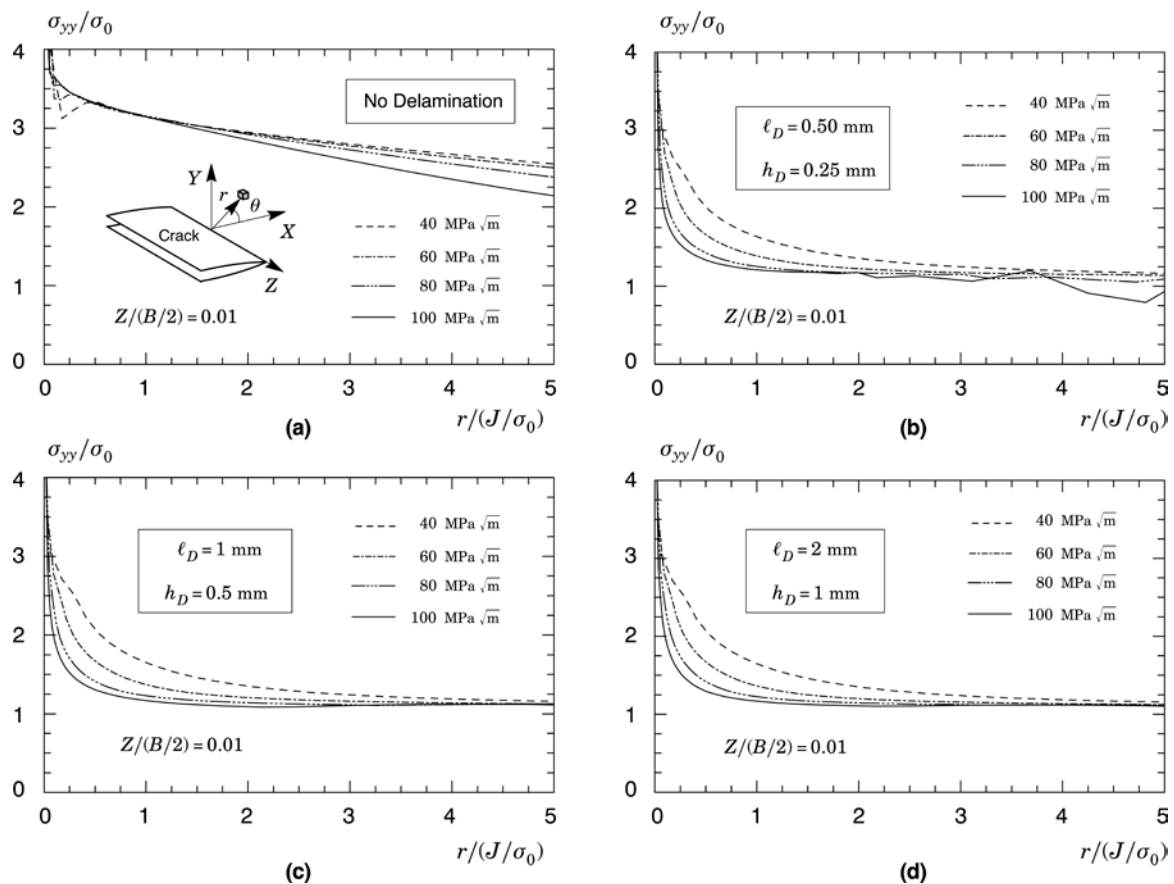


Figure 4. Development of near-tip opening stresses (σ_{yy}) with increased deformation levels, as characterized by K_J , at the specimen center plane and $\theta=0$: (a) No delamination; (b) 0.5x0.25 mm delamination; (c) 1x0.5mm delamination and (d) 2x1mm delamination.

Variation of the Crack Driving Force Over the Crack Front

Figure 5 displays the distribution of J over the crack front, denoted J_{local} , with increased levels of loading, as characterized by increased K_J -values, for the models with and without transverse delamination crack. These J -values are normalized by the maximum J -value attained over the crack front, denoted J_{max} for each case so that the ratio J_{local}/J_{max} identifies the point over the crack front at which the crack driving force is maximum. It is also readily understood here that the K_J -values describing the increasing load levels derive from the thickness average values of J , denoted J_{avg} , which are slightly different than the J_{max} -values attained over the crack front.

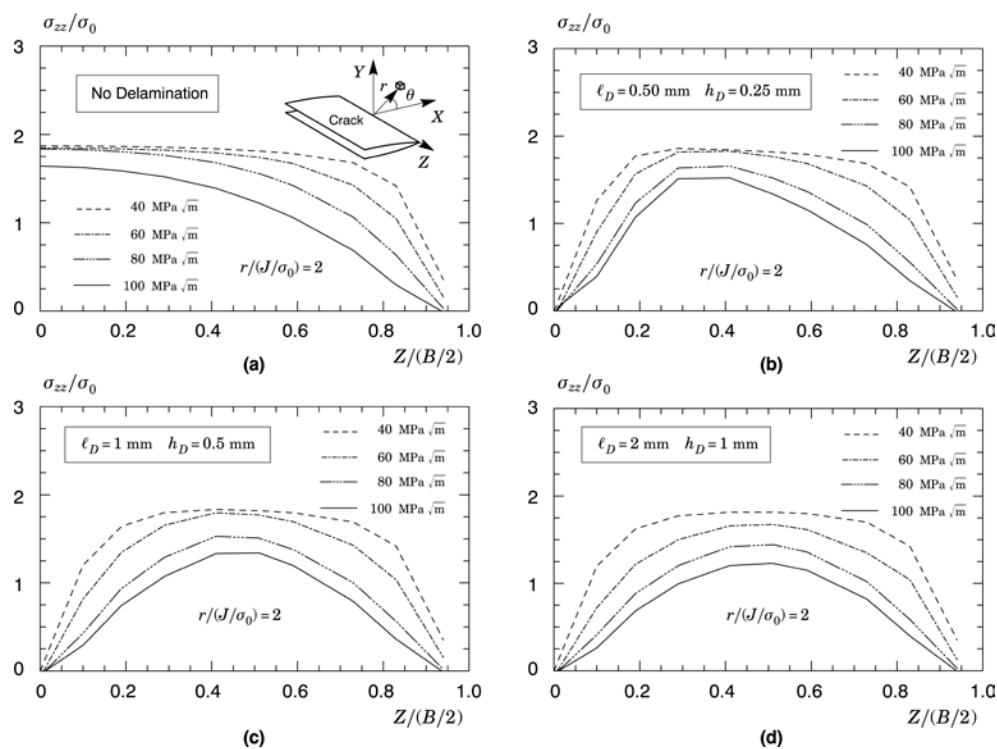


Figure 5. Distribution of out-of-plane stresses (σ_{zz}) over the crack front with increased deformation levels, as characterized by K_I , at the normalized crack-tip distance, $r/(J/\sigma_0) = 1$: (a) No delamination; (b) 0.5x0.25 mm delamination; (c) 1x0.5mm delamination and (d) 2x1mm delamination.

The results shown in Figure 6(a) corresponding to the model without a delamination crack reveal that the maximum J -value occurs over a relatively large portion of the specimen center plane region ($0 \leq Z/(B/2) \leq 0.2 \sim 0.25$) and then gradually decreases to much lower J -values as the stress-free surface is approached. This behavior is entirely consistent with other previous studies, including the work of Nevalainen and Dodds [12]. Similar to the observations made previously, a different picture emerges when a delamination crack with varying size is introduced into the model. Here, the J -values at the center plane drop precipitously to attain essentially similar levels as those corresponding to the stress-free surface. Observe, however, that the J -distributions peak over a relatively narrow portion of the thickness ligament ranging from $Z/(B/2) \approx 0.25$ for the smaller delamination crack to $Z/(B/2) \approx 0.5$ for the larger delamination crack.

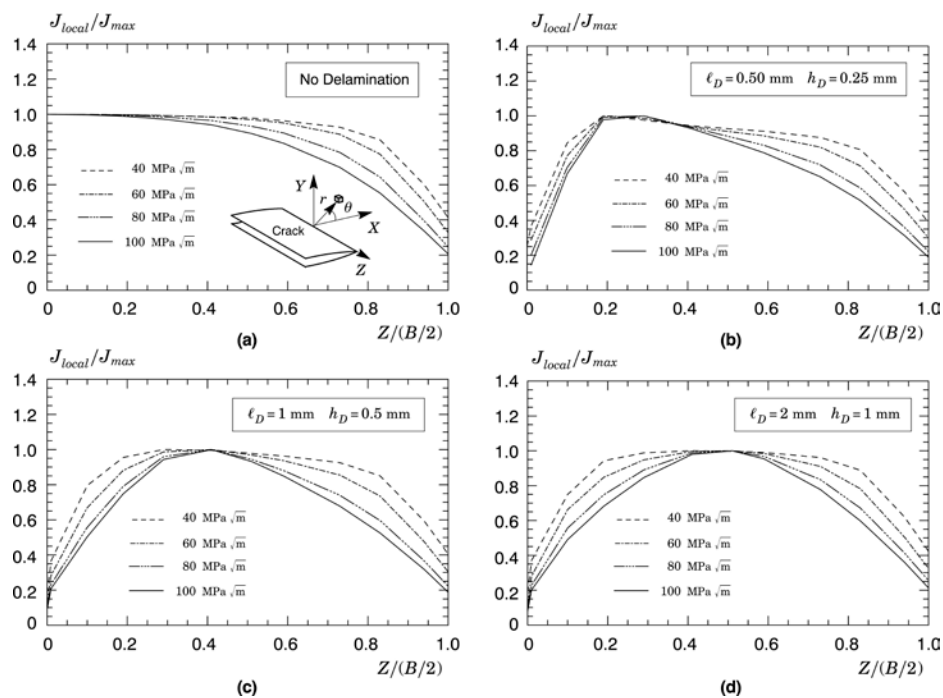


Figure 6. Distribution of the J -integral over the crack front with increased deformation levels, as characterized by K_J : (a) No delamination; (b) 0.5x0.25mm delamination; (c) 1x0.5mm delamination and (d) 2x1mm delamination.

Mode I Opening Stress Zones Over the Crack Front

Additional insight into the effects of transverse delamination cracking on the 3-D crack front fields can be gained by examining the development of opening stress zones (σ_{yy}) over the crack front. Figures 7 and 8 show the opening stress contours for which $\sigma_{yy} \geq 2\sigma_o$ over the crack front for the models with and without a transverse delamination crack at two distinct levels of loading, $K_J = 40 \text{ MPa}\sqrt{\text{m}}$ and $K_J = 100 \text{ MPa}\sqrt{\text{m}}$. In the context of the present study, these high stress regions $\sigma_{yy} \geq 2\sigma_o$ approximately quantify the size of the near-tip fracture process zone over which cleavage fracture takes place.

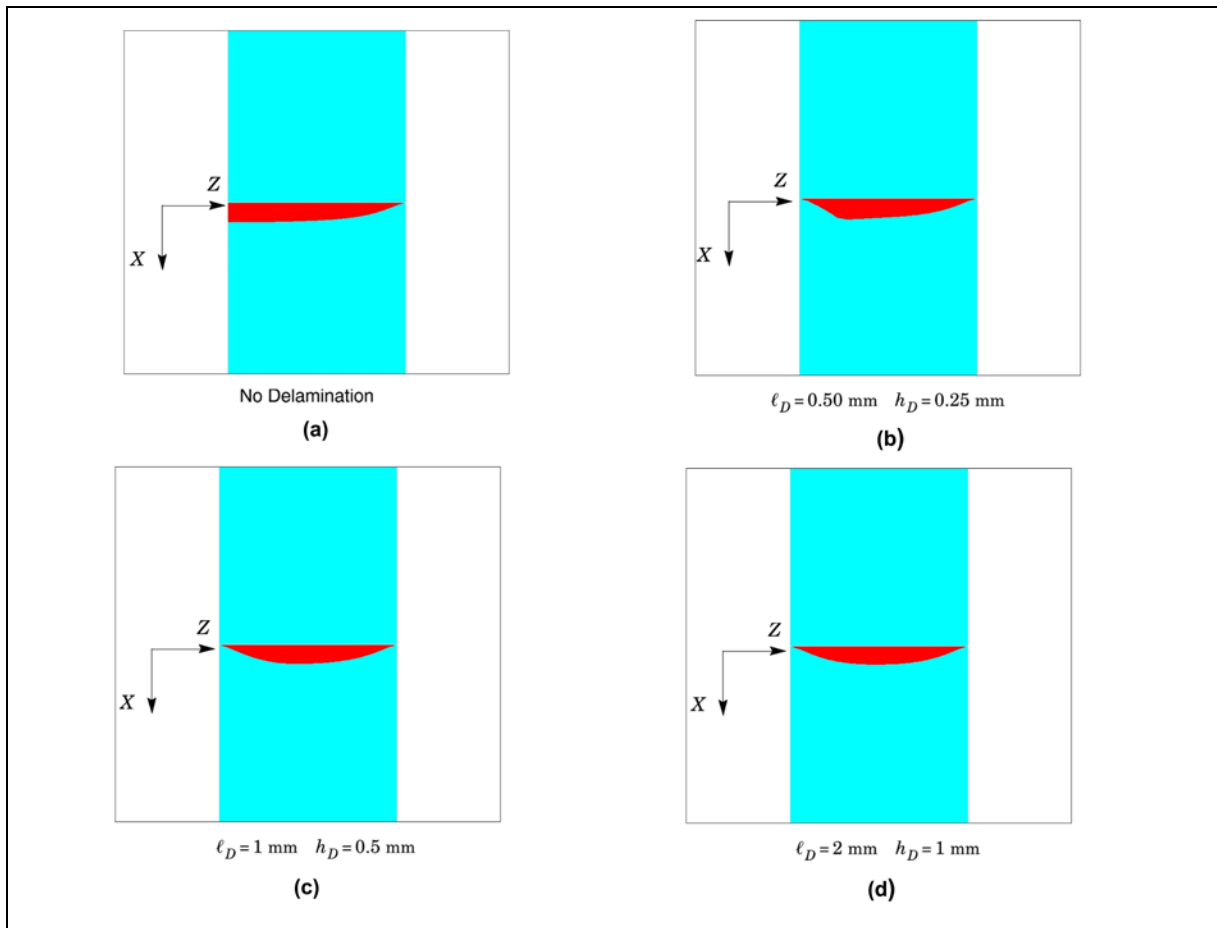


Figure 7. Opening stress zones for which $\sigma_{yy} \geq 2\sigma_o$ over the crack front for the models with and without transverse delamination crack at $K_I = 40\text{MPa}\sqrt{\text{m}}$: (a) No delamination; (b) 0.5x0.25 mm delamination; (c) 1x0.5 mm delamination and (d) 2x1 mm delamination.

Not surprisingly, the stress contours for the models with and without a transverse delamination crack differ significantly. The delamination crack clearly promotes a marked stress redistribution over the crack front for all load levels and delamination sizes. In particular, Figure 7(b) demonstrates the strong impact of even a small delamination crack on the near-tip stress fields caused by the dramatic loss of out-of-plane constraint. Observe, however, that the effects of delamination on the stress contour maps are less pronounced for larger delamination cracks. Here, the high stress regions $\sigma_{yy} \geq 2\sigma_o$ for the 1x0.5 mm and 2x1 mm delamination cracks are similar, though less intense than the corresponding stress contours for the model without a transverse delamination. The trends shown here are consistent with those shown in previous Figures 4 and 5 in that the introduction of a delamination crack produces a stress-free surface at the center plane which relaxes the through-thickness constraint and shifts the near-tip highly stressed region to the middle portion of crack front.

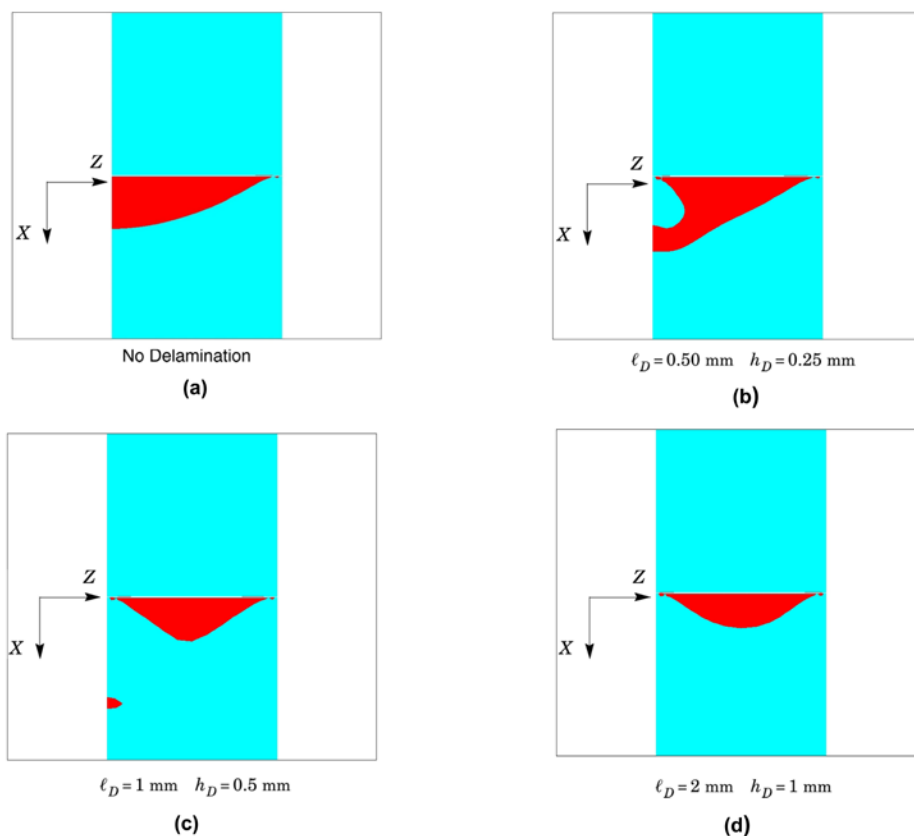


Figure 8. Opening stress zones for which $\sigma_{yy} \geq 2\sigma_o$ over the crack front for the models with and without transverse delamination crack at $K_{Jc} = 100 \text{ MPa}\sqrt{\text{m}}$: (a) No delamination; (b) 0.5x0.25 mm delamination; (c) 1x0.5mm delamination and (d) 2x1 mm delamination.

Concluding Remarks

This study describes an extensive numerical investigation of the crack front fields and effects of crack-tip constraint in conventional SE(B) fracture specimens with prescribed crack-divider delamination cracks. The 3-D numerical models have a center-plane delamination crack with varying prescribed length, ℓ_D , and height, h_D , at the onset of loading which is adequately descriptive of the local conditions affecting macroscopic fracture behavior of the analyzed fracture specimens. The simulations are conducted on a plane-sided SE(B) geometry having mechanical properties corresponding to a 14YWT nanostructured ferritic alloy (NFA-1) tested at room temperature to measure the fracture toughness properties. The exploratory work described here supports the following key conclusions:

1. Formation of a transverse center-plane delamination crack creates a stress-free surface at the center plane thereby relaxing the through-thickness constraint and, at the same time, shifting the near-tip highly stressed region to the middle portion of the remaining specimen thickness ligament corresponding approximately to crack front locations of $Z/(B/2) \approx 0.4-5.0$. Perhaps more importantly, the formation of a crack divider delamination at the specimen center plane drastically changes the distribution of the macroscopic driving force over the crack front with potential significant effects on the fracture toughness behavior. In particular, the onset of through-thickness splitting effectively divides the bulk of the specimen so that only a reduced portion of the crack front is subjected to high levels of crack-tip loading (as measured by J or K_J) thereby potentially enhancing fracture toughness.

2. The 3-D numerical analyses show that the formation of even a small transverse delamination crack at the specimen midplane promotes a marked stress redistribution over the specimen thickness which likely causes the formation of another transverse delamination crack at the center portion of the remaining thickness ligament. While the present analyses do not incorporate the growth of the delamination crack with increased loading, and thus not including history effects on the evolving crack front stress fields and crack front constraint, the present numerical results provide very plausible qualitative support for the multiple delamination cracking observed in the fracture surface of the tested SE(B) specimens.

References

- [1] M. E. Alam, N. J. Cunningham, D. Gragg, K. Fields, G. R. Odette, D. T. Hoelzer and S. A. Maloy, "Mechanical Properties Characterization of a Large Best Practice Heat of 14 YWT NFA1", DOE/ER-0313/56 (2014), DOE Fusion Reactor Materials Program Semiannual Progress Report (2014).
- [2] D. J. Embury, J. N. Petch, E. A. Wraith, S. E. Wright, "The Fracture of Mild Steel Laminates", Transactions of the Metallurgical Society of AIME, 239 (1967) 114-118.
- [3] W. B. Morrison, "Influence of Testing Direction on the Mechanical Properties of Wrought Steel", Metals Technology, 2 (1975) 33-41.
- [4] G. Baldi, G. Buzzichelli, "Critical Stress for Delamination Fracture in HSLA Steels", Metal Science (1978) 459-472.
- [5] K. T. V. Rao, W. Yu, R. O. Ritchie, "Cryogenic Toughness of Commercial Aluminum-Lithium Alloys: Role of Delamination Toughness", Metallurgical Transactions A, 20A (1989) 485-497.
- [6] K. T. V. Rao, R. O. Ritchie, "Mechanical Properties of Al-Li Alloys - Part 1: Fracture Toughness and Microstructure", Materials Science and Technology, 5 (1989) 882-895.
- [7] K. T. V. Rao, R. O. Ritchie, "Mechanical Properties of Al-Li Alloys - Part 2: Fatigue Crack Propagation", Materials Science and Technology, 5 (1989) 896-907.
- [8] S. Kalyanam, A. J. Beudoin, R. H. Dodds, F. Barlat, "Delamination Cracking in Advanced Aluminum-Lithium Alloys - Experimental and Computational Studies", Engineering Fracture Mechanics, 76 (2009) 2174-2191.
- [9] American Society for Testing and Materials, Standard Test Method for Measurement of Fracture Toughness", ASTM E1820-2011 (2011).
- [10] American Society for Testing and Materials, Standard Test Method for Determination of Reference Temperature, T_0 , for Ferritic Steels in the Transition Range, ASTM E1921-13a (2013).
- [11] B. Healy, A. Gullerud, K. Koppenhoefer, A. Roy, S. RoyChowdhury, J. Petti, M. Walters, B. Bichon, K. Cochran, A. Carlyle, J. Sobotka, M. Messner, R. H. Dodds, "WARP3D: 3- D Dynamic Nonlinear Fracture Analyses of Solids Using Parallel Computers", Structural Research Series (SRS 607) UILU-ENG-95-2012, University of Illinois at Urbana-Champaign, <http://code.google.com/p/warp3d> (2013).
- [12] M. Nevalainen, R. H. Dodds, "Numerical Investigation of 3-D Constraint Effects on Brittle Fracture in SE(B) and C(T) Specimens", International Journal of Fracture, 74 (1995) 131-161.

2.3 STRUCTURAL AND CHEMICAL EVOLUTION IN NEUTRON IRRADIATED AND HELIUM-INJECTED FERRITIC ODS PM2000 ALLOY—Hee Joon Jung, Dan J Edwards, Richard J Kurtz (Pacific Northwest National Laboratory), Takuya Yamamoto, Yuan Wu and G. Robert Odette (University of California, Santa Barbara)

This extended abstract reports on some of the major results in a paper recently published in the *Journal of Nuclear Materials* <http://dx.doi.org/10.1016/j.jnucmat.2016.11.022>.

An investigation of the influence of helium on damage evolution under neutron irradiation of an 11 at% Al, 19 at% Cr ODS ferritic PM2000 alloy was carried out in the High Flux Isotope Reactor (HFIR) using a novel *in situ* helium injection (ISHI) technique. Helium was injected into adjacent TEM discs from thermal neutron $^{58}\text{Ni}(n_{\text{th}},\gamma)$ $^{59}\text{Ni}(n_{\text{th}},\alpha)$ reactions in a thin NiAl layer. The PM2000 undergoes concurrent displacement damage from the high-energy neutrons. The ISHI technique allows direct comparisons of regions with and without high concentrations of helium since only the side coated with the NiAl experiences helium injection. The corresponding microstructural and microchemical evolutions were characterized using both conventional and scanning transmission electron microscopy techniques. The evolutions observed include formation of dislocation loops and associated helium bubbles, precipitation of a variety of phases, amorphization of the Al_2YO_3 oxides (which also variously contained internal voids), and several manifestations of solute segregation. Notably, high concentrations of helium had a significant effect on many of these diverse phenomena. These results on PM2000 are compared and contrasted to the evolution of so-called nanostructured ferritic alloys (NFA).

SUMMARY

Understanding how helium interacts with the defects produced under irradiation, how it accumulates into pressurized cavities that can eventually grow large enough to reach the critical size of unstable void growth (helium is no longer needed for the voids to grow), are key issues that require well designed experiments to probe the effect of such large levels of helium under fusion relevant conditions. One of the approaches to control this inventory of helium is to develop Fe-Cr based ferritic alloys with a high density of oxide particles, which act as trapping sites for the helium and prevent it from accumulating into helium bubbles large enough to transition into unstably growing voids. Several of these and other ferritic alloys were injected with helium while being neutron irradiated to achieve He/dpa rates relevant to fusion applications.

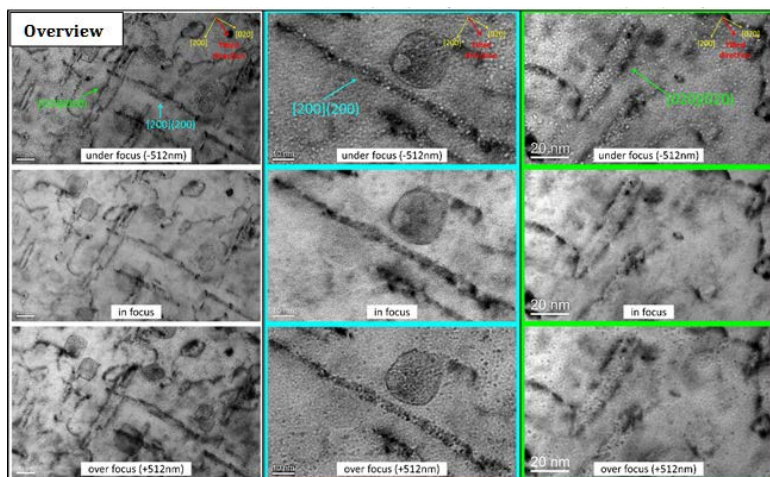


Figure 1. Three sets of BFTEM images at different magnification with under/in/over-focus near [001] zone from the helium-implanted side: sample is tilted off the [001] zone axis toward the [020] direction to show the presence of helium bubbles on $\langle 100 \rangle\{100\}$ dislocation loops.

This in-situ injection of helium was accomplished by using NiAl coatings on various ferritic alloys, 3-mm discs of which were irradiated in the HFIR at ORNL to 773K to 21 dpa, producing 1230 appm He in the coated side of the disc due to transmutation of the Ni via the two-step $^{58}\text{Ni}(n_{\text{th}},\gamma)$ $^{59}\text{Ni}(n_{\text{th}},\alpha)$ reaction. This unique experiment allowed TEM samples to be extracted via FIB milling from the NiAl coated side and from the opposite side, enabling a direct comparison between two identically neutron irradiated

samples, one with helium injection and the other with no helium injection. PM2000, a large grained FeCrAl ferritic alloy, was included in this experiment. Although not considered a prime candidate material for fusion because of the 5-wt% Al, it does provide a useful alloy to compare with the nanostructured ferritic alloys (NFA) such as 12YWT and 14YWT. Possessing a 1 mm grain size and lower density of oxide particles than the two NFA materials, the much lower fraction of grain boundary interfaces and oxide metal/interfaces, both trapping sites for helium, yielded a material considerably more swelling resistant than anticipated due to an unexpectedly strong synergy between the helium and the dislocation loops.

Figure 1(a) provides examples of dislocation loops imaged off the [100]-zone axis. At this orientation, both edge-on $\langle 100 \rangle \{100\}$ and inclined $\frac{1}{2} \langle 111 \rangle \{111\}$ are visible. Through focal imaging revealed a clear association between small helium bubbles (<3 nm in size) and loops of both types. This association promoted a high density of much larger loops of both loops types compared to the side with no helium injection, and it accentuated the population of sessile $\langle 100 \rangle$ loops relative to the $\frac{1}{2} \langle 111 \rangle$ loops. This synergy between the loops and helium also prevented the helium bubbles from coarsening and reaching the critical size (>3 nm) to achieve unstable void growth. The oxide particles were found to have completely amorphized, and each particle in the helium-injected side contained a single large void inside the particle volume. In the non-helium injected side, a much smaller fraction of the particles contained a single void, and no helium bubbles or voids were found to be associated with the dislocation loops. While the presence of large levels of helium altered the dislocation structure and created voids inside the amorphous oxide particles, it did not seem to have impact on the chemical changes inside the material. Both sides exhibited precipitation of a newly discovered $\text{Fe}_3(\text{Al,Cr,Ti})$ intermetallic phase, which were easily imaged using precipitate dark field as shown in Figure 2 both the neutron irradiated and the ISHI side of the 3-mm disc. Additionally, alpha prime formation was found equally in both sides, and didn't appear to be substantially effected by the presence of the loops, helium bubbles, nor the precipitation of a high density of $\text{Fe}_3(\text{Al,Cr,Ti})$ precipitates.

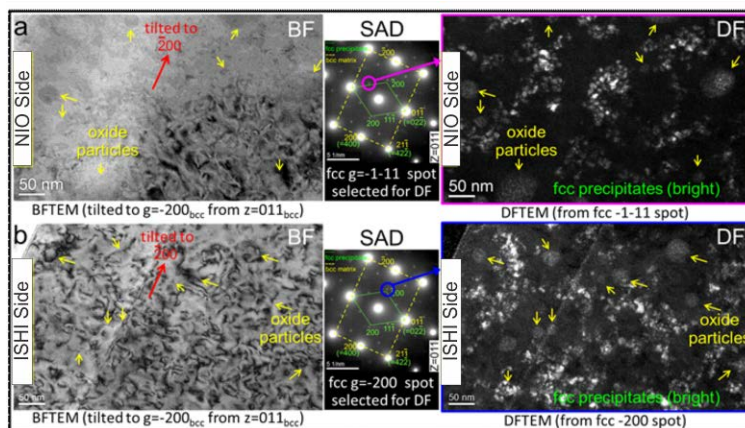


Figure 2. BFTEM images taken near a 011 zone in (a) the NIO side and (b) the ISHI side. The middle image is an SAD pattern from the corresponding area shown in the BFTEM. Precipitate DFTEM images, shown at the right, were taken using the indicated fcc $g = \bar{1}11$ and fcc $g = \bar{2}00$ respectively. The amorphous oxide particles (indicated by yellow arrows) are also visible because the selected area aperture also captured a portion of the amorphous halo near the fcc diffraction spot.

This experiment revealed high levels of helium can be controlled, that is, kept in a high density of small cavities, by a synergistic reaction between dislocation loops and helium. This mechanism isn't necessary observed in other ferritic alloys, possibly due to the competing effects of nearby grain boundaries and a different composition.

Acknowledgement

This research has been supported by the U.S. Department of Energy, Office of Science, Office of Fusion Energy Sciences (DE-AC06-76RL0-1830).

2.4 HIGH TEMPERATURE HELIUM IMPLANTATION OF NI/FE – Y₂Ti₂O₇ BILAYERS—T. Stan, Y. Wu, G.R. Odette, T. Yamamoto (University of California Santa Barbara), and Y. Wang (Los Alamos National Laboratory)

OBJECTIVE

The objective of this work is to gain insight into the behavior and final fate of He in Nanostructured Ferritic Alloys by studying a surrogate system: He implantation and characterization of Ni/Fe - Y₂Ti₂O₇ bilayers.

SUMMARY

The 2.5 nm average diameter Y-Ti-O nano-oxides (NOs) in Nanostructured Ferritic Alloys (NFAs), help impede dislocation climb and glide, stabilize dislocation and grain structures, and trap He in harmless nm-scale bubbles. To complement other studies of the NOs themselves, mesoscopic-scale bilayer interfaces were fabricated by electron beam deposition of Fe films on {100}, {110}, and {111} Y₂Ti₂O₇ (YTO) bulk single crystal substrates. Four Fe-YTO orientation relationships were observed, and reported here. After encapsulating the bilayers with Ni, the Fe side was high temperature (700 °C) ion implanted using 1.6 MeV He⁺ to a dose of 2.26x10¹⁶ He/cm². Radiation enhanced diffusion led to the intermixing of Ni and Fe, and to the formation of Kirkendall 1μm voids at the Ni/Fe-YTO interfaces. Further, He bubbles were seen in all of the Ni/Fe films, as well as inside of some YTO substrates. No bubbles were observed at the metal-oxide interfaces.

PROGRESS AND STATUS

Introduction

Nanostructured Ferritic Alloys (NFAs) are a promising class of Fe-Cr-based stainless steels with outstanding mechanical properties, are thermally stable up to 950°C, and are remarkably irradiation tolerant [1–4]. NFAs contain a high density of $N \approx 5 \times 10^{23}/m^2$ of YTO nano-oxides with an average diameter of $\langle d \rangle \approx 2.5$ nm. The NOs impede dislocation climb and glide, stabilize dislocation and fine grain structures, and most notably, trap He in fine-scale bubbles at the matrix-NO interfaces. The high density of bubbles prevents the formation of growing voids and He accumulation at grain boundaries, which would otherwise degrade the dimensional stability, creep and fracture properties of most structural alloys, as is the case for conventional 9 Cr tempered martensitic steels. He bubbles also act as recombination sites for vacancies and self-interstitials, thus promoting radiation damage self-healing.

Research to characterize NO compositions, structures, misfit strains, core shell structures, interface characteristics, and NO-matrix orientation relationships (ORs) is continuing [5–8]. Most of the smallest NOs are the Y₂Ti₂O₇ (YTO) fcc pyrochlore [7–15]. Detailed characterization and analysis of the NO-matrix interfaces is needed to develop first principles and atomic-scale models that are part of multi-scale efforts to guide the selection of processing paths and to predict the behavior of NFAs and NOs in irradiation service environments. YTO-matrix ORs are of particular interest, because they impact the selection of compositions and processing paths, service stability, mechanical properties and irradiation tolerance of NFAs. Important interface characteristics include their structures, chemistries, defects, misfit strains, free energies and, perhaps most importantly, NO interactions with He. The embedded NOs and their interfaces are challenging to characterize, partly due to their small nm-scale size.

A comprehensive first principles study by Jiang et al. [16–18] showed that He is deeply trapped in the YTO NOs at an energy of ~1.4 eV lower than in the Fe-Cr matrix. Coupled with the ultra high NO sink strength, this ensures that the eventual fate of He is to reside in nm-scale bubbles on the oxide interfaces. The sequence of events is as follows. First He migrates to, and is deeply trapped in, the NOs. However, the He energy is even lower in sufficiently sized NO-matrix interface bubbles, that quickly nucleate and grow, thereby draining the He from the NOs. Thus characterization of the matrix-NO-interface He partitioning is critically important and is one of the major goals of the experiment described below.

To study the He transport and fate in a controlled fashion, our approach was to deposit Fe on oriented YTO single crystal substrates to create bilayers with mesoscopic-scale interfaces that facilitate detailed characterization studies. Ideally, the bilayer interfaces are the same, or similar to, those found in the embedded NOs. As well as facilitating He and point defect transport and fate studies, characterization of the Fe-YTO interfaces will provide input to first principles interface modeling.

Experimental

The details of sample fabrication and characterization techniques are covered in previous publications and Fusion Semiannual Reports [19]. In summary, YTO single crystals were oriented to have {100}, {110} and {111} surfaces and corresponding 2 mm thick wafers were cut from the rod using a wire saw. An Allied Multiprep was used to mechanically polish the wafers using a sequence of diamond lapping films and colloidal silica. The substrates were then Aqua Regia etched and cleaned with acetone, isopropanol, and reverse osmosis water. However, one {110} substrate was Aqua Regia etched and rinsed with only tap water.

The YTO single crystal wafers were loaded into an electron beam deposition system and heated to 1073 K (800°C) at a rate of 0.166 K/s. After outgassing for 1 h, 2.2 μm of Fe was deposited at a rate of ~8 nm/s (250 s total) and chamber pressure of 3×10^{-6} torr. After deposition the Fe-YTO bilayers were allowed to sit in vacuum at 1073 K (800°C) for a minimum of 30 min. The bilayers were then slowly cooled to room temperature prior to unloading. The resulting films were characterized using an FEI Quanta 400F field-emission scanning electron microscope (SEM) equipped with an electron backscatter diffraction (EBSD) detector. The bilayers were then cut into ~3 mm x 3 mm cubes, and were coated on all six sides with 1 μm Ni using a sputtering deposition system at Argonne National Laboratory.

He implantations were performed at the Ion Beam Implantation Laboratory at Los Alamos National Laboratory. Four bilayers were mounted on a 7° tilted wedge to prevent He channeling through low-index Fe crystallographic directions. The assembly was loaded into a TANDEM implanter, pumped down to $\sim 4 \times 10^{-7}$ Torr, and the temperature was slowly raised to 700° C. The temperature was continuously monitored in three locations: inside the heater, inside the assembly, and <1 mm away from the sample surface. A defocused 1.6 MeV He⁺ ion beam was used to implant the bilayers to a dose of 2.26×10^{16} He/cm², dose rate of 1.4×10^{11} He/cm²/s, and implantation time of ~162000 s (~45 hrs).

SRIM/TRIM was used to calculate the He implantation profile (black curve and left vertical axis) and damage profile (red curve and right vertical axis) shown in Figure 1. The maximum He concentration is 10797 appm He at a depth of 2.55 μm into the bilayer, or 0.65 μm from the Fe-YTO interface. As is clearly seen in Figure 1, the He concentration profile is fully within the Fe layer as we did not want to implant He directly into the interface or YTO substrate. The red curve shows the damage profile, which has a maximum of 0.47 dpa at a depth of 2.52 μm into the bilayer, or 0.68 μm from the Fe-YTO interface. On average, 87 vacancies are produced for each implanted He ion. If all of the He would evenly distribute throughout the Fe+Ni layers (3.2 μm thick together) and none would enter the YTO, the average He concentration would be 837 appm.

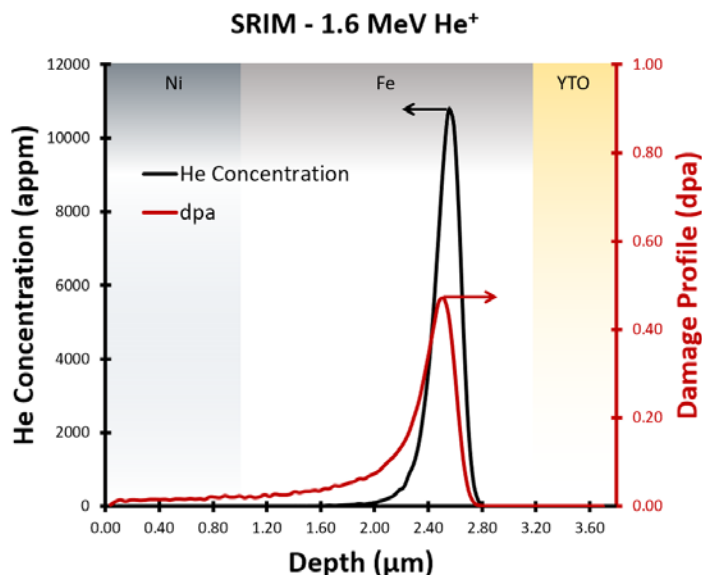


Figure 1. SRIM/TRIM calculated He concentration profile (black curve and left vertical axis) and displacement damage profile (red curve and right vertical axis) for the 1.6 MeV He⁺, 2.26×10^6 He/cm², implantation into a 1 μm thick Ni coating, 2.2 μm thick Fe film, and arbitrarily thick YTO substrate.

An FEI HELIOS Focus Ion Beam (FIB) tool was used to first deposit ~1 μm of protective platinum over areas of interest. Cross sectional lift-outs of the Fe-YTO bilayers were extracted, thinned to <40 nm, and a low energy 2 keV 5.5 pÅ gallium beam was used for the final cleaning. High-resolution transmission electron microscopy (HRTEM), scanning TEM (STEM), and energy dispersive xray (EDX) observations were carried out on a 300 keV FEI Titan TEM at UCSB.

Results and Discussion

SEM and EBSD Characterization

Figure 2 contains SEM and EBSD data of the bilayers investigated in this study. The images were taken prior to Ni coating and He implantation, and are named according to the YTO substrate orientation. For example, the Fe- $\{100\}$ YTO bilayer is a 2 μm Fe film on a $\{100\}$ YTO oriented substrate. Of the two $\{110\}$ YTO bilayers, one is termed Fe- $\{110\}$ YTO etch to identify the unique cleaning step mentioned previously. The scans from the Fe- $\{100\}$ YTO bilayer are shown in the first column (Figures 2a, 1b, 1c), the scans from the Fe- $\{110\}$ YTO bilayer are shown in the second column (Figures 2d, 1e, 1f), etc. The top row in Figure 2 contains SEM images of the Fe films. Inverse pole figure Z-direction (IPFZ) maps are shown in the second row, and are colored according to the Fe surface orientation. Green indicates $\{110\}$ out-of-plane orientations and red indicates $\{100\}$ orientations. The bottom row contains the same EBSD data as the IPFZ maps, but using an Euler representation where each full crystallographic orientation is assigned a unique color. All nine images show a 20 μm x 20 μm representative surface area and are equally scaled to facilitate side-by-side comparison.

The Fe- $\{100\}$ YTO bilayer SEM image in Figure 2a shows 0.5 μm to 8 μm elongated grains. The EBSD IPFZ map in Figure 2b is colored completely green, indicating very strong $\{110\}$ Fe texturing. Black areas in Figure 2b (and in the other EBSD figures) are locations where the Fe orientation could not be indexed, often due to the presence of grain boundaries. The Euler Map in Figure 2c is colored pink and orange; however, there are in fact two shades of pink and two shades of orange, indicating four in-plane variants of the $\{110\}$ Fe grains (further discussed with Figure 3).

Figure 2d shows an SEM image from the Fe- $\{110\}$ YTO bilayer indicating roughly 2 μm – 4 μm grains. The film surface is not smooth and has visible ledges. The IPFZ map in Figure 2e shows orange and pink orientations, although slight coloration variants are also observed. The Euler map in Figure 2f shows a red orientation that covers the majority of the Fe film, but patches of the film are colored magenta and purple. These orientations are similar and indicate axiotaxial texturing (further discussed with Figure 3).

Figure 2g is an SEM image from the Fe- $\{110\}$ YTO etch bilayer. Grain boundaries are not observed as seen in the Fe- $\{100\}$ YTO and Fe- $\{110\}$ YTO bilayers, but 0.5 μm topographical mounds are seen. The IPFZ map in Figure 2h is colored completely red, indicating a strong $\{100\}$ Fe out-of-plane orientation for the entire film. The Euler map in Figure 2i shows slight color variations indicating that the film is actually composed of patches of closely oriented grains, roughly the same size as seen in the previous two depositions.

Figure 2j is an SEM image of the Fe- $\{111\}$ YTO bilayer indicating one continuous film. Individual grains are not seen, but the film surface contains ledges similar to those in Figure 2d. The EBSD IPFZ map is colored completely red, indicating strong $\{100\}$ Fe texturing. The Euler map in Figure 2l is completely dark red indicating only one continuous orientation without grain boundaries.

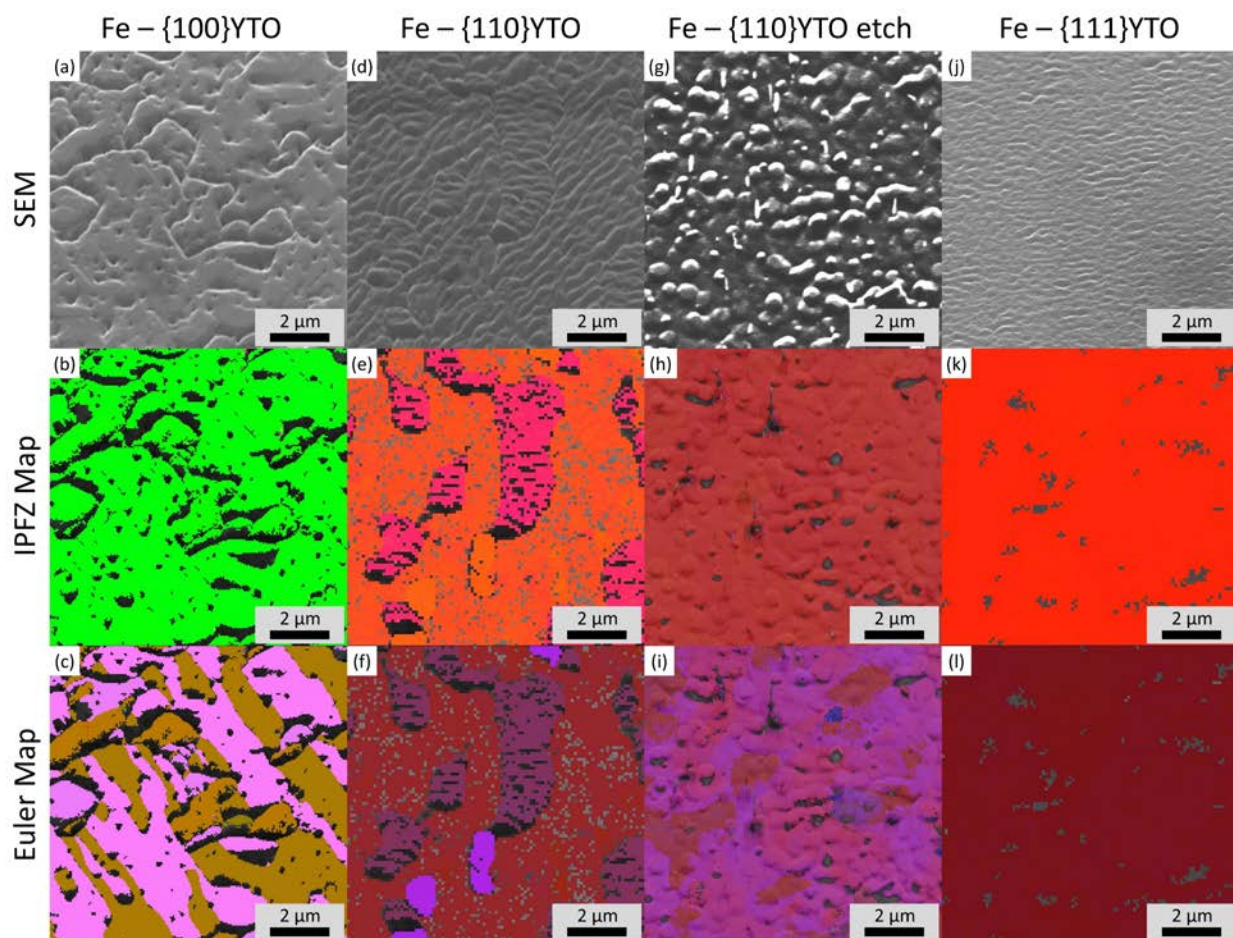


Figure 2. SEM and EBSD data from the bilayers (four columns). SEM images from the Fe surfaces are shown in the top row. EBSD IPFZ maps are shown in the middle row, colored according to the out-of-plane Fe orientation. The bottom row shows Euler maps colored according to the full 3D orientation of each grain.

Figure 3 has four columns, one for each bilayer, showing Fe and YTO pole figures (PFs) and the associated 3D representations. The top row in Figure 3 contains $\langle 100 \rangle$ and $\langle 110 \rangle$ PFs from the Fe film. The spots are colored according to the out of plane orientations. The second row contains the same PFs from the top row, but colored according to the Euler representation, better showing differences in in-plane orientations. The third row contains PFs from the YTO substrates, colored according to the surface orientation. The fourth row in Figure 3 shows 3D representations of the Fe variants and the YTO substrate orientation.

The first column in Figure 3 contains EBSD data from the Fe- $\{100\}$ YTO bilayer, and is complimentary to the first column in Figure 2. The two PFs in Figure 3a show strong $\{110\}$ Fe texturing, as indicated by the spot in the center of the $\langle 110 \rangle$ PF. The Euler PFs in Figure 3b contain four colors (pink1, pink2, orange1 and orange2) indicating four in-plane variants of the $\{110\}$ grains. The $\langle 100 \rangle$ PF in Figure 3c has a spot at the center, confirming the $\{100\}$ YTO substrate orientation. Figure 3d shows 3D representations of the four $\{110\}$ Fe variants and the $\{100\}$ YTO. The film to substrate crystallographic OR is obtained by overlapping the spots from the Fe PFs with those from the YTO PFs. The OR is: $\{110\}$ Fe// $\{100\}$ YTO and $\langle 111 \rangle$ Fe// $\langle 110 \rangle$ YTO, and was observed in previous depositions on $\{100\}$ YTO. However, this OR has not been observed for embedded NOs.

The second column in Figure 3 contains EBSD data from the Fe- $\{110\}$ YTO bilayer. The streaks in the IPFZ (Figure 3e) and Euler (Figure 3f) PFs indicate axiotaxial texturing. The spots near the pole figure center are off from $\{100\}$ Fe by $\sim 7^\circ$. The presence of a spot in the bottom right quadrant of the $\langle 110 \rangle$ Fe PFs indicate that the Fe grains have off-axis rotations about the $\langle 110 \rangle$ Fe direction. The YTO PFs in Figure 3g indicate a good $\{110\}$ YTO orientation. The 3D representations in Figure 3h show three examples of the Fe orientations along with the YTO substrate. The OR for this film is roughly $\{104\}$ Fe// $\{110\}$ YTO, with multiple in-plane variants, some of which have $\langle 100 \rangle$ Fe// $\langle 110 \rangle$ YTO. This axiotaxial OR was observed in previous depositions on $\{110\}$ YTO, but not observed for embedded NOs.

EBSD data from the Fe- $\{110\}$ YTO etch bilayer are shown in the third column of Figure 3. The bilayer has the same substrate orientation as the Fe- $\{110\}$ YTO sample, but a strong $\{100\}$ Fe texture as indicated by the center spot in the $\langle 100 \rangle$ Fe PFs in Figures 3i and 2j. The purple, pink, and red spots in Figure 3j overlap significantly and do not show the same streaking as in Figure 3f. The 3D representations are shown in Figure 3l, and are almost identical to each other. The YTO PFs in Figure 3k indicate a well oriented $\{110\}$ YTO substrate. The Fe-YTO OR for this bilayer is: $\{100\}$ Fe// $\{110\}$ YTO and $\langle 100 \rangle$ Fe// $\langle 110 \rangle$ YTO. This OR was observed in previous depositions and for embedded NOs. However, previous studies show that this Fe orientation is accompanied by a ~ 2 nm Ca-rich layer at the Fe-YTO interface.

Last, the EBSD data from the Fe- $\{111\}$ YTO bilayer is shown in the fourth column of Figure 3. The PFs indicate a strong $\{100\}$ Fe texturing, and the YTO PFs in Figure 3o confirm the $\{111\}$ YTO substrate orientation. The Fe and YTO 3D representations are shown in Figure 3p. The OR is $\{100\}$ Fe// $\{111\}$ YTO and $\langle 100 \rangle$ Fe// $\langle 110 \rangle$ YTO. This OR was observed in previous depositions but not in embedded NOs.

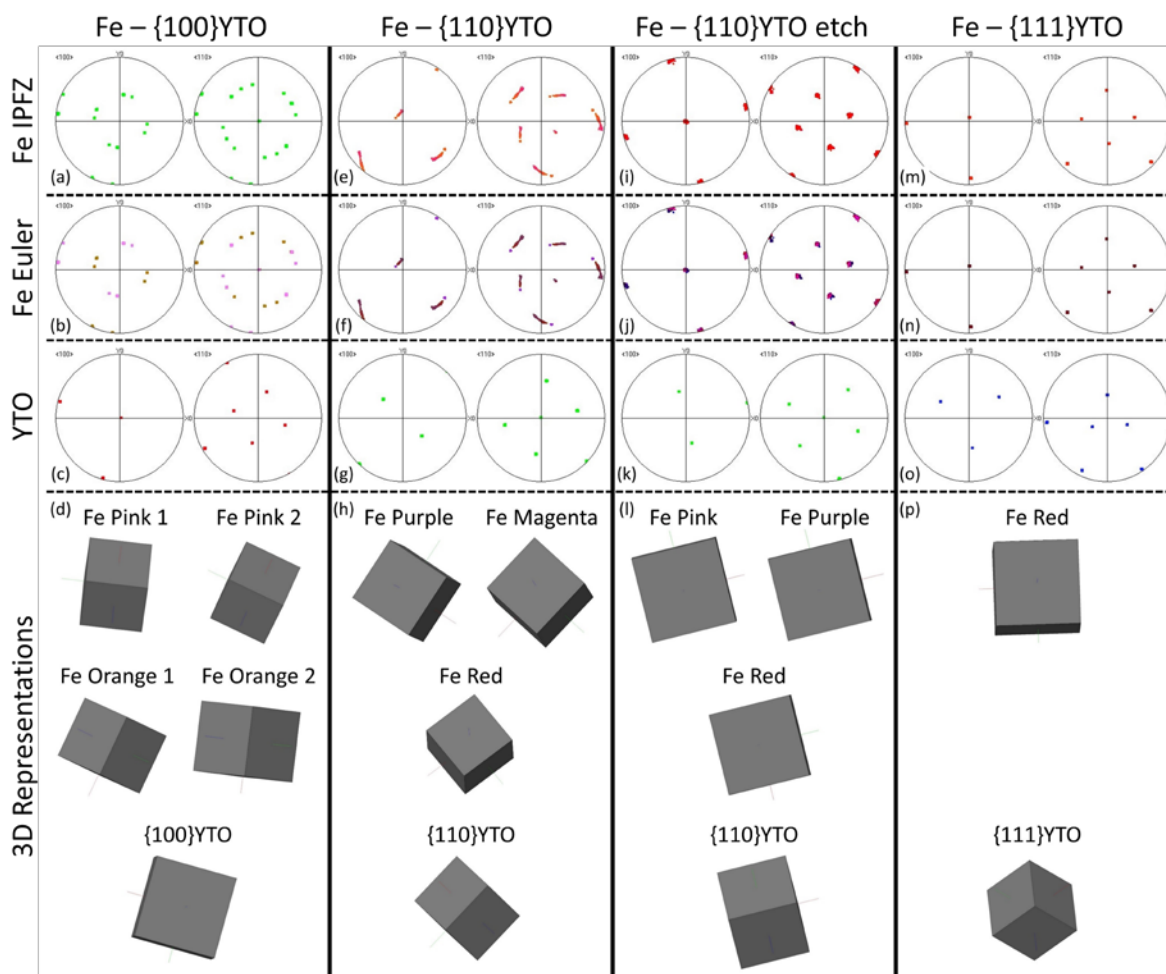


Figure 3. EBSD pole figures (PFs) and 3D representations of the four bilayers observed in this study. The top row indicates Fe PFs colored according to the IPFZ out-of-plane orientation. The second row shows Fe PFs colored according to the Euler orientations. The third row shows IPFZ PFs from the YTO substrate. The bottom row contains 3D reconstructions of the orientations seen in the Euler PFs, showing both Fe and YTO orientations.

TEM Characterization

Low magnification STEM imaging was used to characterize the bilayer microstructures after the Ni coating and subsequent high temperature He implantation. The multipart Figure 4 contains cross-sectional micrographs of the four bilayers. The average film thickness, Fe orientation, YTO orientation and Ni content is indicated in each image. The figures are equally scaled to facilitate side-by-side comparisons.

Figure 4a shows the microstructure of the Ni/Fe- $\{100\}$ YTO bilayer. There is no observable interface between the Ni coating and the initial Fe deposition. The Ni and Fe formed one continuous metallic film with an average thickness of $\sim 3.12 \mu\text{m}$ and with $\sim 0.5 \mu\text{m}$ wide recrystallized grains. EDX point scans were used to measure the Ni content at four locations along the metallic film as indicated in Figure 4a. The Ni content is ~ 33 at% at the top of the film, and ~ 24 at% close to the metal-oxide interface. An average of 29 at% Ni is present in the film, which is expected given that the Fe film and Ni coating were initially $\sim 2.2 \mu\text{m}$ and $\sim 1 \mu\text{m}$ thick, respectively. Notably, there is no Ni inside the YTO substrate. Large

cavities are present at the Ni/Fe-YTO interface, and are shown in black in the STEM images. The seven interfacial cavities in Figure 4a range in size from a few nm² to ~0.5 μm x ~2 μm. Vertical dark streaks are observed in the {100}YTO substrate, which are an artifact of the FIB processing. Material is preferentially milled in areas below the cavities.

Figure 4b shows the microstructure of the Ni/Fe-{110}YTO bilayer. The average film thickness is 3.33 μm, slightly more than the Ni/Fe-{100}YTO bilayer in Figure 4a. Again, recrystallized grains are observed in the Ni/Fe layer. A gradient in the Ni composition is seen with 41 at% Ni present at the surface and 9 at% Ni at the Ni/Fe-YTO interface. Unlike the Ni/Fe-{100}YTO bilayer, there are very few cavities at the Ni/Fe-{110}YTO interface shown in Figure 4b. Only three cavities are observed, with the largest being ~0.25 μm wide. The two dark holes in the YTO substrate are an artifact of the FIB lift-out sample preparation.

Figure 4c shows the microstructure of the Ni/Fe-{110}YTO etch bilayer. The initial Fe thickness was ~2.0 μm, thus the resulting metallic film thickness is ~2.93 μm, as expected. Similar to the Ni/Fe-{100}YTO bilayer, the Ni distribution is roughly uniform. The Ni/Fe-{110}YTO etch bilayer has the largest interfacial cavities observed in this study. The left of Figure 4c shows two cavities which have coalesced, a small ~0.3 μm wide cavity, and a large ~2 μm wide cavity.

Figure 4d shows the microstructure of the Ni/Fe-{111}YTO bilayer. The average film thickness is 3.22 μm, and the Ni concentration varies with proximity to the Ni/Fe-YTO interface. The interfacial cavity size is ~0.75 μm, similar to the Ni/Fe-{100}YTO bilayer. Four large cavities are observed, the largest being ~1 μm wide.

Three main observations are made by comparing the four bilayers. First, there is an inverse relationship between the film thickness and the cavity size. The Ni/Fe-{110}YTO bilayer which has the thickest film (~3.33 μm) has the fewest and smallest interfacial cavities, while the Ni/Fe-{110}YTO etch bilayer has the thinnest film (~2.93 μm) and has the largest cavities. Note that during FIB fabrication of the TEM lift-outs, the interfacial cavities are preferentially milled by the gallium beam. Thus, the actual cavity sizes in the Fe-YTO film are slightly smaller than what is presented in Figure 4.

Second, there is a correlation between the uniformity in Ni concentration and the cavity size. The two bilayers with nearly-uniform Ni distributions have large cavities, while the bilayers with a gradient in Ni concentration have smaller cavities. Also, the thicker films have a larger concentration gradient than the thin films. Diffraction pattern analysis of the Ni/Fe layer indicates that the film is no longer bcc α-Fe. The known phases in the Ni-Fe binary system are mostly fcc with lattice parameter of ~3.5 Å. The metastable Fe₃Ni phase which has the fcc L1₂ structure is of particular interest as it has a composition close to that of the Ni/Fe film (33% Ni). However, the diffraction pattern from the Ni/Fe film does not have the symmetry expected in a cubic system, and requires further analysis.

The presence of interfacial cavities can be explained by the Kirkendall effect. Diffusion couples may exhibit porosity if the two elements diffuse into each other at different rates. In the case of Fe and Ni, the intrinsic diffusion coefficient for Fe is higher than the coefficient for Ni [20]. Thus, the flux of Fe atoms moving toward the Ni coating is balanced by the fluxes of Ni atoms and vacancies moving toward the Fe-YTO interface. The interface acts as a heterogeneous nucleation site for the large cavities. Furthermore, the closer the initial Ni coating is to the interface, the less distance the vacancies travel before nucleating a cavity, and the sooner the cavity begins to grow. Thus, as was observed in the experiment, bilayers with a thinner Fe layer have larger cavities. An estimated intrinsic diffusion coefficient for Ni in Fe at 1500K is $D'_{Ni} \approx 2.2 \times 10^{-14}$ m²/s, and the implantation time in this experiment is $t \approx 1.6 \times 10^5$ s. The characteristic diffusion distance for Ni is $x = \sqrt{(D'_{Ni}t)} = 0.06$ μm. The Ni clearly diffused much further into the Fe layer (2 μm), thus the observed microstructure and interfacial cavities are due to radiation enhanced diffusion.

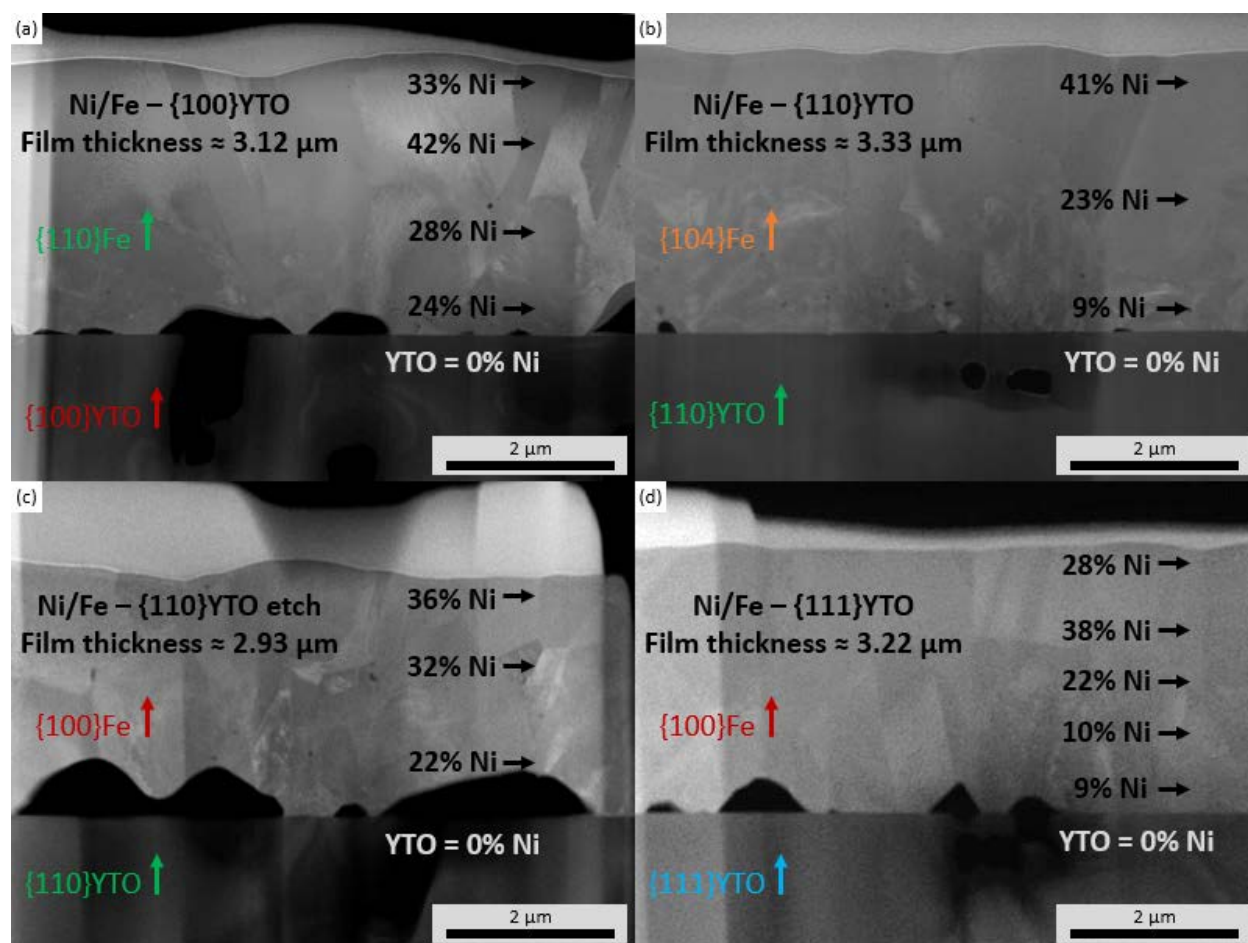


Figure 4. Low magnification cross-section images of the (a) Fe - {100}YTO, (b) Fe - {110}YTO, (c) Fe - {110}YTO etch and (d) Fe - {111}YTO bilayers. The average film thicknesses, Fe orientations, YTO orientations, and at% Ni measurements are indicated in each image.

Figure 5a is an under focused bright field TEM image from the Ni/Fe-{100}YTO bilayer. The red marks indicate the size and location of He bubbles. A large $d = 31 \text{ nm}$ bubble is present at a distance of $\sim 100 \text{ nm}$ from the metal-oxide interface; however, the average bubble diameter for the area shown in Figure 5a is $\langle d \rangle \approx 2.4 \text{ nm}$. No bubbles were observed at the Ni/Fe-YTO interface. Bubbles are identified by under focusing or over focusing the image such that moiré fringes reveal the bubble size and location. However, this defocusing also enhances contrast of the Fe/Ni-YTO interface which convolutes the signal from the bubbles. Possible surface oxide on the TEM lift-out also affects the contrast. Thus a full He inventory cannot be obtained for the Fe/Ni-YTO interface. However, we are confident that there are no clearly observable bubbles with $d > 2 \text{ nm}$ at the metal-oxide interface. Figure 5b shows the area below a large cavity in the Ni/Fe-{110}YTO etch interface. Small bubbles are clearly seen in the YTO substrate.

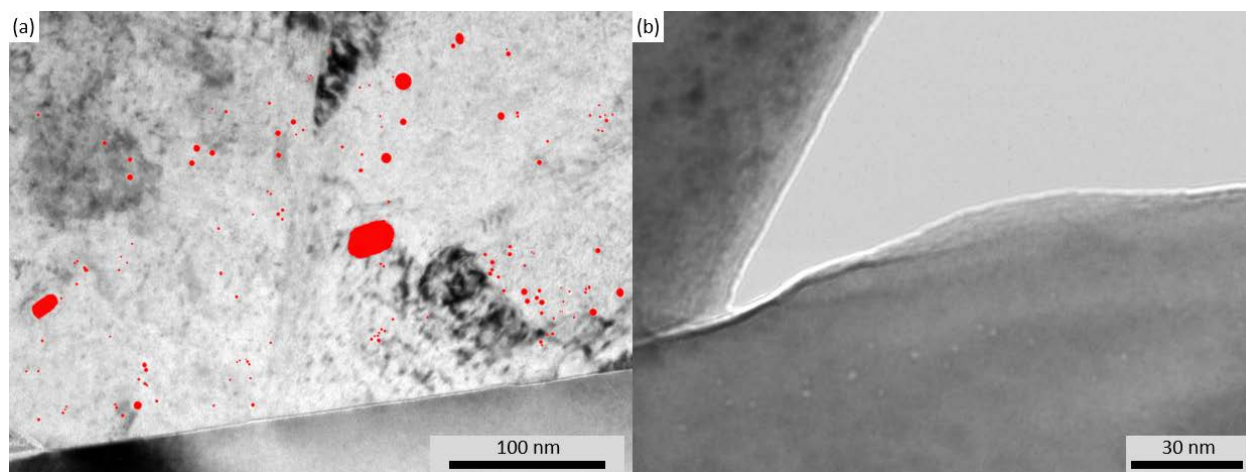


Figure 5. (a) Underfocused bright field TEM image of the Ni/Fe- $\{100\}$ YTO bilayer. Red marks indicate the location and size of He bubbles. (b) TEM image of the area under a large cavity in the Ni/Fe- $\{110\}$ YTO etch bilayer showing the presence of bubbles below the metal oxide interface.

The bubbles in representative sections of all four bilayers were analyzed. The plots in Figure 6 indicate the (a) bubble diameters, (b) number densities, and (c) He profiles as a function of distance from the Ni/Fe-YTO interfaces. The data for each bilayer was split into two charts for clarity.

Figure 6a shows the bubble diameters d in the bilayers. The average $\langle d \rangle$ for the entire Ni/Fe layers are 3.03 nm, 4.71 nm, 3.18 nm, and 4.30 nm for the 100YTO, 110YTO, 110YTO etch, and 111YTO bilayers, respectively. The bubble size slightly increases with depth or the Ni/Fe-110YTO bilayer, while it slightly decreases for the Ni/Fe-111YTO bilayer. Overall, there are no clear trends relating bubble sizes and proximity to the Ni/Fe-YTO interfaces.

Figure 6b shows the bubble number densities N calculated as number of bubbles per volume. The average $\langle N \rangle$ for the Fe/Ni layers are 2.21×10^{-5} , 7.06×10^{-5} , 2.12×10^{-5} , and 1.64×10^{-5} bubbles/ m^3 for the 100YTO, 110YTO, 110YTO etch, and 111YTO bilayers, respectively. Overall, there is a slight increase in bubble density as a function of distance from the metal-oxide interface. However, the trends are more closely associated with variations in microstructure. For example, the Ni/Fe-100YTO bilayer has a peak bubble diameter of $d = 7.59$ nm at a distance of 1.2 μm from the interface. This is due to the presence of a grain boundary that locally contains larger bubbles than the rest of the metallic film.

Figure 6c shows the total He count at different depths in the sample. Note that the He profile for the Fe-111YTO bilayer is scaled differently. The number of He atoms per bubble was calculated using a calibrated equation of state model which accounts for the implantation temperature (700 $^{\circ}C$). The average He concentrations are 505 appm He, 357 appm He, 414 appm He, and 2202 appm He for the 100YTO, 110YTO, 110YTO etch, and 111YTO bilayers, respectively. Note that the number of He atoms in a bubble increases exponentially with the bubble radius. The variations in He content are mostly due to the presence of large bubbles at microstructural features such as grain boundaries. There are no clear trends relating the bubble size to the proximity of the Ni/Fe-YTO interface.

The Ni/Fe-111YTO bilayer has a much higher He content than the other three bilayers. One explanation is that the bubble-rich region observed in this TEM lift-out is not representative of the full metallic film. The surrounding part of the metallic layer may have less He. Another possibility is that some of the circular microstructural features (especially atypically large ones) may not be bubbles, but precipitates of a second phase. Further analysis is required.

An average concentration of 837 appm He was implanted into the bilayers. The amount of He retained in the form of bubbles within the Ni/Fe films is 60%, 43%, and 49% for the 100YTO, 110YTO, and 110YTO

etch bilayers, respectively. It is unknown how much He was retained in the large interfacial Kirkendall cavities, and within the observed bubbles within the YTO substrates.

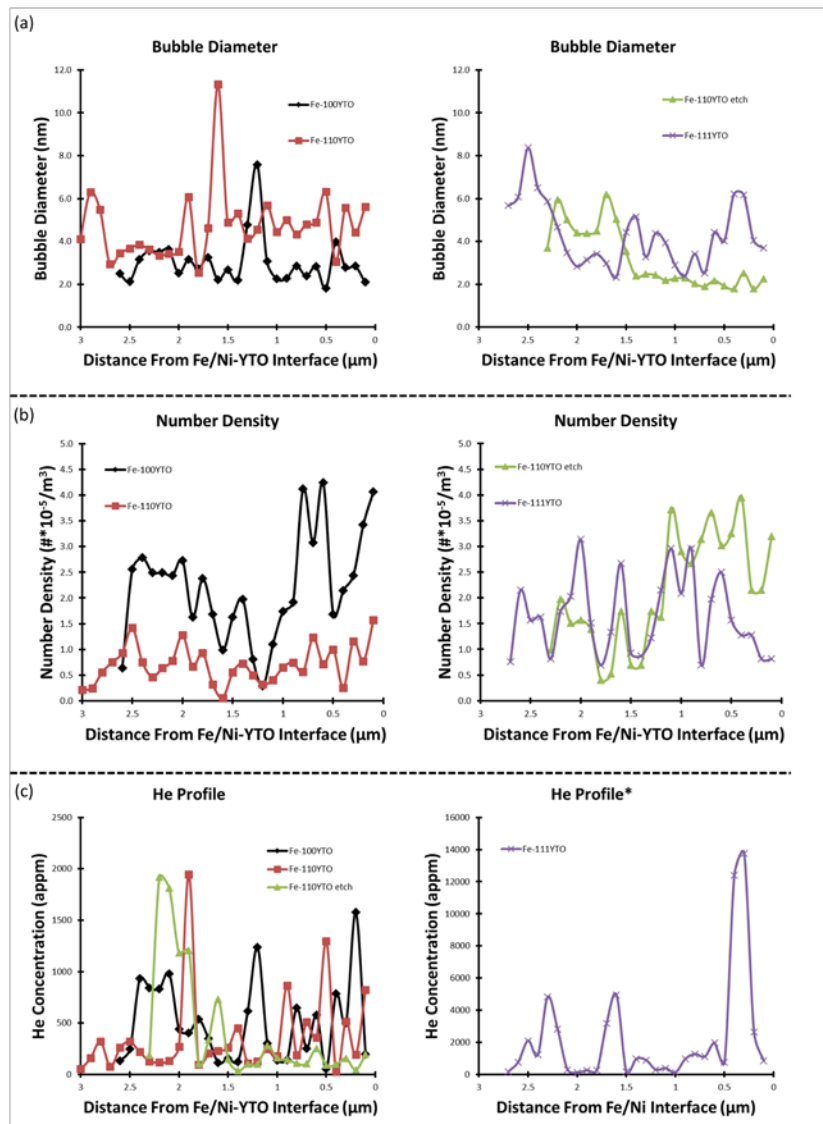


Figure 6. Bubble analysis from the four bilayers. (a) Bubble diameter, (b) number density, and (c) He profile as a function of distance from the Fe/Ni-YTO interface. *The two He profiles in (c) are on different scales.

Summary and Future Studies

In summary, mesoscopic-scale bilayer interfaces were fabricated by electron beam deposition of Fe films on {100}, {110}, and {111} $Y_2Ti_2O_7$ (YTO) bulk single crystal substrates. Four Fe-YTO orientation relationships were observed, and reported here. After encapsulating the bilayers with Ni, the Fe side was high temperature (700 °C) ion implanted using 1.6 MeV He^+ to a dose of 2.26×10^{16} He/cm². Radiation enhanced diffusion led to the intermixing of Ni and Fe, and to the formation of 1 μ m Kirkendall voids at the

Ni/Fe-YTO interfaces. Further, He bubbles were seen in all of the Ni/Fe films, as well as inside of some YTO substrates. No bubbles were observed at the metal-oxide interfaces.

Future studies include bulk spectroscopy measurements of the bilayers. The Ni/Fe-{100}YTO, Ni/Fe-{110}YTO, and the Ni/Fe-{111}YTO bilayers were cut into two, and the metallic film was removed from one of the halves. By comparing the He contents of the metallic (Ni/Fe+YTO) samples with those of just YTO, the partitioning of He will be reported.

Acknowledgements

The authors thank D. Stave and G. Seward (UCSB) for help with various parts of the data acquisition and analysis, J. Tesmer (LANL) for help with He implantation, and L. Stan (ANL) for Ni coating the bilayers. Crystal growth was supported by NSF DMR 1350002. The characterization was done at the UCSB CNSI Microstructure and Microanalysis Facility: an NSF MRSEC, supported by NSF DMR 1121053. This work was supported by the U. S. Department of Energy, Office of Fusion Energy Sciences, under grant DE-FG03-94ER54275.

References

- [1] G. Robert Odette: *JOM*, 2014, vol. 66, p. 2427.
- [2] G.R. Odette, M.J. Alinger, and B.D. Wirth: *Annu. Rev. Mater. Res.*, 2008, vol. 38, pp. 471–503.
- [3] N. Cunningham, Y. Wu, D. Klingensmith, and G.R. Odette: *Mater. Sci. Eng. A*, 2014, vol. 613, pp. 296–305.
- [4] Y. Dai, G. R. Odette, and T. Yamamoto: *The Effects of Helium in Irradiated Structural Alloys*, 1st ed., Elsevier Inc., 2012.
- [5] Emmanuelle A. Marquis: *Appl. Phys. Lett.*, 2008, vol. 93, pp. 10–13.
- [6] S. Liu, G.R. Odette, and C.U. Segre: *J. Nucl. Mater.*, 2014, vol. 445, pp. 50–56.
- [7] V. Badjock, M.G. Walls, L. Chaffron, J. Malaplate, and K. March: *J. Nucl. Mater.*, 2015, vol. 456, pp. 292–301.
- [8] Yuan Wu, Jim Ciston, Stephan Kräemer, Nathan Bailey, G. Robert Odette, and Peter Hosemann: *Acta Mater.*, 2016, vol. 111, pp. 108–15.
- [9] J. Ribis and Y. De Carlan: *Acta Mater.*, 2012, vol. 60, pp. 238–52.
- [10] J. Ribis and S. Lozano-Perez: *J. Nucl. Mater.*, 2014, vol. 444, pp. 314–22.
- [11] Karl Dawson and Gordon J. Tatlock: *J. Nucl. Mater.*, 2014, vol. 444, pp. 252–60.
- [12] M. Tamura, H. Sakasegawa, K. Shiba, H. Tanigawa, K. Shinozuka, and H. Esaka: *Metall. Mater. Trans. A*, 2011, vol. 42, pp. 2176–88.
- [13] Y. Wu, E. M. Haney, N. J. Cunningham, and G. R. Odette: *Acta Mater.*, 2012, vol. 60, pp. 3456–68.
- [14] A. J. London, B. K. Panigrahi, C. C. Tang, C. Murray, and C. R M Grovenor: *Scr. Mater.*, 2016, vol. 110, pp. 24–27.
- [15] R. Kasada, N. Toda, K. Yutani, H. S. Cho, H. Kishimoto, and A. Kimura: *J. Nucl. Mater.*, 2007, vol. 367–370 A, pp. 222–28.
- [16] Litong Yang, Yong Jiang, G. Robert Odette, Wenchong Zhou, Zuming Liu, and Yong Liu: *Acta Mater.*, 2013, vol. 61, pp. 7260–70.
- [17] Litong Yang, Yong Jiang, G. Robert Odette, Takuya Yamamoto, Zuming Liu, and Yong Liu: *J. Appl. Phys.*, 2014, vol. 115, p. 143508.
- [18] Litong Yang, Yong Jiang, Yuan Wu, G. Robert Odette, Zhangjian Zhou, and Zheng Lu: *Acta Mater.*, 2016, vol. 103, pp. 474–82.
- [19] Tiberiu Stan, Yuan Wu, George R. Odette, Kurt E. Sickafus, Hannah A. Dabkowska, and Bruce D. Gaulin: *Metall. Mater. Trans. A Phys. Metall. Mater. Sci.*, 2013, vol. 44, pp. 4505–12.
- [20] Henrik Strandlund and Henrik Larsson: *Acta Mater.*, 2004, vol. 52, pp. 4695–4703.

2.5 HELIUM SEQUESTRATION AT NANOPARTICLE-MATRIX IN HELIUM+HEAVY ION IRRADIATED NANOSTRUCTURED FERRITIC ALLOYS

C. M. Parish, K.A. Unocic, L. Tan, D.T. Hoelzer, Y. Katoh (Oak Ridge National Laboratory), S.J. Zinkle (ORNL and University of Tennessee), S. Kondo (Kyoto University), L.L. Snead (Massachusetts Institute of Technology)

OBJECTIVE

This work intends to determine the disposition of He in nanostructured ferritic alloys (NFA) by advanced electron microscopy method after dual-beam simultaneous He + Fe irradiations.

SUMMARY

The disposition of He in three classes of materials – FeCr-based NFA, FeCrAl NFA and castable nanostructured alloy (CNA) – have been explored by means of scanning/transmission electron microscopy (STEM) combined with multivariate statistical analysis (MVSA) data mining. In particular, this report focuses on directly relating bubbles/cavities to engineered precipitates at high resolution.

PROGRESS AND STATUS

Introduction

In the fusion environment, high levels of transmutation helium will give rise to void swelling or grain boundaries helium embrittlement which will restrict the long term survival of materials in fusion first-wall/blanket structures. In order to mitigate the helium effects, high densities of very small sinks such as oxide nanoprecipitates are introduced in alloys to collect the helium into a subcritical bubble population more resistant to swelling and embrittlement. Different classes of nanostructured ferritic alloys have been developed to try to fulfill this aim, however, a key feasibility issue of how well each materials accommodates the copious transmutation helium production is still unknown due to lack of available facility to produce high levels of simultaneous neutron damage and transmutation helium. In this reporting period, we have interrogated four nanostructured ferritic alloys – castable nanostructured alloys containing Ti-W-Ta-carbides, Fe-9Cr containing Y-Ti-O nanoclusters and two Fe-12Cr-5Al NFAs containing Y-Zr-O or Y-Hf-O clusters – after simultaneous dual-beam Fe + He ion implantation (650 °C, 50 dpa, 15 appm He/dpa) in order to determine the disposition of helium in these materials by advanced electron microscopy.

Experimental Procedure

The samples were irradiated at the DuET facility, Institute of Advanced Energy, Kyoto University, Japan. A SRIM simulation of damage and helium injection is shown in Figure 1. TEM and STEM imaging and microanalysis were performed at ORNL in the LAMDA lab using the FEI Talos F200X instrument. X-ray EDS spectrum images were evaluated via multivariate statistical analysis (MVSA) [1] using the AXSIA code of Sandia National Laboratories [2], along with data file format conversion and post-processing codes written in MATLAB in-house.

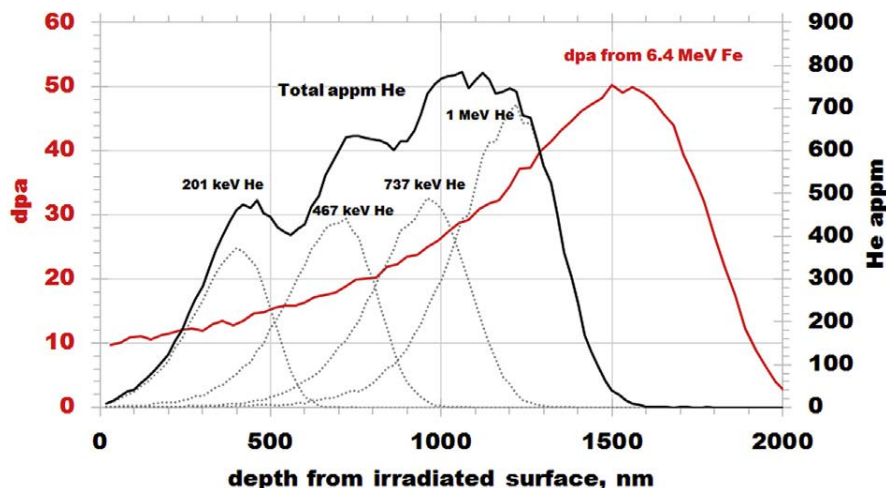


Figure 1. SRIM estimates of dpa and He appm. Red line: dpa level. Black lines: He content. Reprinted from [3].

Results

Bubble distributions

The three NFAs showed fine grains and high-density, sub-5 nm nano-oxide dispersions prior to irradiation. The CNA showed a lath microstructure and tens of nm carbide dispersion prior to irradiation. Following irradiation, the bubble distributions were examined by TEM. Fresnel-defocused bright field (BF) TEM images of the irradiated midrange (500-1000 nm depth) helium-bearing zones of the four materials are shown in Figure 2. Precipitates and He bubbles are found to be easily differentiated in the CNA material, but are far more difficult to discern in the three NFA-type materials. Bubbles are often apparently present on precipitates, especially in the CNA where the precipitates are easier to discern in TEM than in the NFA alloys, where the nanoprecipitates are difficult to observe in conventional TEM. In broad summary, the CNA alloy shows ~8 nm diameter bubbles, whereas the three mechanically-alloyed NFAs had ~3 nm bubbles. The derived bubble number densities for the NFA alloys are ~20 times higher than in the CNA, and the volume fraction of detected bubbles is roughly the same in the CNA and the NFA alloys.

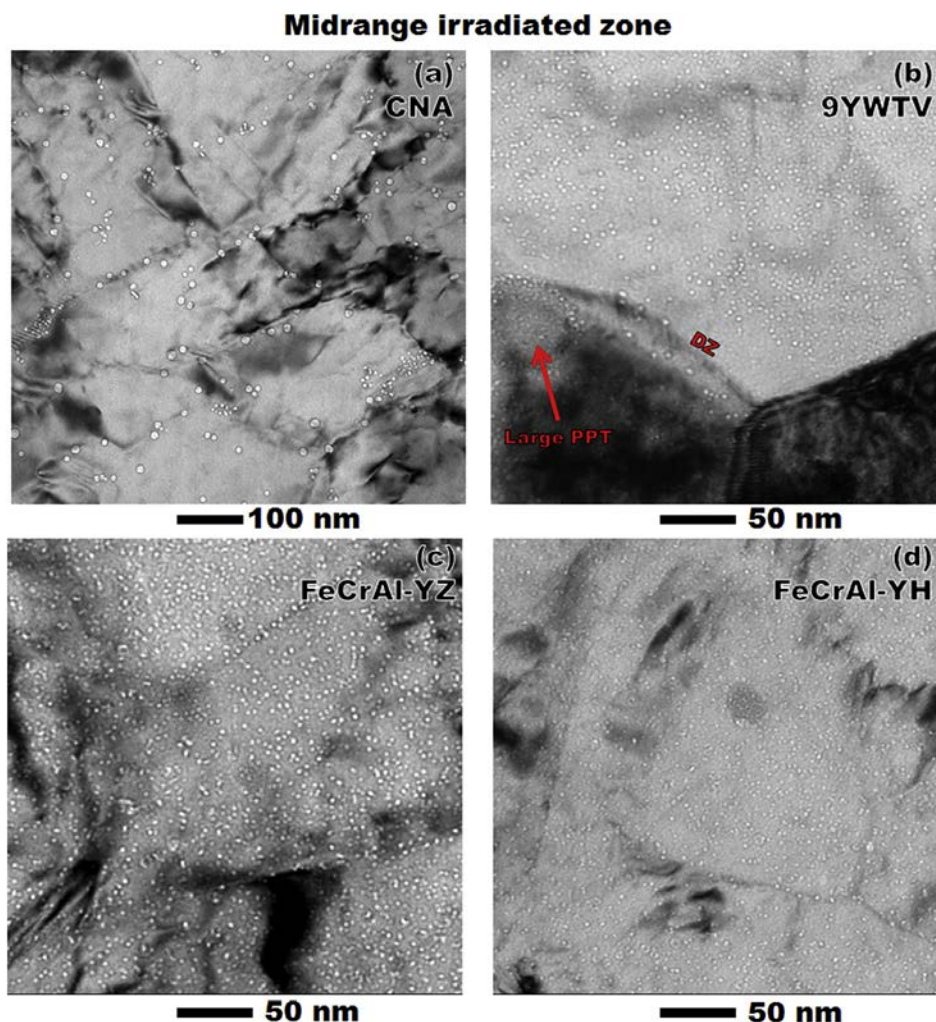


Figure 2. Fresnel-contrast TEM images of the midrange irradiated zone in the four alloys. In (b), “DZ,” denotes cavity denuded zone near a grain boundary; and “PPT” denotes a precipitate. Depths 500-1000 nm correspond to a nominal average damage of 20 dpa. Reprinted from [3].

Relation of bubbles to nanoprecipitates

It is very difficult to directly relate bubbles to nanoprecipitates in NFAs, as the nano-scale precipitates show little contrast under most imaging modes (i.e., BF-TEM and BF-STEM) and bubbles and low-atomic-number precipitates (i.e., oxides) show similar contrast under HAADF-STEM and Fe-M-edge EFTEM, the two most common imaging modes that do show nanoprecipitates. A robust method of X-ray spectrum imaging in a high-efficiency STEM followed by MVSA data mining has been established to separate the nanoprecipitates from the bubbles [4].

MVSA data mining of the spectrum image (SI) provides a more cogent and compact view of the data (Figure 3). To reiterate, MVSA bilinear factor-model methods, as used here, reduce the high-rank, noisy SI into a small set of score image/loading spectrum pairs, which allow improved qualitative interpretation of the underlying chemical makeup of the interrogated specimen region [2,5]. The first two components show Fe-K/Fe-L lines (in different ratios), and describe the matrix. The matrix is broken into two components due to absorption of the soft Fe-L X-rays in the finite foil thickness (consistent with the estimated 100 nm sample thickness). MVSA component #3 shows a large (~170 nm) Cr-rich precipitate, and Cr-rich small precipitates, and a background level of Cr present across the region. MVSA #4

describes Cr-W-carbide nature of the large precipitates. MVSA #5 shows Ti-Ta-W-oxycarbide nature of the small, dispersed precipitates.

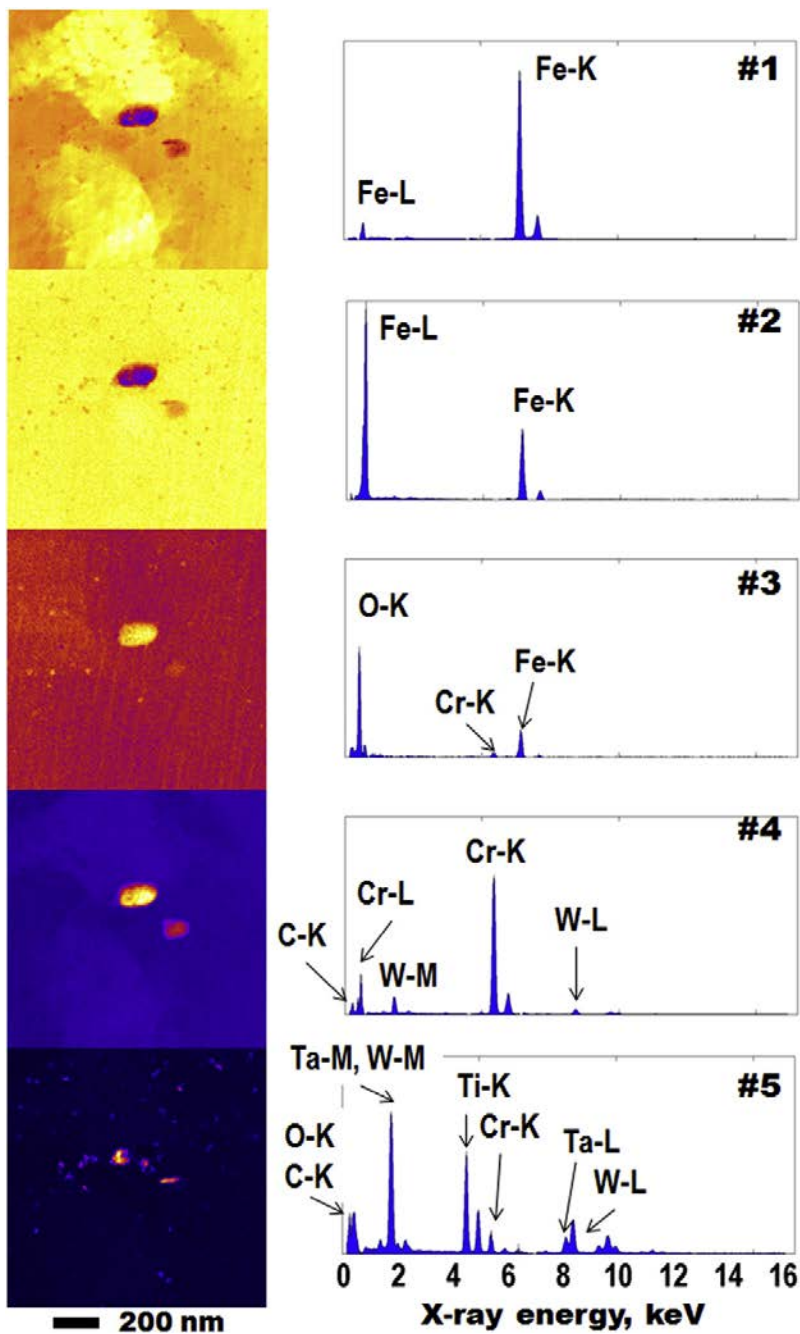


Figure 3. Multivariate statistical analysis decomposition of the X-ray data in Fig. 3, CNA sample. Binned to 256×256 pixel for analysis. Binned $2 \times$ in energy, truncated to 0.17-16.15 keV. Reprinted from [3].

Figure 4 shows images from a region of the CNA in BF-TEM mode, HAADF-STEM mode, Fresnel BF-STEM, and an MVSA decomposition score image showing the precipitates. Apparently in the CNA a large number of small bubbles appear (e.g., red arrow, Figure 4) on some of the precipitates, skewing the fraction of precipitate affiliated cavities to a relatively high value. Most of the bubbles on the surfaces of these precipitates are very small and will likely contain a small fraction of the aggregate He and overall cavity volume.

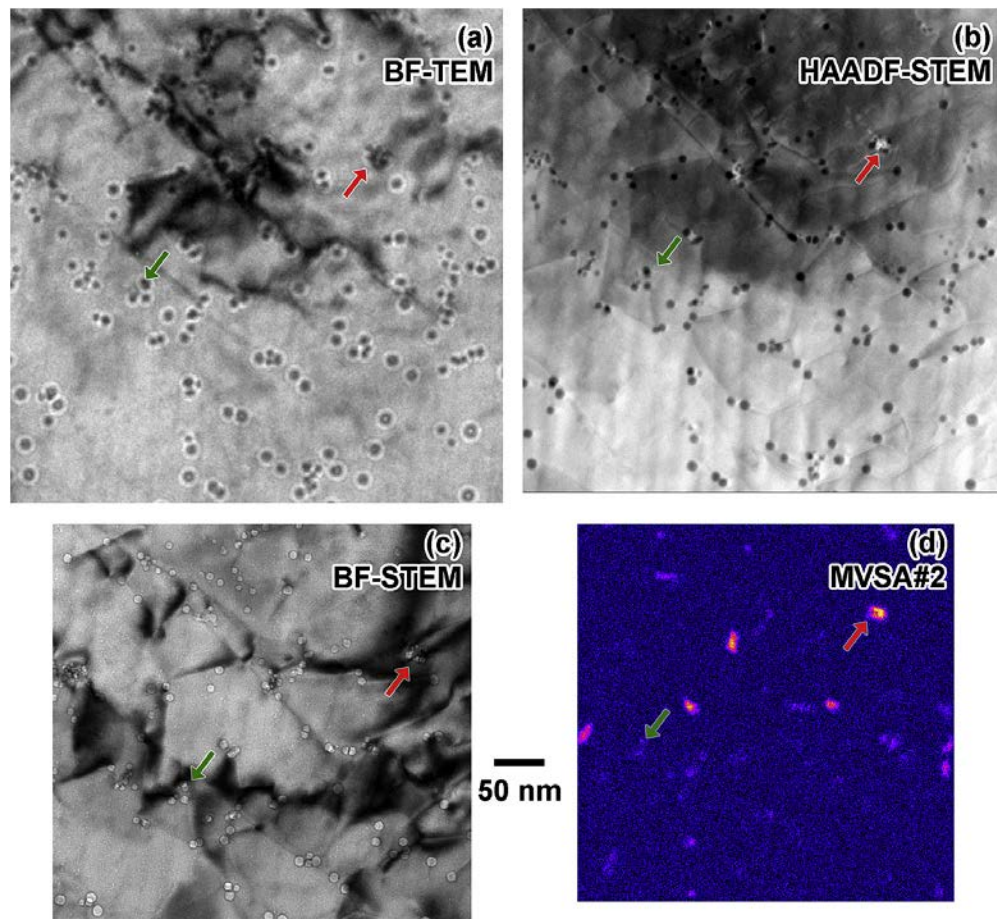


Figure 4. Matched images from one region of the CNA material. BF-TEM, HAADF-STEM, Fresnel BF-STEM, and MVSA score image #2 from an X-ray spectrum image. Bubbles are visible in (a)-(c) and precipitates in (b) and (d). Red arrow denotes a large precipitate, and green arrow a small precipitate. Reprinted from [3].

In addition to the CNA alloys, the bubble-precipitate affiliations were also interrogated by the same methods for the other three alloys. Figure 5 shows the instance of bubbles-precipitates affiliation in FeCrAl alloy; the helium bubbles can be apparently seen to be affiliated with precipitates. By comparing the HAADF, BF, and MVSA images, an approximate count of the precipitate-associated cavities as a fraction of total cavities can be made. Table 1 shows the results of bubbles associated with a precipitate for the four alloys, the CNA showed ~32% affiliations of the cavities (bubbles) with MVSA-EDS identified precipitates and FeCrAl presents roughly 40% of the bubbles affiliated with precipitates.

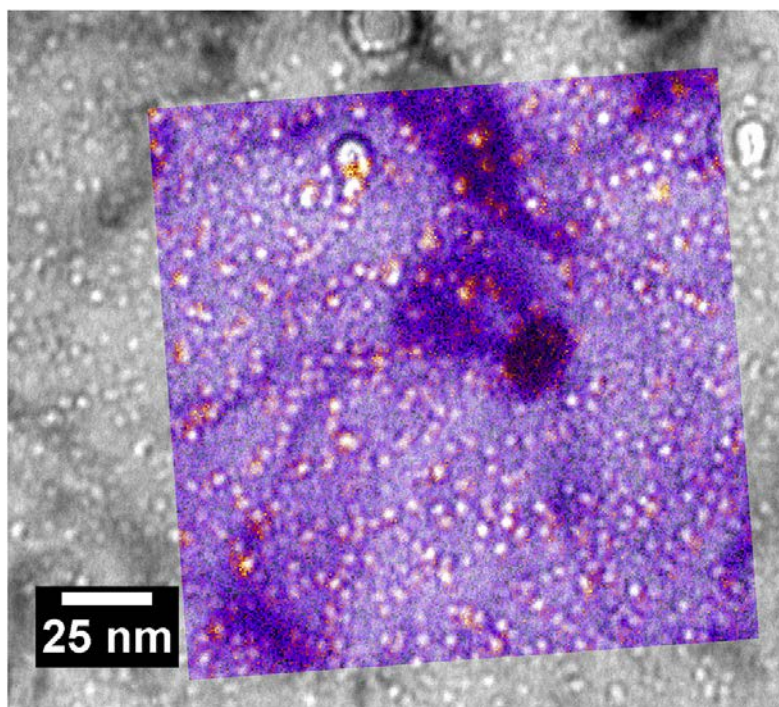


Figure 5. Overlay of Fresnel BF-TEM and MVSA component for the FeCrAl-YZ specimen. Reprinted from [3].

Table 1. Bubbles or cavities associated with a precipitate Reprinted from [3]

Alloy	Bubbles counted	(cavities)	Bubbles (cavities) counted	Precipitate-associated fraction
CNA	109		35	32%
9YWTV	337		103	31%
FeCrAl-YZ	165		65	39%
FeCrAl-YH	88		35	40%

Summary

We have employed advanced electron microscopy methods to interrogate the helium sequestration at nanoparticle-matrix interfaces in four developmental nano-featured ferritic alloys which were subjected to simultaneous heavy-ion and helium bombardment at 650 °C. High-efficiency X-ray mapping using an advanced STEM system is very helpful to image the precipitate populations and relate them to the bubbles, and these determinations are made easier, faster, and more statistically robust by MVSA rank-reduction of the X-ray spectrum images. After irradiation, the dispersions in the NFAs and CNA all survived and a dense population of helium bubbles formed. Bubbles were larger (~8 nm) in the CNA than the NFAs (~3 nm), with lower density of bubbles in the CNA ($\sim 5 \times 10^{21}/\text{m}^3$) compared to the NFAs ($\sim 10^{23}/\text{m}^3$). The CNA showed a higher concentration of cavities along grain boundaries than the NFAs. In all four alloys, roughly 30-40% of the bubbles were in close association with precipitates, indicating the success of the engineered nanostructures in sequestering helium. All four alloy designs appear promising for future fusion or fast fission applications. Further experiments, particularly neutron irradiations, will be performed to fully explore the behavior of the precipitate/nanocluster-bubble interactions.

Acknowledgements

Talos F200X STEM instrument provided by the Department of Energy, Office of Nuclear Energy, Fuel Cycle R&D Program and the Nuclear Science User Facilities.

References

- [1] C.M. Parish, Multivariate statistics applications in scanning transmission electron microscopy X-ray spectrum imaging, in: P.W. Hawkes (Ed.), *Advances in Imaging and Electron Physics*, vol. 168, 2011, pp. 249-295.
- [2] P.G. Kotula, M.R. Keenan, J.R. Michael, Automated analysis of SEM X-ray spectral images: a powerful new microanalysis tool, *Microsc. Microanal.* 9 (2003) 1-17.
- [3] C.M. Parish, K.A. Unocic, L. Tan, S.J. Zinkle, S. Kondo, L.L. Snead, D.T. Hoelzer, Y. Katoh, Helium sequestration at nanoparticle-matrix interfaces in helium + heavy ion irradiated nanostructured ferritic alloys, *Journal of Nuclear Materials*, 483 (2017) 21-34.
- [4] C.M. Parish, M.K. Miller, Aberration-corrected X-ray spectrum imaging and Fresnel contrast to differentiate nanoclusters and cavities in helium-irradiated alloy 14YWT, *Microsc. Microanal.* 20 (2014) 613-626.
- [5] M.R. Keenan, Multivariate analysis of spectral images composed of count data, in: H.F. Grahn, P. Geladi (Eds.), *Techniques and Applications of Hyperspectral Image Analysis*, John Wiley & Sons, Chichester, 2007, pp. 89-126.

2.6 ON THE ASSOCIATION BETWEEN BUBBLES AND NANO-OXIDES IN ANNEALED AND HELIUM IMPLANTED 14YWT—Y. Wu, T. Stan, T. Yamamoto, G. R. Odette (University of California Santa Barbara), and J. Ciston (Lawrence Berkeley National Laboratory)

OBJECTIVE

The objective of this study is to use high resolution transmission electron microscopy to characterize the association between He bubbles and coarsened Y-Ti-O nano-oxides.

SUMMARY

To further the understanding of the interaction between helium and nano-oxides (NOs) in nanostructured ferritic alloys (NFAs), a 14YWT alloy was annealed to coarsen the NOs, and He implanted to produce He bubbles. High resolution transmission electron microscopy shows that smaller NOs are associated with smaller bubbles, while some of the largest NOs (>6 nm) have two bubbles. Most bubbles nucleate near dislocation cores at {111} NO facets.

PROGRESS AND STATUS

Introduction

Fusion reactors will require advanced materials with tolerance to intense high-energy neutron fluxes that generate helium concentrations reaching thousands of atomic parts per million and hundreds of atomic displacements per atom over the operating lifetime. Neutron irradiation along with other synergistic effects can lead to void swelling, embrittlement and irradiation creep [1-3]. Managing transmutation-produced helium is a grand challenge for turning the promise of C-free fusion power into a reality. Nanostructured ferritic alloys (NFAs) are promising candidate structural materials, which are dispersion strengthened by an ultrahigh density of order $\approx 5 \times 10^{23}/\text{m}^3$ of Y-Ti-O nano-oxides (NOs) averaging ≈ 2.5 nm in diameter, with volume fractions of order 0.5% [1-3]. NOs, significantly, trap otherwise highly damaging helium in harmless nm-scale interface bubbles [1-3]. Preventing the formation of larger bubbles allows NFAs to manage very high concentrations He produced in fusion reactors. Understanding the characteristics of the NO-bubble association is important to developing, qualifying and optimizing NFAs.

Very small NOs and bubbles (<2 nm), are difficult to image simultaneously using conventional transmission electron microscopy (TEM) techniques. Thus, to facilitate characterization, a 14YWT-NFA alloy was annealed to coarsen the NOs, prior to He implanted to form bubbles. The resulting microstructures were analyzed using bright field TEM and high resolution scanning transmission electron microscopy (STEM).

Experimental Procedure

Sample fabrication and preliminary characterization of the annealed and He implanted 14YWT alloy was presented in a previous Fusion Semiannual Report [5]. In summary, a coupon of NFA-14YWT (V540H) was annealed at 1200 °C for 8.2×10^5 seconds (228 hrs) in vacuum. 1 MeV He⁺ ions were implanted at the Kyoto University DuET facility in Japan at 700°C at a dose rate of 1.2×10^{12} He/cm²/s. A spinning degrader foil was used to spread the He implantation profile, which is shown as a red solid curve in Figure 1. TEM examinations were carried out over the full ≈ 1.5 μm implanted region. The peak He concentration is 4100 apm at a depth of ~ 1.2 μm .

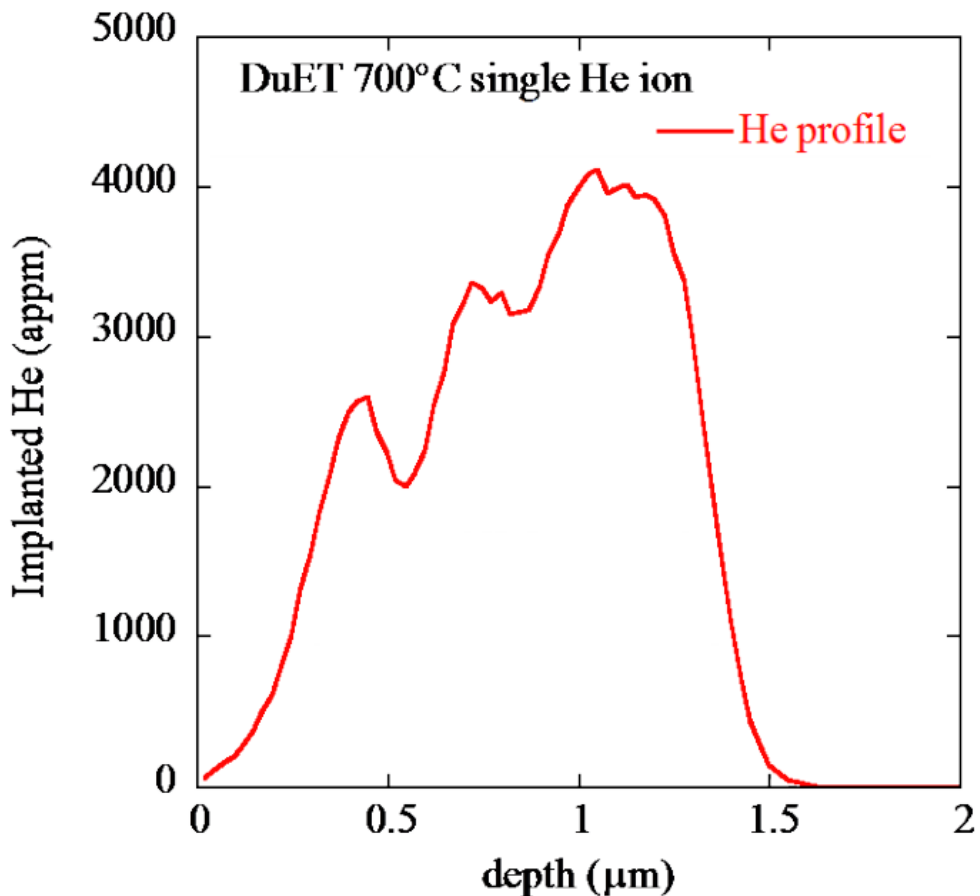


Figure 1. SRIM simulation of the He implantation profile.

Electron backscatter diffraction (EBSD) was carried out on an FEI Quanta 400F field-emission scanning electron microscope (SEM). Four TEM lift-outs were fabricated using a FEI HELIOS Focused Ion Beam (FIB) tool. A 2 kV, 5.5 pA low energy ion beam was used to clean the lift-out and remove residual gallium damage. Preliminary TEM characterization was done on a 300 keV FEI Titan at UCSB to check the lift-out orientations and thicknesses. Foils were then imaged using the TEAM 1 aberration corrected TEM at LBNL in both high resolution TEM and high resolution STEM modes. The lattice spacing's and inter-planar angles were measured using ImageJ.

Results and Discussion

SEM and EBSD Characterization

Figure 2 shows EBSD data from the 14YWT alloy. The band contrast image in Figure 2a shows the wide variation in grain sizes from $<0.5 \mu\text{m}$ to $>30 \mu\text{m}$. The inverse pole figure z-direction map in Figure 2b is colored according to the out-of-plane crystallographic orientation of the grain. For example, a green grain indicates $\{110\}$ type surface orientations. EBSD was used to identify grains with a $\langle 100 \rangle$ zone axis used for TEM. Further, since the implantation depth of interest is $\sim 1.2 \mu\text{m}$, grains of similar or slightly larger size were studied.

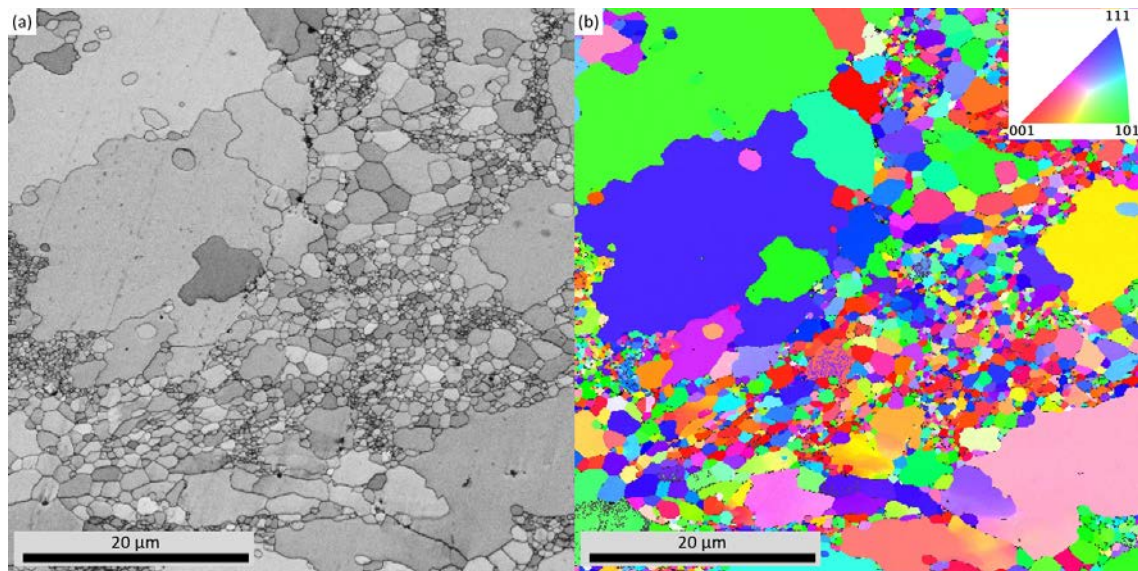


Figure 2. (a) EBSD band contrast and (b) inverse pole figure z-direction maps from the surface of a 14YWT alloy.

TEM Characterization

Figure 3a shows a cross-sectional view of the 14YWT alloy. The large $2.5 \times 2.8 \mu\text{m}$ grain is viewed through the $\langle 100 \rangle$ zone axis and appears dark. He was implanted through the top surface, as indicated by the yellow arrow, to a maximum depth of $\sim 1.5 \mu\text{m}$. Figure 3b is a higher magnification under-focused bright field TEM image from a $200 \times 180 \text{ nm}$ region just below the grain surface where the expected He concentration is $<250 \text{ appm}$. In the under-focused condition, the cuboidal NOs have a black outline and bubbles appear as white circles. Most bubbles in this region have a diameter of $d \approx 3.5 \text{ nm}$, and are found at the corners of cuboidal precipitates (black arrows in Figure 3b). This result is significant because it indicates that the preferred bubble nucleation site on NOs is at the corners. Smaller $d < 2 \text{ nm}$ bubbles may also exist in the area, but could not be imaged due to limitations of the microscope and interfering signals from other features.

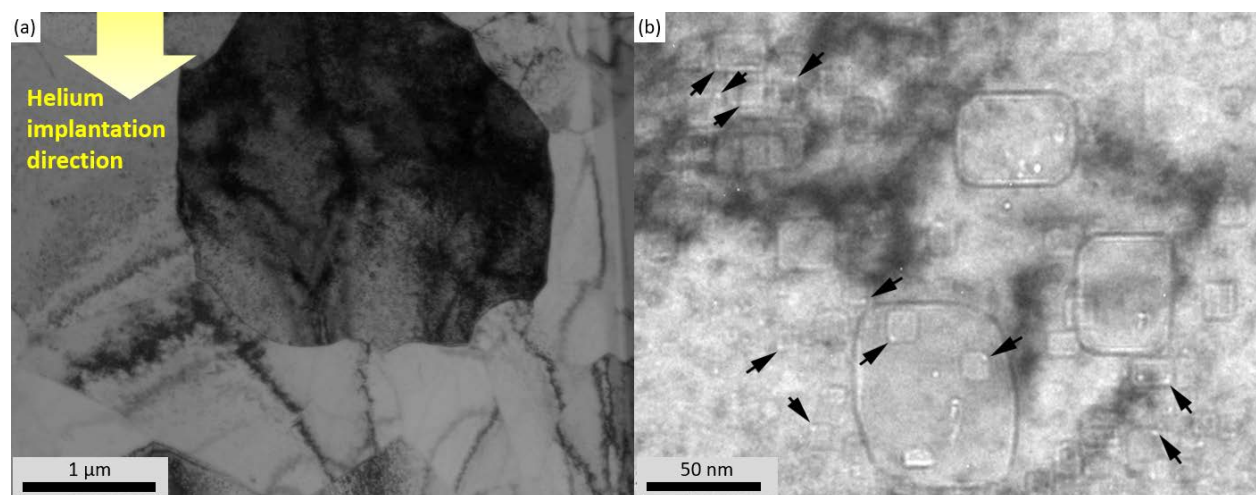


Figure 3. (a) Low magnification bright field TEM image of a large grain for a $\langle 100 \rangle$ zone axis. (b) An under-focused bright field TEM image from the top of the grain in Figure 2a showing faceted NOs. Black arrows indicate the location of bubbles, most of which reside on NO corners.

The HRSTEM image in Figure 4a was taken using the TEAM 1 aberration corrected TEM at LBNL. The image shows cuboidal NOs with attached bubbles (dark contrast). Two crystallographic orientation relationships (ORs) with the matrix were identified. The 7.1 nm NO has a cube-on-cube OR $\{100\}\text{Fe}/\{100\}\text{NO}$ with $\langle 100 \rangle\text{Fe} \parallel \langle 100 \rangle\text{NO}$. The 6.1 nm NO has a cube-on-edge OR $\{100\}\text{Fe}/\{110\}\text{NO}$ with $\langle 100 \rangle\text{Fe} \parallel \langle 100 \rangle\text{NO}$. The plot in Figure 4b shows the correlation between bubble size and NO size. The red trend line has a positive slope of ~ 0.85 indicating that the NOs are roughly 15% larger than the attached bubbles. Note that the R value of 0.615 indicates a lot of scatter in the data.

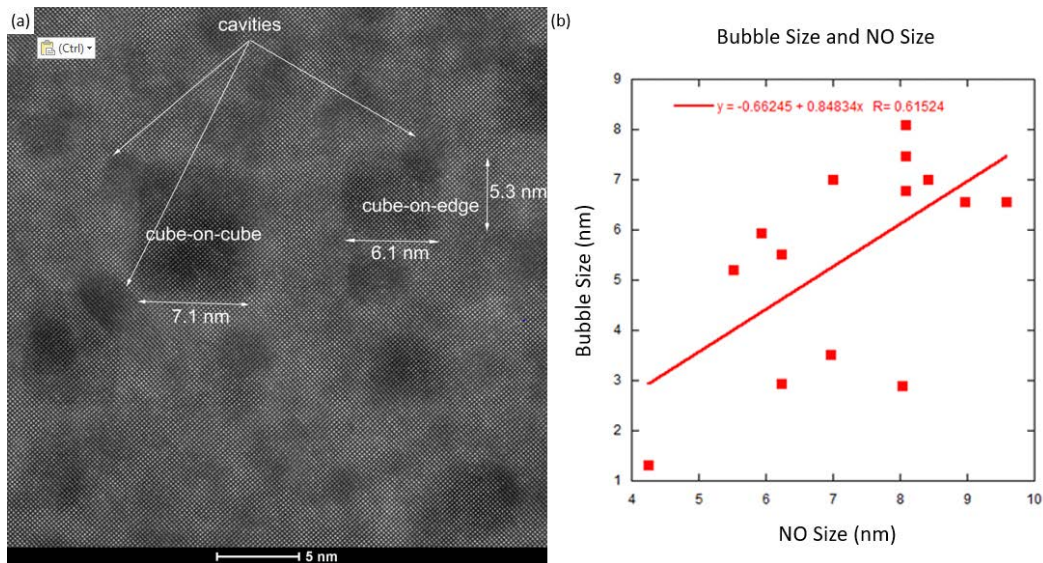


Figure 4. (a) HRSTEM image of an area near the peak He implanted region showing NOs and attached bubbles. (b) Plot showing the relationship between bubble size and NO size.

Table 1 summarizes the characteristics from some of the NOs and bubbles observed in this study, including those from Figure 4. Larger NOs have larger bubbles, and some of the largest NOs (>6 nm) have two bubbles.

Table 1. Summary of NOs and bubbles observed in this study

NO index	NO size (nm)	Matrix – NO Orientation Relationship	# of bubbles attached to the NO	Bubble diameter (nm)
1	8.0	Cube-on-edge	2	2.6
2	6.2	Cube-on-cube	2	2.4
3	7.0	Not available	2	3.25
4	2.8	Not available	1	1.4
5	3.3	Not available	1	1.7
6	4.7	Not available	1	1.3
7	4.2	Not available	1	1.4

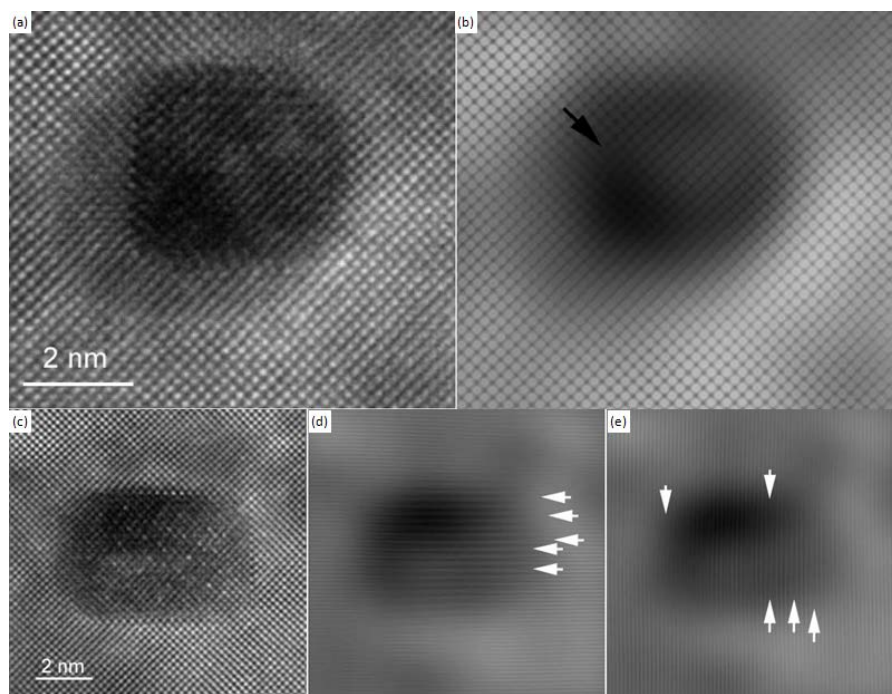


Figure 5. (a) and (c) HRSTEM images of 3 – 5 nm NOs and 1 – 2 nm bubbles (dark contrast). (b) Processed image of the NO in part (a) showing the location of a misfit dislocation near the NO – bubble interface. Inverse FFT images of the NO in (c) are shown for the (d) {400} and (e) {440} reflections. White arrows indicate the location of misfit dislocations.

Figures 5a and 5c are HRSTEM images showing two 3 – 5 nm NOs associated with 1 – 2 nm bubbles (dark contrast). Figure 5b is a processed image of Figure 5a, more clearly showing the location of atomic columns. The black arrow indicates the location of a dislocation near the bubble-NO interface. The NO in Figure 5c has the $Y_2Ti_2O_7$ pyrochlore structure, and a cube-on-edge orientation relationship with the matrix. This OR was previously seen in [4]. The dark areas indicate the presence of bubbles, which are found at NO the corners. Figures 5d and 5e are inverse Fast Fourier Transformed (FFT) images of the NO in Figure 5c, and were obtained by isolating {400} and {440} reflections, respectively. The inverse FFT analysis reveals dislocations along the NO – matrix interfaces, some of which are marked with white arrows. The atomic lattice mismatch between the $Y_2Ti_2O_7$ NO and the matrix leads to interfacial misfit dislocations, shown with white arrows in Figures 5d and 5e.

Figure 6a shows a raw HRSTEM image of a NO and two bubbles which were selected for in-depth analysis. Figure 6b shows the NO outline in yellow dashed lines, and the bubbles in blue. The faceted NO is 3.5 x 5.9 nm, and has two bubbles with $d = 2.6$ nm and 1.3 nm. A 3D rendering of the NO and bubbles is shown in Figure 6c. FFT analysis indicates that the NO has the $Y_2Ti_2O_7$ pyrochlore structure, a cube-on-edge OR with the matrix, and is viewed through the $\langle 110 \rangle_{Y_2Ti_2O_7}$ zone axis. The 3D rendering in Figure 6d shows the many faces, edges, and corners of the polyhedral $Y_2Ti_2O_7$ precipitate as viewed edge-on. The largest facets are {100} cube faces, followed by {111} corners, while the {110} edges are the smallest. The size of each facet is indicated in Figure 6b.

The matrix-oxide interfacial ORs were obtained by indexing the NO surfaces, and are shown Figure 6e. The top and bottom interfaces have the rotated cube-on-cube OR: {100}Fe//{100}NO with $\langle 100 \rangle_{Fe} // \langle 100 \rangle_{NO}$. The cuboidal NO has six faces, but the two on the top and bottom have a different OR than the other four. Two of the four faces are labeled with {100} face in Figure 6d, and have an edge on cube OR: {110}Fe//{100}NO with $\langle 100 \rangle_{Fe} // \langle 100 \rangle_{NO}$. The side interfaces have a cube-on-edge OR: {100}Fe//{110}NO with $\langle 100 \rangle_{Fe} // \langle 110 \rangle_{NO}$. And the diagonal OR is edge-on-corner: {110}Fe//{111}NO

with $\langle 100 \rangle_{\text{Fe}} // \langle 110 \rangle_{\text{NO}}$. Notably, this OR is also found for thin film Fe deposition on $\{111\}$ $\text{Y}_2\text{Ti}_2\text{O}_7$ single crystal substrates [6]. Clearly, by comparing Figure 6c with Figure 6e, the smaller bubble is attached to the $\{111\}$ NO facet, while the larger bubble is centered on the $\{111\}$ NO facet, but has grown to the point where it is wetting the surrounding NO facets. Finally, Figure 6f is an inverse FFT image where black arrows indicate dislocation cores. The dislocations are on $\{111\}$ NO planes and near the bubbles. Thus, bubbles likely nucleate at dislocations on $\{111\}$ NO surfaces, then grow and envelop other NO facets.

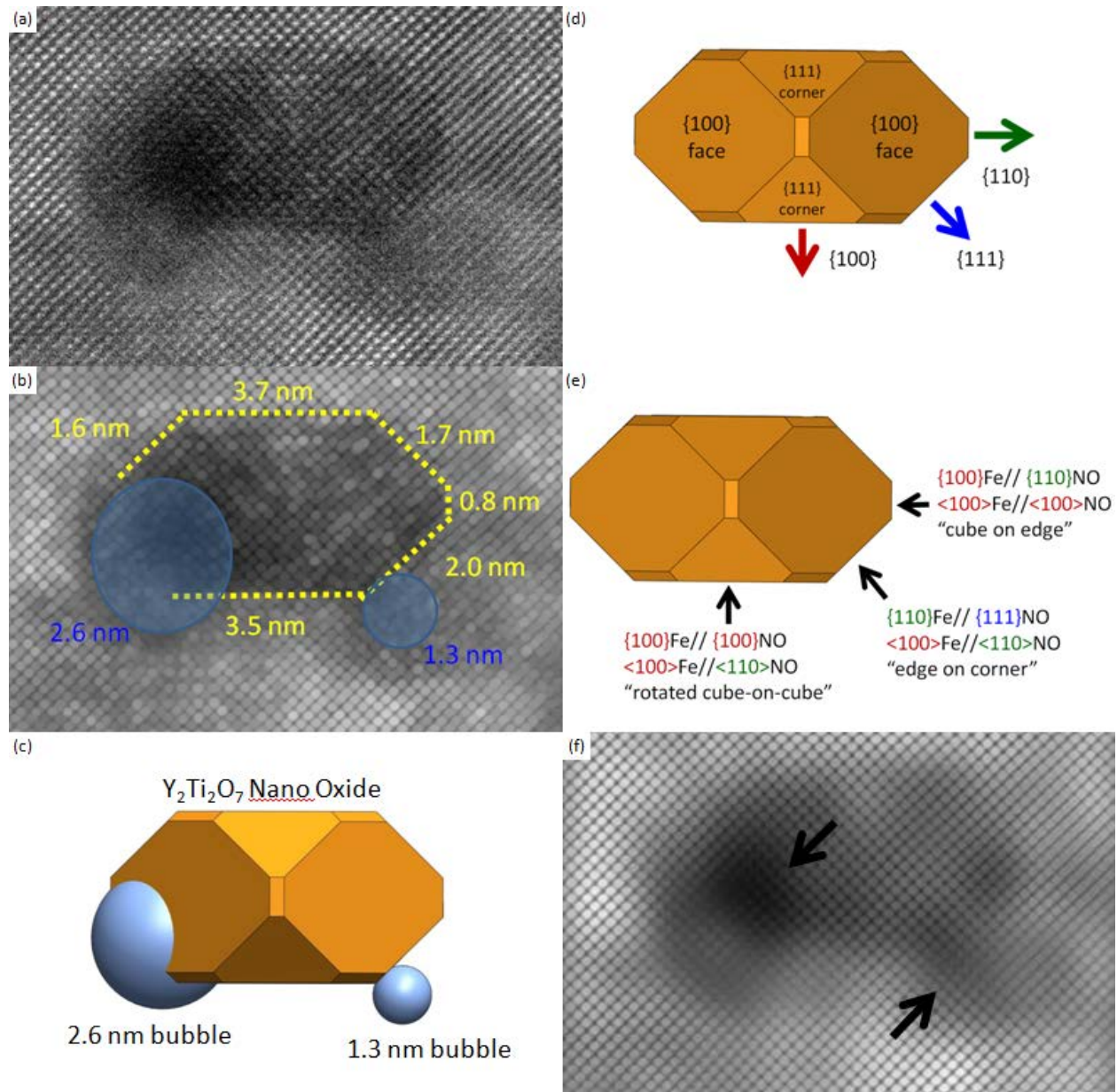


Figure 6. (a) Raw HRSTEM image. (b) Processed image outlining a NO with yellow dashed lines, and two bubbles. (c) 3D rendering of the NO and bubbles. (e) Indexed NO surfaces and (f) the interfacial orientation relationships with the matrix. (f) Inverse FFT images indicating dislocations near the bubble – NO interfaces.

Summary

- A 14YWT NFA was annealed to coarsen the NOs, and He was implanted at 700°C to produce He bubbles.
- Small bubbles are associated with smaller oxides, while some of the largest NOs (>6 nm) have two bubbles.
- Most bubbles nucleate at {111} NO facets and near dislocation cores.
- Future studies include further TEM observation using the TEAM-1 TEM at LBNL, and electron energy loss spectroscopy (EELS) measurements on bubbles to obtain He densities.

Acknowledgements

Research at UCSB was supported by the Department of Energy Office of Fusion Energy Sciences (Grant No. DE-FG03-94ER54275) and the Office of Nuclear Energy (Grant No. DE-FC07-07ID14825). TEM specimen preparation and TEM measurements were carried out in the UCSB Materials Research Laboratory Microstructure and Microanalysis Facility, supported by the Materials Research Science and Engineering Center Program of the National Science Foundation under Award No. DMR05-20415. Aberration corrected TEM observation was supported by Molecular Foundry at LBNL under approved award proposal #3976.

References

- [1] G.R. Odette, M. J. Alinger, B. D. Wirth, *Annu. Rev. Mater. Res.* 38, 2008, 471-503.
- [2] G.R. Odette, *JOM*. 66, 2014, 24272441.
- [3] Y. Dai, G. R. Odette, T. Yamamoto, *Comprehensive Nuclear Material*. 1, 6, 2012, 141.
- [4] Y. Wu, J. Ciston, S. Kraemer et al., *Acta Mater.* 111, 2016, 108-115.
- [5] Y. Wu, T. Stan, T. Yamamoto, G.R. Odette, *Fusion Semiannual Progress Report for Period Ending June 30, 2016*, DOE/ER-0313/60, U.S. Department of Energy, 42.
- [6] T. Stan, Y. Wu, G.R. Odette, et al. *Metal. and Mater. Trans. A*, 44, 2013, 4505 – 4512.

3. CERAMIC COMPOSITE STRUCTURAL MATERIAL DEVELOPMENT

3.1 LOW TEMPERATURE AIR BRAZE PROCESS FOR JOINING SILICON CARBIDE COMPONENTS USED IN HEAT EXCHANGERS, FUSION AND FISSION REACTORS, AND OTHER ENERGY PRODUCTION AND CHEMICAL SYNTHESIS SYSTEMS—J.R. Fellows, C.A. Lewinsohn (Ceramatec, Inc.), Y. Katoh, T. Koyanagi (Oak Ridge National Laboratory)

Abstract of a paper in press for Ceramic Engineering and Science Proceedings

Fabrication of large, or complex, components from silicon carbide, or other technical ceramics, used in heat exchanger devices, energy production and chemical synthesis systems, and for components within fusion and fission reactors require robust joining processes. Ceramatec has developed a novel method for achieving bonds using an air brazing process. For silicon carbide joining, the braze acts under certain conditions to promote diffusion bonding. The resulting joined regions are thought to form by rapid interdiffusion of the diffusion-enhancing braze material and silicon and carbon species, resulting in a microstructure more similar to one formed by diffusion bonding than brazing. Processing of these joints is accomplished at relatively low temperatures, 900°C-1200°C in air, with minimal applied load. The brazed joint strength was found to be statistically equivalent to monolithic control samples at room temperature. Oxidation testing, using dry oxygen and saturated steam, was conducted at 1000°C for 1000 hours on joined specimens, resulting in further microstructural development of the joint, with subsequent shear testing showing no appreciable reduction in strength. Torsion tests on irradiated joined samples show that the joint's mechanical integrity is resistant to radiation degradation.

3.2 LOW ACTIVATION JOINING OF SiC/SiC COMPOSITES FOR FUSION APPLICATIONS: MODELING THERMAL AND IRRADIATION-INDUCED SWELLING EFFECTS ON INTEGRITY OF Ti₃SiC₂/SiC JOINT—B.N. Nguyen, C.H. Henager, Jr., and R.J. Kurtz (Pacific Northwest National Laboratory) M. Ferraris (Politecnico di Torino, Italy) Y. Katoh (Oak Ridge National Laboratory)

OBJECTIVE

This work developed a continuum damage mechanics model that incorporates thermal expansion combined with irradiation-induced swelling effects to study the origin of cracking observed in recent irradiation experiments. Micromechanical modeling using an Eshelby-Mori-Tanaka approach was used to compute the thermoelastic properties of the Ti₃SiC₂/SiC joint needed for the model. In addition, a microstructural dual-phase Ti₃SiC₂/SiC model was developed to determine irradiation-induced swelling of the composite joint at a given temperature resulting from differential swelling of SiC and the Ti₃SiC₂ MAX phase. Three cases for the miniature torsion hourglass (THG) specimens containing a Ti₃SiC₂/SiC joint were analyzed corresponding to three irradiation temperatures: 800°C, 500°C, and 400°C.

SUMMARY

Referring to the studies on the miniature THG specimen with the fully bonded joint [1-2], we have investigated the same THG specimen made of CVD-SiC substrates joined by a 10-to-15-micron Ti₃SiC₂/SiC bonding layer. Such a specimen was tested in the High Flux Isotope Reactor (HFIR) at Oak Ridge National Laboratory at 800°C and 5 dpa. Before testing, SEM examination indicated no transverse cracks or microcracks in the bonding layer or at the interfaces. After the irradiation experiment, limited crack propagation along the interface between the bonding layer and the CVD substrate was observed, however, the interface bonding appeared mainly intact. Microcracks were also found in the Ti₃SiC₂/SiC joint layer, but no extensive crack propagation was observed. No irradiation experiments were reported at temperatures lower than 800°C for the Ti₃SiC₂/SiC-joined CVD-SiC specimens although Ref. [1] reports experiments at 500°C and 3 dpa for similar specimens containing a bonding layer made of a different material.

The objective of our work is to understand through numerical analyses the origin of microcracking in THG specimens containing a dual-phase Ti₃SiC₂/SiC joint layer and to predict damage initiation and development in these specimens subjected to heating to selected temperatures and neutron irradiation at those temperatures. Three irradiation temperatures are considered: 400°C, 500°C and 800°C. A continuum damage modeling approach with support of micromechanical modeling has been developed. In this work, irradiation directly causing material degradation that affects mechanical properties is not modeled, but the developed modeling approach accounts for the *irradiation-induced swelling* that can cause subsequent damage if the material is constrained. This report expands the methods developed and discussed in our previous reports [2-3] on this subject to model and predict cracking due to residual stresses caused by the mismatch of thermoelastic properties in combination with the swelling mismatch between the joint and joint materials. The details of this work including the model formulation and analysis results are reported in a journal article in preparation [4].

PROGRESS AND STATUS

Introduction

As discussed in Ref. [1], joining SiC to itself or to other materials is a critical technological need that has not been resolved. There are two key issues identified in Ref. [1]. The first issue is about the poor irradiation stability that was observed through limited data available on the irradiation of joints and joining materials. The second one is the lack of a widely accepted standard test method for joining of SiC.

In addition to the above issues, there is a general lack of predictive modeling tools that can either assist in designing a ceramic joint to sustain irradiations, or provide guidance to develop a joining method for SiC and its composites. This work attempts to address the lack of modeling tools by developing a damage model to elucidate the origin of cracking observed in ceramic joints subjected to heating followed by neutron irradiations at elevated temperatures (up to 800°C). The model relies on continuum damage mechanics (CDM) in its formulation and uses micromechanical modeling to identify the material parameters or properties that are not known or available.

The modeling work was performed for the MAX-phase joining in which the composite made of SiC and Ti_3SiC_2 is produced using the displacement reaction between SiC and TiC [5]: $3TiC + 2Si \rightarrow Ti_3SiC_2 + SiC$. Pacific Northwest National Laboratory (PNNL) has developed a tape casting process to join ceramics using this reaction [6]. Previous modeling work using CDM for the unirradiated Ti_3SiC_2/SiC joint and joining SiC subjected to torsion was reported in [2]. The Ti_3SiC_2 MAX phase joining for SiC was previously evaluated for the effects of irradiation at $800^\circ C$ [1].

Model Formulation

Approach

The continuum damage mechanics (CDM) model formulated in this work to account for the material thermal expansion combined with the irradiation-induced swelling is derived from a model by Nguyen et al. [7] that was reformulated in [2] for unirradiated THG specimens subjected to torsion. The constitutive relations of the elastic damage model derived from a thermodynamic potential reads:

$$\Phi(\varepsilon_{ij}^m, T, D) = \frac{1}{2} C_{ijkl}(T, D) \varepsilon_{ij}^m \varepsilon_{kl}^m \quad (1)$$

$$\sigma_{ij} = C_{ijkl}(T, D) (\varepsilon_{kl} - \varepsilon_{kl}^{th} - \varepsilon_{kl}^s) = C_{ijkl}^0(T) (1-D) (\varepsilon_{kl} - \varepsilon_{kl}^{th} - \varepsilon_{kl}^s) = C_{ijkl}^0(T) (1-D) \varepsilon_{kl}^m \quad (2)$$

where $C_{ijkl}(T, D)$ is the material elastic stiffness tensor that varies with temperature T and is affected by the microcracking damage phenomenologically described by the damage variable, D . A linear stiffness reduction law of $C_{ijkl}(T, D)$ with D is used in Eq. (2) where $C_{ijkl}^0(T)$ is the initial stiffness tensor without material damage. ε_{ij} , ε_{ij}^m , ε_{ij}^{th} , and ε_{ij}^s are the total, mechanical, thermal and swelling-induced strains, respectively. In Eq. (1), the decoupling between the damage, thermal and swelling effects is assumed, and for a given temperature, the elastic stiffness tensor is assumed to vary linearly with D . In addition, we neglect the damage directly caused by neutron irradiation for the CVD-SiC and MAX phase composite studied in this work. Thus, damage in the material is induced only by the mechanical deformation that is resulted from thermal expansion and swelling.

ε_{ij}^{th} is computed in terms of the temperature-dependent coefficients of thermal expansion (CTEs) $\alpha_{ij}(T)$ and temperature change as:

$$\varepsilon_{ij}^{th} = \alpha_{ij}(T) \Delta T \quad (3)$$

For the incorporation of the irradiation-induced swelling strain tensor, ε_{ij}^s , we use a model proposed by Ben-Belgacem et al. [8] that expresses the isotropic swelling strain as:

$$\varepsilon_{ij}^s = \frac{S}{3} \delta_{ij} \quad (4)$$

with $\delta_{ij} = \begin{cases} 1 & \text{if } i = j \text{ and } i, j = 1, \dots, 3 \\ 0 & \text{if } i \neq j \end{cases}$ and S denotes the swelling strain magnitude. In this work S can

increase from 0 to a saturation value, S_{max} that is a function of the irradiation temperature and swelling regime. S represents the volumetric strain caused by irradiation-induced swelling. The thermal and swelling strains are treated similarly in the continuum mechanics framework here, however, Eqs. (3) and (4) clearly show that thermal strains vanish if the temperature change is reduced to zero whereas irradiation-induced swelling strains subsist after irradiation.

The damage evolution law was obtained using the concepts of thermodynamics of continuous media [9-10] and a damage criterion dependent on the damage threshold function $F_c(T, D)$ [11, 7]:

$$dD = \frac{\frac{\partial C_{ijkl}(T, D)}{\partial D} \varepsilon_{ij}^m d\varepsilon_{kl}^m}{\frac{\partial F_c(T, D)}{\partial D}} \quad (5)$$

This damage evolution law can describe microcracking damage caused by tensile stresses or shear damage caused by shear stresses [2]. As ceramics may not suffer from microcracking under a compressive stress state, at this stage of the model development, damage is not activated under a compressive state of stress. As the thermal and swelling strains are related to the mechanical strain as $\varepsilon_{ij}^m = \varepsilon_{ij} - \varepsilon_{ij}^{th} - \varepsilon_{ij}^s$, the thermal expansion and swelling effects directly govern the damage evolution law (5). Damage evolution is computed incrementally according to Eq. (5) until attaining the saturation state at which $D = D_{cr}$, and the material fails and can no longer carry loads. Fracture is predicted to occur if $D = D_{cr}$ and is captured by a vanishing element technique [12-13]. In this work, to quantify how close the material is to fracture, a failure indicator is defined by the ratio D/D_{cr} . Accordingly, fracture occurs when the failure indicator equal to unity.

Temperature-dependent Thermomechanical properties

The integration of the constitutive relation including damage requires the identification of the thermomechanical properties including the damage threshold function as functions of temperature for the temperature range of interest. In this work [4], the measured temperature-dependent elastic modulus data from [14] and [15] were used for the SiC and Ti_3SiC_2 materials, respectively. The measured temperature-dependent thermal expansion coefficient data from [13] were used for SiC and from [16-17] for Ti_3SiC_2 . For the joint specimen, the homogenized thermoelastic properties of the Ti_3SiC_2/SiC joint are needed as the joint was modeled as a continuum at the specimen macroscopic scale. To this end, an Eshelby-Mori-Tanaka approach (EMTA) [18] was used to compute the elastic modulus and CTEs of Ti_3SiC_2/SiC using the constituent data from the above references and considering 50% volume fraction for each phase and uniform distribution of Ti_3SiC_2 in SiC [4].

Stress-strain behavior

In addition of the thermoelastic properties, the integration of the constitutive relation involving damage requires the identification of the damage threshold function as a function of temperature for the temperature range of interest. The details of the determination of the damage threshold function $F_c(T, D)$ used in Eq. (4) are reported in [4]. For a given temperature, this function can be computed using the method described in [7] for the damage variable values in the $[0, D_{cr}]$ interval by means of the thermodynamic force associated with the damage variable ($F(T, D) = \partial\Phi(T, D)/\partial D$) and the stress-strain response at the same temperature. D_{cr} is small for brittle materials, and this is the case for ceramic materials studied in this work. $D_{cr} = 0.2$ is assumed for SiC and is approximated to vary from 0.14 to 0.2 for Ti_3SiC_2/SiC for temperatures varying from 25°C to 800°C [4]. Tensile uniaxial stress-strain responses as functions of temperature are estimated considering the stability of CVD-SiC mechanical properties in the [25°C, 800°C] temperature range of interest [14] and temperature-dependent bending strength data reported in [6] for the Ti_3SiC_2/SiC composite [4].

Irradiation-induced swelling

Application of the damage model accounting for irradiation-induced swelling requires the knowledge of the saturation swelling strain, S_{max} for a given material (Eq.(4)) in the ranges of irradiation dose and temperature considered. Snead et al. [14] gathered historical and published swelling data from various studies for high-purity CVD-SiC. This work uses the data collected in [14] for the saturable regime of point defect swelling of CVD-SiC (in the 25-to-1000°C range) [4]. Accordingly, S_{max} values for SiC irradiated at 400°C, 500°C, and 800°C are 2%, 1.4% and 0.8%, respectively.

While limited swelling data for the MAX phase, Ti_3SiC_2 recently have been published [19], similar data for the Ti_3SiC_2/SiC composite are not available. Therefore, a method to predict swelling of this composite induced by neutron irradiation in the same ranges of irradiation dose and temperature as for the

constituent SiC and Ti_3SiC_2 is needed. To this end, we have developed in this work [4] a microstructural dual-phase model for $\text{Ti}_3\text{SiC}_2/\text{SiC}$ in which each phase of the composite is discretized and allowed to reach the saturation swelling strain corresponding to the experimental swelling data [14,19] at a prescribed irradiation temperature. A digital image of the $\text{Ti}_3\text{SiC}_2/\text{SiC}$ joint microstructure was used to create a FE mesh of this dual-phase system using the OOF2¹ public domain software [3-4]. This has allowed a detailed discretization of the microstructure and the ability for ABAQUS[®] to assign individual constitutive laws to each phase. The meshed microstructure with the constituent phase distribution is shown in Figure 1(a). Figure 1(b) presents a local snapshot showing the high-resolution mesh at the interfaces between the SiC (colored in blue) and the ternary MAX Ti_3SiC_2 (yellow) phase.

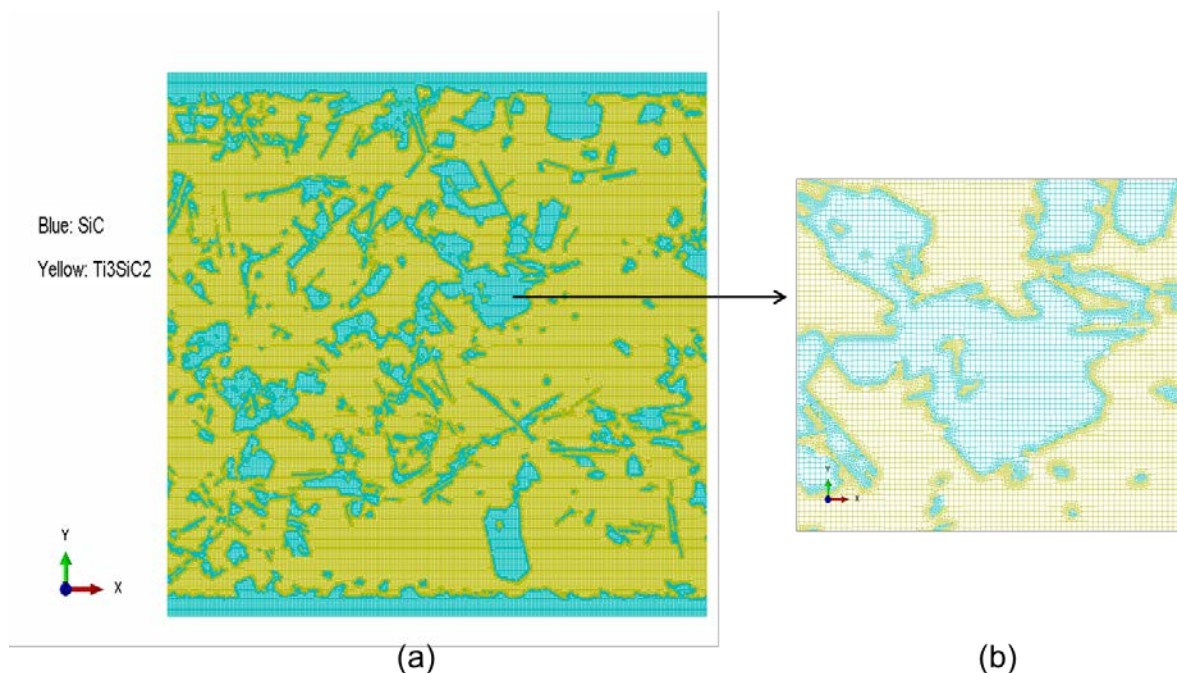


Figure 1. (a) The dual-phase finite element mesh of the $\text{Ti}_3\text{SiC}_2/\text{SiC}$ joint microstructure, (b) A local snapshot showing the detailed mesh [3-4].

In order to solely capture the irradiation-induced swelling of the $\text{Ti}_3\text{SiC}_2/\text{SiC}$ composite without the thermal expansion effect, the dual-phase microstructure model was assumed to be initially and uniformly at a prescribed irradiation temperature. Next, irradiation-induced swelling was applied to each constituent phase and was allowed to evolve to the respective saturation value. The saturation swelling levels applied to SiC were taken from [14] and those for Ti_3SiC_2 from [19]. Saturation swelling of SiC at 400°C is the highest (2%) while at 800°C saturation swelling of Ti_3SiC_2 is the highest and is of 1.47% according to [19]. Table 1 gathers the saturation swelling levels (S_{max}) for all the materials. The S_{max} values for SiC and $\text{Ti}_3\text{SiC}_2/\text{SiC}$ have subsequently been used in the thermomechanical analysis of the THG joint specimen subjected to irradiation-induced swelling at the irradiation temperatures considered in this work [4].

Table 1. Saturation swelling levels from [14] for SiC, from [19] for Ti_3SiC_2 , and predicted by the dual-phase model for the $\text{Ti}_3\text{SiC}_2/\text{SiC}$ composite [4]

Irradiation Temperature	SiC [13]	Ti_3SiC_2 [18]	$\text{Ti}_3\text{SiC}_2/\text{SiC}$ (Prediction)
400°C	2%	0.77%	1.15%
500°C	1.4%	0.82%	1.0%
800°C	0.8%	1.47%	1.26%

¹ Software developed at the National Institute of Standards and Technology

RESULTS

Analysis of the THG Joint Specimen Subjected to Heating, Irradiation Swelling and Cooling

The damage model incorporating the thermal expansion combined with irradiation-induced swelling effects was implemented in ABAQUS® by means of user-subroutines. It has then been used with ABAQUS® to analyze the THG joint specimen subjected to heating followed by irradiation-induced swelling at a prescribed irradiation temperature, and cooling to room temperature after irradiation swelling [4]. The analyses were performed for three cases corresponding to irradiation temperatures: 800°C, 500°C and 400°C. The 800°C case was discussed in detail here as the experimental observation about joint damage after neutron irradiation had been reported for this case [1]. The three-dimensional (3D) FE mesh of the THG joint specimen used in all the analyses and the associated material assignment are given in Figures 2(a) and 2(b). The specimen is simply fixed at its bottom surface while its other surfaces are not constraint so that it can freely deform due to temperature change or irradiation-induced swelling.

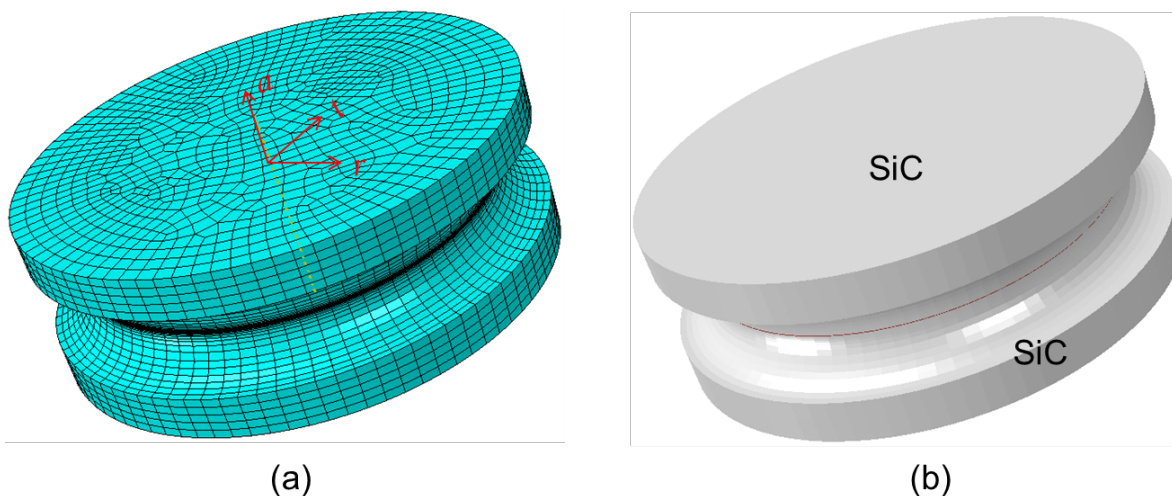


Figure 2. (a) 3D finite element mesh of the THG joint specimen with a local cylindrical coordinate system, r - t - a defined for stress/strain computations - (b) material assignment showing the SiC substrates (colored in gray) joint by a 10-micron thick Ti_3SiC_2/SiC layer (in red) [4].

In the 800°C case, the specimen is first uniformly heated from room temperature to 800°C. Next, it is incrementally subjected to irradiation-induced swelling at 800°C to the swelling levels corresponding to the saturation values given in Table 1. Figures 3(a) and 3(b) show the damage distributions at the ends of heating and of irradiation-induced swelling at this temperature. A view through a vertical section is shown in Figure 3. Minor damage is accumulated at the notch as a result of heating, and further damage in this region including the joint and adjacent SiC is found under irradiation-induced swelling. Figures 3(a) and 3(b) show that only minor and localized damage is predicted at the notch region and damage does neither deeply progress inside the SiC substrates nor significantly expand inside the joint. The damage development at the end of cooling presented in Figures 4(a) and 4(b) clearly shows localized damage in the notch area and its vicinity. During cooling the mismatch of swelling strains between the joint and the SiC substrates (Table 1) that subsist after irradiation has caused more damage for the joint and SiC at the notch area, but damage remains limited in this area. Figures 4(a) and 4(b) also indicate that the joint has not failed after cooling to room temperature following irradiation-induced swelling at 800°C. Damage prediction for the 800°C case is consistent with the SEM observation in [1] for this case. Katoh et al. [1] observed crack propagation along the interface between the bonding layer and the substrate, but the interface bonding appeared intact before the forced debond (by a torsion test).

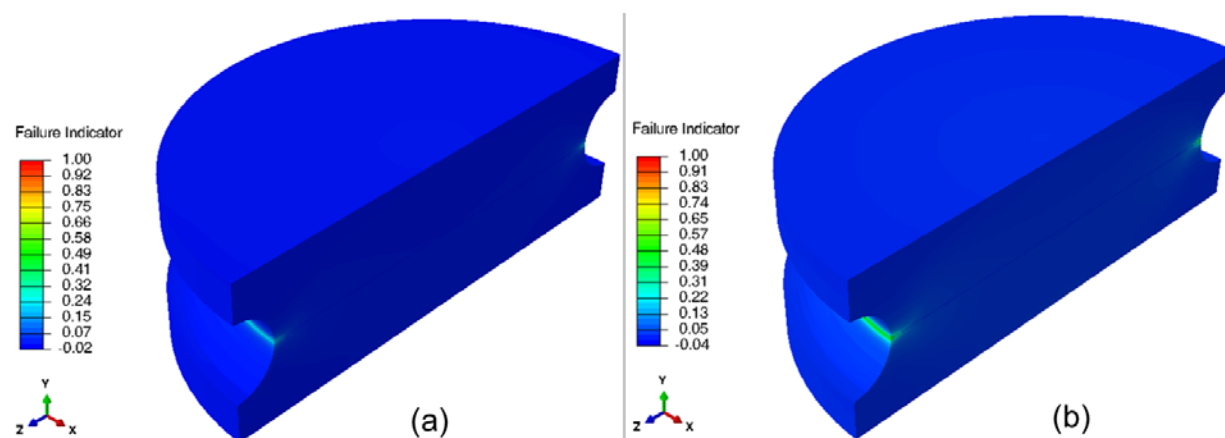


Figure 3. (a) Damage distribution at the end of heating to 800°C (view through a vertical section) – (b) Further damage development due to irradiation-induced swelling at 800°C [4].

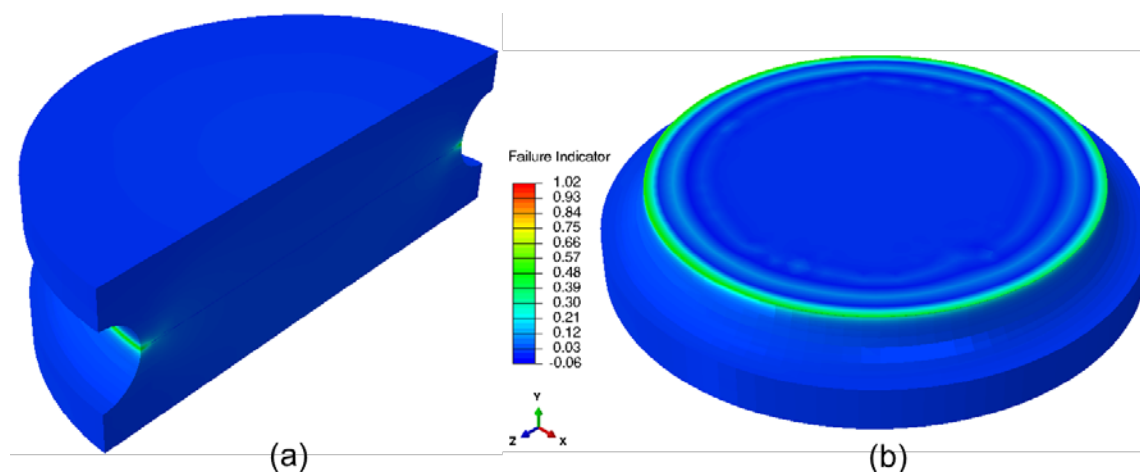


Figure 4. Damage distribution after irradiation-induced swelling at 800°C and cooling to room temperature: (a) view through a vertical section – (b) view through a horizontal section passing through the middle of the joint layer [4].

In the 500°C case, the specimen is uniformly heated to 500°C. It is then subjected to incremental swelling caused by neutron irradiation until reaching the respective saturation swelling levels at 500°C (1.4% for SiC and 1% for Ti_3SiC_2/SiC , Table 1). Compared to the 800°C case, heating to 500°C has caused less significant damage at the notch area in the SiC substrates adjacent to the joint due to the mismatch of thermoelastic properties between the joint and SiC substrates. However, the application of radiation-induced swelling at 500°C has led to further damage development inside the whole layer of the joint. Following irradiation-induced swelling at 500°C, the THG specimen is cooled to room temperature. During cooling the joint has failed. Figures 5(a) and 5(b) show the complete failure of the joint indicated by the failure indicator equal to unity in the whole joint layer.

In the 400°C case, the THG specimen is uniformly heated to 400°C. It is then subjected to incremental swelling caused by neutron irradiation until reaching the respective saturation swelling levels at 400°C (2% for SiC and 1.15% for Ti_3SiC_2/SiC , Table 1). First, very minor damage has occurred at the notch due to the mismatches of thermoelastic properties between the joint and SiC as explained for the previous cases. Nevertheless, during irradiation-induced swelling, the important mismatch of swelling between these materials at 400°C (Table 1) has caused important tensile stresses in the joint leading to joint

failure. Table 2 summarizes the findings regarding damage and failure of the THG specimen from all the analyses using the damage model.

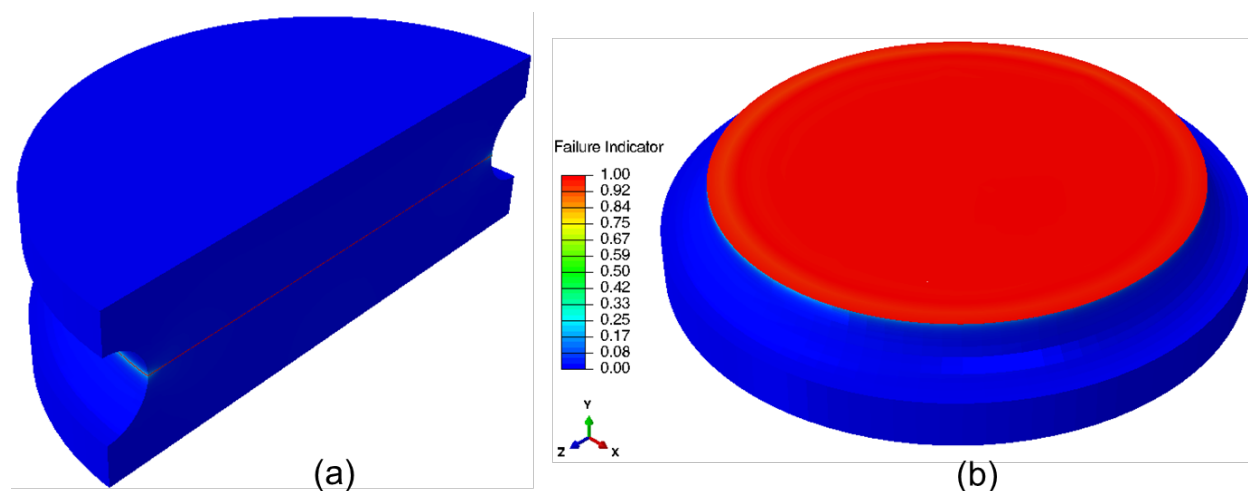


Figure 5. Damage distribution after irradiation-induced swelling at 500°C and cooling to room temperature: (a) view through a vertical section – (b) view through a horizontal section passing through the middle of the joint layer [4].

Table 2. Findings from damage analyses of the THG specimen [4]

Irradiation Temperature	SiC Substrates	Ti ₃ SiC ₂ /SiC Joint
400°C	Negligible damage	Negligible damage during heating – failed during irradiation-induced swelling
500°C	Negligible damage	Negligible damage during heating – failed during cooling to room temperature
800°C	Slightly damaged at the notch area	Slightly damaged at the notch area

Conclusions

We have further developed a continuum damage mechanics model previously formulated for brittle ceramics [7, 2] to incorporate the thermal expansion combined with irradiation-induced swelling effects to elucidate the origin of cracking observed in some THG specimens subjected to heating to a prescribed temperature following by neutron irradiation at that temperature, and cooling to room temperature after irradiations [4]. Micromechanical modeling using an Eshelby-Mori-Tanaka approach was applied to compute the thermoelastic properties of the Ti₃SiC₂/SiC composite joint needed for inputs to the damage model. In addition, a microstructural dual-phase Ti₃SiC₂/SiC model was also developed to determine irradiation-induced swelling of the composite joint at a given temperature resulting from swellings of SiC and the Ti₃SiC₂ MAX phase. Three cases for the THG specimens were analyzed corresponding to three irradiation temperatures: 800°C, 500°C, and 400°C. The damage model has been shown to provide good agreement with experimental observations following SiC joint irradiations in HFIR at 800°C. The model predicted joint failure for the irradiation temperatures of 400°C and 500°C. The predictive modeling tool developed in this paper has been demonstrated to be effective and robust to support the design of joining ceramics and its composites.

Acknowledgements

This research was supported by Office of Fusion Energy Sciences, U.S. Department of Energy (DOE) under Contract DE-AC05-76RL01830.

References

- [1] Katoh, Y., L.L. Snead, T. Cheng, C. Shih, W.D. Lewis, T. Koyanagi, T. Hinoki, C.H. Henager Jr, and M. Ferraris, *J. Nucl. Mater.*, 2014. 448(1-3): p. 497-511.
- [2] Henager Jr., C.H., B.N. Nguyen, R.J. Kurtz, T.J. Roosendaal, B.A. Borlaug, M. Ferraris, A. Ventrella, Y. Katoh, *J. Nucl. Mater.*, 466 (2015) 253–268.
- [3] Henager Jr., C.H., B.N. Nguyen, R.J. Kurtz, M. Ferraris, Y. Katoh, in *Fusion Reactor Materials Program Semiannual Progress Reports*, Vol. 60, F. Wiffen, R. Godfrey, and B. Waddell, Editors. 2016, ORNL: Oak Ridge, TN. p. 65-71.
- [4] Nguyen, B.N., C.H. Henager, Jr., and R.J. Kurtz, "Modeling Thermal and Irradiation-induced Swelling Effects on Integrity of Ti₃SiC₂/SiC Joint, 2017, *in preparation*.
- [5] Radhakrishnan, R., C.H. Henager, J.L. Brimhall, S.B. Bhaduri, *Script. Mater.*, 34 (1996) 1809–1814.
- [6] Henager Jr., R.J. Kurtz, *J. Nucl. Mater.*, 417 (2011) 375–378.
- [7] Nguyen, B.N., B.J. Koeppel, S. Ahzi, M.A. Khaleel, and P. Singh, *J. Am. Ceram. Soc.*, 2006. 89(4): p. 1358-1368.
- [8] M. Ben-Belgacem, V. Richet, K.A. Terrani, Y. Katoh, L.L. Snead, *J. Nucl. Mater.*, 447 (2014) 125–142.
- [9] Lemaître, J. and J.-L. Chaboche, *Mécanique des Matériaux Solides*. 1985, Paris, France: Dunod.
- [10] Maugin, G.A., *The Thermomechanics of Plasticity and Fracture*. 1992, Cambridge, UK: Cambridge University Press.
- [11] Renard, J., J.P. Favre, and T. Jeggy, *Compos. Sci. Technol.*, 46(1) (1993) 29-37.
- [12] Tvergaard, V., *Int. J. Fract.*, 31(3) (1986) 183-209.
- [13] Nguyen, B.N. and V. Kunc, *Int. J. Damage Mech.*, 19(6) (2010) 691-725.
- [14] Snead, L.L., T. Nozawa, Y. Katoh, B. Thak-Sang, S. Kondo, and D.A. Petti, *J. Nucl. Mater.*, 2007. 371(1-3): p. 329-77.
- [15] Barsoum, M.W., M. Radovic, A. Ganguly, T. Zhen, P. Finkel, S.R. Kalidindi, and E. Lara-Curzio, *Acta Mater.*, 2006. 54(10): p. 2757-67.
- [16] Barsoum, M.W., T. El-Raghy, C.J. Rawn, W.D. Porter, H. Wang, E.A. Payzant, and C.R. Hubbard, *Journal of the Physics and Chemistry of Solids*, 1999. 60(4): p. 429-39.
- [17] Gao, H. R. Benitez, W. Son, R. Arroyave, M. Radovic, *Mater. Sci. & Engn A*, 676 (2016) 197–208.
- [18] Nguyen, B.N., *EMTA User's Guide*. Pacific Northwest National Laboratory, Richland, WA, 2010, PNNL-19997.
- [19] Ang, C., S. Zinkle, C. Shih, C. Silva, N. Cetiner, and, Y. Katoh, *J. of Nucl. Mater.*, 483 (2017) 44-53.

3.3 POSITRON ANNIHILATION SPECTROSCOPY INVESTIGATION OF VACANCY DEFECTS IN NEUTRON-IRRADIATED 3C-SiC—Xunxiang Hu ¹, Takaaki Koyanagi ¹, Yutai Katoh ¹, Brian D. Wirth ^{1,2}
(¹Oak Ridge National Laboratory, ²University of Tennessee, Knoxville)

Abstract of a manuscript submitted to Physical Review B

Positron annihilation spectroscopy characterization results for neutron-irradiated 3C-SiC are described here, with a specific focus on explaining the size and character of vacancy clusters as a complement to the current understanding of the neutron irradiation response of 3C-SiC. Positron annihilation lifetime spectroscopy was used to capture the irradiation temperature and dose dependence of vacancy defects in 3C-SiC following neutron irradiation from 0.01 to 31 dpa in the temperature range from 380 to 790°C. The neutral and negatively charged vacancy clusters were identified and quantified. The results suggest that the vacancy defects that were measured by positron annihilation spectroscopy technique contribute very little to the transient swelling of SiC. In addition, coincidence Doppler broadening measurement was used to investigate the chemical identity surrounding the positron trapping sites. It was found that silicon vacancy-related defects dominate in the studied materials and the production of the antisite defect C_{Si} may result in an increase in the probability of positron annihilation with silicon core electrons.

3.4 VACANCY EFFECTS ON THE FORMATION OF HELIUM AND KRYPTON CAVITIES IN 3C-SiC IRRADIATED AND ANNEALED AT ELEVATED TEMPERATURES*

—Hang Zang, Wenbo Liu, Tao Li, Chaohui He, Di Yun (Department of Nuclear Science and Technology, Xi'an Jiaotong University, China) Weilin Jiang, Arun Devaraj, Danny J. Edwards, Charles H. Henager Jr., Richard J. Kurtz (Pacific Northwest National Laboratory) and Zhiguang Wang (Institute of Modern Physics, Lanzhou, China)

* Study performed during Dr. Zang's visit to PNNL

Extended abstract of a paper in Nuclear Instruments and Methods in Physics Research B
<http://dx.doi.org/10.1016/j.nimb.2016.11.017> [1]

ABSTRACT

Polycrystalline 3C-SiC was sequentially irradiated at 400 and 750 °C with 120 keV He²⁺ and 4 MeV Kr¹⁵⁺ ions to 10¹⁷ and 4×10¹⁶ cm⁻², respectively. The Kr¹⁵⁺ ions penetrated the entire depth of the He²⁺ ion implantation region. Three areas of He²⁺, Kr¹⁵⁺ and He²⁺ + Kr¹⁵⁺ ion implanted 3C-SiC were created through masked overlapping irradiations. The sample was subsequently annealed at 1600 °C in vacuum and characterized using cross-sectional transmission electron microscopy and energy-dispersive x-ray spectroscopy. Compared to the He²⁺ ion only implanted 3C-SiC, helium cavities in the He²⁺ and Kr¹⁵⁺ co-implanted 3C-SiC had a smaller size but higher density. At 25 dpa, presence of He in the co-implanted 3C-SiC significantly promoted cavity growth; much smaller voids were formed in the Kr¹⁵⁺ ion only irradiated 3C-SiC at the same dose. In addition, local Kr migration and trapping at cavities occurred, but long-range Kr diffusion in 3C-SiC was not observed up to 1600 °C.

HIGHLIGHTS

Bright-field TEM images of Kr-implanted 3C-SiC at the depth of ~600 nm are shown in Figures 1(a)-(c) under different imaging conditions. The observed features show a bright contrast in under-focus mode (Figure 1(a)) and a darker contrast in over-focused mode (Figure 1(b)), indicating that those features are cavities. Analytical results from the high-resolution TEM image (Figure 1(c)) suggest that the spherical cavities exhibit a small average size (~3 nm) and a high density (~4×10¹⁷ cm⁻³) with a local dose of 25 dpa. The selected area electron diffraction (SAED) pattern shown in Figure 1(d) indicates that the probed region is crystalline 3C-SiC with a [110]-zone axis. The EDS results of the cavities at the depths of 300 and 1500 nm are shown in Figures 1(e) and (f), respectively. While Kr peak at 1500 nm is evident in the EDS spectrum, it is absent at 300 nm. The data in Figure 1 also suggest that there is no long-range Kr diffusion in 3C-SiC at temperatures up to 1600 °C. Apparently, effective trapping of Kr at cavities of varied sizes is responsible for the immobility of the gas species. The results from this study suggest that 3C-SiC can effectively confine fission gas Kr at very high temperatures and may find potential applications as a nuclear waste form.

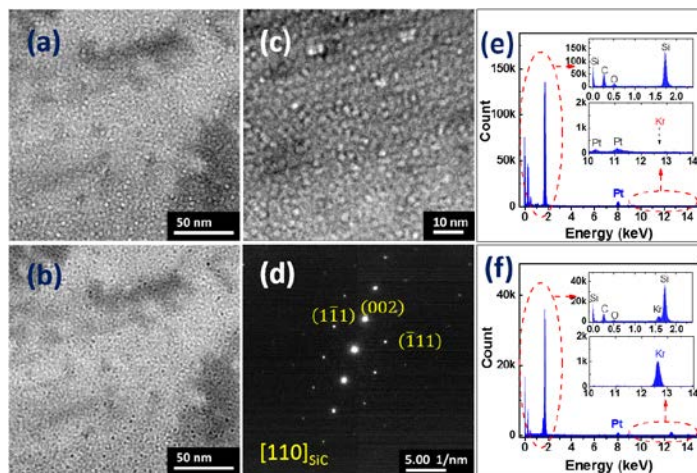


Figure 1. Bright-field TEM images of cavities in Kr ion implanted 3C-SiC: (a) under-focused, (b) over-focused, (c) high resolution, (d) SAED pattern; (e) and (f) are the EDS spectra at the depths of 300 and 1500 nm from the surface, respectively [1].

Figure 2(a) shows a low-resolution view of He cavities in both He and Kr ion implanted 3C-SiC. A higher-resolution image for the He cavities at the peak (~510 nm) is shown in Figure 2(b), and the size distribution of the He cavities estimated from Figure 2(b) is shown in Figure 2(c). The maximum diameter of the He cavities is determined to be ~27 nm, but most of the cavities are much smaller. For the convenience of comparing cavity sizes in Kr ion implanted sample, a statistical analysis has been made for cavities larger than 3 nm. The results indicate that the cavities in the sample have an average size of 9 nm with a density of $\sim 1.4 \times 10^{17} \text{ cm}^{-3}$. The size and density of the cavities in 3C-SiC produced under various implantation and annealing conditions from this study are summarized in Table 1. Compared to He implanted 3C-SiC at 4 dpa, the average cavity size is slightly smaller and density is larger in He and Kr implanted sample at 25 dpa with the same He depth profile. This result suggests that a higher dose or vacancy concentration leads to formation of smaller He cavities with a higher concentration. The small He clusters are probably formed during the first He²⁺ ion implantation due to a high concentration (7 at. %) of He. The vacancies produced in the second Kr¹⁵⁺ ion implantation play a key role in the growth of the cavities during annealing at 1600 °C. Compared to He ion implanted 3C-SiC, the smaller size and higher density of the cavities in He and Kr ion implanted 3C-SiC may be understood because a higher vacancy concentration increases the probability for He-vacancy interaction, resulting in more nucleation sites for He cavity formation in the cavity growth stage. Formation of more He cavities consumes more He atoms, leading to an overall smaller He cavity size. In addition, there is a very significant effect of the presence of He atoms on cavity growth. The presence of He atoms results in a much larger cavity size at the same dose (25 dpa) and under the same annealing conditions. The results suggest He trapping and aggregation at vacancies in 3C-SiC is the primary mechanism for growth of He cavities.

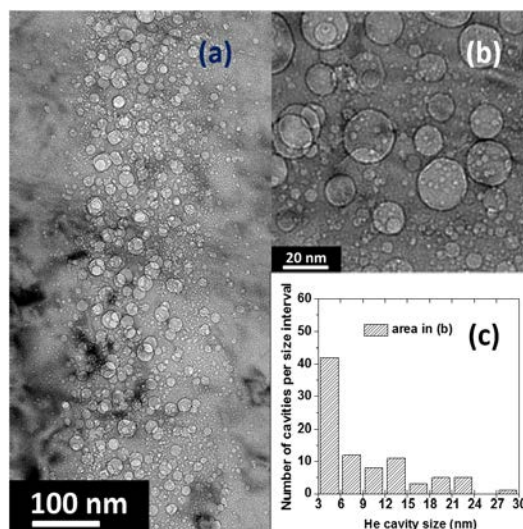


Figure 2. (a) Bright-field TEM image of helium cavities in He and Kr ion implanted 3C-SiC, (b) a high-resolution image near the depth of the He peak, and (c) size distribution of helium cavities estimated from (b), excluding those smaller than 3 nm [1].

Table 1. Size and density of the cavities in implanted and annealed 3C-SiC

Sample	He Imp. Temp. (°C)	He Peak Conc. (at.%)	Kr Imp. Temp. (°C)	Dose [§] (dpa)	Ann. Temp. (°C) Time (h)	Ave. Cavity Size (nm)	Ave. Cavity Density (cm ⁻³)
3C-SiC (He)	400	7	-	4	1600; 3	15 ^{&}	$\sim 9.4 \times 10^{16}$ ^{&}
3C-SiC (Kr)	-	-	750	25	1600; 3	3	$\sim 4.0 \times 10^{17}$
3C-SiC (He+Kr)	400	7	750	25	1600; 3	9 ^{&}	$\sim 1.4 \times 10^{17}$ ^{&}

[§]At depth 450 nm for 3C-SiC (He) and (He+Kr) and at 600 nm for 3C-SiC (Kr).

[&]Only for cavities larger than 3 nm.

Acknowledgement

This research has been supported by the U.S. Department of Energy, Office of Science, Office of Fusion Energy Sciences (DE-AC06-76RL0-1830).

References

- [1] Hang Zang, Weilin Jiang, Wenbo Liu, Arun Devaraj, Danny J. Edwards, Charles H. Henager Jr., Richard J. Kurtz, Tao Li, Chaohui He, Di Yun and Zhiguang Wang, Nucl. Instrum. Methods Phys. Res. Sect. B 389-390 (2016) 40-47; <http://dx.doi.org/10.1016/j.nimb.2016.11.017>.

4. HIGH HEAT FLUX MATERIALS AND COMPONENT TESTING

4.1 DESIGN AND DEVELOPMENT OF NOVEL Cu ALLOYS FOR FUSION ENERGY APPLICATIONS—Ying Yang (Oak Ridge National Laboratory), Steven J. Zinkle (University of Tennessee at Knoxville and Oak Ridge National Lab), and Lance Snead (Massachusetts Institute of Technology)

OBJECTIVE

This study aims at developing high strength, high conductivity Cu alloys with improved thermal creep strength for long pulse fusion high heat flux structures, through an accelerated approach of computational thermodynamics guided alloy design.

SUMMARY

During the six months from June to December 2016, we have completed the electrical conductivity measurements on previously developed Cu-Cr-Nb-Zr alloys, developed a thermodynamic database for the Cu-Cr-Ta-Zr alloy systems, and designed and fabricated one new Cu-Cr-Nb-Zr plus two new Cu-Cr-Ta-Zr alloys.

PROGRESS AND STATUS

Electrical conductivity measurements

Room temperature electrical resistivity measurements were performed on Cu-2.25Cr-1.35Nb-0.3Zr and Cu-2.25Cr-1.35Nb-0.15Zr alloys. The thermomechanical treatment of these alloys following casting consisted of 50% cold rolling, solutionizing at 970°C for 20 minutes, water quenching, and then aging at 475°C for 3 h. Following heat treatment, miniature sheet tensile specimens were fabricated with an overall length of 16 mm and gage dimensions of 5 mm x 1.2 mm x 0.75 mm. Control electrical measurements were performed on similar tensile specimens machined from an archive GlidCop Al25 oxide dispersion strengthened copper plate (19.28 nΩ-m resistivity, 89.4% International Annealed Copper Standard, IACS). The measured conductivities for the two CuCrNbZr alloys were 57.8% IACS for the 0.3%Zr alloy and 56.5% for the 0.15%Zr alloy. Transmission electron microscopy characterization and tensile testing from room temperature to 500°C will be performed in the near future.

Computational thermodynamic guided new alloy design

Due to the lack of experimental information, thermodynamic description of the Cu-Cr-Ta-Zr quaternary system was obtained through extrapolation of Gibbs energy functions of binary systems Cu-Cr, Cu-Ta, Cu-Zr, Cr-Ta, Cr-Zr, and Ta-Zr. The predicted phase diagrams of Cu-involved systems, i.e., Cu-Cr-Zr, Cu-Cr-Ta, Cu-Zr-Ta and Cu-Cr-Zr-Ta are illustrated in Figure 1. For the Cu-Cr-Ta-Zr quaternary system, the Zr content is fixed at 0.15 wt%. The calculated results show that for Cu-based alloys, the phases that are in equilibrium with Fcc-Cu are Bcc-Cr, Cu₅Zr, Cr₂Ta-C15 and Bcc-Ta.

The phases that are in equilibrium with Fcc-Cu in the Cu-Cr-Ta-Zr system are similar to those identified in the Cu-Cr-Nb-Zr system. Therefore, a parallel alloy design strategy was employed for the Cu-Cr-Ta-Zr alloys. A bimodal precipitate distribution was designed, with the Cr₂Ta-C15 Laves phase being grain boundary (GB) precipitates and Bcc-Cr, Bcc-Ta and/or CuZr intermetallic compounds as matrix precipitates. Two Cu-Cr-Ta-Zr alloys were designed. The first alloy has Cr₂Ta-C15 serving as GB precipitates and the Bcc-Cr, Cu₅Zr and Cu₅₁Zr₁₄ as the matrix precipitates. The full-scale diagram showing the phase fraction vs temperature for alloy one is shown in Figure 2(a). The precipitate stability is detailed in Figure 2(b).

The second alloy is similar to the first one, except the Bcc-Ta precipitates were used for matrix precipitates. The phase fraction vs temperature for alloy two is shown in Figure 3(a), with the precipitate stability detailed in Figure 3(b).

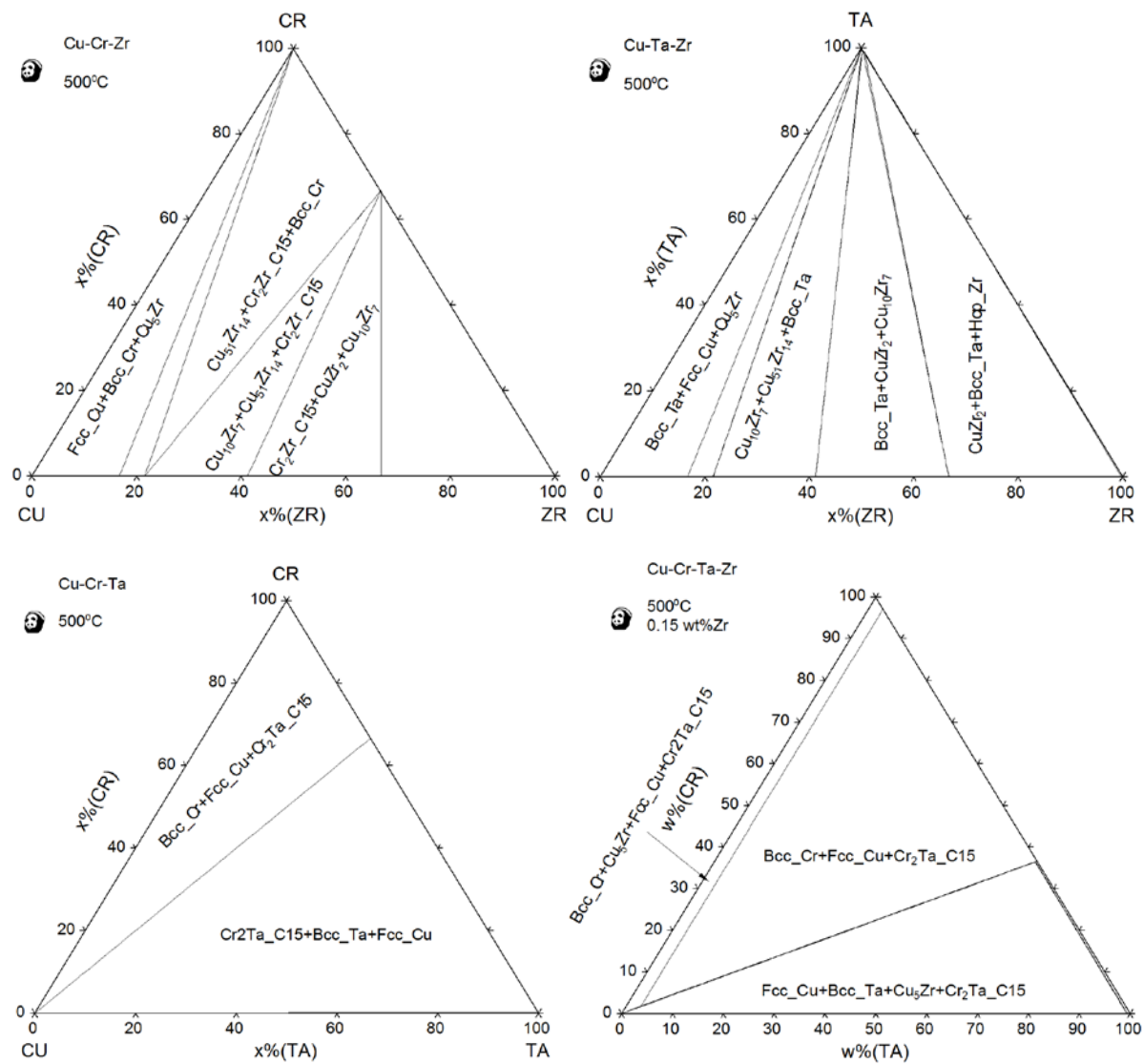


Figure 1. Predicted isothermal sections of phase diagram at 500°C for the Cu-Cr-Zr, Cu-Ta-Zr, Cu-Cr-Ta and Cu-Cr-Ta-Zr systems.

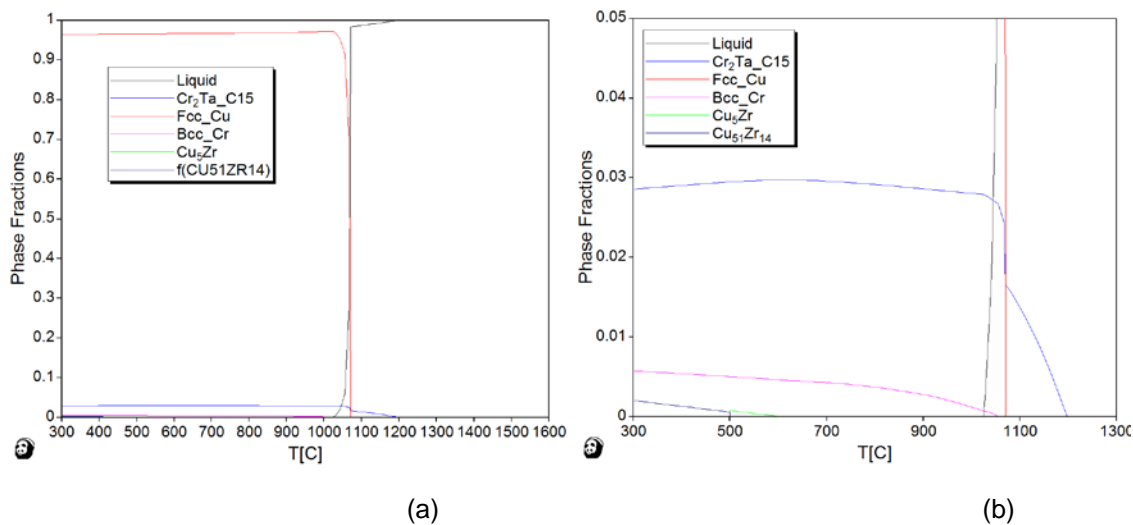


Figure 2. Calculated phase fraction vs temperature for alloy #1.

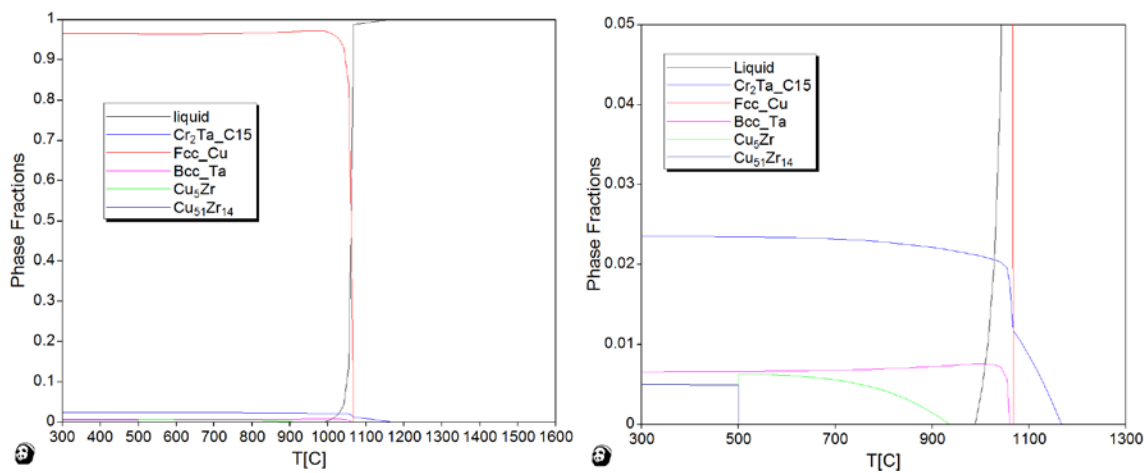


Figure 3. Calculated phase fraction vs temperature for alloy #2.

The third new alloy is a Cu-Cr-Nb-Zr alloy. Instead of using Bcc-Cr as the matrix precipitate as those in the previously developed Cu-Cr-Nb-Zr alloys, the new alloy utilizes the Bcc-Nb as the matrix precipitates, thereby to explore the strengthening role of the Bcc-Nb phase as matrix precipitates in Cu. The calculation results are shown in Figure 4 in enlarged scale.

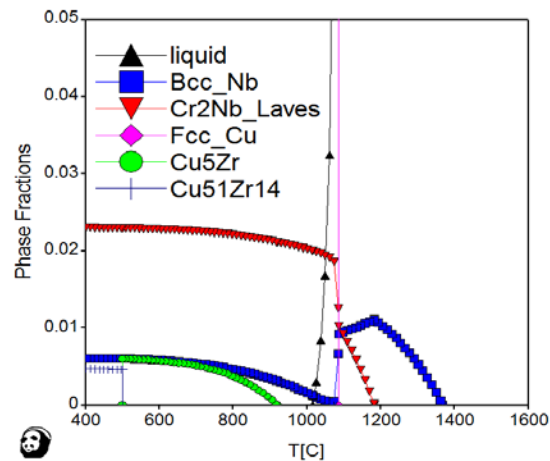


Figure 4. Calculated phase fraction vs temperature for alloy #3.

New alloy fabrication and heat treatment

Based on these thermodynamic calculation results, three new alloys have been fabricated by traditional arc melting and drop casting. The Cr and Ta (or Cr and Nb) had to be pre-alloyed to avoid the vaporization of Cu. The as-cast alloy has dimensions 0.5 in. x 0.5 in. x 4 in. The castings were cold rolled to 70%-reduction in thickness. The as-rolled alloys have been solutionized at 970°C for 20 mins followed by water quench and then aged at 475°C for 3 h. The as-heat treated alloys are shown in Figure 5, with “S” the solutionized state and “a” the aged state. These materials are now waiting for optical and electronic microscopy characterization to confirm the designed microstructure.



Figure 5. As heat-treated materials in plate form, ready for optical and electron microscopy analysis.

4.2 MECHANICAL PROPERTIES CHARACTERIZATION OF 90-97wt% WNiFe HEAVY ALLOYS—M.E. Alam, S. Pal, K. Fields, G. R. Odette (University of California, Santa Barbara)

OBJECTIVE

The objective of this research is to characterize the mechanical properties of a series of WNiFe alloys to understand and qualify them for future fusion reactor divertor, and other applications.

SUMMARY

Ductile phase toughening (DPT) is a promising approach to improve toughness of brittle materials like tungsten (W). Four commercial liquid phase sintered W-based alloy composites, containing 90, 92.5, 95 and 97 wt.% W, with the balance of a 7:3 wt. % Ni:Fe ductile solid solution phase, was characterized. Microhardness increases with increasing W% slowly at room temperature (RT), but more rapidly at liquid nitrogen temperature (LN₂). Tensile strength increases and ductility decreases with decreasing temperature up to 95W, and remains relatively unchanged at 97W. Pre-cracked single edge notch bend bar fracture toughness tests at RT shows stable crack growth with average maximum load initiation toughness, K_{Jc} , $\approx 102 \pm 7 \text{ MPa}\sqrt{\text{m}}$, relatively independent of the W fraction up to 95 wt.%, but decreasing to $\approx 73 \pm 13 \text{ MPa}\sqrt{\text{m}}$ for the 97W alloy. Low temperatures toughness tests show the brittle-to-ductile transition temperature (BDTT) increases with increasing W fraction from $\approx -150^\circ\text{C}$ for 90W to $\approx -50^\circ\text{C}$ for 97W alloy.

PROGRESS AND STATUS

Introduction

Background information and the room temperature tensile and fracture toughness data were discussed in earlier semi-annual report [1]. A series of lower temperature microhardness, tensile and fracture toughness studies are reported here.

Experimental Procedures

Four commercially available (Mi-Tech Metals, Indianapolis, In, USA) liquid-phase sintered W-NiFe composites, received as a 100mmx100mmx14mm plate form, with 90, 92.5, 95 and 97 W (wt.%) and balance 7:3 Ni:Fe were studied. Details of the materials and sample preparation can be found elsewhere [1].

Vickers microhardness measurements were performed on the polished surfaces at a 500g load using LECO M-400A semi-automated hardness tester at RT and the reported values are based on the average of 10 to 15 indents. Zwick microhardness tester was used to indent at LN₂ conditions, using 500g-load. A small stainless steel chamber, insulated outside, was placed below the indenter. Specimens were placed inside the chamber, LN₂ was poured continuously until stopped boiling, and kept ~5 min under relatively tranquil LN₂ before test. Uniaxial tensile tests were performed on EDM fabricated flat dog-bone shaped sub-sized specimens with a gauge section length x width x thickness of 5.0x1.2x0.5 mm³ from room temperature to LN₂. The tensile specimens were sanded with 1500 grit to remove any surface contamination, minor cracks or local residual stresses due to the electrical discharge machining (EDM). An 810 MTS servo-hydraulic universal testing machine equipped with cooling chamber was used. A controlled liquid nitrogen-air mixture was injected into the cooling chamber to achieve the targeted temperature, and held for 30 to 45 minutes before testing. The tensile tests were conducted at a displacement rate of 0.30 mm/min, equivalent to a strain rate $\approx 10^{-3}/\text{s}$ on at least 3 specimens at each condition.

Fracture toughness tests were conducted from ambient temperature down to LN₂ temperature on the fatigue pre-cracked single-edged notch three point bend (3PB) specimens with nominal dimensions of 16 mm in length, 3.3 mm width and 1.65 mm thickness. The same 810 MTS servo-hydraulic universal testing machine equipped with cooling chamber was again used for this purpose. The specimens were pre-cracked to a nominal crack length (a)-to width (W) ratios, (a/W), from 0.35 to 0.5. To facilitate in-situ optical observation of the crack tip region, the fracture specimen sides were sanded with a sequence of

2000 grit, 9 μ , 3 μ and 1 μ paper. The fracture tests were carried out at a crosshead speed of 0.04mm/min. ASTM E1921 [2] was used to evaluate both the elastic and plastic components of fracture toughness for the 3PB tests. The K_{Jc} were calculated at the maximum load (P_m) in the load-displacement (P-d) curve. Three to four specimens were tested at each condition.

Results

Microstructure

Roughly spheroidal W particle size increases from $\sim 18\mu\text{m}$ for 90W to $\sim 38\mu\text{m}$ for 97W, and are surrounded in the interconnected skeleton of a Ni-rich ductile phase (DP). The DP area decreases from $\sim 21.4\%$ for 90W to 9.3 % for 97W. Multiple EDX scans show that the particles are close to 100% W, while the DP is approximately 50Ni, 30W and 20Fe (wt.%). Details of the microstructure studies have been reported previously [1].

Microhardness (μH)

Vicker's microhardness (H_v) results for W-alloys tested at room temperature and LN_2 have been shown in Figure 1. Average hardness increases with increasing W fraction both at RT and LN_2 . However, μH is substantially higher at LN_2 ($507 \pm 7 \text{ kg/mm}^2$ for 90W and $609 \pm 21 \text{ kg/mm}^2$ for 97W) than that of RT test ($321 \pm 9 \text{ kg/mm}^2$ for 90W and $344 \pm 9 \text{ kg/mm}^2$ for 97W). Pure W was also tested both at room temperature and LN_2 and yielded 358 ± 39 and $686 \pm 79 \text{ kg/mm}^2$, respectively. No noticeable crack near, or at the edges of the indented area has been observed in any conditions.

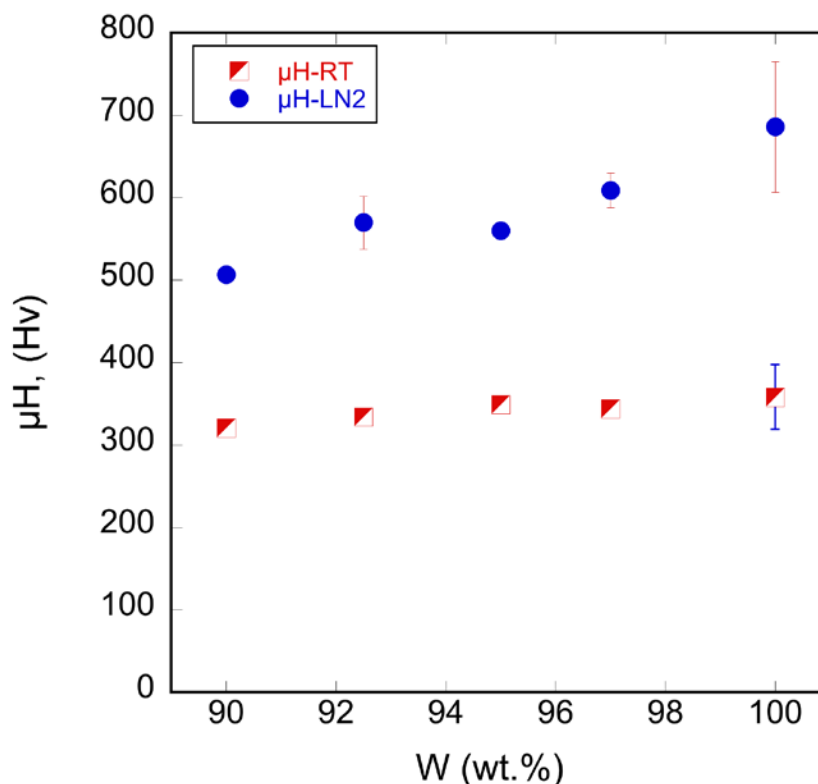


Figure 1. Vicker's microhardness of WHAs' as a function of temperature and W fraction.

Tensile Properties

Figure 2 shows the engineering stress-strain (s - e) curves along with 0.2% yield strength (s_y), ultimate tensile strength (s_u) and total elongation (e_t) tested from room temperature down to liquid nitrogen temperature. Tensile results are also summarized in Table 1. Room temperature s (e) curves are generally similar, although the total elongation systematically decreases with increasing W . Significant strain hardening is observed in all cases, which is quite common in typical two-phase alloys including WNiFe [3-4]. The s_y does not vary significantly with W fraction. However, ultimate tensile stress (s_u), uniform (e_u) and total (e_t) elongations decrease with increasing W , and there is a noticeable strength and ductility drop-off between 95 and 97W. Fracture in these alloys takes place almost immediately after reaching ultimate tensile stress, with very minimal to no necking.

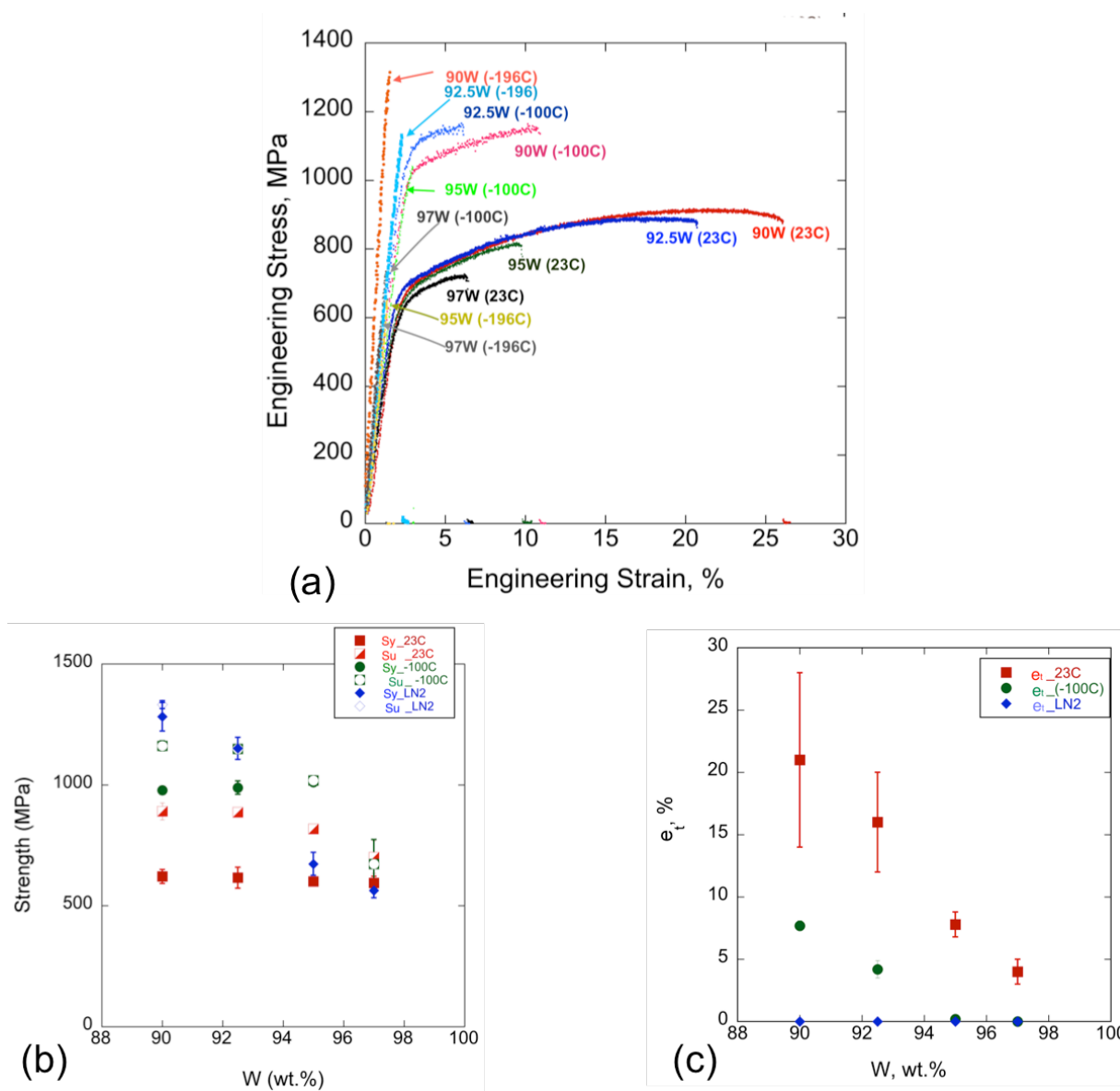


Figure 2. (a) Engineering s - e curves, (b) 0.2% s_y and s_u , and (c) e_t of WHA's as a function of temperature and W %. Red squares: 23°C, green circles: -100°C and blue diamonds: -196°C.

Table 1. Tensile properties of WNiFe alloys as a function of W fraction and temperatures

Temp (°C)	Alloys	s_y (MPa)	s_u (MPa)	e_u (%)	e_t (%)
23	90W	621 ± 29	891 ± 35	18 ± 4	21 ± 7
	92.5W	616 ± 44	886 ± 12	13.5 ± 2.2	16 ± 4
	95W	600 ± 15	818 ± 10	7.3 ± 1	8 ± 1
	97W	594 ± 27	701 ± 67	3.4 ± 1	4 ± 0.7
-100	90W	978 ± 16	1162 ± 20	7.5 ± 0.4	7.7 ± 0.4
	92.5W	989 ± 28	1149 ± 16	4.0 ± 0.7	4.2 ± 0.7
	95W	1019 ± 18	1019 ± 18	0	0
	97W	673 ± 101	673 ± 101	0.0	0.0
-196	90W	1292 ± 59	1332 ± 16	0.2 ± 4	0.2 ± 0.4
	92.5W	1151 ± 46	1151 ± 46	0	0
	95W	673 ± 48	673 ± 48	0	0
	97W	563 ± 31	563 ± 31	0	0

$s_y=0.2\%$ yield stress, $s_u=$ ultimate tensile stress, $e_u=$ uniform elongation, $e_t=$ total elongation.

In general, strength increases and ductility decreases at lower temperatures when compared with room temperature. At LN₂, all the specimens break elastically, without showing any plastic deformation ($e_t \approx 0\%$), except one for 90W that shows $e_u=e_t=0.6\%$. The low temperature tensile strengths ($s_y \approx s_u$) also decrease with increasing W and the strength for 97W is lower or similar to that at room temperature. At -100°C, s_y is almost same (but higher than RT) up to 95W, and then drops sharply at 97W. The s_u decreases gradually with increasing W. At -100°C limited ductility occurs only for the 90W and 92.5W alloys.

The SEM fractographs of room temperature tensile test on WNiFe alloys manifest four local failure modes, namely: W-W intergranular fracture (WW), W cleavage (WC), W-DP interfacial separation (WD), and Ni:W:Fe ductile phase rupture (DR), and also reported by many other research groups studied on similar WHA's [4-5]. SEM micrographs of the fracture surfaces of the broken RT tensile specimens, shown in Figure 3, illustrate all of these failure modes. The W-W interfacial boundary is the weakest, and the W-W interfacial increases with increasing W. Specimen fracture initiates by WW at the W-W particle interfaces, and continues by crack propagation through the W-DP accompanied by W cleavage. Figure 3 shows that the fraction of WC is highest for 90W, and minimal for 97W alloys that experience more WW separation. Notably, WC appears to correlate with higher strength and ductility (see Table 1). In contrast, lower temperature fracture surface shows increasing amount of cleavage fracture with decreasing ductility (Figure 4). For example, all four WHA's show cleavage fracture at LN₂. Moreover, out-of-plane cracks were also observed at lower temperature fracture surfaces.

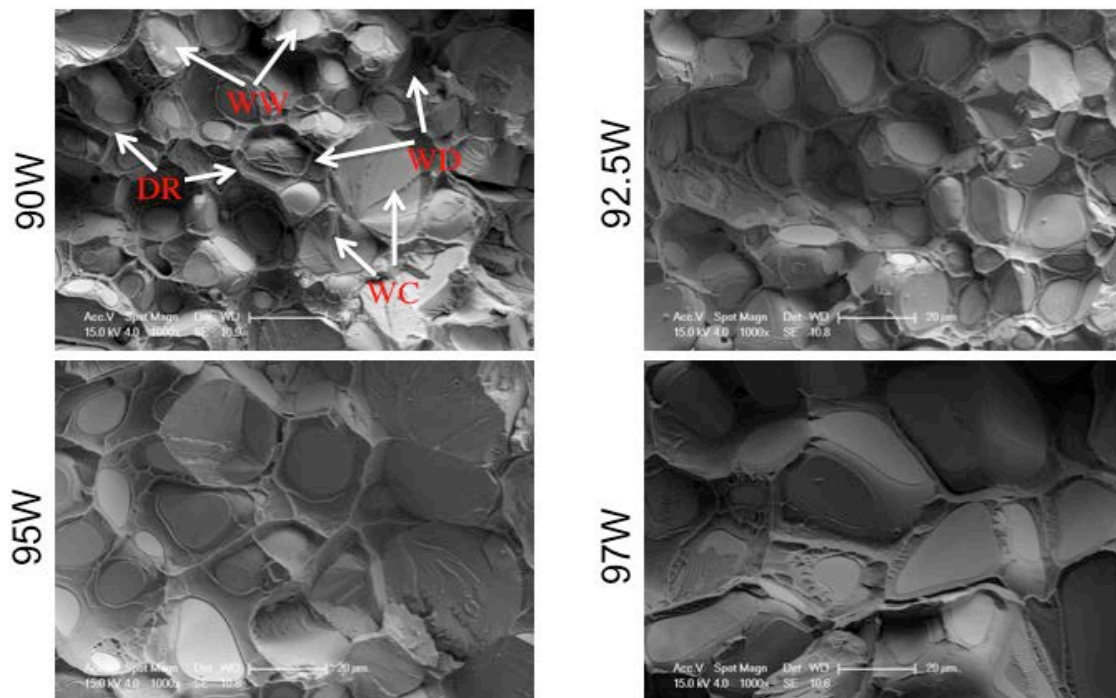


Figure 3. SEM fractographs of the room temperature tensile fracture surfaces for the 4 WNiFe alloys.

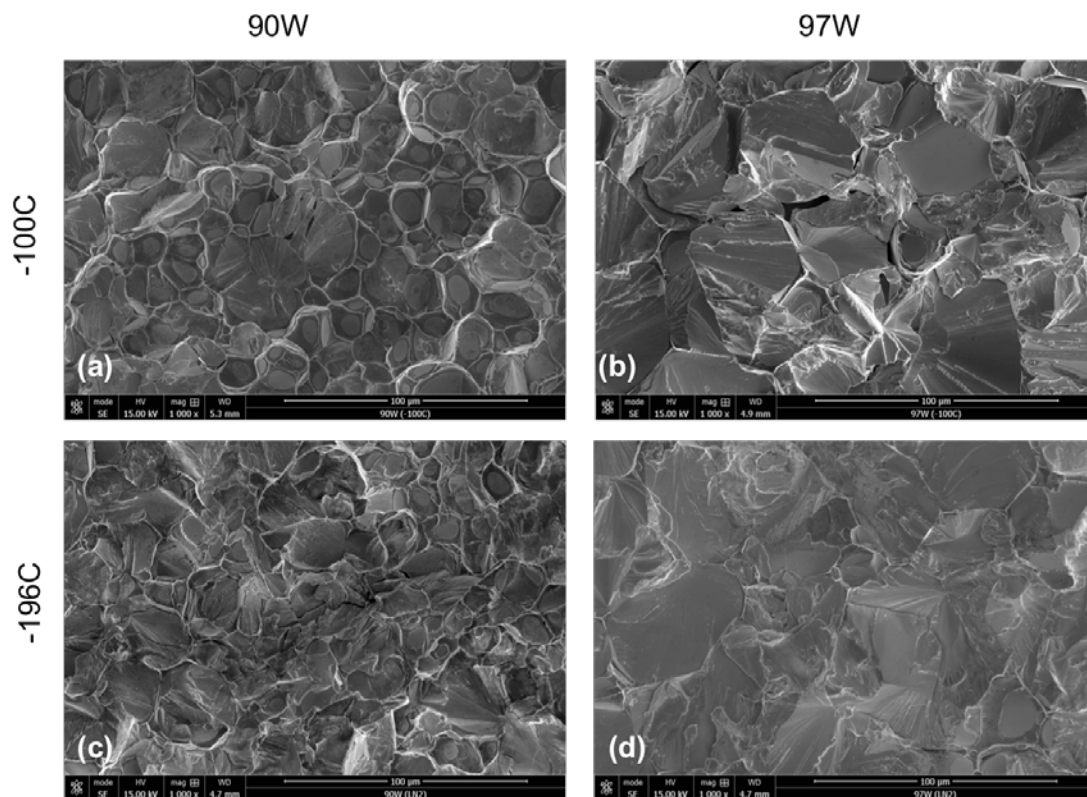


Figure 4. SEM fractographs showing tensile fracture surfaces of 90W (left column) and 97W (right column) tested at -100°C (top row: a-b) and LN_2 temperature (bottom row: c-d).

Fracture Toughness

Fracture toughness test were conducted from room temperature down to liquid nitrogen temperature for all WHA's. Tests were conducted on fatigue pre-cracked single edged notch specimens using 3-point bend fixtures. Details of the room temperature fracture toughness results, including their fracture mechanisms were reported previously [1]. In summary, all alloys tested at RT show continuous load drop after maximum load (P_m) with increasing displacement (d), indicating stable crack growth (Figures. 5a-8a). Maximum load initiation toughness value, K_{Jc} , averaged $102 \pm 7 \text{ MPa}\sqrt{\text{m}}$ for 90W-95W WHA, but dropped to $73 \pm 13 \text{ MPa}\sqrt{\text{m}}$ for the 97W alloy (see Table 2, and Figure 9). Room temperature fracture mechanisms include: crack wake bridging, crack branching, massive process zone crack tip plasticity, and tungsten cleavage and slip plane in the W-particles [1]. The local fracture modes are roughly similar to those observed for room temperature tensile tests.

Table 2: Fracture toughness properties of WNiFe alloys as a function of W fraction and temperatures

Temp (°C)	Toughness, K_{Jc} (MPa $\sqrt{\text{m}}$)			
	90W	92.5W	95W	97W
23	100 ± 20	96 ± 9	110 ± 17	73 ± 13
-50	-	59 ± 9	65 ± 4	40 ± 2
-100	73 ± 4	48 ± 5	35 ± 4	32 ± 0.1
-150	50 ± 1	-	-	-
-196	36 ± 3	30 ± 3	27 ± 5	25 ± 2

Figure 5 shows normalized load-displacement (P-d) curves for the 90W-Ni:Fe alloys (W1). The normalization involves adjusting the actual P-d data to a common $a/W = 0.5$. Note that with a few exceptions, the normalized peak loads for the redundant tests are similar. All the specimens tested down to -100°C show stable crack growth (Figure 5a and b). However, one of three tested specimen fails unstably at -150°C (see Figure 5c), as do all the specimens tested at LN_2 temperature (see Figure 5d), marking the BDTT of 90W-NiFe alloy $\approx -150^\circ\text{C}$. Unlike RT test, lower temperature tests show that the specimens reach to their peak load P_m with minimum plastic yielding, corresponding to their lower toughness values, even though the P_m is higher (see Table 2 and Figures 5 and 9). However, K_{Jc} of 90W at LN_2 ($\approx 36 \pm 3 \text{ MPa}\sqrt{\text{m}}$) is still much higher than that of room temperature pure W ($\approx 8 \pm 6 \text{ MPa}\sqrt{\text{m}}$). The area of the near-crack-tip plastic process zone shrinks with decreasing temperature. SEM fractographs (not shown here) shows that the local fracture mechanisms are similar to those observed in the lower temperature tensile tests for the 90W alloy. The fraction of W-cleavage (WC) fracture increases with decreasing temperature along with deep, out-of-plane W trans-particle cracks.

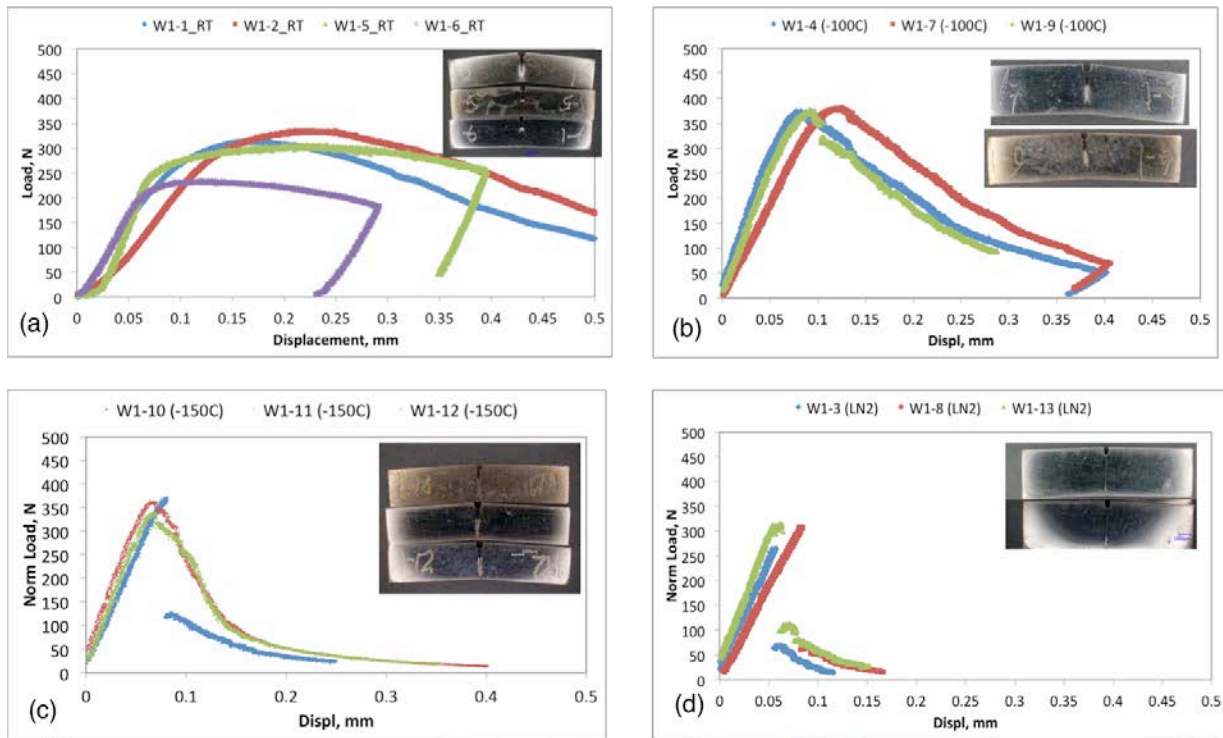


Figure 5. P-d curves for 90W-NiFe alloy at: (a) RT, (b) -100°C, (c) -150°C, and (d) LN₂, respectively.

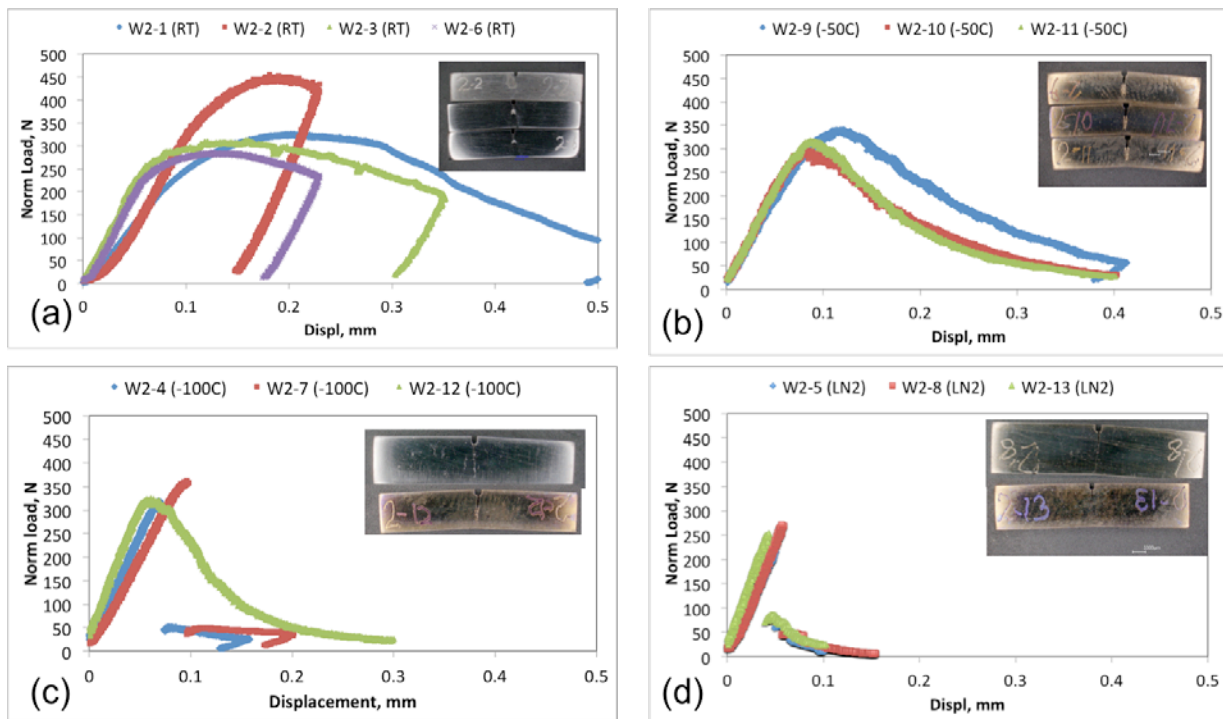


Figure 6. P-d curves for 92.5W-NiFe alloy at: (a) RT, (b) -50°C, (c) -100°C, and (d) LN₂, respectively.

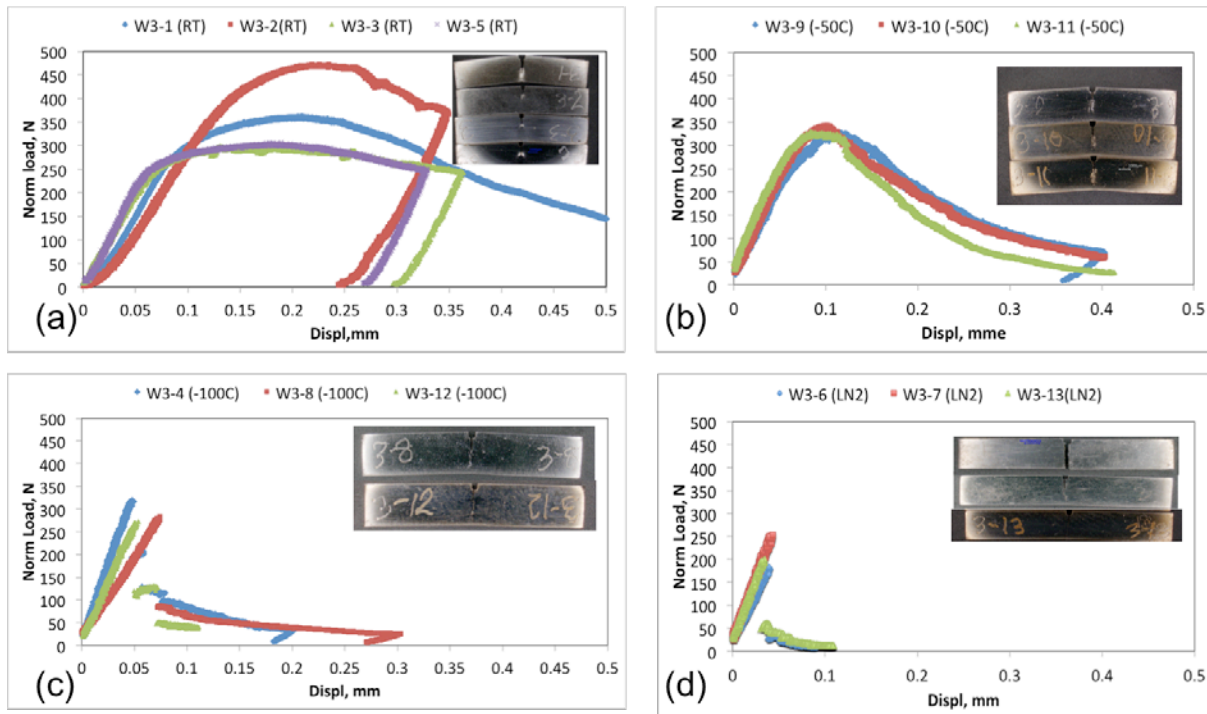


Figure 7. P-d curves for 95W-NiFe alloy at: (a) RT, (b) -50°C, (c) -100°C, and (d) LN₂, respectively.

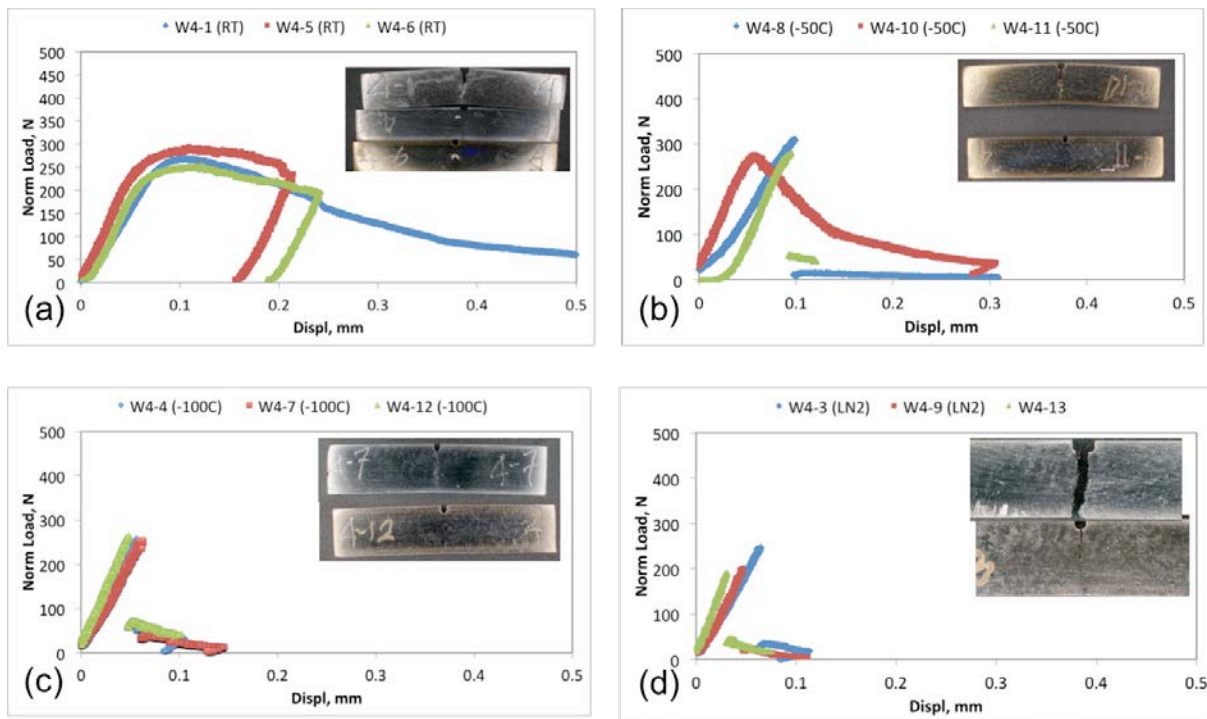


Figure 8. P-d curves for 95W-NiFe alloy at: (a) RT, (b) -50°C, (c) -100°C, and (d) LN₂, respectively.

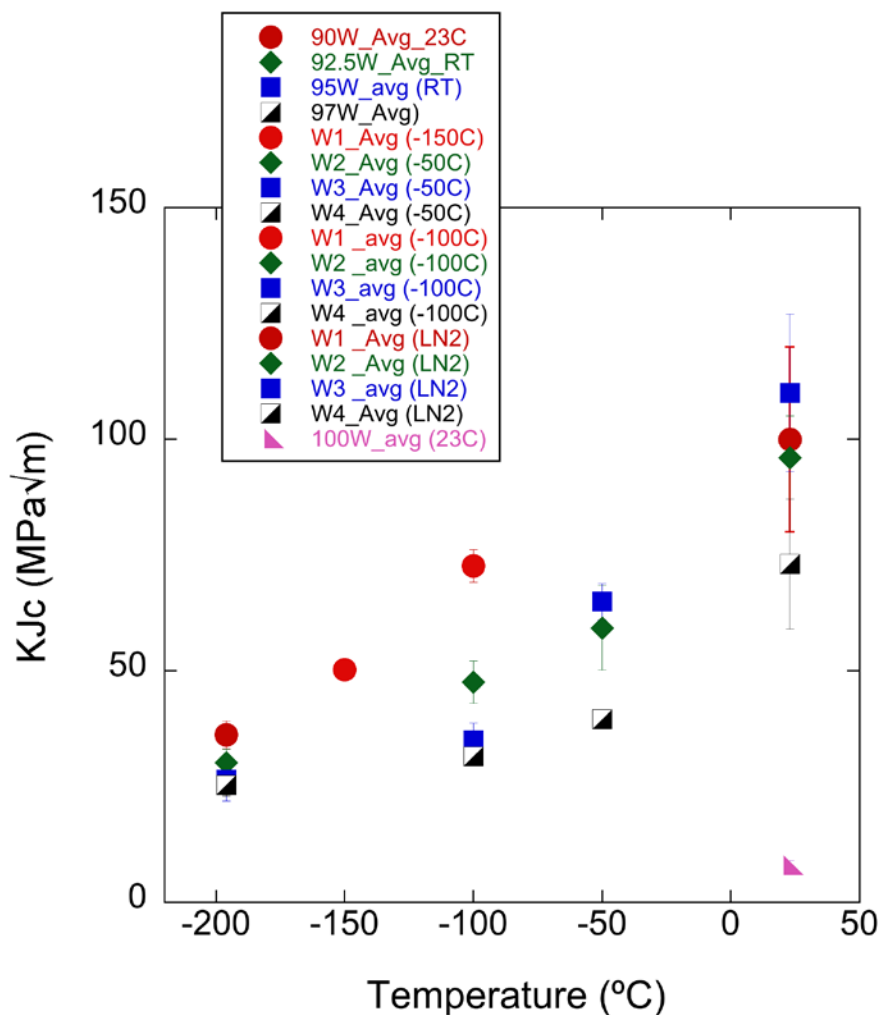


Figure 9. Fracture toughness, K_{Jc} , of WNiFe alloys as a function of W and temperature. Red circle: 90W (W1), green diamond: 92.5W (W2), blue square: 95W (W3), half-black square: 97W (W4), and purple triangle: 100W.

Though the room temperature K_{Jc} is nearly independent of the W (or DP fractions up) to 95W alloys, but lower temperature toughness shows different trends. All the specimens tested at -50°C show stable ductile tearing with K_{Jc} averaging $\approx 59 \pm 9 \text{ MPa}\sqrt{\text{m}}$ (Table 2 and Figure 6). However, only one of three 92.5W specimens tested at -100°C experienced stable ductile tearing, while others at -100°C and all at LN_2 break unstably. Thus, it is reasonable to say that the BDTT of 92.5W alloy is $\approx -100^{\circ}\text{C}$ with a K_{Jc} value $\approx 48 \pm 5 \text{ MPa}\sqrt{\text{m}}$. Similar to 92.5W alloy, 95W alloy also show stable crack growth at -50°C (see Figure 7). However, all the specimens tested at -100°C and LN_2 show only elastic fracture. Thus the BDTT of 95W alloy is estimated as -75°C with $K_{Jc} \approx 50 \pm 15 \text{ MPa}\sqrt{\text{m}}$. Only one specimen shows stable crack growth at -50°C for 97W, while others at -50°C and lower temperatures show unstable cleavage fracture (Figure 8). Therefore, a reasonable estimation for 97W is $\approx -50^{\circ}\text{C}$ at toughness $\approx 40 \pm 2 \text{ MPa}\sqrt{\text{m}}$. In general, contrary to tensile test strength, fracture toughness P-d curves show that the maximum load mostly drop with decreasing temperature. Minimal to no plastic yielding occurs at lower temperature. All the specimens tested at LN_2 fracture unstably with nearly similar toughness value ($25\text{--}36 \text{ MPa}\sqrt{\text{m}}$), irrespective to W fraction. SEM fractographs also show $\approx 100\%$ W-particle cleavage fracture along with out-of-plane W-particle cracking for LN_2 test.

Conclusion and Future Work

- The average microhardness value slightly increases with increasing W fraction. The microhardness is almost doubled at LN₂.
- Tensile strength increases and ductility decreases for lower temperature tensile tests when compared with room temperature. s_u drops with W%, so as e_t ($\approx 24\%$ for 90W to 3% for 97W at RT, and $\approx 8\%$ for 90W to 0% for 95W onwards at -100°C).
- The RT fracture toughness measurements on four 90-97 wt.% WNiFe alloys showed that the K_{Jc} is $\approx \times 10$ -15 higher than that of typical monolithic W (8 MPa \sqrt{m}).
- Extremely stable crack growth is observed for all alloys at RT. Multiple toughening mechanisms include crack wake bridging, micro-cracking, micro-crack bridging, crack deflection, and extensive process zone plasticity.
- Low temperature toughness test also show stable ductile tearing at -100°C and somewhat mixed (stable + unstable) behavior at -150°C for 90W, and marked as its BDTT. The estimated BDTT for 92.5W, 95W, and 97W alloys is -100°C, -75°C and -50°C, respectively.
- High temperature toughness test will be conducted in future. W-coated WHA's using SPS will also be tested to understand the crack propagation mechanisms through WNiFe alloys, along with in-situ XRD deformation studies.

Acknowledgement

We like to acknowledge the support provided by U.S. Department of Energy through the Office of Fusion Energy Sciences (DOE PNNL Tungsten: 8-442520-22403-3 ROF02).

References

- [1] M.E. Alam, S. Pal, K. Fields and G.R. Odette, "Ductile Phase Toughening of 90-97wt.% W-NiFe Heavy Metal Alloys", in DOE/ER-0313/60 - Volume 60, Semiannual Progress Report, June 30 (2016) 93-102.
- [2] ASTM E1921-13a, Standard Test Method for Determination of Reference Temperature, T_o , for Ferritic Steels in the Transition Range, ASTM International, West Conshohocken, PA, 2013.
- [3] Z-H. Zhang, F-C. Wang, S-K. Li and L. Wang, "Deformation characteristics of the 93W-4.9Ni-2.1Fe tungsten heavy alloy deformed by hydrostatic extrusion", Materials Science and Engineering A 435-436 (2006) 632-637.
- [4] U. R. Kiran, A. Panchal, M. Sankaranarayana, G.V.S. N. Rao, T.K. Nandy, "Effect of alloying addition and microstructural parameters on mechanical properties of 93% tungsten heavy alloys", Materials Science & Engineering A 640 (2015) 82-90.
- [5] KMO Zamora, JG Sevillano, MF Perez, "Fracture toughness of W heavy alloys", Materials Science and Engineering A, 157 (1992) 151-160.

4.3 EXPERIMENTAL MEASUREMENTS OF SURFACE DAMAGE AND RESIDUAL STRESSES IN MICRO-ENGINEERED PLASMA-FACING MATERIALS- David Rivera, Richard Wirz, Nasr M. Ghoniem (University of California, Los Angeles)

SUMMARY

The thermomechanical damage and residual stresses in plasma-facing materials operating at high heat flux are experimentally investigated. Materials with micro-surfaces are found to be more resilient, when exposed to cyclic high heat flux generated by arc-jet plasma. We demonstrate that W surfaces with micro-pillar type surface architecture have significantly reduced residual thermal stresses after plasma exposure, as compared to those with flat surfaces. X-ray diffraction (XRD) spectra of the W-(110) peak reveal that broadening of the FWHM for micro-engineered samples is substantially smaller than corresponding flat surfaces. Cyclic plasma heat loading is shown to anneal out most of the residual stresses in micro-engineered surfaces, consistent with relaxation of residual thermal. The initial residual stress state of flat W samples is compressive (-1.3 GPa), and after 50 plasma cycles, it relaxes to -1.0 GPa. Micro-engineered samples show that the initial residual stress state is compressive at (-250 MPa), and remains largely unchanged after plasma exposure.

PROGRESS AND STATUS

Approach

The demand of higher performance materials is even greater in future technologies that will require materials to operate in substantially more aggressive environments. In such applications, PFM encounter unprecedented severe thermomechanical environments, as plasma ions and electrons slam onto the surface. Many physical degradation phenomena ensue, including material loss by ablation, blistering, sputtering and evaporation, as well as genuine thermomechanical damage in the form of extensive plastic deformation and complex surface cracking. The environment severity is correlated with two main parameters. The first is the total amount of absorbed energy density that passes through the surface, Γt (kWh/cm²); a measure of the material lifetime. The second load-related parameter is the instantaneous heat flux, Γ (MW/m²). While Γt is indicative of the duration through which the material will have to survive successive amounts of energy, delivered to its surface either continuously or intermittently, Γ is associated with the response time scale of the material itself to instantaneous pulses of energy. Generally, if Γ is high, the material lifetime is low, and vice-versa. Figure 1 shows the relationship between the lifetime Γt (kWh/cm²) and the instantaneous surface power density (heat flux) Γ (MW/m²) for a number of technological applications.

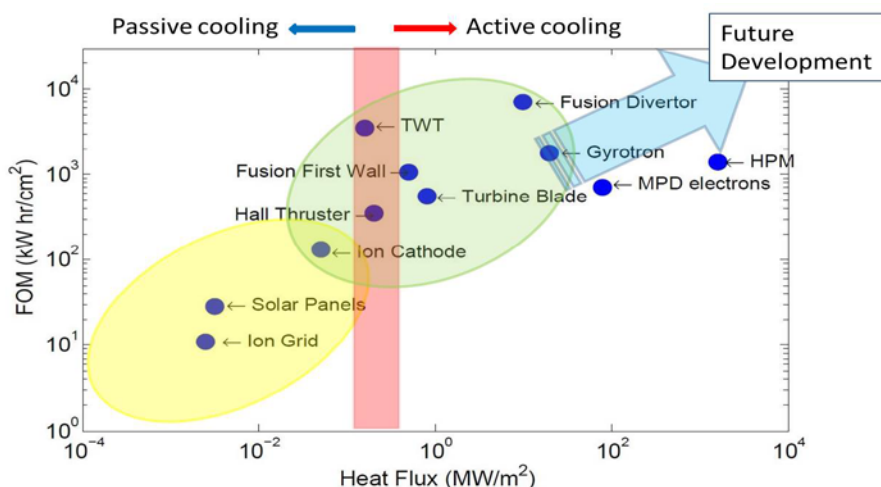


Figure 1: Representation of the Figure of Merit (Lifetime) of various devices as a function of the instantaneous surface heat flux.

Severe plasma transients are expected to greatly influence the integrity of plasma-facing components in fusion energy systems, notably the tungsten armor in most of existing divertor designs. Typical design-base transients contain an amount of energy in between 0.1 and 0.5 MJ/m² for the Joint European Torus (JET) and between 1 and 5 MJ/m² for the International Tokamak Experimental Reactor (ITER), lasting duration between 0.1 and 1 ms, respectively. Such transients are expected to cause surface fracture, plasticity, and grain motion in polycrystalline tungsten. Among the operational scenarios of interest is the response of tungsten to edge localized modes, which carry energy densities on the order of 1 MJ/m² and time durations in the range of 0.1-0.5 ms, which can result in severe damage to the tungsten armor in the form of cracking and localized melting of the material [1]. Cyclic thermal transients are generally associated with complex plasticity and fracture phenomena. In particular, the response of a material facing cyclic high heat flux loading can be either elastic, plastic, ratcheting, shakedown, or fracture. Ratcheting is the continuous accumulation of plastic strain with each passing cycle up to the point of failure, and is considered detrimental. Shakedown describes an initial degree of plastic deformation, quickly reaching equilibrium in subsequent loading cycles. A detailed analysis of the residual stress state of the micro features comprising the coating is necessary to provide an avenue for improvement in the coating process. If the surface layer is structured so as to allow expansion and contraction without these large residual stresses, one might be able to develop a material that is more resistant to high heat flux thermomechanical effects. We have recently developed such a material concept, where an “armor” coating is deposited by CVD on top of the main structure, with the main function being thermomechanical damage mitigation [2]. The present work extends the experimental investigations presented in reference [2].

A number of researchers have attempted designing refractory metal coatings from a traditional standpoint where a flat surface is deposited onto a substrate and exposed to a thermally harsh environment [3, 4, 5, 6]. Although efforts along this path have proved successful in protecting the underlying structure, improvements are still achievable through the advent of castellated armor concepts [2]. In such designs, freestanding structures, such as micro-pillars are grown onto a surface, and are capable of protecting it through reduction of residual thermal stresses. Similar concepts have been proposed at a macroscopic scale, yet function largely in the same way [7, 8]. A unique multiphase material system is developed and investigated here. Experimental results characterizing the mechanical response of surfaces designed with coatings of uniform micro-pillar geometry, each comprised of a rhenium core surrounded by a tungsten shell, will be discussed here. The composite nature of micro architected surfaces, coupled with the mechanical strength and ductility furnished by small feature size, make these material concepts suitable for shielding the underlying structure from the effects of severe plasma transients. The experimental effort presented in this article will aim to show that the plastic distortion induced by thermal loading of micro architected surfaces is mitigated relative their planar counterpart.

The objective of this work is to develop plasma-resilient, micro-engineered, refractory metal armor (coating) to resist thermal shock and harmful thermal residual stresses during severe plasma transients. The focus is on manifestations of thermomechanical damage in the form of surface fracture and residual plastic stresses, recognizing that other factors may have to be taken into account, such as vacuum compatibility, erosion, and fuel retention, when these materials are to be used in practice.

Micro-Engineered Material Fabrication

Textured and foam-type plasma-resilient materials are fabricated by the Chemical Vapor Deposition (CVD) process at Ultramet, Inc. Purity levels in excess of 99.99% are achievable. In addition, the CVD process exhibits the greatest throwing power, or ability to uniformly deposit materials onto/into intricately shaped or textured substrates, thus allowing fabrication of near-net shape parts with geometries that cannot be produced through conventional processing and machining. Metal deposits are formed on the substrate at the molecular level, while the gaseous reaction byproducts are exhausted from the system. The typical deposition rate for metals is 0.1 in/hr. The CVD tungsten is deposited at just 550 °C through

the hydrogen reduction of its hexafluoride under vacuum, flowed over a heated substrate. Deposition of other refractory metals such as molybdenum and rhenium is similarly performed through the thermal decomposition and reduction of metal halides.

An example of a dendritic/pillar-like coating can be seen in Figure 2. The height of the pillars generally extends 15-30 μm from the base and can range in diameter from 2 - 5 μm . They are fabricated through a chemical vapor deposition process in which rhenium dendrites are first formed on the surface of a given substrate (tungsten in the case seen here), and subsequently given a thin protective layer of W on the order of 0.3 - 1 μm thick. The combination of materials (Re and W) provides these geometric features with a composite structure and thus their stress response during thermal loading will differ relative to that seen in traditional planar surfaces. The differing stress response can be further attributed to the small scale of the geometry. Designing structures at the micron and nano scales have been shown to induce the well-known “size effect” in which traditionally brittle materials can sustain large amounts of plastic strain without fracture [9, 10, 11]. Micro architected coatings harness the superior mechanical properties afforded by the size effect into the design scheme, this results in a heat shield, which benefits from both the freedom of expansion provided by independently moving micro-features as well as a betterment of inherent mechanical strength common to micron and submicron scale structures. Additionally the selection of tungsten and rhenium to form the basis for the micro composite structure allows for significant inter-diffusion between the two metals at elevated temperature [12], effectively alleviating any detrimental interfacial stresses which may lead to premature failure. While the current research will show the superior performance of thin layers of micro- engineered surfaces in response to plasma transients, it may be feasible in the future to develop a thick structure composed of many layers that have the same micro-engineered features.

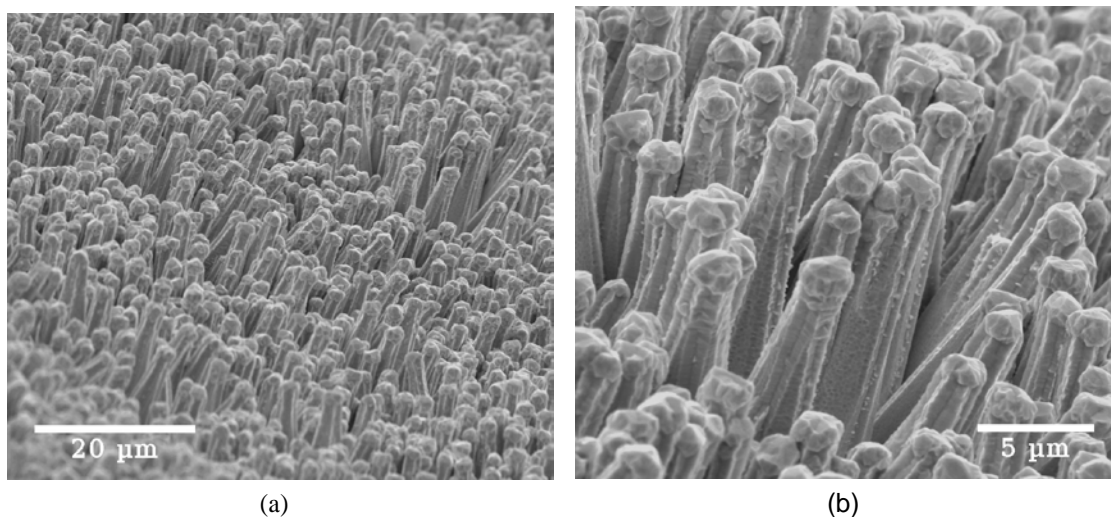


Figure 2: Example of a micro-engineered armor surface consisting of densely packed W-coated Re pillars.

High Heat Flux Experimental Setup

In order to test the response of micro architected surfaces under a thermal load, two W substrates were coated with a dendritic surface consisting of Re pillars covered with a thin layer of W. SEM images of these coatings, fabricated by Ultramet Inc., are shown in Figure 2. The samples were then exposed to a cyclic thermal loading, using a high heat flux testing apparatus, designed at UCLA and described in reference [11]. The specimens, given internal identifiers of PW60 4 and PW60 5, are shown in their pristine (unexposed) condition in Figure 3. The approach here is to show the possibility of micro engineering surfaces to mitigate plasma damage. Once this is proven, other material combinations and engineered armor can be developed to enhance functional performance in other areas (e.g. neutron radioactivity,

vacuum and tritium retention, fuzz formation, blistering, and sputtering erosion.

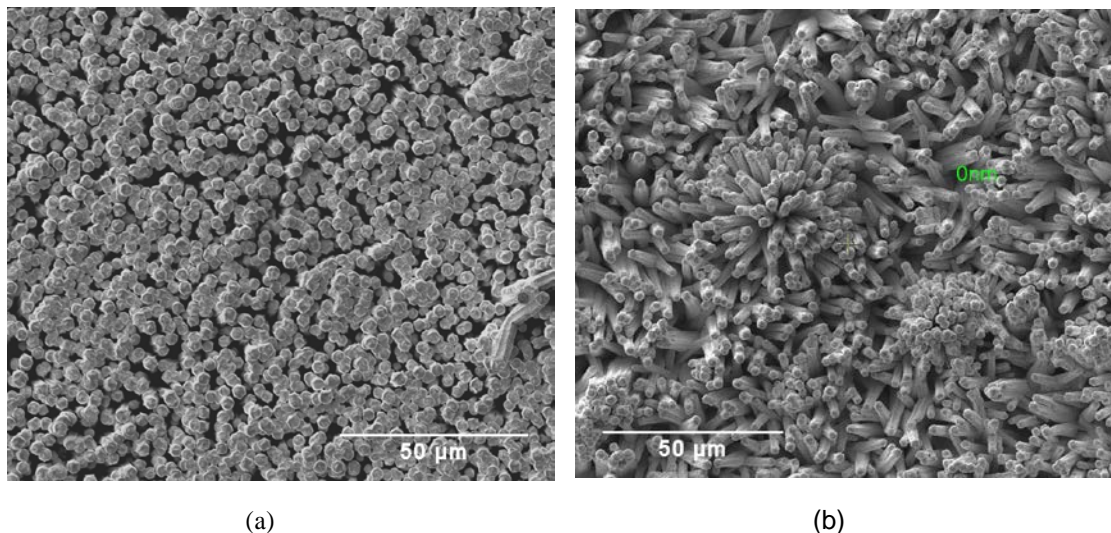


Figure 3: Un-exposed microarchitected samples of the dendritic variety, both consisting of Re dendrites coated with W (a) PW60 4. Note the oriented nature of the pillars grown normal to the surface, (b) PW60 5, pillars appears to be grown in a more random nature as compared to PW60 4.

Thermomechanical Plasma Testing Facility

The High Energy Flux Testing facility (HEFTY), designed and built at UCLA, provides for the ability to study thermomechanical damage using a commercial arc-jet plasma gun (Praxair SG-100). In order to study the effects of long duration plasma transients ($> 10 \text{ MW/m}^2$), samples that are thermally exposed in the system are simultaneously water cooled via a specially designed flange onto which they are mechanically fastened during the course of a test. The cooling circuit is a closed loop, where traditional calorimetry methods can be used to calibrate the magnitude of the heat flux received by the sample. The heat flux provided by the gun was measured with a heat flux sensor, and calibrated through calorimetry, was determined to be in the range $13 - 16 \text{ MW/m}^2$ at a 2.54 cm distance from the gun nozzle, as seen in Figure 4.

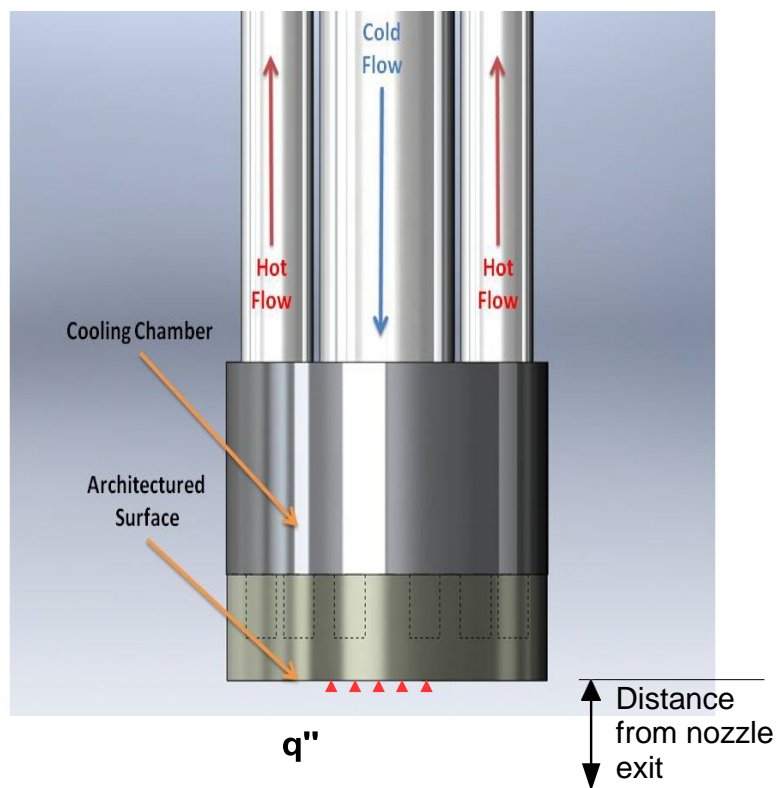


Figure 4: Schematic of the experimental set-up during plasma exposure. A sample was placed a distance of 2.54 cm from the gun nozzle, and the heat flux at this distance was measured as 14.5 ± 1.5 MW/m².

The energy flux impinging upon a sample can be controlled by simply modifying the distance between the sample face and the gun nozzle exit, as seen in Figure 4. In this manner, a range of damage modes caused by different heat flux values can be studied. In addition, the high cooling rates afforded by water jet impingement allow the investigation of damage effects caused by long duration plasma transients (e.g. recrystallization, dislocation reorganization, grain growth etc.). The HEFTY facility can be used for studies of thermal shock [13, 14, 15], thermomechanical fatigue, and fatigue-creep interactions. The system is controlled via a LabView program, thus allowing controlled pulsed operation capabilities. An image of a sample being exposed in the HEFTY facility is shown in Figure 5(a). Before exposure, the chamber is pumped down to low vacuum levels and back-filled with argon gas to mitigate oxidation of the tungsten surface at high temperature. The samples themselves are mechanically attached to a specialized cooling flange via a series of bolts. An illustration of the sample geometry used in the experimental setup reported here can be seen in Figure 5(b). The samples are typically 5.08 cm in diameter and 1.5 mm thick. Large compressive stresses are generated upon pulsing as a result of the sample thermal exposure area being smaller than the sample size itself, as seen in Figure 5(b). The generated large compressive radial stress, the magnitude of which can be controlled by cooling, is the driving force for quantitative thermomechanical damage that is presented in this work.

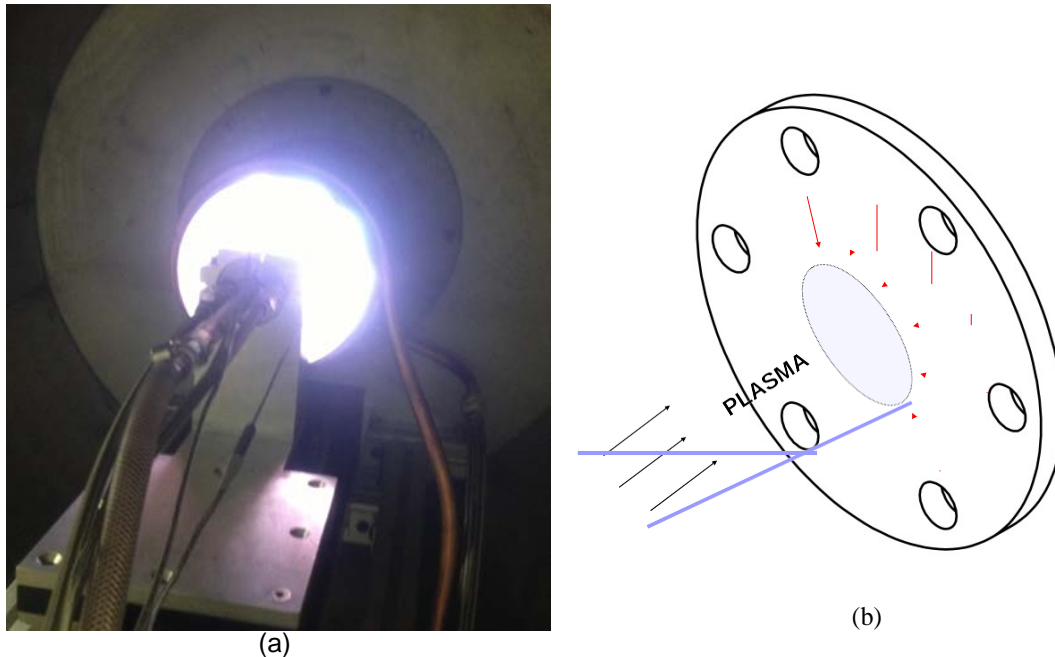


Figure 5: (a) Demonstration of the plasma arc-jet firing onto a tungsten sample, (b) A sample being exposed to a plasma column in HEFTY. Note the holes on the perimeter of the sample are used to fasten the specimen onto a specialized flange so as to provide for active cooling. The exposed area on the sample is smaller than the overall sample size, which leads to the build-up of large compressive thermal stresses.

Heat Flux Measurement

Heat flux measurement techniques include differential temperature sensors (e.g. thermopiles, layered resistance temperature devices or thermocouples), calorimetric methods involving a heat balance analysis, energy supply or removal methods (e.g. using a heater to generate a thermal balance), and indirectly through measurement of mass transfer that can be correlated with heat transfer [16]. Each of these methods has a specific design and application. In our experimental setup, we determine the heat flux on the sample surface by two independent techniques. The first is a calorimetric method, where the temperature rise of the cooling water stream is measured during a fixed number of thermal cycles. Measurement of the temperature rise, together with the water flow rate, results in determination of an average value of the heat flux by conserving thermal power on the sample. The input-heating rate from the plasma arc-jet is balanced by the absorbed energy in the water stream. The second method is based on the development of a heat flux sensor, shown in Figure 6(b), and using it in an *inverse problem* of determining an unknown heat flux from transient temperature measurements. The developed sensor is a variant of a null-point calorimeter, and is comprised of a copper cone with a small bore hole drilled through the back. The hole stops just short of penetrating through the length of the cone, and leaves a thin section between the exposed tip and the attached thermocouple, as seen in Figure 6(a). This set-up allows for the transient temperature signal to be compared with Finite Element Analysis (FEA) data, so as to match the incident plasma heat flux. The simulated temperature signal is generated by importing the sensor geometry to a commercial FEA solver (COMSOL), and applying an estimated heat flux value to the tip of the cone where the heat flux is impinging. The inverse problem is solved iteratively, where various values of the heat flux are assumed to be constant within the 6 s period of a single pulse, and the FEA simulated signal is matched with the measured temperature transient signal. Figure 6(b) presents a picture of the fabricated sensor prior to a test. The two methods of measurements (water calorimetric, and transient temperature matching) have produced results within 10%. When the plasma gun nozzle distance is 2.54 cm from the sample surface, the measured heat flux is $14.5 \pm 1.5 \text{ MW/m}^2$.

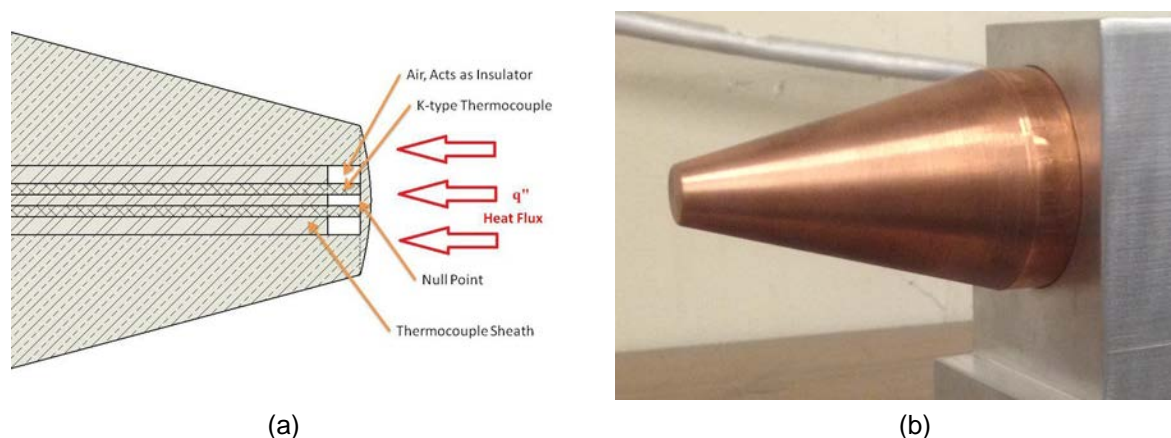


Figure 6: Heat flux sensor used for heat flux determination. (a) The principle of operation relies on matching a transient temperature signal to FEA simulations. The thermocouple is attached to the back of the exposed sensor tip. (b) Fabricated sensor prior to testing.

Characterization of Surface Damage

A series of plasma exposure tests were performed on uncoated and coated samples in order to examine the nature of thermomechanical damage, and relate it to the surface architecture. In both cases of smooth sample surfaces and micro-engineered surfaces, the cooling rate of the sample is varied. When the samples are uncooled and are subjected to a limited number of plasma pulses, extensive damage is generally observed. On the other hand, by varying the water flow rate, the rate of heat removal from the back of the samples can be adjusted, and the sample stress state can thus be controlled. We will first discuss the results of plasma exposure of micro-engineered samples, followed by observations of thermomechanical damage of smooth uncoated samples.

The pillar architecture of the coated surfaces of samples PW60 4 and PW60 5 is comprised of a rhenium core that has a hexagonal cross-section, and is coated by a thin layer of tungsten. Typical measured dimensions of the pillar are as follows: Re core diameter at the base = $5 \mu\text{m}$, at the tip = $3 \mu\text{m}$, pillar height = $20 \mu\text{m}$, W coating thickness = $0.3 \mu\text{m}$, pillar areal surface density = $8 \times 10^{10} \text{ m}^{-2}$. Samples PW60 4 and PW60 5 were subjected to a total of 200 and 250 plasma pulses, respectively ($\Gamma = 14.5 \pm 1.5 \text{ MW/m}^2$). Each pulse had 10-s duration ($t_{\text{on}} = 6 \text{ s}$, $t_{\text{off}} = 4 \text{ s}$). The specimens were characterized using scanning electron microscopy (SEM) and X-ray diffraction (XRD) techniques at 50 pulse intervals. Broadening of the full width at half-max (FWHM) and the shift in the X-ray diffraction peaks are correlated with SEM observations of surface damage. The FWHM was used as a measure of plastic distortion induced by thermal loading. XRD was also employed to investigate the texturing of the coatings prior to exposure and account for recrystallization induced by the high surface temperatures during testing. The initial XRD pattern for both PW60 4 and PW60 5 can be seen in Figure 7. The absence of the (211) peak in PW60 4 is an indication of a larger degree of texturing in the sample relative to the PW60 5 sample. This can be further confirmed by SEM examinations, as shown in Figure 4, where the more random nature of pillars is observed in the PW60 5 sample.

Observations of Surface Fracture

Micro-engineered Samples

Following the initial 50 thermal plasma cycles, sample PW60 4 exhibited light cracking along many of its constituent micropillars, as shown in figure 8. This cracking pattern can be explained by considering the source of stress evolution during plasma cycles in the micro-pillars. The cross-section of an individual

pillar can be seen in figure 9, which reveals the composite-like nature of the micro-pillar. The Re core of the pillar is coated by a thin W layer (0.2-0.5 μm) on the outside. During the heating phase of the plasma pulse, the Re core expands against the W coating, which effectively acts as a casing for the Re dendrite. Considering that the thermal expansion coefficient of Re ($9.1 \times 10^{-6} \text{ K}^{-1}$) is almost twice as large as that of W ($4.3 \times 10^{-6} \text{ K}^{-1}$), the expansion/contraction of Re during thermal cycling will put the W coating under tension/compression, respectively. The tensile stress in the W coating can be shown to be sufficient to cause plastic flow during thermal loading, and depending on the thickness of the coating (W) can lead to either compressive or tensile states of residual stress. This finding is used to design pillars that are more resistant to thermal fracture by appropriate selection of the pillar geometry.

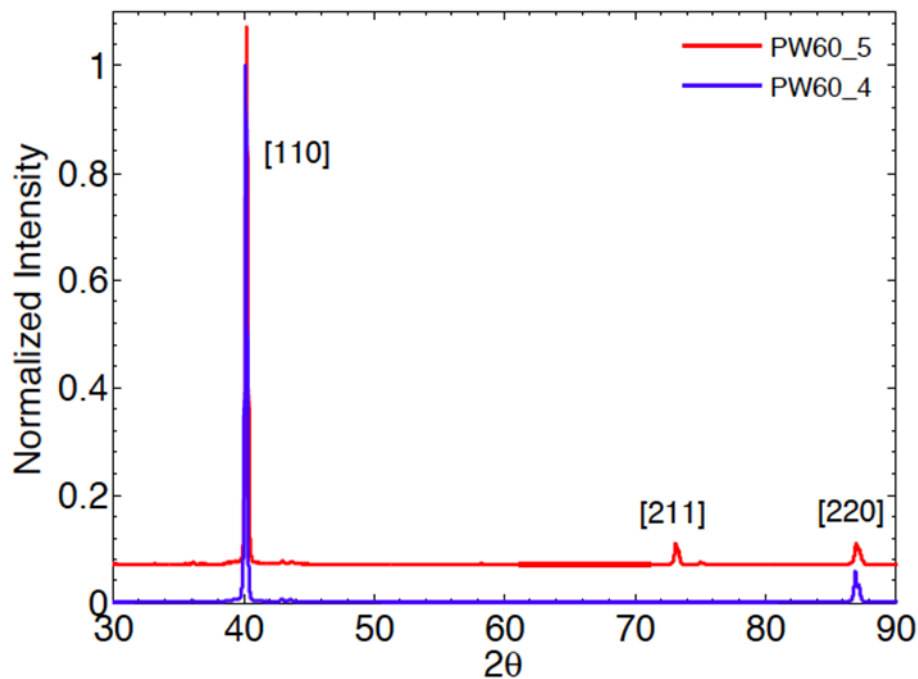
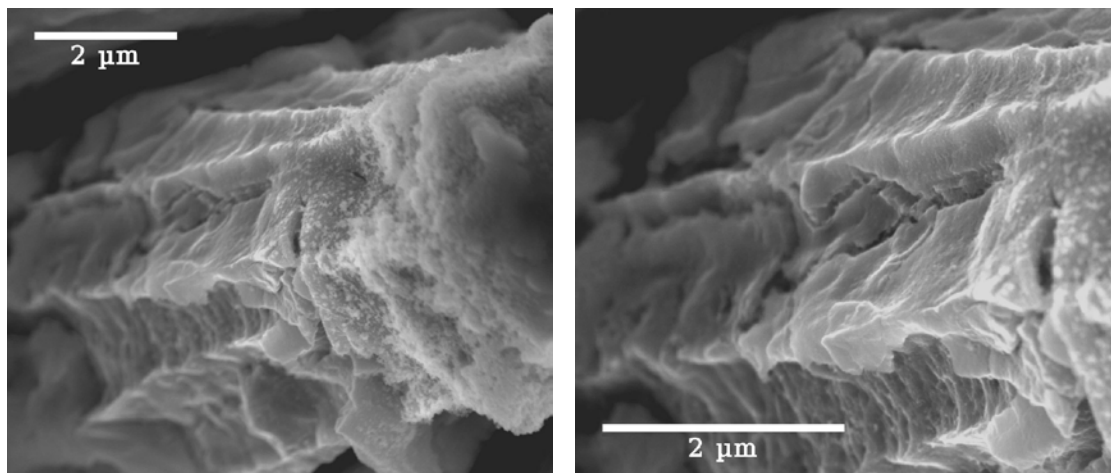


Figure 7: Comparison of W over Re microarchitected specimens, both diffraction patterns represent two samples in pristine condition, note the large degree of texturing present, strong preferred orientation in the $\langle 110 \rangle$ direction, substrate thickness is 0.060 in (1.5 mm), the increased degree of texturing seen in PW60 4 is apparent from the missing (211) peak relative to PW60 5.



(a)

(b)

Figure 8: W coated Re pillar showing light cracking along its facets.

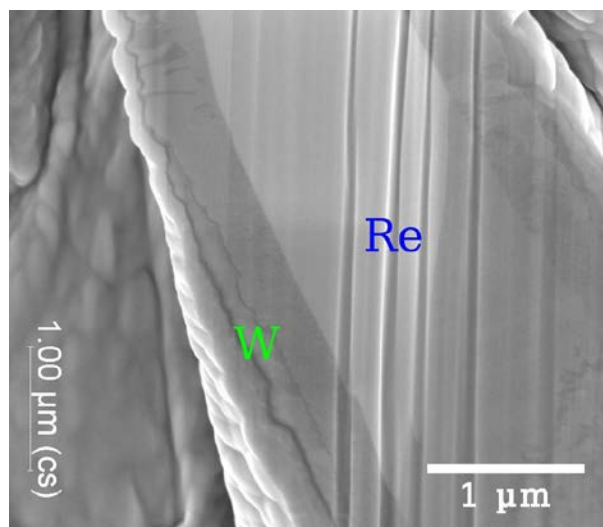


Figure 9: Cross-section of a W coated Re pillar.

Smooth Planar Samples

Before turning the attention to a description of thermomechanical damage in smooth, planar samples, we point out the importance of controlling the sample-cooling rate. Adjustments in the cooling rate provide an opportunity to study distinct damage modes, manifest as either fracture, plastic deformation, or a combination of both. High cooling rates lead to a controlled temperature rise in the sample, thus allowing control over residual thermal stresses. On the other hand, when cooling is totally shut off, the sudden rise of sample temperature leads to thermal shock type fracture.

Experiments on planar tungsten samples under high cooling and long duration plasma transients ($t_{\text{on}}=6$ s, $t_{\text{off}}=4$ s) have shown that the samples begin to recrystallize after roughly 1100 cycles of $\Gamma=14.5$ 1.5

MW/m^2 . The appearance of recrystallization leads to the generation of micro-cracks on the specimen surface [11]. X-ray diffraction (XRD) measurements of pre-exposure and post-exposure planer tungsten can be seen in Figure 10. The presence of freshly nucleated grains is evident from the emergence of previously absent diffraction peaks before plasma exposure. Recrystallization is known to have deleterious effects on the fracture toughness of tungsten [17], and results in surface micro-cracks.

To study thermal shock response, samples with smooth planar surfaces were suddenly exposed to several plasma pulses without any active cooling of the sample, and surface fracture was observed. Large residual tensile stresses, generated upon sample cool-down, cause specimen fracture in the central exposed area. Radial confinement of the hot exposed central region of the sample by the cooler surrounding material, as illustrated in Figure 5(b), is the primary reason of observed thermal shock fracture. The combination of large compressive stress seen by the exposed area of the sample and the reduced flow stress of tungsten at elevated temperature (only 290 MPa at 727 °C for polycrystalline tungsten) results in significant residual tensile stresses at the exposed region of the specimen upon cool-down. The effective outcome of this sequence of events is a complex surface fracture pattern of the sample, as shown in Figure 11(a). SEM images of a sample tested without active cooling is shown in Figure 11(b), where fracture is clearly seen spanning the surface of the specimen.

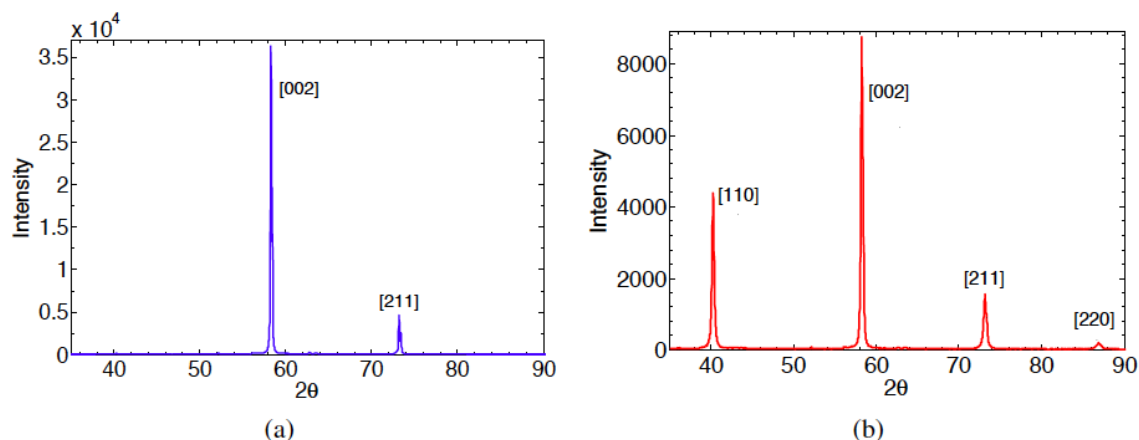


Figure 10: Recrystallization in planar tungsten exposed to long duration plasma transients (a) unexposed XRD spectrum, (b) exposed XRD spectrum showing the emergence of new diffraction peaks (110) and (220) caused by the nucleation of stress free grain.

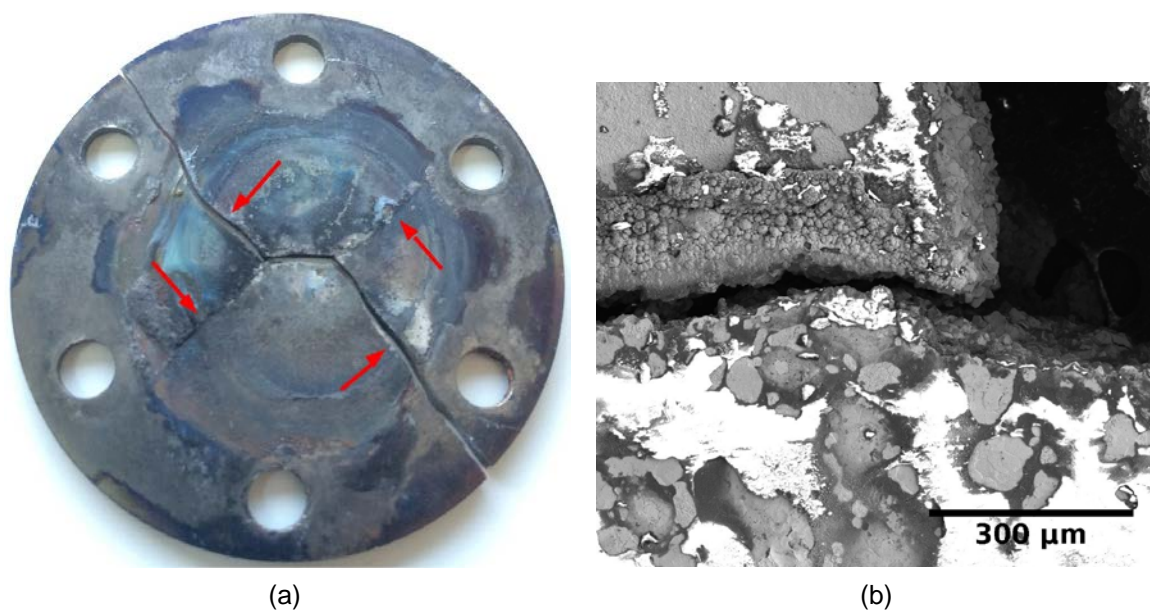


Figure 11: Surface crack pattern in the smooth planar W sample exposed to a 16 MW/m^2 heat flux (not cooled),

In Figure 11(a) cracks were initiated at the sample center and spanned the diameter of the sample splitting the specimen in two pieces of roughly equal size, cracks are indicated by the red arrows, (b) SEM image of the crack pattern showing possible melting of the surface as indicated by the splat pattern near the crack opening.

A remarkable aspect of thermomechanical fracture in W is the dual nature of its response, being either brittle or ductile, depending on the local temperature at any given region. When the fracture surface is more closely examined, it is interesting to note that the central exposed region of the specimen fails by ductile tearing, while the sample periphery fractures in a completely brittle manner. This is evidenced by a dimpled fracture surface, shown in Figure 12(a). The periphery regions of the sample, which are unexposed to the incoming plasma fail in a brittle manner. This can be observed by reference to Figure 12(b), which shows the relatively flat cleavage planes of the fracture surface. The transition from ductile tearing to brittle fracture within one sample is attributable to the radial temperature gradient in the sample as a result of plasma heating being supplied only to the central region. The appearance of both ductile and brittle failure modes in the same specimen presents an opportunity for further studies of the Ductile-to-Brittle-Transition (DBTT) phenomenon in W under thermomechanical conditions.

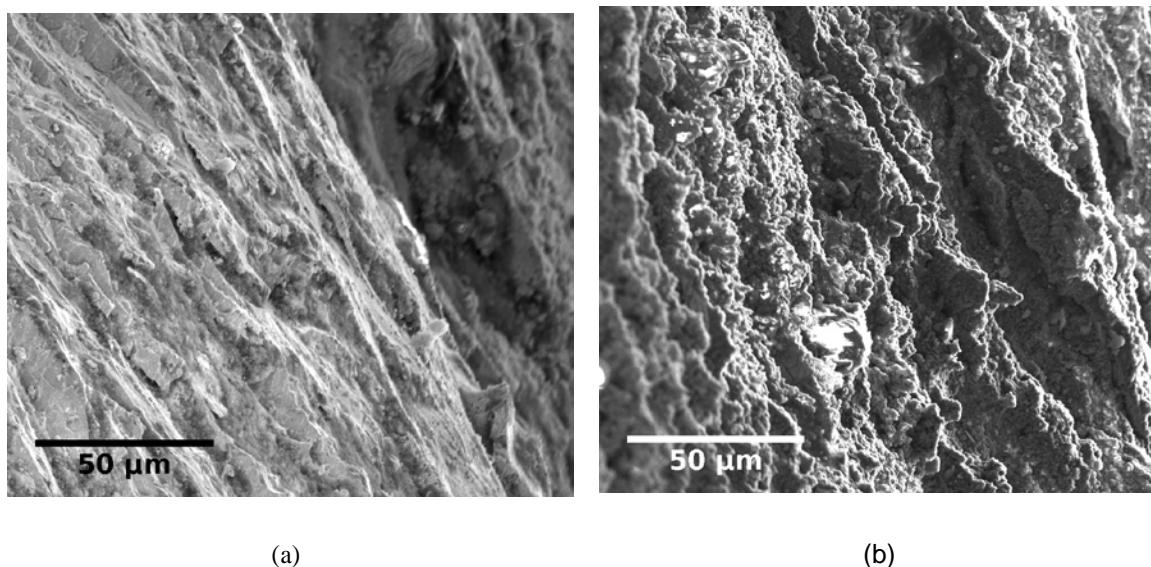


Figure 12: The fracture surface of a smooth planar specimen tested without active cooling. (a) Dimpled ductile failure at the exposed region of the sample, where temperatures are highest, (b) Brittle failure at the periphery of the sample, which is not exposed to the incoming plasma source.

The observed thermomechanical damage mode can range from fracture at low cooling conditions to controlled plastic deformation when samples are vigorously cooled. Under conditions with no active cooling, excessive thermal stresses coupled with a low flow stress at elevated temperature lead to thermal shock fracture. Nevertheless, this type of fracture is not entirely of a brittle manner, but shows a transition from a ductile tearing mode in regions where the plasma deposits its energy to a classical brittle mode in sample zones that are not in contact with the plasma source. However, when the temperature is controlled via active cooling, thermal stresses are correspondingly reduced, causing only plastic deformation without initiation of fracture. This is further confirmed through X-ray diffraction studies of residual stresses, as presented next in subsection 4.2. Plastic deformation is indeed evident in highly cooled samples, yet fracture is avoided or largely mitigated in comparison with non-cooled specimens.

X-Ray Diffraction Analysis of Residual Plastic Strain

Residual plastic strain can be qualitatively, and in some cases quantitatively measured with the X-ray diffraction (XRD) technique [18, 19, 20, 21]. The fundamental basis of the method is Bragg's law of diffraction: $n\lambda = 2d\sin\theta$, where λ is a fixed X-ray wavelength, d the interatomic spacing, and θ the diffraction angle. Measurements of the diffracted radiation intensity give an XRD spectrum, where peaks in a stress-free condition are associated with specific crystal planes for single crystals. A shift in the peak intensity to larger diffraction angles is correlated with a decrease in the interatomic spacing, d . During plastic deformation, dislocation motion on glide planes results in local lattice rotations and curvature, while the displacement field emanating from dislocation cores expands or contracts nearby interatomic spacing. The first effect (lattice rotation and curvature) is manifest in broadening of the XRD signal, while the second (dilatation/contraction) appears as a shift in the diffraction angle. Since the measurement is basically a surface method, the normal stress is zero and one has a condition of plane stress on the surface. The in-plane stress at an angle ϕ from a predetermined principal direction on the surface (σ_ϕ) is obtained from a set of measurements of the inter-planar spacing, d_ψ , and d_n at angles ψ to the surface normal and perpendicular to the surface, respectively. The residual stress is then given by:

$$\sigma_\phi = \frac{E}{(1+\nu)\sin^2\psi} \left(\frac{d_\psi - d_n}{d_n} \right)$$

The XRD intensity signal is fitted to a curve, where both the peak angle and the full signal width at half maximum (FWHM) are obtained. Both FWHM and the shift angle can be used to analyze the state of plastic deformation near the surface. Although peak-broadening data can give information regarding the amount of plastic strain, it is not ideal for the quantitative determination of the residual stress, in particular in cases when the grain size exceeds 100 nm [19, 22]. In such cases it is best to resort to alternative XRD tools; one particular analytical technique is the $\sin^2(\psi)$ method [18, 19].

This later quantity is obtained as the slope of a line relationship between the lattice parameter and $\sin^2(\psi)$. By plotting a series of lattice parameter values from XRD profiles over a range of tilt angles ψ , a linear relationship can be established between the lattice parameter d and $\sin^2(\psi)$, from which the slope $\frac{\partial d}{\partial \sin^2(\psi)}$ can be quickly determined. Finding values of lattice parameters d for each angle of tilt ψ makes use of the fact the position of the diffraction peak will shift if elastic strain is present in the material.

In order to study the effects of repeated plasma pulsing on the plastic deformation of tungsten at high temperature, a smooth planar W sample was exposed to 1100 cycles with $\Gamma=25 \text{ MW/m}^2$, $t_{\text{on}}=4 \text{ s}$, $t_{\text{off}}=6 \text{ s}$, resulting in a total surface energy density of 110 GJ/m^2 (3 kWh). The sample was actively cooled during this experiment. Broadening of the (200) peak after plasma exposure is clearly shown in figure 13. Because the high surface temperature results in recrystallization and recovery of the material, peak broadening is a qualitative measure of the dislocation density, and hence residual plastic strain near the surface layer.

To determine the *relative* change in the residual surface stress when the material is micro-engineered to have a pillar architecture coating, X-Ray Diffraction (XRD) profiles of specimens PW60 4 and PW60 5 were examined. XRD spectra of micro-engineered samples were contrasted with those of planar W specimens subjected to a similar plasma exposure. Since the FWHM can be regarded as a qualitative measure of the degree of plastic deformation present in the surface, the FWHM of the (110) peak for all specimens was recorded after every 50 cycles, and plotted against the absorbed energy density (GJ/m^2). The results of the comparison are displayed in figure 14. The plot reveals a marked reduction in the plastic strain in the micro-engineered material relative to that of planar W. The rate of FWHM increase (slope) with absorbed plasma thermal energy is reduced by almost a factor of 4 for micro-engineered samples as compared to smooth planar samples.

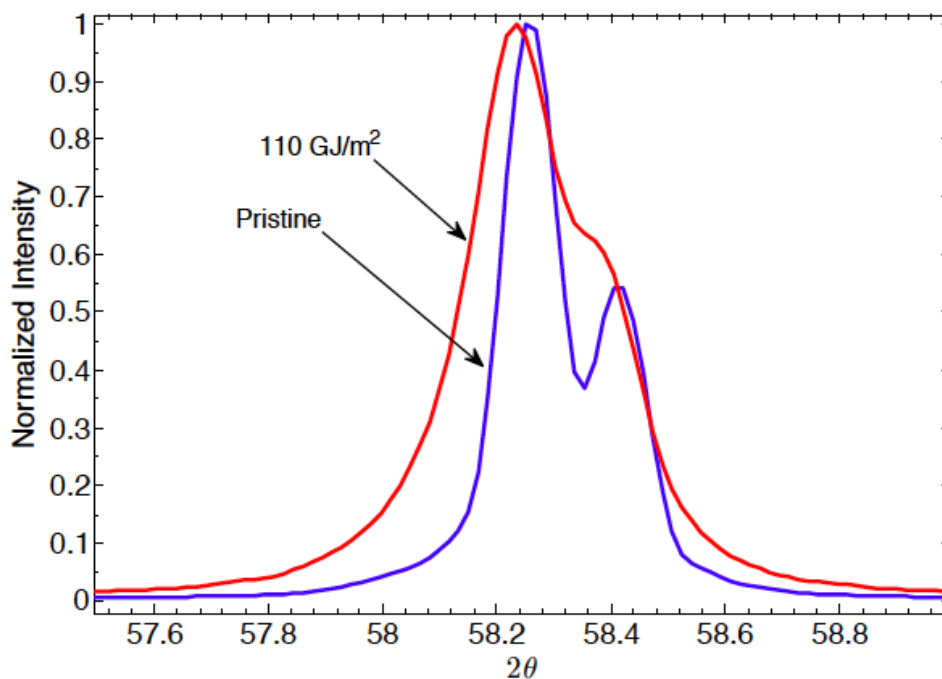


Figure 13: (200) peak FWHM before and after plasma exposure. Peak broadening is observed as a function of repeated plasma exposure, and is a qualitative measure of residual plastic strain.

Following the comparison of residual plastic strain between planar and micro-engineered samples, we further investigate changes in the surface stress in micro-engineered samples. The (110)-diffraction peaks for specimens PW60 5 and PW60 4 are plotted in Figures 15(a) and 15(b), respectively. The shift in the peaks, shown in Figures 16(a) and 16(b), after the initial 50 pulse exposure, is clearly noted in both samples. We note that in the PW60 5 sample, the peak shifts towards smaller Bragg angles, indicating a tensile stress, while the PW60 4 (110) peak moves towards larger Bragg angles, consistent with a residual compressive stress. This difference in the nature of the residual stress is attributed to pillar geometry, where the Re core size and the W coating thickness determine the stress state following plastic deformation. Thinner W coatings on the Re core will tend to remain in a state of compressive surface stress, while the thicker variants result in a tensile surface stress.

The XRD peaks move back towards their initial position with increasing plasma exposure, indicating that the dislocation microstructure in the W coating is annealed, gradually relieving the plastic strain built up during the first set of plasma pulses (see Figures 16(a) and 16(b)). This behavior is a consequence of the competition between plastic hardening during deformation and a simultaneous annealing or annihilation of dislocation density at elevated temperatures. The more gradual relaxation of PW60 5 towards its initial Bragg angle as well as its increased peak broadening relative to PW60 4 (as seen in Figure 14) is thought to be due to the highly oriented nature of sample PW60 4. The majority of the plastic strain is concentrated along the length of dendrites, because the X-ray beam generating the diffraction pattern is primarily striking the top or caps of the pillars. Thus, the plastic strain in PW60 4 may be reduced relative to PW60 5, where an increased portion of the signal is generated from locations along the length of the pillars where strain is expected to be greatest.

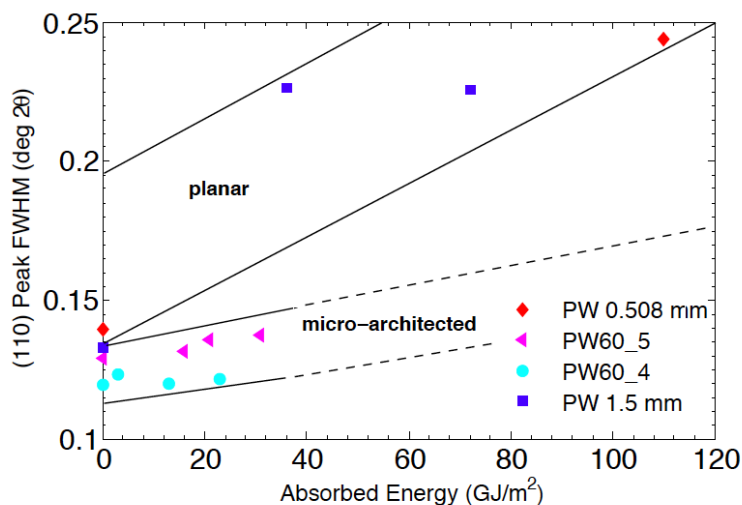


Figure 14: Dependence of the FWHM of the (110) peak on absorbed energy density. Note the tendency of the micro-architected material PW60 4 and PW60 5 to retain smaller plastic strain as compared to the planar counterpart.

0.508 and 1.5 are the respective thicknesses (mm) of planar samples tested in HEFTY (PW).

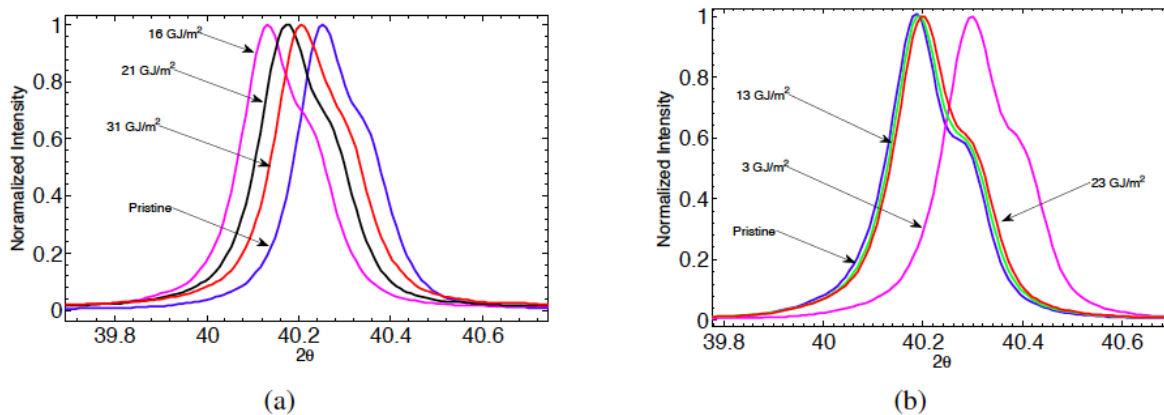


Figure 15: XRD spectra before and after plasma exposures. (a) Sample PW60 5, residual tensile stress, dendrites were $2.1 \mu\text{m}$ at the tip and showed significant tapering/increase in diameter towards the base, (b) PW60 4 residual compressive stress, dendrites were $3.6 \mu\text{m}$ in diameter at the tip and showed limited tapering relative to PW60 5.

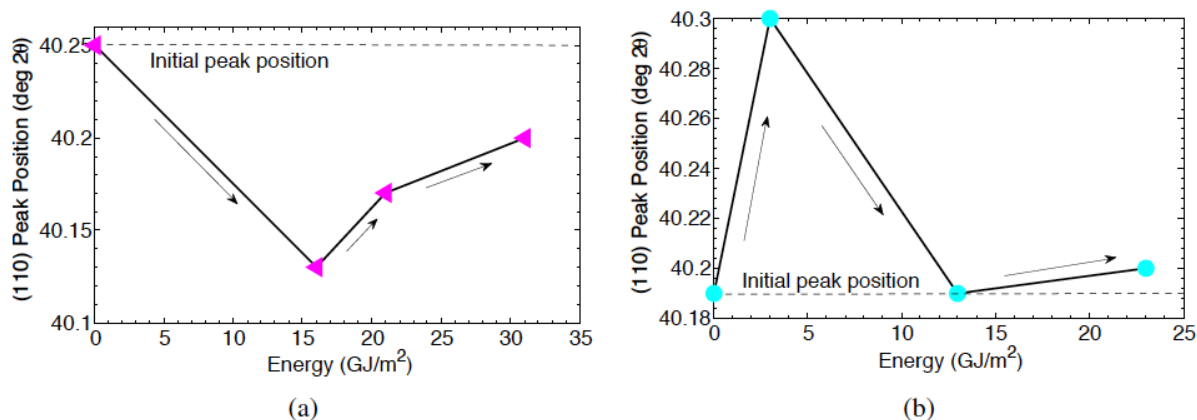


Figure 16: XRD (110) peak position as function of absorbed plasma energy density. (a) Sample PW60 5, initially the peak shifts to lower Bragg angles indicating a tensile residual stress. Residual stress relaxation is evident upon repeated exposure, as the Bragg angle begins to move back toward its initial position, dendrites were $2.1 \mu\text{m}$ at the tip and showed significant tapering/increase in diameter towards the base, (b) Peak shift in sample PW60 4 indicating a residual compressive stress. Dendrites were $3.6 \mu\text{m}$ in diameter at the tip and showed limited tapering relative to PW60 5.

The residual stress state of both planar and micro architected surfaces was examined through the use of the $\sin^2(\psi)$ technique, both before and after thermal pulsing (with active cooling). The results show that the initial residual stress state for highly polished flat tungsten samples is compressive, and on the order of 1.3 GPa. The compressive surface stress is attributed to the effect of surface polishing before plasma exposure. After 50 plasma cycles, the stresses relax to a compressive value of 1.0 GPa, representing a stress relaxation of 300 MPa. In contrast, micro-engineered materials (sample PW60 6) exposed to the same thermal cycling environment show that the initial residual stress state for the surface is compressive at 250 MPa, and remains largely unchanged after plasma exposure. For reference, tungsten powder was analyzed using the same methodology, and showed a tensile stress value of 300 MPa. This comparison is evidence of the essentially stress-free state of the micro-engineered surface after plasma exposure. This particular sample (PW60 6) was highly tapered, with an average tip diameter of $1 \mu\text{m}$. In some cases, the base of the pillars widened to nearly $5 \mu\text{m}$, and does not show strong preferred orientation, as can be observed in Figure 17.

The largely stress-free condition of the micro-engineered material relative to its planar counterpart allows the plasma-exposed surface to sustain large thermal loads without catastrophic failure. Two factors aid the surface in sustaining thermomechanically-induced stresses without failure. First, the strain tolerant nature of the structure itself gives the top layer the ability to freely expand and contract as depicted in the figure, without damaging thermal strains. This is similar to what has been achieved in the design of Thermal Barrier Coatings (TBC) that was successfully introduced for thermal protection of jet engine turbine blades. Second, the fundamentally ductile nature of the tungsten - rhenium alloy system results in a greater degree of plastic flow accommodation. As is well documented, W-Re alloys are among the most favorable materials for high temperature applications, as they possess a desirable combination of high flow stress at elevated temperature in addition to good ductility, even at room temperature [23].

The reduction in residual stress seen in micro-engineered surfaces can in part be attributed to the highly ductile nature of the W-Re alloy system. Micro-pillars comprising a micro-engineered surface are composite structures consisting of a Re core and a thin W coating. However, due to the high inter-diffusivity of W and Re [12], this initial composite structure will quickly lose the sharp interfaces between

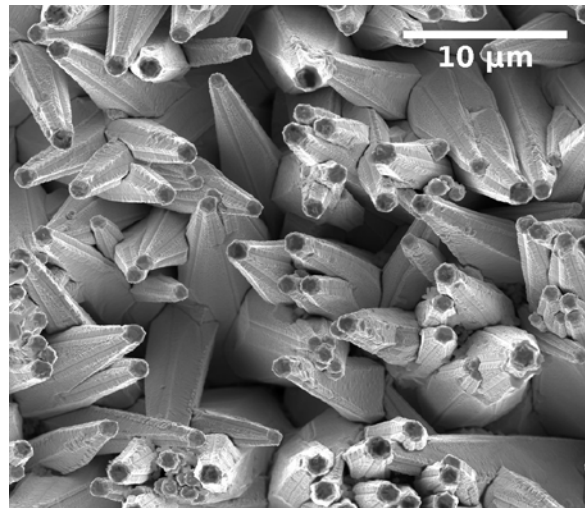


Figure 17: SEM image of sample PW60 6. Measured residual stress before and after plasma exposure remained largely unchanged at a compressive value of 250 MPa. The exposure parameters were 50 cycles at $\Gamma=16\text{MW/m}^2$, $t_{\text{on}}=6\text{ s}$, $t_{\text{off}}=4\text{ s}$.

W and Re, and form a more diffuse bond between the two metals. Since the pillars making up the micro-engineered surface are of such small dimensions (only $5\text{ }\mu\text{m}$ in diameter with the W overcoat being $0.5\text{ }\mu\text{m}$ in thickness), they will inter-diffuse forming a graded W-Re alloy. This effect has the benefit of quickly alleviating any stresses in the composite, which arise from sharp changes in the coefficient of thermal expansion. Effectively, the composite relaxes the thermal stresses after the first several minutes of operation to come to an equilibrium configuration consisting of a ductile refractory metal alloy.

Conclusions

The potential for development of materials systems with tailorable properties has been a point of interest in materials science for many years [24, 25]. Through modifications in surface geometry, it has been shown that materials can be made to move beyond their apparent intrinsic limitations and produce structures with improved mechanical properties, such as increased ductility and strength. Surfaces with micro-engineered architecture are effective in reducing plastic strain in situations of extreme thermal loading due to plasma exposure.

Micro-engineered surfaces have been shown in this work to be more resistant to plastic deformation in plasma facing materials. This behavior was observed through the analysis of XRD peak broadening data, which demonstrated reduced levels of plastic strain for micro-engineered surfaces relative to their planar counterparts. The reduction in plastic deformation is further confirmed by residual stress determination via the $\sin^2(\psi)$ method. Analysis using this technique shows that residual stresses in micro-engineered surfaces are largely absent after thermal plasma cycling, whilst planar surfaces exposed to the same test conditions retain residual stresses of up to 1.0 GPa in magnitude. The reduction in residual stress is a direct result of the strain tolerant nature of the micro-engineered surface, which allows free expansion of the geometric features comprising the surface. Additionally, the strong tendency for inter-diffusion between W and Re allows the microstructure to quickly relax any stresses associated with coefficient of thermal expansion mismatch at the interface of the two metals. The inter-diffusion between W and Re at elevated temperature gradually transitions the micro-pillars comprising the surface from a composite-like structure with sharp interfaces between constituent parts (W and Re)

to an increasingly homogeneous distribution of material, effectively forming an alloy. The inherently favorable nature of W-Re alloys for high temperature applications provides the micro-engineered surface with a ductile characteristic, a necessary condition for damage resistance under pulsed high heat flux conditions. Pillar geometry is shown to play a key role in the performance of the micro-engineered surface. When the Re core diameter is large relative to the W shell thickness, cracking can ensue along the height of the structure as tensile hoop stresses are easily generated from the thermal expansion mismatch between W and Re. To prevent fracture of the pillars, the W shell thickness must be sufficient to resist the expansion of the Re core, resulting in a compressive residual stress in the W shell.

Acknowledgements

This work, which is a reproduction of an article published in the Journal of Nuclear Materials, is partially supported by the Air Force Office of Scientific Research (AFOSR), Award No: FA9550-16-1-0444 with UCLA, and by the US Department of Energy, Award Number DE- FG02-03ER54708 with UCLA. The technical assistance of Phil Chiu, Nick Tarasi, and Dan Goebel with the HEFTY control system, and that of Chao Li and Professor Mark Goorsky with XRD analysis is greatly appreciated.

References

- [1] S Pestchanyi, I Garkusha, and I Landman. Simulation of residual thermostress in tungsten after repetitive ELM-like heat loads. *Fusion Engineering and Design*, 86(9):1681–1684, 2011.
- [2] S. Sharafat, N.M. Ghoniem, M. Anderson, B. Williams, J. Blanchard, and L. Sneed. Micro-engineered first wall tungsten armor for high average power laser fusion energy systems. *Journal of Nuclear Materials*, 347(3): 217–243, 2005.
- [3] X Liu, L Yang, S Tamura, K Tokunaga, N Yoshida, N Noda, and Z Xu. Thermal response of plasma sprayed tungsten coating to high heat flux. *Fusion engineering and design*, 70(4):341–349, 2004.
- [4] X Liu, S Tamura, K Tokunaga, N Yoshida, N Noda, L Yang, and Z Xu. High heat flux properties of pure tungsten and plasma sprayed tungsten coatings. *Journal of nuclear materials*, 329:687–691, 2004.
- [5] Kazutoshi Tokunaga, Yusuke Kubota, Nobuaki Noda, Yoshio Imamura, Akira Kurumada, Nobuaki Yoshida, Toshiaki Sogabe, Toshiyuki Kato, and Bertram Schedler. Behavior of actively cooled mock-ups with plasma sprayed tungsten coating under high heat flux conditions. *Fusion engineering and design*, 81(1):133–138, 2006.
- [6] Y Yahiro, M Mitsuhara, K Tokunaga, N Yoshida, T Hirai, K Ezato, S Suzuki, M Akiba, and H Nakashima. Characterization of thick plasma spray tungsten coating on ferritic/martensitic steel f82h for high heat flux armor. *Journal of Nuclear Materials*, 386:784–788, 2009.
- [7] A Rene Raffray, Siegfried Malang, and Xueren Wang. Optimizing the overall configuration of a helium-cooled w-alloy divertor for a power plant. *Fusion engineering and design*, 84(7):1553–1557, 2009.
- [8] EA Mogahed and IN Sviatoslavsky. 3d thermo-mechanical analysis of the ITER limiter small scale specimen. In *Fusion Engineering, 1997. 17th IEEE/NPSS Symposium*, volume 1, pages 381–384. IEEE, 1997.
- [9] Ladislav Kubin. *Dislocations, Mesoscale Simulations and Plastic Flow*, volume 5. Oxford University Press, 2013.
- [10] M Pozuelo, YW Chang, and J-M Yang. In-situ microcompression study of nanostructured mg alloy micropillars. *Materials Letters*, 108:320–323, 2013.
- [11] David Rivera, Tamer Crosby, Andrew Sheng, and Nasr M Ghoniem. Characterization of thermomechanical damage on tungsten surfaces during long-duration plasma transients. *Journal of Nuclear Materials*, 455(1):500–506, 2014.

- [12] YF Hua, ZX Li, X Zhang, JH Du, CL Huang, and MH Du. Inter-diffusion analysis of joint interface of tungsten–rhenium couple. *Journal of Nuclear Materials*, 416(3):270–272, 2011.
- [13] G Pintsuk, A Prokhotseva, and Inge Uytendhouwen. Thermal shock characterization of tungsten deformed in two orthogonal directions. *Journal of Nuclear Materials*, 417(1):481–486, 2011.
- [14] Muyuan Li, Mathias Sommerer, Ewald Werner, Stefan Lampenscherf, Thorsten Steinkopff, Philipp Wolfrum, and Jeong-Ha You. Experimental and computational study of damage behavior of tungsten under high energy electron beam irradiation. *Engineering Fracture Mechanics*, 135:64–80, 2015.
- [15] M Wirtz, J Linke, G Pintsuk, L Singheiser, and M Zlobinski. Comparison of thermal shock damages induced by different simulation methods on tungsten. *Journal of Nuclear Materials*, 438:S833–S836, 2013.
- [16] PRN Childs, JR Greenwood, and CA Long. Heat flux measurement techniques. *Proceedings of the Institution of Mechanical Engineers, Part C: Journal of Mechanical Engineering Science*, 213(7):655–677, 1999.
- [17] AV Babak. Effect of recrystallization on the fracture toughness of tungsten. *Powder Metallurgy and Metal Ceramics*, 22(4): 316–318, 1983.
- [18] ASM International Handbook Committee. *ASM Handbook, Volume 10 - Materials Characterization*. ASM International, 1986.
- [19] BD Cullity. *Elements of x-ray diffraction*. Addison-Wesley Publishing. USA, 1978.
- [20] I Groma and F Székely. Analysis of the asymptotic properties of x-ray line broadening caused by dislocations. *Journal of applied crystallography*, 33(6):1329–1334, 2000.
- [21] BE Warren and BL Averbach. The effect of cold-work distortion on x-ray patterns. *Journal of Applied Physics*, 21(6):595–599, 1950.
- [22] VD Mote, Y Purushotham, and BN Dole. Williamson-hall analysis in estimation of lattice strain in nanometer-sized zno particles. *Journal of Theoretical and Applied Physics*, 6(1):1–8, 2012.
- [23] PL Raffo and TE Mitchell. Yielding, work hardening, and cleavage in tantalum–rhenium alloy single crystals. Technical report, Lewis Research Center, Cleveland, 1968.
- [24] Amit Misra and Ludovic Thilly. Structural metals at extremes. *MRS Bull*, 35(12):965–976, 2010.
- [25] Roger Naslain. Design, preparation and properties of non-oxide CMCs for application in engines and nuclear reactors: an overview. *Composites Science and Technology*, 64(2): 155–170, 2004.

4.4 NEUTRON IRRADIATION EFFECTS IN TUNGSTEN—L.M. Garrison, Y. Katoh, M. McAlister (Oak Ridge National Laboratory), L. L. Snead (MIT), T. S. Byun (PNNL)

OBJECTIVE

The objective of this work is to evaluate the effects of neutron irradiation on the mechanical properties and microstructures of tungsten-based materials to aid in developing plasma-facing materials for fusion reactors.

SUMMARY

Approximately 440 TITAN program samples were irradiated in HFIR at temperatures from 70 to 900°C and fast neutron fluences of 0.01 to 20 $\times 10^{25}$ n/m² (E>0.1 MeV). Single crystal tungsten samples irradiated up to 9 $\times 10^{25}$ n/m² (E>0.1 MeV) have been tensile tested. All samples tensile tested at 22°C had brittle failures. Before irradiation, ductility is observed starting at 300°C test temperature. For material irradiated to 0.55 dpa at 430°C the ductile to brittle transition temperature (DBTT) seen in tensile tests shifted above 300°C, and for material irradiated to 0.4 dpa at 700°C the DBTT shifted above 500°C.

PROGRESS AND STATUS

All tensile data for single crystal tungsten irradiated up to 9 $\times 10^{25}$ n/m² (E>0.1 MeV) have been analyzed and are summarized in Table 1. For samples with less plastic deformation than necessary to define the 0.2% yield stress (YS), “brittle” has been entered in the YS column and the stress at fracture is listed in the ultimate tensile stress (UTS) column. The uniform elongation (UE) and total elongation (TE) are listed for material for which they could be measured. A few of the higher dose samples fractured in handling or shipping (listed as broken in handling “B.I.H.”) and were not tensile tested. It is believed that there was no sudden impact in handling on these samples, so they give a qualitative indication that the material has lost ductility and fracture toughness at those irradiation conditions. Information is grouped by material type, <110> and <100> tungsten, and irradiation temperature, and within those groups is listed in increasing dpa. The conversion 0.195 dpa= 1×10^{25} n/m² (E>0.1 MeV) was used, as calculated by M. E. Sawan, Fusion Eng. Des., 87(5-6), 551-555 (2012).

Some of these results have been presented in a preliminary form before, but the values presented here are more accurate than the preliminary data. See the section “Tensile data uncertainty discussion” for details on how the data was analyzed and the factors that contribute to the uncertainty.

Table 1. Tensile property summary for single crystal tungsten

Capsule	Sample Identification	Irradiation Temp. (°C)	Fast Fluence ($\times 10^{25}$ n/m ² , E>0.1 MeV)	dpa	Test Temp. (°C)	YS (MPa)	UTS (MPa)	UE (%)	TE (%)
<110> Tungsten control samples									
	1W55			0	22	brittle	439	0.2	0.2
	1W56			0	90	brittle	225	0	0
	1W57			0	300	233	299	3.3	50.9
	1W58			0	400	118	196	25.6	58.6
	1W59			0	500	71	167	26.2	53.4

	1W60			0	650	73	135	42.7	75.8
<110> Tungsten, irradiated 90°C									
PC1A	1W05	90	0.02	0.004	22	654	671	0.5	0.5
PC1A	1W06	90	0.02	0.004	90	584	619	1.2	1.3
PC1A	1W15	90	0.02	0.004	300	272	321	3.3	53.5
PC2A	1W25	90	0.1	0.02	22	674	674	0.2	0.2
PC2A	1W26	90	0.1	0.02	90	667	667	0.2	0.3
PC2A	1W35	90	0.1	0.02	300	458	458	0.5	43.2
<110> Tungsten, irradiated 360-460°C									
TB-300-1	1W01	370	0.02	0.004	22	brittle	773	0.04	0.04
TB-300-1	1W02	370	0.02	0.004	300	376	440	1.8	18.7
TB-300-2	1W47	460	0.1	0.02	22	brittle	844	0	0
TB-300-2	1W48	461	0.1	0.02	300	485	485	0.2	25.9
TB-300-3	1W50	360	0.52	0.10	22	brittle	507	0	0
TB-300-3	1W49	360	0.52	0.10	300	471	471	0.2	35.0
T9G-11	1W07	430	2.82	0.55	22	brittle	278	0	0
T9G-11	1W08	430	2.82	0.55	300	brittle	683	0	0
<110> Tungsten, irradiated 690-830°C									
TB-500-1	1W13	800	0.08	0.02	22	brittle	627	0	0
TB-500-1	1W14	800	0.08	0.02	500	206	238	4.0	20.6
TB-650-1	1W23	830	0.13	0.03	22	brittle	813	0	0
TB-650-1	1W24	830	0.13	0.03	650	261	278	1.0	13.3
TB-650-2	1W53	800	0.46	0.09	22	brittle	592	0	0
TB-650-2	1W54	800	0.46	0.09	650	407	424	1.5	21.1
TB-500-2	1W51	690	0.54	0.10	22	brittle	393	0	0
TB-500-2	1W52	690	0.54	0.10	500	518	530	0.02	11.9
T9C-14	1W17	700	2.2	0.43	22	brittle	359	0	0
T9C-14	1W18	700	2.2	0.43	500	1176	1214	0.4	0.5
TB-500-3	1W19	769	9	1.8	22	B.I.H.	—	—	—
TB-500-3	1W20	769	9	1.8	22	B.I.H.	—	—	—
<100> Tungsten, control samples									
	W56			0	22	brittle	322	0	0

	W57			0	90	brittle	298	0	0
	W58			0	300	222	507	3.3	3.3
	W59			0	500	66	204	29.9	45.3
	W60			0	650	60	188	72.6	94.2
<100> Tungsten, irradiated 90°C									
PC1A	W05	90	0.02	0.004	22	brittle	667	0.1	0.1
PC1A	W15	90	0.02	0.004	90	brittle	497	0	0
PC1A	W16	90	0.02	0.004	300	338	378	4.8	4.8
PC2A	W36	90	0.1	0.02	22	brittle	1177	0.02	0.02
PC2A	W37	90	0.1	0.02	90	brittle	966	0	0
PC2A	W38	90	0.1	0.02	300	471	473	0.2	1.8
<100> Tungsten, irradiated 360-460°C									
TB-300-1	W01	370	0.02	0.004	22	brittle	776	0	0
TB-300-1	W02	370	0.02	0.004	300	472	476	0.2	5.1
TB-300-2	W03	460	0.1	0.02	22	brittle	909	0	0
TB-300-2	W04	461	0.1	0.02	22	B.I.H.	—	—	—
TB-300-3	W52	360	0.52	0.10	22	brittle	716	0	0
TB-300-3	W53	360	0.52	0.10	22	B.I.H.	—	—	—
T9G-11	W08	430	2.82	0.55	22	brittle	225	0	0
T9G11	W07	430	2.82	0.55	22	B.I.H.	—	—	—
<100> Tungsten, irradiated 690-830°C									
TB-500-1	W13	800	0.08	0.02	22	brittle	460	0	0
TB-650-1	W24	830	0.13	0.03	22	brittle	416	0	0
TB-650-1	W25	830	0.13	0.03	650	241	286	4.4	19.7
TB-650-2	W27	800	0.46	0.09	22	brittle	385	0	0
TB-650-2	W26	800	0.46	0.09	22	B.I.H.	—	—	—
TB-500-2	W54	690	0.54	0.11	22	brittle	286	0	0
TB-500-2	W55	690	0.54	0.11	22	B.I.H.	—	—	—
T9C14	W17	705	2.2	0.43	22	B.I.H.	—	—	—
T9C14	W18	705	2.2	0.43	22	B.I.H.	—	—	—
TB-500-3	W19	770	9	1.8	22	B.I.H.	—	—	—
TB-500-3	W20	770	9	1.8	22	B.I.H.	—	—	—

Figure 1 shows the UTS of all the single crystal tungsten samples tensile tested at room temperature. All tests were brittle fracture, so the UTS is also the fracture stress. The samples broken in handling are represented on the figure as having zero strength at fracture. This is not intended to be an exact measure of their strength, but to illustrate the increasing fragility of the material with increasing dose. Both orientations of single crystal tungsten experienced irradiation hardening at the lowest dose tested, 0.004 dpa. Both orientations also have a peak UTS at 0.02 dpa. Above 0.02 dpa, the UTS steadily decreases until at 1.8 dpa all four of the irradiated samples (two each of <110> and <100>) were broken in handling. The <100> tungsten displayed a bimodal behavior, having both the highest UTS values and also having the most samples broken in handling. TEM and atom probe analysis of these materials showed that the transmutation-produced Re and Os cluster and form precipitates as the dose increases in tungsten. It is believed that these clusters and precipitates play an important role in the strength increase and loss of toughness of irradiated tungsten.

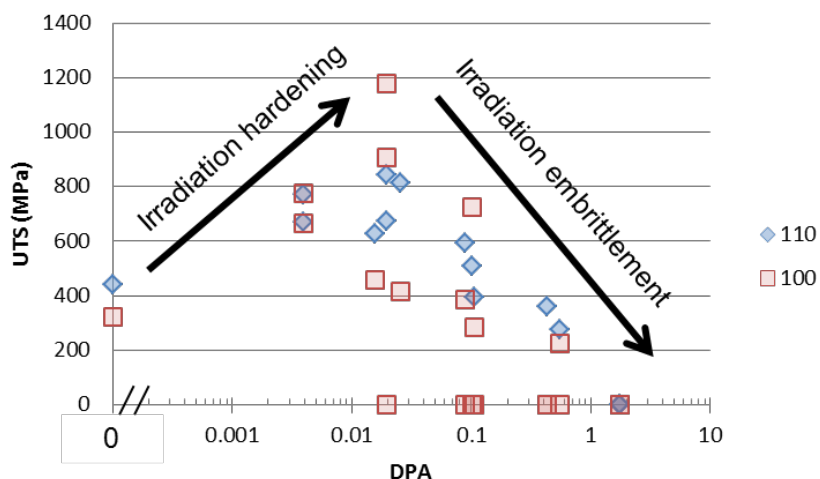


Figure 1. Fracture strength (ultimate tensile strength) for tungsten with crystal orientation <110> and <100> along the tensile axis. All tests were performed at room temperature and each data point represents one test.

The unirradiated samples are referred to by their Sample ID and their test temperature, for example, W56-22 is the unirradiated sample W56 tested at 22°C. For irradiated samples, the text labels include the Sample ID, dpa, irradiation temperature, and test temperature in that order. For example, 1W15-0.004-90-300 was irradiated to 0.004 dpa at 90°C and tested at 300°C.

The tensile tests were performed without an extensometer, so the crosshead motion was used to calculate the strain. This method adds error from the machine compliance in the elastic region of the data. For all the tensile curves, the elastic regions have been removed and replaced with a vertical line. The plastic deformation portions of the curves are unchanged except shifted to start at zero strain.

Single crystal tungsten, unirradiated

The unirradiated tensile data for the single crystal tungsten are shown in Figures 2 and 3. Both <100> and <110> tungsten exhibited ductility starting at 300°C, but the <100> sample only had 3.3% TE while the <110> sample had 50.9%. As test temperature was increased above 300°C both orientations of tungsten showed decreasing UTS with increasing temperature. Although the <100> material seems to transition to ductile behavior at a higher temperature than the <110>, the sample with the largest TE was a <100> sample, W60-650.

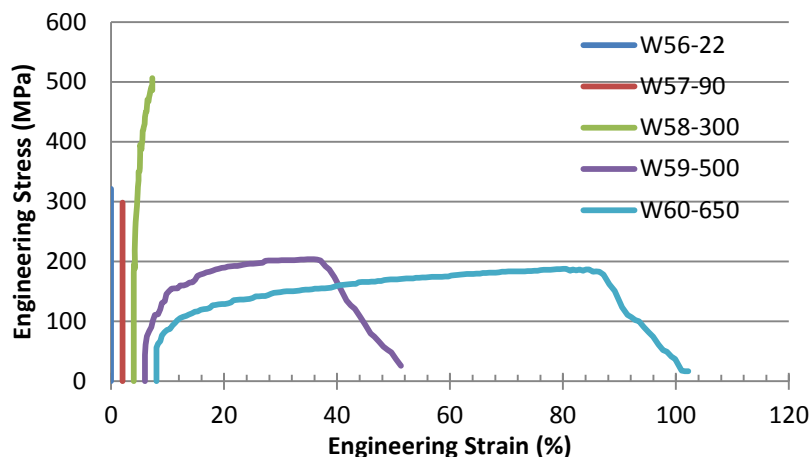


Figure 2. Tensile curves for unirradiated single crystal tungsten with $\langle 100 \rangle$ along the tensile axis, tested at elevated temperatures. Curves are offset by 2% strain increments on the strain axis.

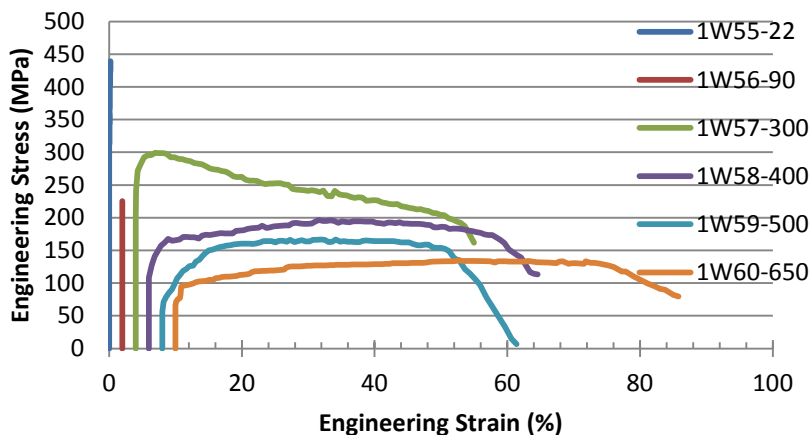


Figure 3. Tensile curves for unirradiated single crystal tungsten with $\langle 110 \rangle$ along the tensile axis, tested at elevated temperatures. Curves are offset by 2% strain increments on the strain axis.

Single crystal tungsten $\langle 100 \rangle$, irradiated at 90°C

The next comparison is between $\langle 100 \rangle$ single crystal tungsten unirradiated and irradiated to 0.004 dpa at 90°C. The tensile curves are plotted with increasing test temperature from left to right, and the unirradiated and irradiated data for each temperature are plotted next to each other (Figure 4). After irradiation and then tested at 22 and 90°C, there is a noticeable increase in UTS as compared to the unirradiated material at the same test temperatures. The irradiated sample tested at 300°C has a higher UTS and slightly longer TE than the unirradiated sample at that test temperature. For these materials irradiated at a low temperature and low dose, the primary defects are loops, which cause the increased strength.

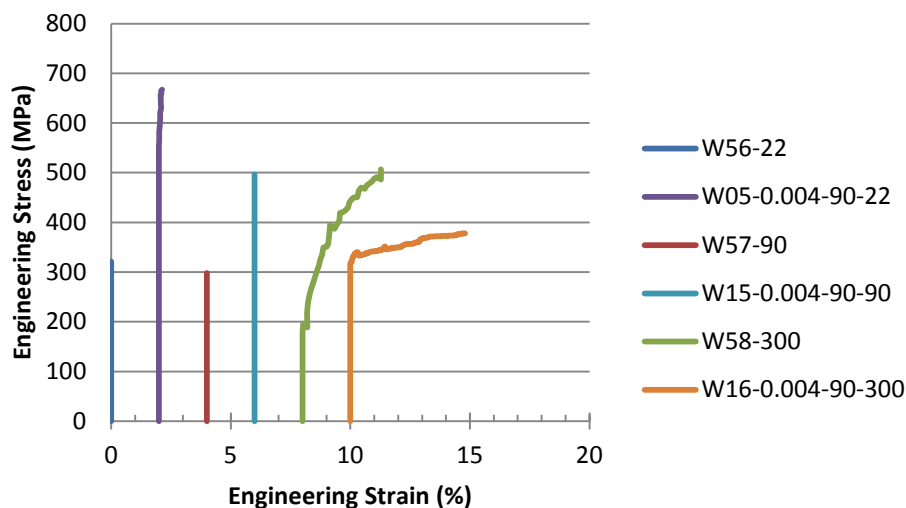


Figure 4. Tensile curves for single crystal tungsten with $\langle 100 \rangle$ crystal direction along the tensile axis before and after irradiation to 0.004 dpa at 90°C and tested at three different temperatures. Curves are offset by 2% strain increments on the strain axis.

Figure 5 compares material irradiated to the higher dose of 0.02 dpa at 90°C to the corresponding unirradiated material. For this higher dose, the UTS of the irradiated material in the brittle regime (test temperature below 300°C) is significantly higher than the UTS of the material irradiated to 0.004 (Figure 4) and the unirradiated material. The sample irradiated to 0.02 dpa and then tested at 300°C has a noticeably lower TE than the unirradiated material at that test temperature. Figure 6 compares the material tested at 300°C but irradiated to different doses. The unirradiated material tested at 300°C shows increased strength until the fracture point, while the irradiated material tested at that temperature shows a flatter profile after the yield point.

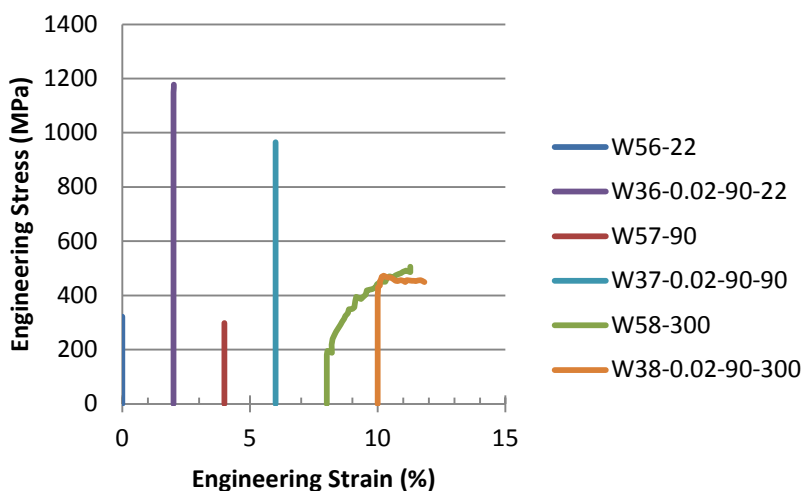


Figure 5. Tensile curves for single crystal tungsten with $\langle 100 \rangle$ crystal direction along the tensile axis before and after irradiation to 0.02 dpa at 90°C and tested at three different temperatures. Curves are offset by 2% strain increments on the strain axis.

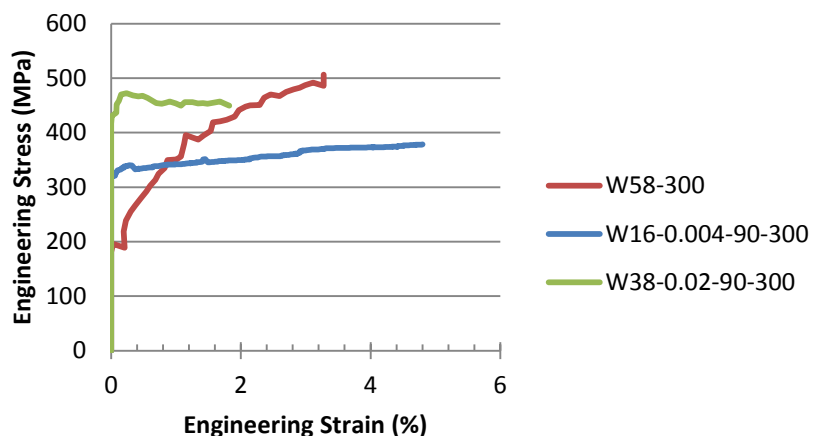


Figure 6. Tensile curves at 300°C for single crystal tungsten with <100> crystal direction along the tensile axis, before and after irradiation to 0.004 and 0.02 dpa at 90°C.

Single crystal tungsten <110>, irradiated at 90°C

Figures 7 and 8 are similar to Figures 4 and 5 except that they show data for the <110> orientation tungsten. For <110> tungsten irradiated to 0.004 dpa at 90°C, Figure 7, the UTS is higher than the unirradiated material but there is a hint of ductility for the tests at 22 and 90°C. For the sample irradiated to 0.004 dpa at 90°C and tested at 300°C, there is very little change in UTS or TE compared to the unirradiated material at the same temperature.

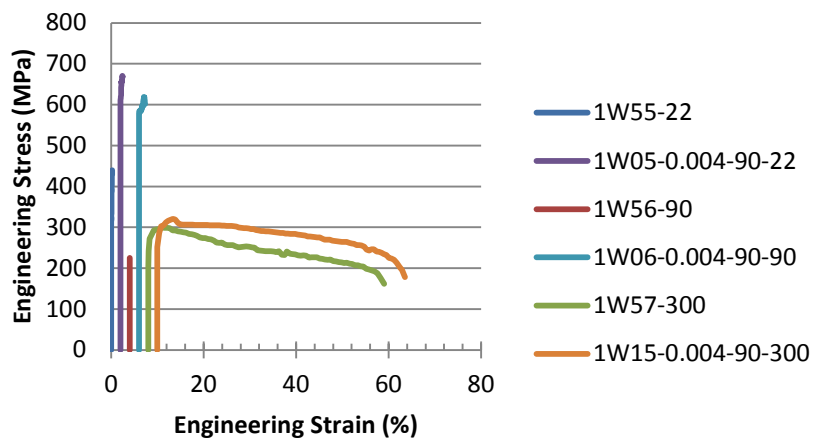


Figure 7. Tensile curves for single crystal tungsten with <110> crystal direction along the tensile axis before and after irradiation to 0.004 dpa at 90°C and tested at three different temperatures. Curves are offset by 2% strain increments on the strain axis.

The <110> tungsten irradiated to 0.02 at 90°C, Figure 8, shows more pronounced changes even for the test at 300°C. Sample 1W35-0.02-90-300 has a significantly higher UTS and lower TE than the unirradiated 1W57-300.

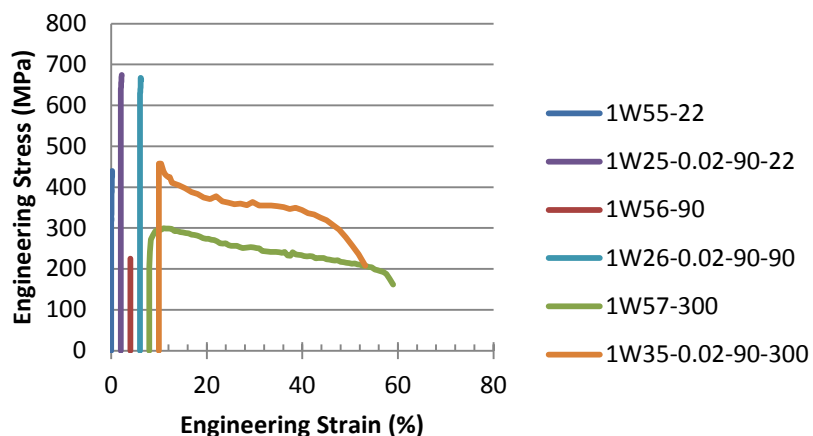


Figure 8. Tensile curves for single crystal tungsten with $\langle 110 \rangle$ crystal direction along the tensile axis before and after irradiation to 0.02 dpa at 90°C and tested at three different temperatures. Curves are offset by 2% strain increments on the strain axis.

The $\langle 110 \rangle$ tungsten irradiated at 90°C and tested at 300°C is compared in Figure 9, showing only a slight change after 0.004 dpa, with the UTS and TE very similar to the unirradiated values. However, for the higher dose of 0.02, there is a noticeable increase in the UTS and decrease in the TE. Additionally, the shape of the curve has changed to have a decrease in strength following the yield stress.

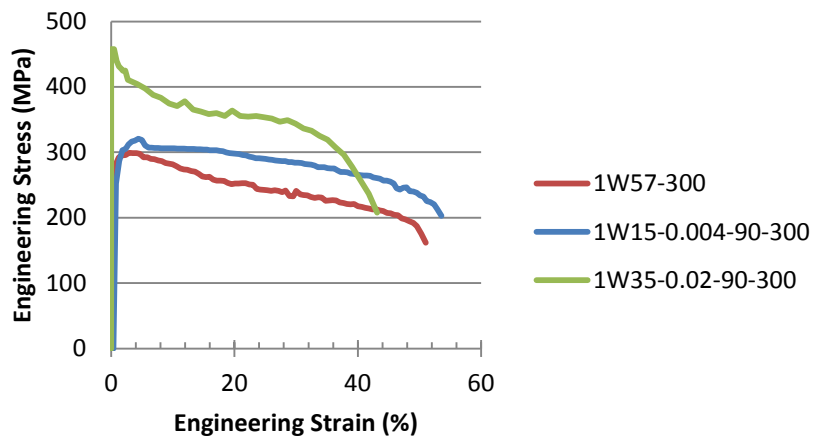


Figure 9. Tensile curves at 300°C for single crystal tungsten with $\langle 110 \rangle$ crystal direction along the tensile axis, tested before and after irradiation to 0.004 and 0.02 dpa at 90°C.

Single crystal tungsten $\langle 100 \rangle$, irradiated at 360-460°C

The single crystal tungsten $\langle 100 \rangle$ irradiated at 360-460°C and tested at 22°C shows an initial increase and then a decrease in UTS with increasing dose (Figure 10).

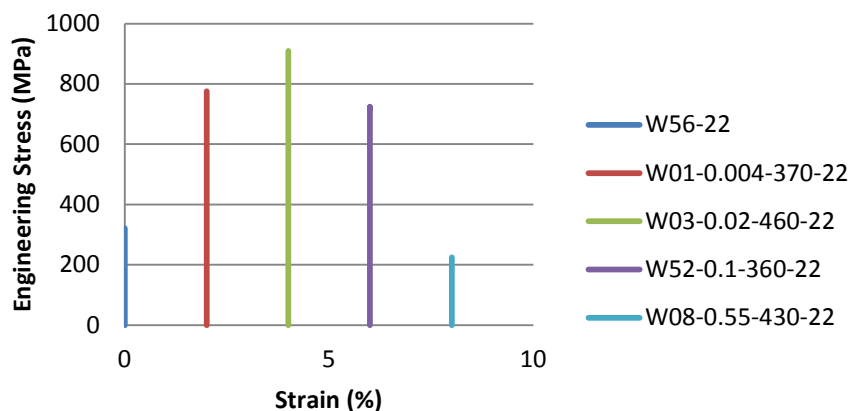


Figure 10. Tensile curves at 22°C for single crystal tungsten with <100> crystal direction along the tensile axis before and after irradiation at 360-460°C. Curves are offset by 2% strain increments on the strain axis.

For the elevated temperature tests, the <100> single crystal tungsten irradiated to 0.004 dpa at 370°C has a flatter plastic region than the unirradiated sample, which continues to increase in strength after the yield point (Figure 11).

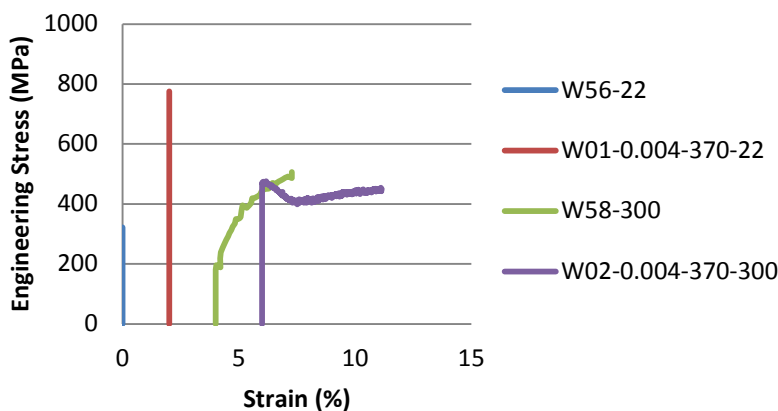


Figure 11. Tensile curves for single crystal tungsten with <100> crystal direction along the tensile axis before and after irradiation to 0.004 dpa at 370°C and tested at two temperatures. Curves are offset by 2% strain increments on the strain axis.

Single crystal tungsten <110>, irradiated at 360-460°C

The single crystal tungsten <110> irradiated at 360-460°C and tested at 22°C also shows an initial increase and then a decrease in UTS with increasing dose (Figure 12).

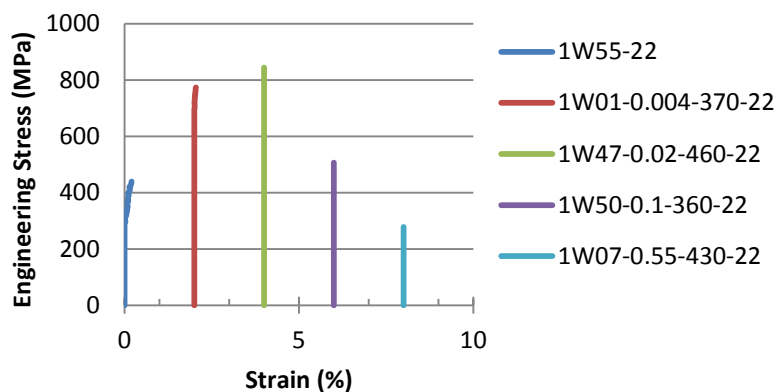


Figure 12. Tensile curves at 22°C for single crystal tungsten with <110> crystal direction along the tensile axis before and after irradiation at 360-460°C. Curves are offset by 2% strain increments on the strain axis.

Figure 13 shows a dose comparison for all single crystal tungsten <110> tested at 300°C. The irradiated samples have lower TE than the unirradiated sample tested at 300°C. At the highest dose of 0.55 dpa no ductility remains, indicating that the tensile test DBTT has shifted above 300°C. Additionally, after irradiation, the shape of the plastic strain curve changes.

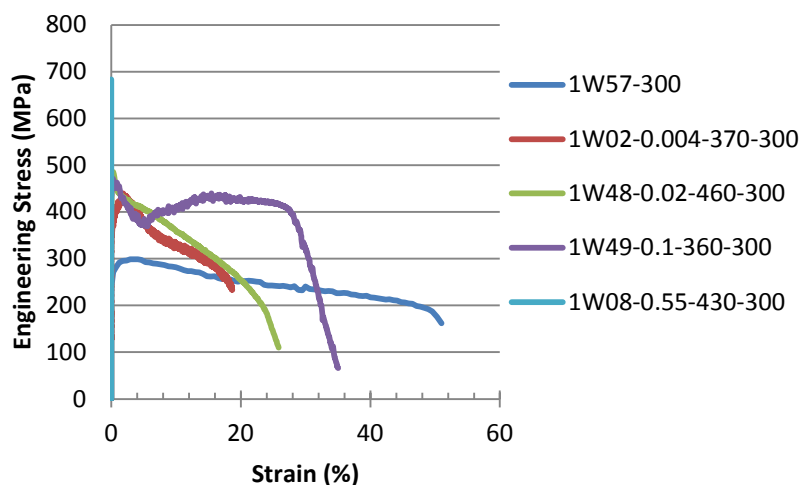


Figure 13. Tensile curves at 300°C for single crystal tungsten with <110> crystal direction along the tensile axis before and after irradiation to 0.004 to 0.55 dpa at 360-460°C.

Single crystal tungsten <100>, irradiated at 690-830°C

The irradiated <100> single crystal tungsten failed in brittle mode for all tensile tests at 22°C, so the UTS is plotted in Figure 14. Samples that were broken in handling are plotted at zero UTS and listed at “none” for the test temperature. More samples were broken in handling from the 690-830°C temperature group than the 90°C or 360-460°C temperature groups. The <100> single crystal tungsten irradiated at 690-830°C shows the same pattern as the tungsten irradiated at 360-460°C; initial increase of UTS followed by decrease in UTS with increasing dose.

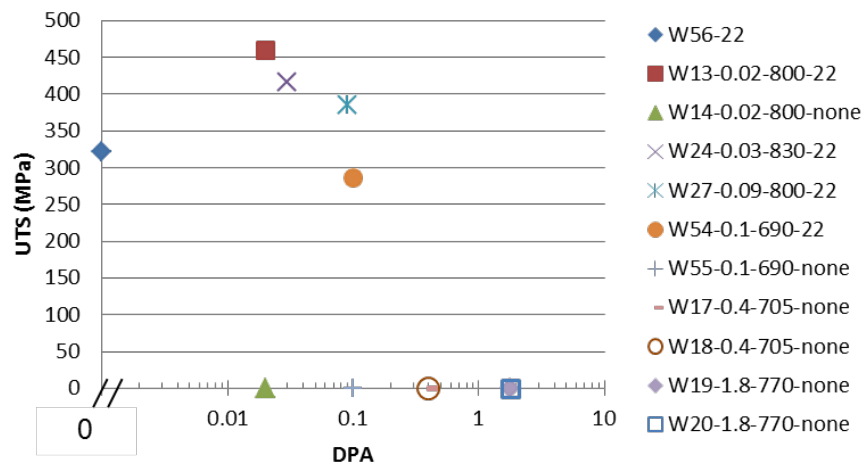


Figure 14. UTS at 22°C for single crystal tungsten with <100> crystal direction along the tensile axis before and after irradiation at 690-830°C.

Single crystal tungsten <100> irradiated to 0.03 dpa at 830°C was tensile tested at 22°C and 650°C (Figure 15). For both test temperatures, the UTS was increased by irradiation. For the tungsten tested at 650°C, it retained ductility after irradiation, but the TE was reduced to 19.7% as compared to 94.2% before irradiation.

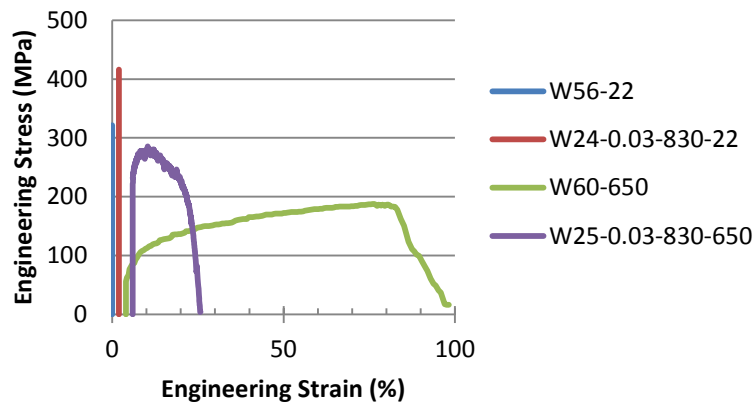


Figure 15. Tensile curves for single crystal tungsten with <100> crystal direction along the tensile axis before and after irradiation to 0.03 dpa at 830°C and tested at two temperatures. Curves are offset by 2% strain on the strain axis.

Single crystal tungsten <110>, irradiated at 690-830°C

The single crystal tungsten <110> irradiated at 690-830°C also had brittle fracture when tested at 22°C, so the UTS is plotted in Figure 16 versus dose. It shows the same trend as the other orientation of tungsten and the tungsten irradiated at lower temperatures, in that the UTS increased and then decreased with increasing dose. There were fewer samples broken in handling of the <110> orientation than the <100> orientation.

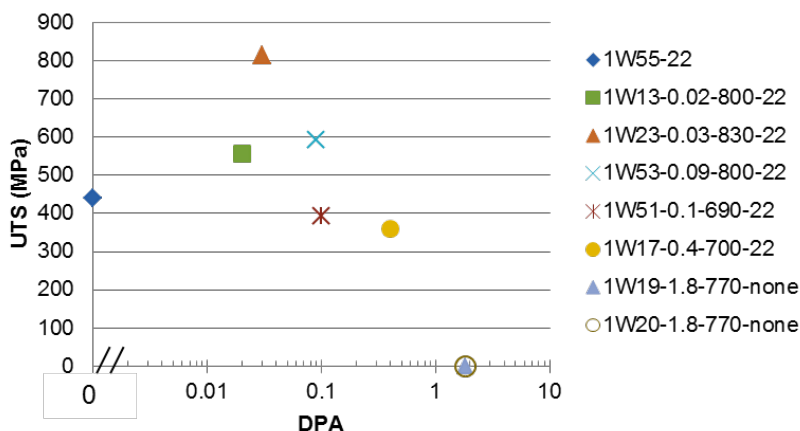


Figure 16. UTS at 22°C for single crystal tungsten with <110> crystal direction along the tensile axis before and after irradiation at 690-830°C.

For single crystal tungsten <110> irradiated at 690-800°C and tested at 500°C, the UTS increased with increasing dose (Figure 17). The tungsten irradiated to 0.4 dpa had a UTS of 1214 MPa and TE of 0.5%, compared to the unirradiated tungsten with 167 MPa UTS and 53.4% TE. For single crystal tungsten <110> irradiated to similar conditions but tensile tested at the slightly higher temperature of 650°C, an increase of UTS with increasing dose was also seen, but the dose did not reach the level where the material transitions to brittle failure at this temperature (Figure 18).

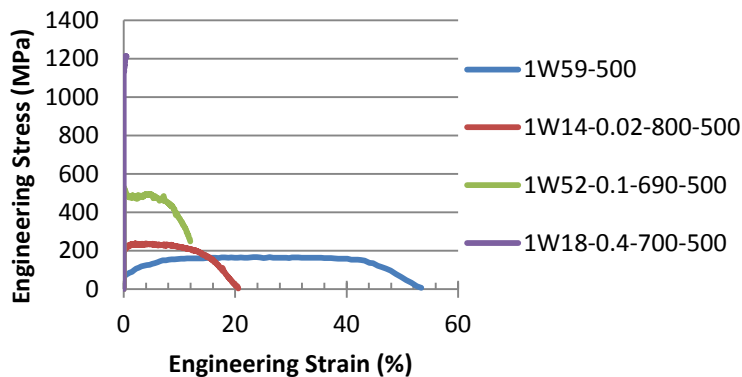


Figure 17. Tensile curves at 500°C for single crystal tungsten with <110> crystal direction along the tensile axis before and after irradiation to 0.02 to 0.4 dpa at 690-800°C.

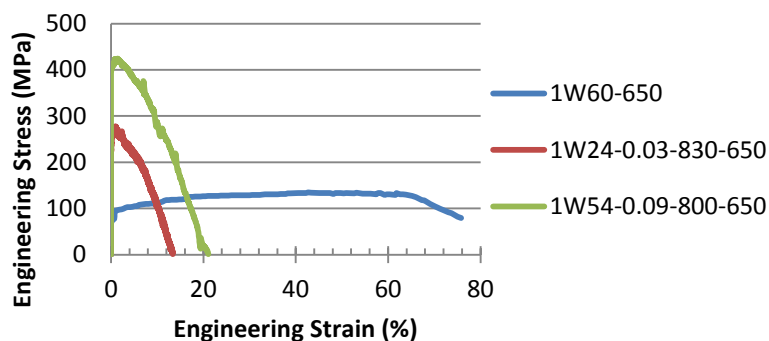


Figure 18. Tensile behavior at 650°C for single crystal tungsten with $\langle 110 \rangle$ crystal direction along the tensile axis before and after irradiation to 0.03 to 0.09 dpa at 800-830°C.

Sources of tensile data uncertainty

The tensile data was analyzed using a program that identified the elastic region, subtracted the elastic region, and identified the 0.2% YS, UTS, UE, and TE. The program requires the user to define the slope in the elastic region. Human judgement and equipment limitations contributed to uncertainty in the data, and these can be grouped into four types. First, in some data sets, the data acquisition rate was lower than optimal which accentuated any noise present, especially in the elastic region of the curves. This made it difficult for the operator to determine the slope in the elastic region, which has an impact on the defined YS value. Second, many of the raw data sets had a horizontal section in the elastic region which was an artifact of the data-taking and was removed when the curves were plotted. This artifact in the elastic region did not affect the calculated YS, UTS, UE, or TE values. The third uncertainty was periodic oscillations in the stress-strain data and occurred in all of the data sets above 300°C. This periodic noise was judged to be an artifact of the testing equipment or data collection rather than a real phenomenon because a) it occurred in the elastic and plastic regions, while real sawtooth features are only seen in the plastic region for monolithic materials, b) the oscillations were usually of the same magnitude and frequency throughout the curve, and c) for many data sets, the magnitude of the oscillations was much larger than that typically seen in materials that show plastic flow instabilities. Rather than using a moving average on the data sets, which would lead to a smoother but still wavy appearance of the data, the outlier points were deleted. This did not perfectly smooth the data, but it was decided to err on the side of less data manipulation instead of artificially smoothing the curves. The final type of uncertainty was judgement on where the fracture point occurred. For the brittle tests, the fracture point was unambiguous. For any case where there was plastic deformation, the fracture point was taken as the last point before any sudden drop in stress. However, for many of the elevated temperature tests, there was no sudden drop in stress. For cases where there appeared to be no sudden drop, the fracture point was taken as the point where the stress reached zero or nearly zero.

4.5 PROGRESS IN THE STUDY OF ION IRRADIATION IN TUNGSTEN—Weilin Jiang, Karen Kruska, Charles H. Henager Jr., and Richard J. Kurtz (Pacific Northwest National Laboratory)

OBJECTIVE

The experimental study intends to generate data to validate the theoretical predictions on defect accumulation and recovery, as well as to investigate microstructural evolution and transmutant precipitation in mono- and poly-crystalline tungsten using ion implantation.

SUMMARY

This progress report describes experimental preparations and presents initial characterization results from x-ray diffraction (XRD) and scanning electron microscopy (SEM) for poly- and mono-crystalline tungsten (W). The XRD data suggest that the polycrystalline sample is single-phase body-centered cubic tungsten with an average crystallite size of ~40 nm. The SEM results indicate that the polycrystalline tungsten has a grain size ranging from 1 to 5 μm without visible large cavities. The high-resolution XRD from a symmetric 2θ - ω scan shows that the monocrystalline tungsten has only one strong, sharp W (222) diffraction peak, confirming that the sample is a (111)-oriented tungsten single crystal. Asymmetric ω scan exhibits multiple peaks around the primary (222) peak, indicating that the single crystal has a mosaic structure. Pole figures from XRD measurements exhibit distinctive (110) and (111) poles, which match the simulation poles for (111) oriented tungsten. Diffraction rings from polycrystalline tungsten are not observed.

PROGRESS AND STATUS

Introduction

Tungsten has been considered as a promising candidate for the first-wall material in the fusion reactor designs due to its high melting point (3693 K), high thermal conductivity (173 W/(m·K)) and low sputtering yield [1]. A great effort has been devoted to the studies of He and D bubble formation and growth [2-4] as well as gas retention and release [5-7] in ion-irradiated polycrystalline tungsten. Recent microscopy studies have focused on the defect production, evolution and transmutant clustering in ion or neutron irradiated polycrystalline [8-13] and monocrystalline tungsten [14]. A comprehensive dataset [15-18] has been published for defect production due to displacement cascades in tungsten and defect recovery during annealing at elevated temperatures up to 2050 K based on molecular dynamics and object kinetic Monte Carlo simulations, respectively. However, very few experiments, if any, have been performed to date for a quantitative study of defect accumulation in monocrystalline tungsten using ion-channeling analysis. This study utilizes the ion-beam method to generate data that could help to validate the theoretical predictions and improve understanding of microstructural evolution and transmutant precipitation in tungsten.

Experimental Procedure

A polycrystalline tungsten sheet of 1 mm in thickness with purity of 99.97% was obtained from Plansee. Major impurities include Mo (12 $\mu\text{g/g}$), Fe (8 $\mu\text{g/g}$) and C (6 $\mu\text{g/g}$), as given in Table 1 from the manufacturer's specification. The sheet was sliced into 10 mm \times 10 mm square samples. The sample surface was polished on one side using the following procedure: (1) grind to 1200 grit using soap and water as lubricant, (2) polish on 6 μm Buehler TexMet pad until uniform polish is achieved, (3) polish on 1 μm Nylon pad on a vibratory polisher for 24 h, and (4) polish on Leco Colloidal Silica on 3M Final B pad on the vibratory polisher for 24 h. In addition, (111)-oriented W single-crystal disks of 12 mm in diameter with one side polished to surface roughness of less than 0.03 μm were obtained from Princeton Scientific Corporation. The purity of the material is 99.999% and major impurities are O (10ppm), N (<5ppm), Mo (4ppm) and C (3ppm), as provided in Table 2 from the manufacturer's specification.

The polycrystalline tungsten was analyzed using a Philips X'Pert multipurpose diffractometer (PANalytical, Almelo, The Netherlands) with a fixed Cu anode ($\lambda_{\text{K}\alpha}=0.154187$ nm) operating at 45 kV and 40 mA. A Göbel mirror for the incident beam and a 0.27-radian parallel plate collimator (PPC) for the diffracted beam were used in this study. A symmetric 2θ - ω scan was performed from $2\theta = 50^\circ$ to 120°

with a step of 0.05° per 6 s. Data analysis was performed using commercial software JADE from Materials Data, Inc. and PDF4+ Inorganic Crystal Structure Database (ICSD). A Philips X'Pert materials research diffractometer (PANalytical, Almelo, The Netherlands) with a fixed Cu anode operating at 45 kV and 40 mA was also used for characterization of monocrystalline tungsten. A hybrid monochromator, consisting of four bounce Ge(220) crystals and a Cu x-ray mirror, was employed in the incident beam path to provide monochromatic x-rays from Cu $K\alpha_1$ ($\lambda=0.154056$ nm and $\Delta\lambda/\lambda=23$ ppm) with a beam divergence of 12 arc sec. An additional monochromator with a three-bounce Ge (220) channel-cut analyzer was placed in front of a proportional counter in the diffracted beam path with the same beam divergence. The diffractometer had the angular precision and reproducibility of 0.0001° and 0.0003° , respectively, for both polar and tilt angles θ and ω . The detector position was calibrated with a direct x-ray beam. A symmetric 2θ scan was performed from $2\theta = 50^\circ$ to 120° with a step of 0.02° per 10 s. An asymmetric ω scan around the W (222) peak was also conducted with an ω offset equal to 0.3009° . Pole figure measurements were made for W (110) at $2\theta = 40.2650^\circ$ and $\omega = 20.1325^\circ$ and W(222) at $2\theta = 114.927^\circ$ and $\omega = 57.4635^\circ$ over the scans from $\phi = 0^\circ$ to 360° and $\psi = 0^\circ$ to 90° at a step of 1° per 1.5 s. Data analysis was performed using Philips X'Pert Texture software. In addition, backscattered electron imaging was performed using scanning electron microscopy (SEM), JEOL JSM-7600F, with an accelerating voltage of 10 kV at a high current setting.

Table 1. Typical impurity levels in monocrystalline tungsten (purity 99.999%) from Princeton Scientific Corporation

Element	Ag	Al	C	Ca	Cl	Co	Cu	Cr	Fe	H	Mg
Level (ppm)	<1	0.20	3.00	0.10	0.30	<0.10	<0.10	0.15	0.6	<0.01	0.25
Element	Mn	Mo	N	Na	Ni	O	S	Si	Ta	V	Zr
Level (ppm)	<0.10	4.00	<5.00	<0.10	0.40	10.0	0.20	0.70	1.00	0.50	<1.00

Results and Discussion

Figure 1 shows the XRD pattern for polycrystalline tungsten. Double-peak structure is observed at high angles, which originates from Cu $K\alpha_1$ and $K\alpha_2$ contributions. All the diffraction peaks are found to well match the powder diffraction database for body-centered cubic (bcc) W (PDF# 00-004-0806) with lattice constant $a = 0.31648$ nm and the material is identified as single-phase polycrystalline tungsten without visible secondary phases. Each individual peak has been well fit for data analysis with the results given in Table 2. From the observed strongest (200) peak, the lattice constant is estimated to be $a = 2d_{200} = 0.31678$ nm. Compared to the database value from (200) diffraction, where $d_{200} = 0.15820$ nm and thus $a = 0.31640$ nm, the difference in the lattice constant is only $\sim 0.1\%$. However, the peak area ratio in Figure 1 is different from the powder database, which might be attributed to some possible preferred grain orientations. The average crystallite size has been estimated based on Scherer formula in the analytical software. The results for all the observed orientations are given in Table 2, which ranges from 35.5 for (200) to 46.6 nm for (222).

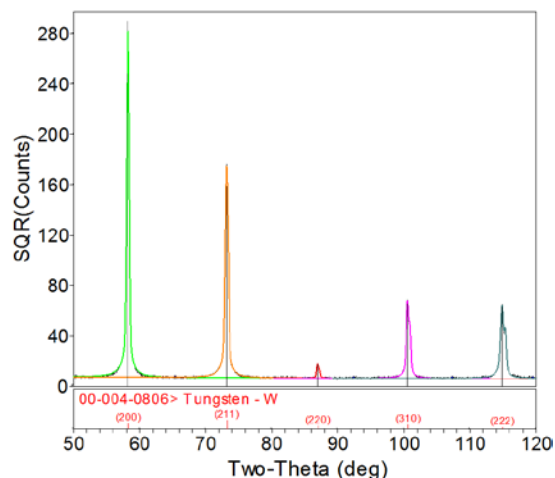


Figure 1. XRD pattern from a symmetric 2θ scan for polycrystalline tungsten.

Table 2. Cu K_{α} x-ray diffraction results for polycrystalline tungsten

Orientation	2θ ($^{\circ}$)	d (nm)	Peak Area	FWHM ($^{\circ}$)	Crystallite Size (nm)
(200)	58.198	0.15839	433494	0.312	35.5(0.2)
(211)	73.128	0.12931	189934	0.327	36.4(0.4)
(220)	86.904	0.11200	1914	0.319	41.6(5.4)
(310)	100.570	0.10014	35356	0.339	43.8(0.8)
(222)	114.876	0.09140	36332	0.370	46.6(0.9)

The grain structure of the polycrystalline tungsten is shown in Figure 2. Backscattered electrons were used for imaging. Some of the large grains appear to show non-uniform contrast, probably due to lattice strain. Grains also appear to be elongated along one direction and are presumably formed during the rolling or forging process. The grain size is estimated to be in the range from 1 to 5 μm . It should be noted that the average grain size cannot be smaller than the average crystallite size determined by XRD (Figure 1) because the latter is the average inter-planar distance between the adjacent planar defects that discontinue the lattice periodicity in a crystalline grain. A large average crystallite size indicates a low defect density in the grains. Large cavities are not observed in the polycrystalline W sample and the material should have a density near 19.26 g/cm^3 . Figure 3 shows a high-resolution XRD pattern from a symmetric $2\theta/\omega$ scan for a monocrystalline tungsten disk. As expected, the data shows only one strong W (222) peak, confirming that the material is a single-phase (111)-oriented W single crystal.

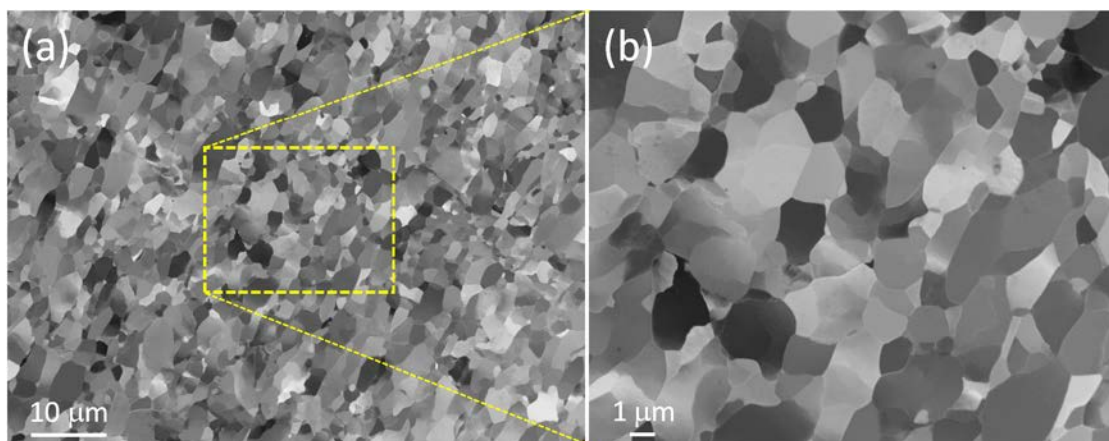
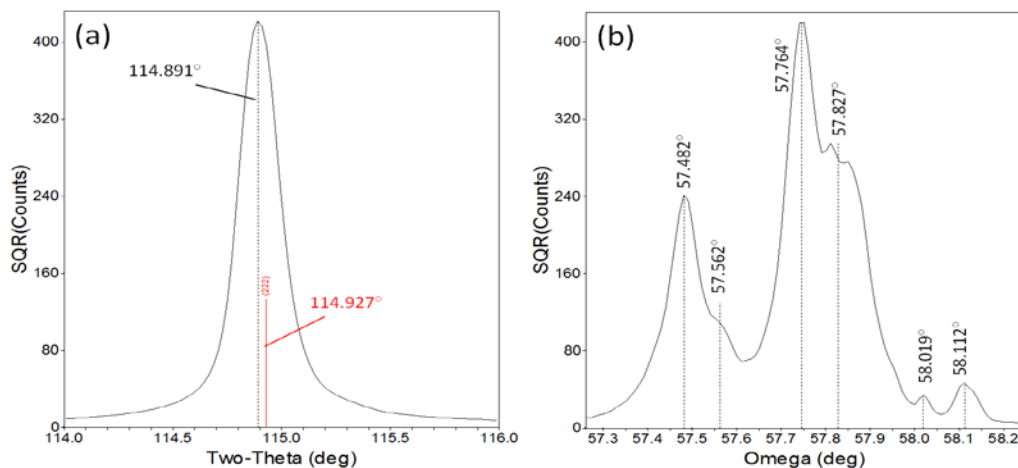
**Figure 2.** Backscattered electron SEM for polycrystalline tungsten.**Figure 3.** XRD patterns from (a) symmetric and (b) asymmetric scans for monocrystalline tungsten.

Figure 3(a) shows a magnified (222) peak that is located at a slightly lower angle (114.891°) than the value (114.927°) from the powder database for bcc W. The lattice spacing between (222) planes in the single crystal is determined to be d_{222} (mono)=0.09139 nm. From Table 2 for polycrystalline W, d_{222} (poly)=0.09140 nm and for powder from the database, d_{222} (database)=0.09137 nm. Since $a=3^{1/2}d_{111}=2\times 3^{1/2}d_{222}$ for a cubic crystal structure, a (mono)=0.31658 nm, a (poly)=0.31662 nm, and a (database)=0.31651 nm. Overall, their difference in lattice constant a is within 0.03% based on the positions of their (222) diffraction peaks. The crystallite size is estimated using Scherer formula based on the peak width and is found to be greater than the instrument upper limit (100 nm). Figure 4(b) shows the result from an asymmetric ω scan for the monocrystalline tungsten. There is a ω offset of 0.3009° in the scan. Fine structures with at least six individual Gaussian peaks are observed, as tentatively indicated with their peak positions in the figure. The data clearly indicates that the single crystal has a mosaic structure with slightly misoriented (111) planes in the individual crystallites. The entire angular range of the mosaic structure is within $\sim 1^\circ$, and the two strongest peaks located at $2\theta=57.764^\circ$ and 57.872° are only misoriented within $\sim 0.05^\circ$. Note that the vertical scale is plotted in units of square root of counts for better showing the fine structure. Other smaller peaks contribute significantly lower diffraction intensities, including the third strongest peak located at 57.482° .

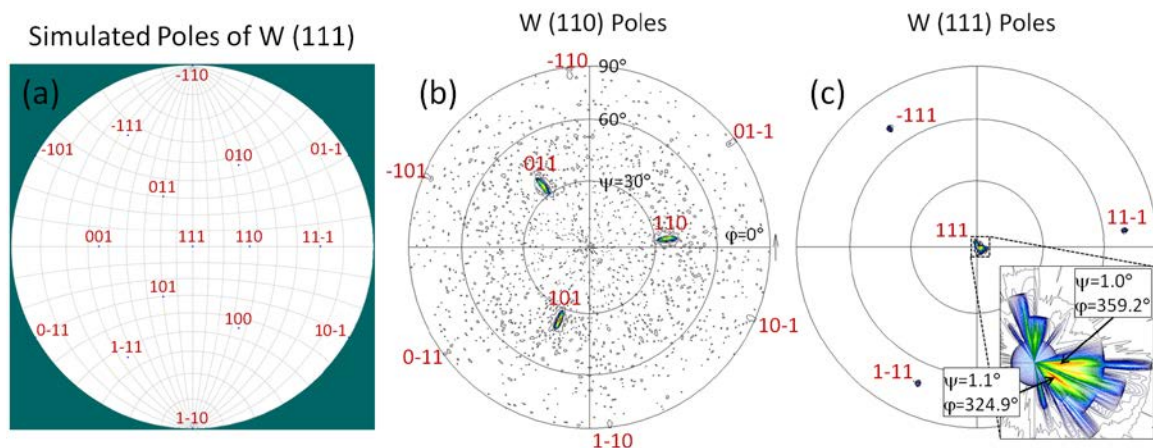


Figure 4. Comparison of (a) simulated poles of (111) oriented monocrystalline tungsten with the experimental results for (b) W (110) and (c) W (222) or W (111) poles.

Figure 4 shows simulation poles of W (111) and experimental data for W (110) and W (222) or W (111) poles of the monocrystalline tungsten disk. All the expected (110) and (111) poles are clearly visible, which exactly match the simulation poles. The poles located at $\psi=90^\circ$ in Figure 5(b) are not supposed to appear in principle, but small diffraction intensities from those peaks are actually visible due to x-ray beam divergence and diffraction peak broadening. No ring structures or additional poles in the pole figures are present, suggesting that the material is single-phase tungsten with a negligible fraction of polycrystalline tungsten, if any, which is consistent with the results in Figure 3. The inset in Figure 5(c) suggests that the single crystal is cut about 1° to the surface (111) plane. There are two local maxima of diffraction intensities at $\psi=1^\circ$ and 1.1° , indicating that the orientation difference of the individual crystallites is within 0.1° . The result is consistent with the observed multiple peaks from the ω scan shown in Figure 4(b). The data in Figures 3, 4 and 5 suggest that the single-crystal tungsten disk has high crystalline quality and is considered to be suitable for ion-channeling study of damage accumulation and recovery that will follow these initial characterizations of the as-received tungsten materials.

Acknowledgements

This research was supported by Office of Fusion Energy Sciences, U.S. Department of Energy (DOE) under Contract DE-AC05-76RL01830. XRD was performed under a general user proposal at the Environmental Molecular Sciences Laboratory (EMSL), a national scientific user facility located at PNNL.

REFERENCES

- [1] R. A. Causey and T. J. Venhaus, *Phys. Scr.* T94 (2001) 9.
- [2] N. Hashimoto, J. D. Hunn, N. Parikh, S. Gilliam, S. Gidcumb, B. Patnaik, and L. L. Snead, *J. Nucl. Mater.* 347 (2005) 307.
- [3] R. F. Radel and G. L. Kulcinski, *J. Nucl. Mater.* 367-370 (2007) 434.
- [4] S. Sharafat, A. Takahashi, Q. Hu, and N. M. Ghoniem, *J. Nucl. Mater.* 386-388 (2009) 900.
- [5] A. A. Haasz, J. W. Davis, M. Poon, and R. G. Macaulay-Newcombe, *J. Nucl. Mater.* 258-263 (1998) 889.
- [6] M. Poon, A. A. Haasz, and J. W. Davis, *J. Nucl. Mater.* 374 (2008) 390.
- [7] B. Tyburska, V. Kh. Alimov, O. V. Ogorodnikova, K. Schmid, and K. Ertl, *J. Nucl. Mater.* 395 (2009) 150.
- [8] A. Xu, C. Beck, D. E. J. Armstrong, K. Rajan, G. D. W. Smith, P. A. J. Bagot, and S. G. Roberts, *Acta Mater.* 87 (2015) 121.
- [9] F. Ferroni, X. Yi, K. Arakawa, S. P. Fitzgerald, P. D. Edmondson, and S. G. Roberts, *Acta Mater.* 90 (2015) 380.
- [10] X. Yi, M. L. Jenkins, K. Hattar, P. D. Edmondson, and S. G. Roberts, *Acta Mater.* 92 (2015) 163.
- [11] X. Yi, M. L. Jenkins, M. A. Kirk, Z. Zhou, and S. G. Roberts, *Acta Mater.* 112 (2016) 105.
- [12] A. Hasegawa, M. Fukuda, K. Yabuuchi, and S. Nogami, *J. Nucl. Mater.* 471 (2016) 175.
- [13] Z. Zhang, K. Yabuuchi, and A. Kimura, *J. Nucl. Mater.* 480 (2016) 207.
- [14] X. Hu, T. Koyanagi, M. Fukuda, Y. Katoh, L. L. Snead, and B. D. Wirth, *J. Nucl. Mater.* 470 (2016) 278.
- [15] W. Setyawan, G. Nandipati, K. J. Roche, H. L. Heinisch, B. D. Wirth, and R. J. Kurtz, *J. Nucl. Mater.* 462 (2015) 329.
- [16] G. Nandipati, W. Setyawan, H. L. Heinisch, K. J. Roche, R. J. Kurtz, and B. D. Wirth, *J. Nucl. Mater.* 462 (2015) 338.
- [17] G. Nandipati, W. Setyawan, H. L. Heinisch, K. J. Roche, R. J. Kurtz, and B. D. Wirth, *J. Nucl. Mater.* 462 (2015) 345.
- [18] W. Setyawan, G. Nandipati, and R. J. Kurtz, *J. Nucl. Mater.* 484 (2017) 30.

4.6 INTERACTION OF INTERSTITIAL CLUSTERS WITH RHENIUM, OSMIUM, AND TANTALUM IN TUNGSTEN—W. Setyawan, G. Nandipati, and R. J. Kurtz (Pacific Northwest National Laboratory)

Extended Abstract of a recently published paper: W. Setyawan, G. Nandipati, R. J. Kurtz, “Ab Initio Study of Interstitial Cluster Interaction with Re, Os, and Ta in W”, Journal of Nuclear Materials 484 (2017) 30-41, doi: 10.1016/j.jnucmat.2016.11.002

The objective of this research is to develop a database of binding energies of interstitial clusters in tungsten to solid transmutation products including Re, Os, and Ta. The database will be used to inform kinetic Monte Carlo simulations of damage accumulation and defect microstructure evolution in bulk tungsten under fusion neutron irradiation. The stability of tungsten self-interstitial atom (SIA) clusters is explored within the density functional theory framework. VASP.5.4.1 software is used to perform the calculations with the pseudo potentials taken from the VASP’s library potpaw_PBE_v5.2.12. Clusters from one to seven SIAs are systematically explored from 1264 unique configurations. Finite-size effect of the simulation cell is corrected based on the scaling of formation energy versus inverse cell volume. Furthermore, the accuracy of the calculations is improved by treating the 5p semicore states as valence states. The results show that small interstitial clusters prefer parallel $\langle 111 \rangle$ dumbbell orientations arranged in compact configurations on two or more $\{110\}$ planes. In fact, the progression of these clusters towards larger size represents the formation of small dislocation loops. These clusters are strongly binding. Three of the most stable clusters in each cluster size are included to obtain an average binding property. The binding energy of a size- n cluster with respect to $n \rightarrow (n - 1) + 1$ reaction increases with size as shown in Figure 1. Extrapolation for $n > 7$ is derived based on the formation energy model of dislocation loops [1, 2], and the empirical formula is presented in Figure 1.

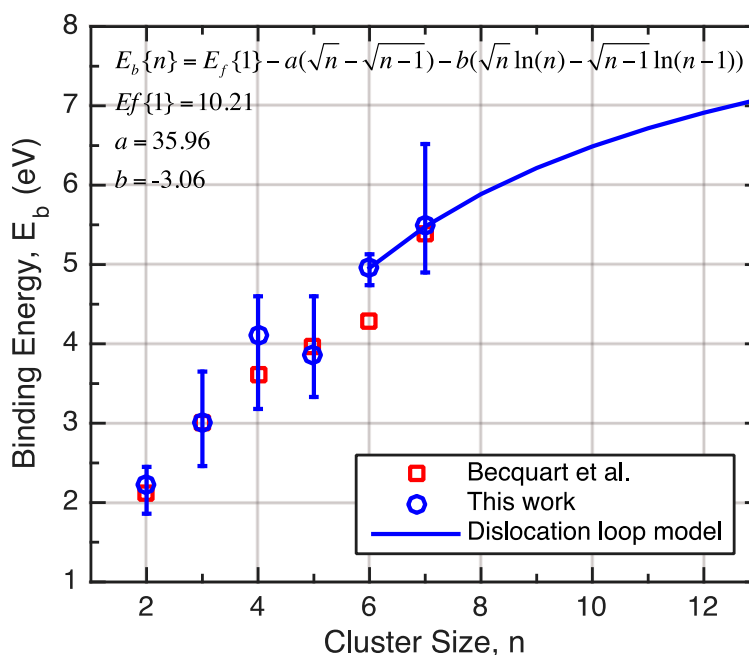


Figure 1. Binding energy of size- n SIA clusters with respect to an $n \rightarrow (n - 1) + 1$ reaction. For this work, the average value over the three most stable clusters for each n is plotted with the tic marks above and below the average values representing the maximum and the minimum values. For $n > 7$, an empirical formula as shown can be used and is based on the formation energy of dislocation loops [1, 2]. The formula is fit to the binding data of size-6 and size-7 clusters. All energies are in eV. The asymptotic value is equal to the formation energy of a single interstitial (a $[111]$ dumbbell) of $E_f\{1\} = 10.21$ eV. For comparison, data from Ref. [3] are plotted as squares.

The interaction of these SIA clusters with Re, Os, or Ta substitutional solutes (representing the prominent solid transmutation products in irradiated W) is studied by replacing one of the conjugate atoms with the solute. Conjugate atoms are those initially at lattice sites but now sharing the sites with SIAs as dumbbells. It is found that these clusters are strongly attracted to Re and Os, but strongly repelled by Ta. The strongest interaction is found when the solute is located on the periphery of the cluster rather than in the middle of it. Averaging over different positions of the solute in the cluster for the three most stable clusters in each size shows that the solute binding energy decreases with size from 0.83 eV ($n = 1$) to 0.70 eV ($n = 7$) for Re, from 1.71 to 1.43 eV for Os, and increases from -0.64 to -0.56 eV for Ta. The results are shown in Figure 2.

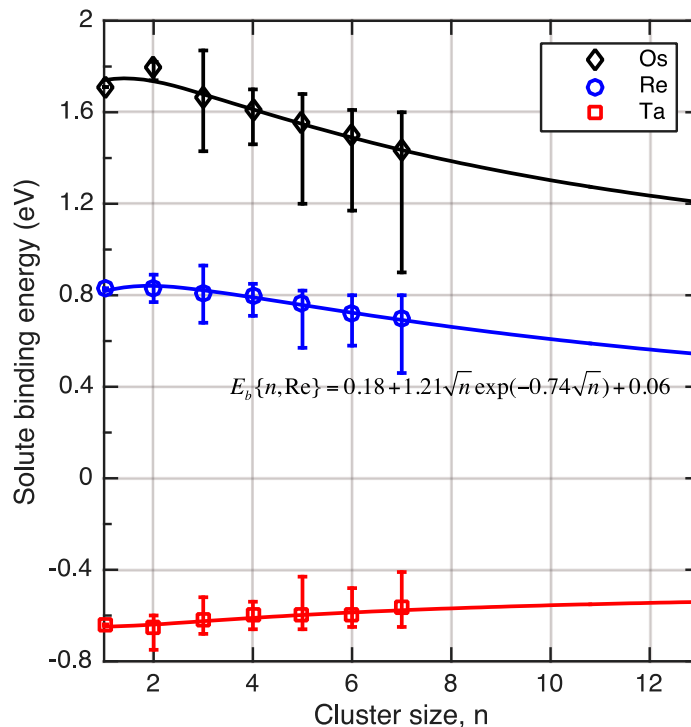


Figure 2. Binding energy of size- n SIA clusters to a Re, Os, or Ta atom substitutionally replacing one of the W dumbbell atoms. The data points represent the average over the three most stable clusters. The tic marks represent the maximum and minimum values. The data points are well reproduced with an empirical formula of $E_b\{n, sol\} = E_{f,s} + c\sqrt{n} \exp(-\beta\sqrt{n}) + d$, where $E_{f,s}$ is the formation energy of the substitutional solute and c , β , and d are the fitting parameters.

Acknowledgement

This research has been supported by the U.S. Department of Energy, Office of Science, Office of Fusion Energy Sciences (DE-AC06-76RL0-1830).

References

- [1] L. Dudarev, R. Bullough, P. M. Derlet, Physical Review Letters 100 (2008) 135503.
- [2] D. J. Bacon, R. Bullough, J. R. Willis, Philosophical Magazine 22 (1970) 31.
- [3] C. S. Becquart, et al., Journal of Nuclear Materials 403 (2010) 75.

4.7 NEUTRON IRRADIATION EFFECTS IN TUNGSTEN-COPPER COMPOSITES—L.M. Garrison, Yutai Katoh (Oak Ridge National Laboratory)

OBJECTIVE

The aim of this work is to evaluate tungsten-copper based composites for potential use in plasma-facing component of future fusion reactors.

SUMMARY

As part of the TITAN program, two types of tungsten-copper composites were irradiated in HFIR at temperatures from 300 to 900°C and fast neutron fluences of 0.01 to 20×10^{25} n/m² at E>0.1 MeV. One material was a tungsten-copper laminate composite composed of 0.1 mm alternating layers of tungsten and copper. The other material was a tungsten-copper powder sintered composite, with 75% W and 25% Cu. Tensile tests of unirradiated and irradiated tungsten-copper sintered composite have been completed.

PROGRESS AND STATUS

Previous analysis of the tungsten-copper laminate composites irradiated in the TITAN program showed that the laminate composites quickly lose ductility after low dose irradiation. The design space for such a continuous composite may be small because of the extreme mismatch of tensile strength in the two materials after irradiation.

As an alternative to the tungsten-copper laminate composite, a powder sintered tungsten copper composite with 75 wt.% W and 25 wt.% Cu was investigated. This material was produced by Mi-Tech Metals Inc. Tungsten, Indianapolis. The material is used in industrial applications such as electrodes. The sintered composite will be referred to as KW. A polished surface of one of the KW composites is shown in Figure 1. There are sharp boundaries between the rounded W particles and the Cu. As expected, no interlayer or mixed phase formed between the elements.

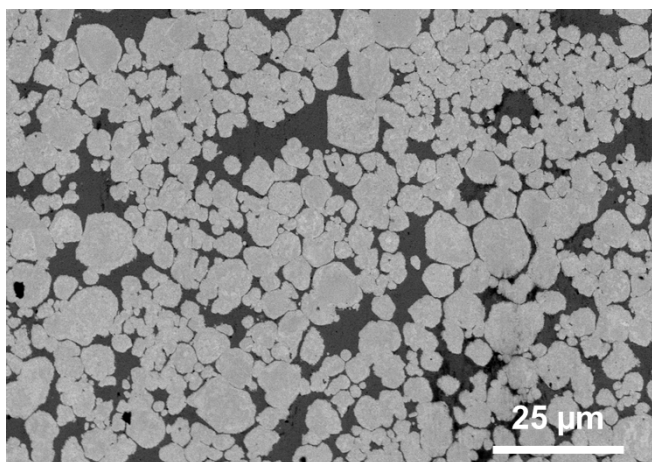


Figure 1. SEM image of the powder sintered tungsten copper composite.

Tensile and Vickers hardness tests have been completed on selected unirradiated and irradiated KW samples at room temperature, Table 1. The tensile yield stress (YS), ultimate tensile stress (UTS), uniform elongation (UE), and total elongation (TE) are listed. For these tungsten materials, the conversion $0.195 \text{ dpa} = 1 \times 10^{25} \text{ n/m}^2$ (E>0.1 MeV) was used, as given by M. E. Sawan, Fusion Eng. Des., 87(5-6), 551-555 (2012).

Table 1. Room temperature tensile and hardness data for the tungsten-copper particle composite

Capsule	ID	T _{irr} (°C)	Fast Fluence ($\times 10^{25}$ n/m ² , E>0.1 MeV)	DPA	Test Temp. (°C)	YS (MPa)	UTS (MPa)	UE (%)	TE (%)	Vickers hardness (HV)
Control	KW22			0	22	483	599	4.80	7.14	—
Control	KW23			0	22	466	577	5.58	7.42	—
TB-300-1	KW00	410	0.02	0.004	22	502	622	3.70	5.94	223.8
TB-500-1	KW08	750	0.08	0.02	22	464	586	4.97	8.40	—
TB-300-2	KW02	450	0.1	0.02	22	532	649	3.72	5.74	238.2
TB-650-1	KW15	780	0.13	0.03	22	473	611	4.67	7.21	252.4
TB-650-2	KW16	760	0.46	0.09	22	534	634	4.19	6.49	—
TB-300-3	KW04	420	0.52	0.10	22	546	634	3.28	5.13	238.4
TB-500-2	KW11	670	0.54	0.11	22	528	622	3.36	5.04	314.9
TB-500-3	KW12	630	9	1.8	22	791	828	0.93	0.98	320.2

UTS, TE, and hardness comparison of tungsten materials

Irradiation temperatures ranged from 90 to 830°C, but are grouped together for this preliminary indication of trends. Figure 2 compares the UTS for 22°C tests of KW composite, tungsten-copper laminate (SW), and two orientations of single crystal tungsten. For the single crystal tungsten, UTS is plotted as zero for cases where the sample was broken in handling. The single crystal tungsten showed irradiation strengthening at very low doses up to a maximum UTS at 0.02 dpa. After this dose, the UTS of the single crystal tungsten decreased. At the maximum tested dose of 1.8 dpa all four single crystal samples were broken in handling, qualitatively indicating the fragility of the material. Irradiation defects and transmutation to Re and Os contribute to the property change in tungsten during irradiation. Single crystal tungsten may be more sensitive to irradiation damage because it does not have grain boundaries or other internal interfaces to act as sinks for the radiation damage. In Figure 2b, dotted lines are drawn to highlight this trend of increasing and then decreasing UTS for each material.

At almost all doses, the SW composite had the highest UTS of the materials. The laminate appears to reach a maximum irradiation strengthening between 0.01 and 0.4 dpa, which is an improvement as compared to the single crystal tungsten. As dose increases beyond 0.4 dpa, however, the laminate UTS drops. In contrast to the single crystal tungsten, at the highest dose tested of 1.8 dpa, the SW composite retains some strength..

The KW data points are connected by a line segment in Figure 2a to help distinguish them. In contrast to the single crystal tungsten and SW composite, the KW composite shows nearly constant UTS values until 0.1 dpa and then an increase in UTS at the highest tested dose of 1.8 dpa. The orange dashed line in Figure 2b is intended to indicate that the KW material may not have reached the peak of irradiation hardening yet or it may decrease at higher doses.

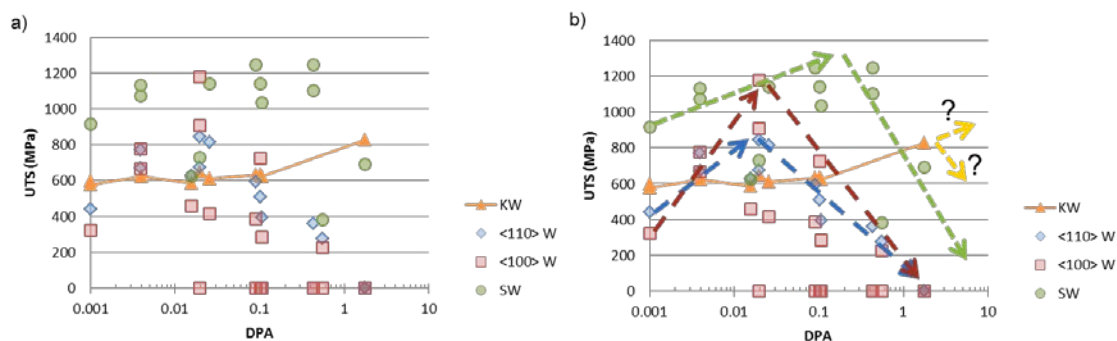


Figure 2. Ultimate tensile stress of the tungsten-copper sintered composite (KW), two orientations of single crystal tungsten, and the tungsten-copper laminate composite (SW), all tensile tested at 22°C.

The three tungsten materials had different trends of TE for 22°C tensile tests (Figure 3). Both crystal orientations of single crystal tungsten had brittle failure or very limited plastic deformation for all tested doses. The maximum TE observed for any of the single crystal tungsten was 0.5 % for 1W05-0.004-90-22. The SW composite initially had a greater TE than the other materials but the TE rapidly decreased with increasing dose. At 0.1 dpa the tungsten-copper laminate had 1% TE and for doses higher than 0.1 there was no measurable plastic deformation. In contrast, the KW composite is more consistent and TE remains above 5% through 0.1 dpa. At the highest dose tested of 1.8 dpa, the KW composite retains 1% TE.

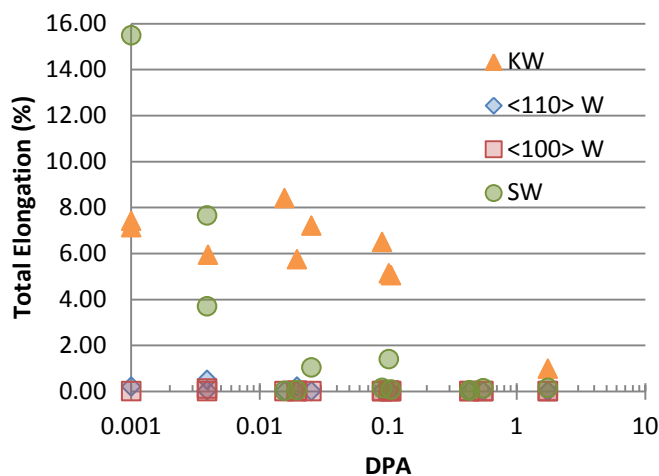


Figure 3. Total elongation comparison for the tungsten-copper particle composite (KW), two orientations of single crystal tungsten, and the tungsten-copper laminate composite (SW), all tensile tested at 22°C.

For each sample, at least five Vickers hardness indents were performed and the measurements averaged to determine the hardness of the material. For each indent, the load weight was 1000 gf and loading time was 10s. For single crystal tungsten, hardness increases with dose up to the highest dose tested of 2.8 dpa (Figure 4). The as-rolled wrought tungsten foil (OW) has the highest hardness in the unirradiated condition because the deformation during rolling introduces many dislocations. The OW tungsten shows a slight increase in hardness up to the highest tested dose of 2 dpa. The KW composite starts with the lowest hardness of these materials because it contains 25 wt.% Cu. With increasing dose, the KW material shows a similar increase in hardness as the OW tungsten, which is less than that of the single crystal tungsten.

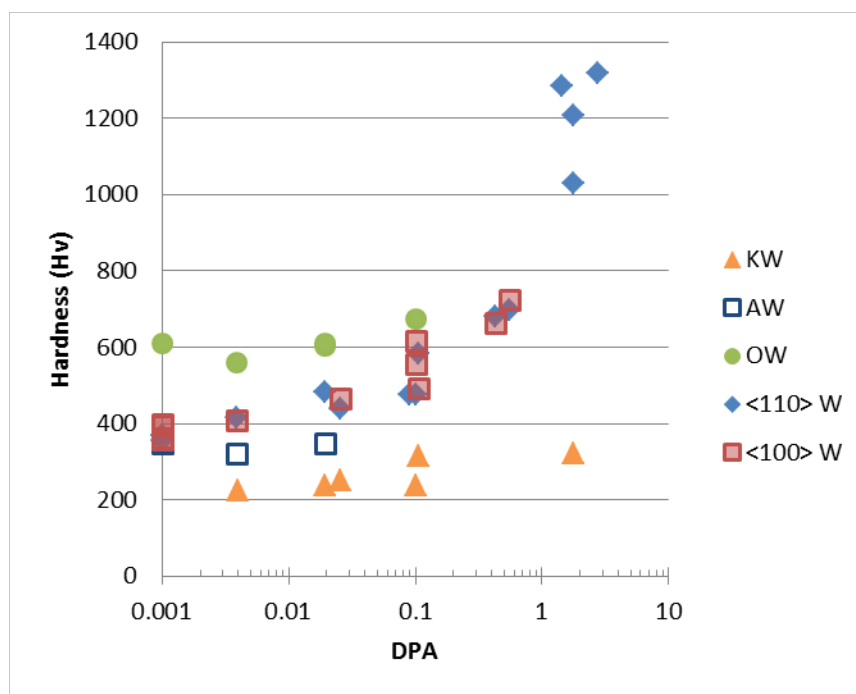


Figure 4. Hardness of the tungsten-copper particle composite (KW), single crystal tungsten with <110> orientation in the plane, single crystal tungsten with <100> orientation in the plane, annealed and recrystallized tungsten foil (AW), and as-rolled tungsten foil (OW).

Tensile data for KW composite, irradiated at 360-460°C

Individual unirradiated samples are labeled by their Sample ID and their test temperature, for example, KW23-22 for the unirradiated sample KW23 tested at 22°C. For irradiated samples, the labels include the Sample ID, dpa, irradiation temperature, and test temperature in that order. For example, KW02-0.02-450-22 was irradiated to 0.02 dpa at 450°C and tested at 22°C.

Figure 5 shows the room temperature tensile curves for the KW material irradiated to different doses at temperatures between 410-450°C. With increasing dose, the total elongation was reduced. There was a slight increase in ultimate strength with increasing dose, but all irradiated material values are similar.

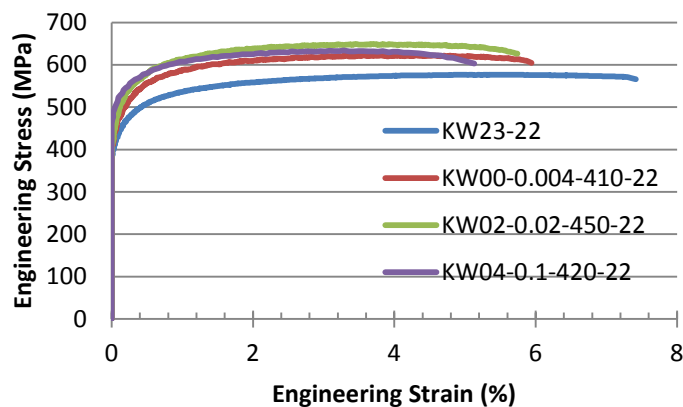


Figure 5. Tungsten-copper sintered composite irradiated at 410-450°C and tensile tested at room temperature. Only the plastic strain is shown.

Figure 6 compares the KW tensile results from Figure 5 with single crystal tungsten (1W) and SW composite irradiated to the same conditions in the range of 360-460°C and tested at room temperature. The SW composite initially has much greater elongation and higher strength than the single crystal tungsten or the KW composite, but quickly loses its ductility with increasing dose. At all doses the single crystal tungsten shows brittle failure with no plastic deformation. The KW shows less change in behavior in this range of irradiation conditions than the single crystal tungsten or SW composite.

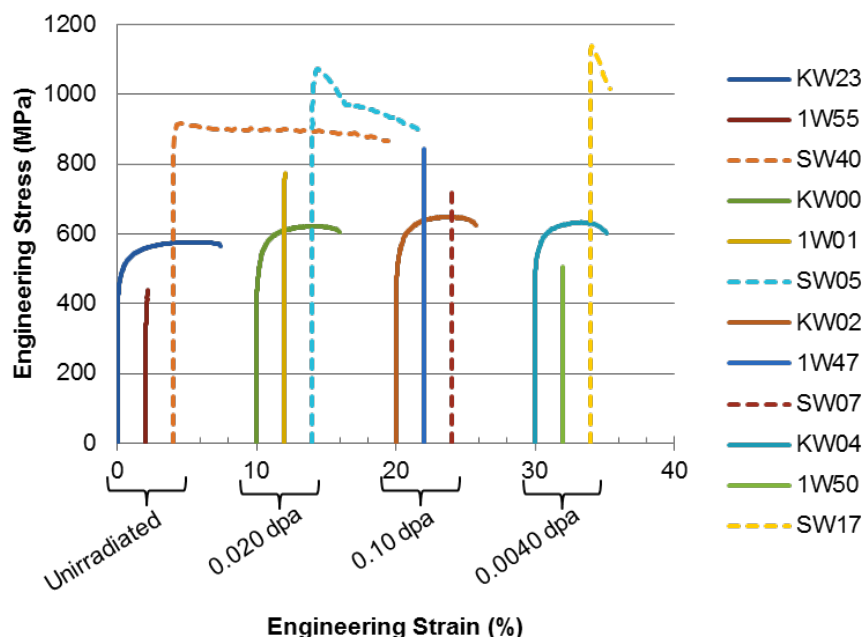


Figure 6. Comparison of tungsten-copper sintered composite (KW), single crystal tungsten with $\langle 110 \rangle$ crystal orientation along the tensile axis (1W), and tungsten-copper laminate composite (SW) irradiated at 360-460°C and tensile tested at room temperature; only the plastic strain is shown. For samples with brittle fracture, a vertical line is plotted from zero to the fracture stress.

Tensile data for KW composite, irradiated at 630-780°C

After irradiation at the higher temperature range, from 630-780°C, and tensile tested at room temperature, the KW tensile results are similar to the lower temperature group up to 0.11 dpa (Figure 7). However, at the highest dose tested, 1.8 dpa, there is a sharp increase in UTS and drop in TE. It is thus postulated that between 0.11 and 1.8 dpa the defect structure changes or accumulates to a critical level that in turn causes the changes in the mechanical behavior.

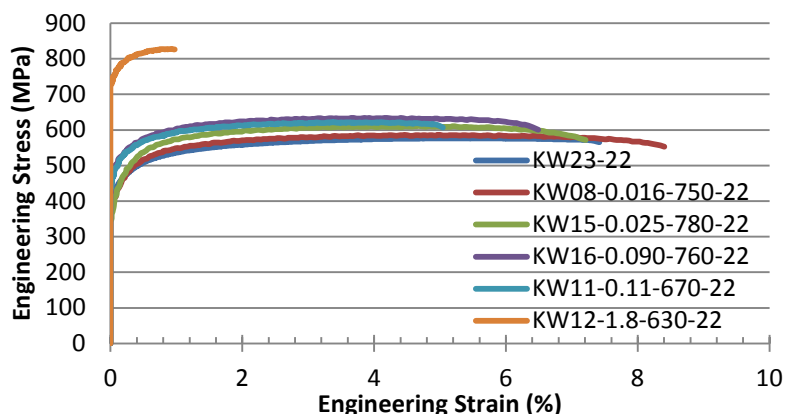


Figure 7. Tungsten-copper sintered composite irradiated at 630-780°C and tested at room temperature, only the plastic strain is shown.

Because the tensile curves for doses up to 0.11 dpa overlap, Figure 8 has an altered y-axis. While generally there is a trend of increased UTS and decreased TE with increasing dose, not every sample fits that pattern. For instance, KW08-0.016-750-22, irradiated to the lowest dose of this group, has a longer TE than the unirradiated material. There is another trend reversal between the UTS of KW11-0.11-670-22 and KW16-0.090-760-22. Between these two samples the one irradiated to the higher dose has the slightly lower UTS. The irradiation temperatures of this group have a spread of 150°C, and the sample at the highest dose that exhibited the much higher UTS and lower TE was also irradiated at the lowest temperature of the group.

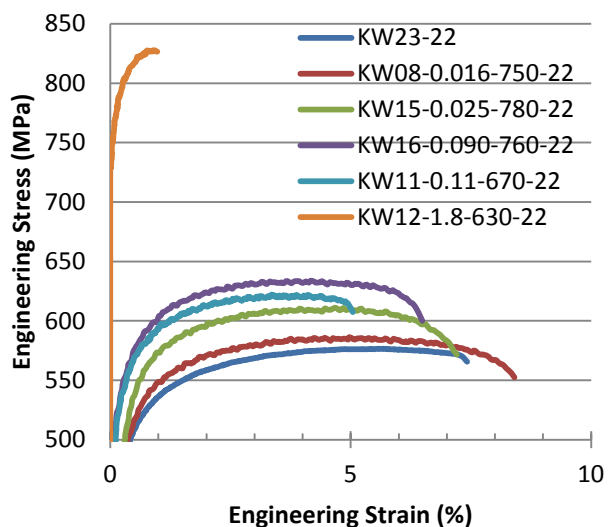


Figure 8. Tensile data from KW composite irradiated at 630-780°C and tested at room temperature. Note, in this figure the y-axis has been truncated.

Figure 9 compares the KW, single crystal tungsten (1W), and SW composite data for the higher temperature irradiated group. Groups of curves with the same dose are offset along the strain axis. The highest dose sample of single crystal tungsten in this figure is plotted with zero strength because it broke in handling. The same trend observed in the lower temperature group is seen here. The SW material quickly loses its ductility but remains stronger than the other materials up through 0.11 dpa. The single crystal tungsten shows brittle failure in all conditions. The KW material has consistent tensile curves through 0.11 dpa, and then has an abrupt increase in strength at 1.8 dpa while maintaining 1% TE.

Although the KW properties were changed by the irradiation, this indicates that after 1.8 dpa, the KW still has a DBTT above room temperature.

The plan for continuing to investigate the KW material includes elevated temperature tensile tests, tensile tests of material irradiated to higher doses, and examination of the microstructure and fracture surfaces.

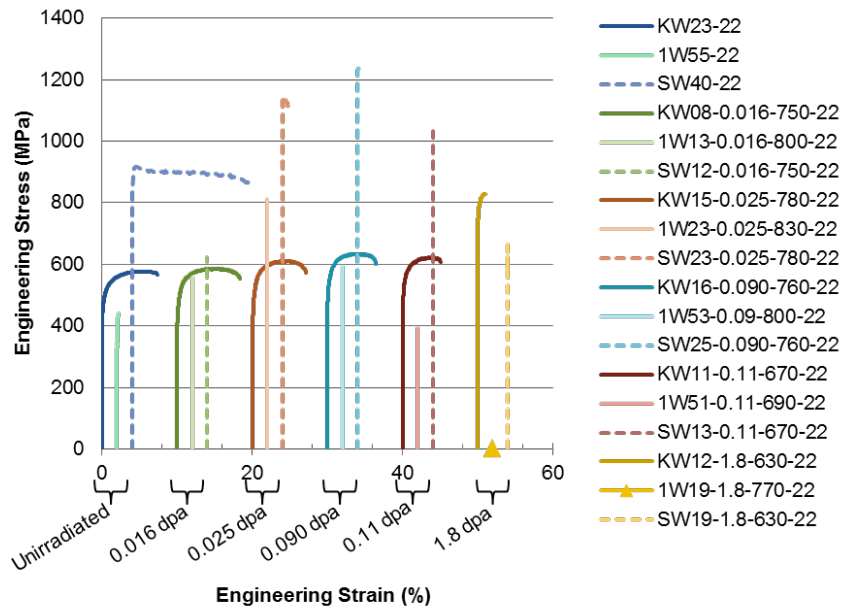


Figure 9. Comparison of tensile curves of the tungsten-copper sintered composite (KW), single crystal tungsten (1W), and tungsten-copper laminated composite (SW). All materials were irradiated at 630-830°C and tensile tested at room temperature; only the plastic strain is shown.

4.8 HIGH-HEAT FLUX TESTING OF LOW-LEVEL IRRADIATED MATERIALS USING PLASMA ARC LAMPS—A.S. Sabau, S. Gorti, C. Schaich, J. Kiggans, Y. Katoh (Oak Ridge National Laboratory)

OBJECTIVE

The objective of this work, part of the PHENIX collaboration with Japan, is testing of irradiated materials that are candidates for divertor components and mock-up divertor components under high-heat flux using Plasma Arc Lamps (PAL).

SUMMARY

Thermo-mechanical model simulations of the high-heat flux testing (HHFT) of W/SiC specimens were completed. Preliminary results indicated that stresses experienced by the specimens during HHFT are relatively small compared to those for the W/F82H specimens. A new line-focus reflector for the Plasma Arc Lamp was designed to increase the heat flux to its maximum achievable for the maximum arc temperature. The fabrication of the reflector is imminent.

PROGRESS AND STATUS

Effort this reporting period was conducted in two main areas: (a) thermo-mechanical analysis of HHFT of W/SiC specimens, and (b) increasing the heat flux available with the PAL facility.

The data acquired during HHFT of W/SiC specimens at ORNL in collaboration with Dr. Kenzo Imano of Osaka University, Japan, as part of his assignment for the joint US/Japan PHENIX program, was analyzed. Specimens were those supplied by the Japanese in the PHENIX program. The main variables in the high-heat flux testing were the number of cycles at high heat flux and average cycle duration (Table 1). The diameter of the W/SiC specimens was 10 mm. The thickness SiC was 1 mm while the W thickness was 1 or 2 mm.

Table 1. High-heat flux testing of W/SiC. Main variables were the tungsten layer thickness and number of cycles at high-heat flux

No.	W thickness [mm]	¹ No. Cycles	¹ Average cycle time [s]	Cycle duration [s]	Max. Heat Flux [W/cm ²]	Average Heat Flux [W/cm ²]	Total heat input [MJ/cm ²]	Total time at high-heat flux [s]
1	2	122	11.1	10-15	288	264	0.361	1,356
2	2	100	10.9	5-15	300	274	0.301	1,094
3	1	101	11.3	10-15	288	272	0.311	1,146
4	1	132	13	10-18	288	274	0.478	1,731

¹ Number of cycles at heat fluxes above 210 W/cm².

The thermo-mechanical models for the simulation of entire HHFT tests were implemented in the ABAQUS™ software and numerical simulations were conducted for samples S1 and S3 by taking into account the actual high-heat flux cycles. Temperature-dependent thermophysical and elastic mechanical properties for the SiC were used as input in the numerical simulations of the HHFT. One of the main modeling assumptions is that the clamp is a rigid body, i.e., the distance between the clamp surface and the back side of the Cu washer was held constant. For the last HHFT cycle, the calculated temperatures at the top surface of W are shown in Figure 1 for thermal contact conduction (TCC) per unit area (between the SiC and Cu washer) of 4,000, 5,000, 6,000 and 7,000 [W/m²K]. The calculated temperatures showed that the temperatures were relatively low. This data also indicate that the HHFT

cycle duration can be shortened to 7-8 s, as the surface temperatures approached the linear change regime in this short time.

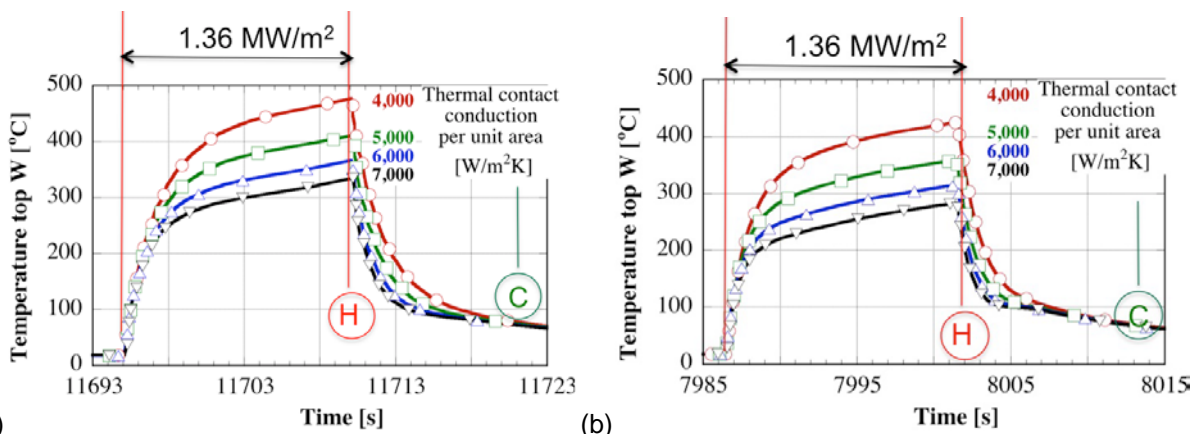


Figure 1. Calculated temperature evolution during a HHF cycle for several values of thermal contact conduction between the SiC and Cu washer.

The results for the Von Mises stress [in Pa] and for a TCC of 5,000 [W/m²K] are shown in Figures 2 and 3 at high temperature (Hot), i.e., right at the end of the HHF, and at room temperature (Cold), respectively. The stresses are shown on a deformed mesh in order to illustrate the changes in the specimen geometry during HHFT, with the deformation scale of 50. The left-hand-side of each figure is the centerline of the specimen. In order to illustrate the mechanical effect of clamping, the results are shown in Figure 3 for an unclamped specimen, although at the same thermal contact conduction as the clamped specimen. The following observations can be made with respect to the stress and deformation results:

- At high temperatures, the specimen bulged *upward* at its center, resting on the clamp outer edges,
- At room temperature, before clamp removal, the specimen is undeformed as it underwent only elastic deformation. The stresses are highest in the SiC but are still very low at approximately 7 MPa.
- For the clamped specimen (Figure 2), the predicted residual stresses are highest in W and are located around the edge of the specimen in the clamped region. However, the stresses are small, approximately 74 MPa at a W temperature of 400 C. The highest stress levels at the W-SiC interface were approximately 50 MPa.
- For the unclamped condition (Figure 3), the predicted residual stresses are highest at the W/SiC interface, at approximately 50 MPa.

For the un-clamped condition, the stresses in W would be under predicted, while the stresses in the SiC (actually, at the W-SiC interface) would be over-predicted.

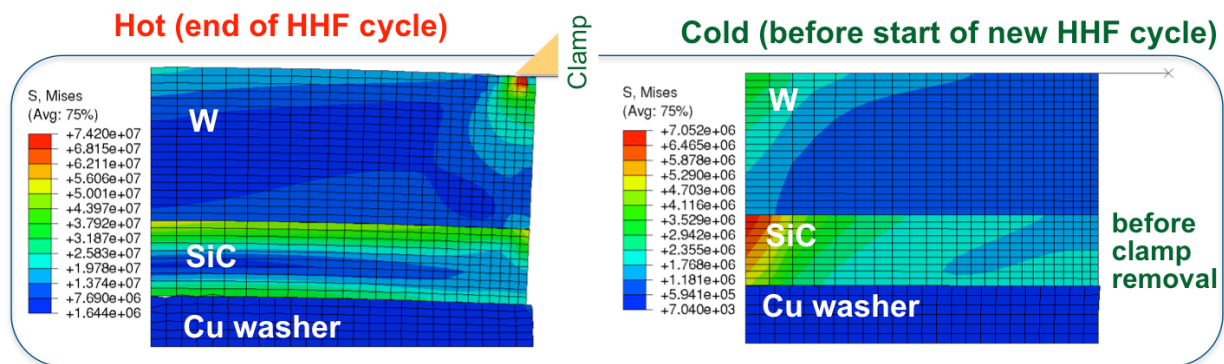


Figure 2. Von Mises stress results for S1 specimen at high temperature (Hot), i.e., right at the end of the HHF, and at room temperature (Cold). The SiC-Cu TCC per unit area was 5,000 [W/m²K].

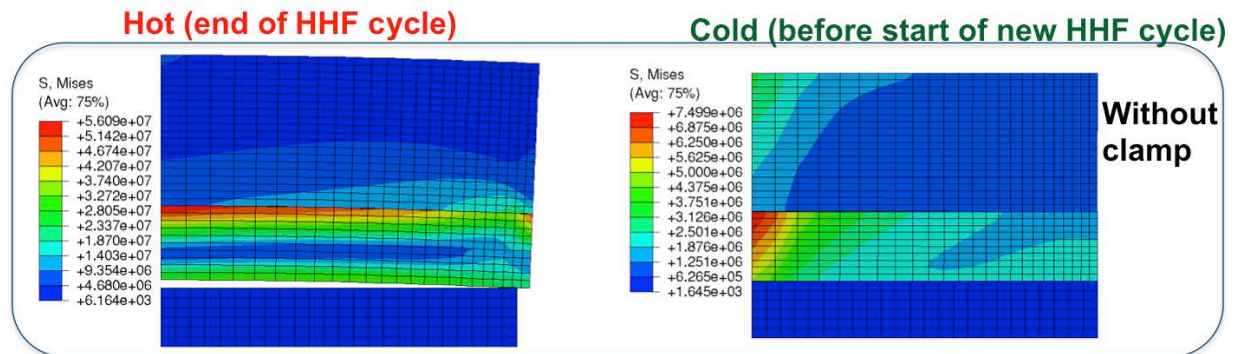


Figure 3. Von Mises stress results for an *unclamped* S1 specimen at high temperature (Hot), i.e., right at the end of the HHF, and at room temperature (Cold). The SiC-Cu TCC per unit area was 5,000 [W/m²K].

An effort is underway focused on increasing the incident heat flux from PAL using a new line-focus reflector. The new reflector was designed by Mattson Technologies, Inc. Mattson Technologies conducted simulations for various reflector shapes using a proprietary model of the volumetric distribution of the heat source within the plasma arc, which is confined in a quartz tube. The actual thicknesses of quartz fixtures (windows, dome or cylinder) used for radiological containment were considered in the model simulations conducted at Mattson Technologies, illustrated in Figure 4.

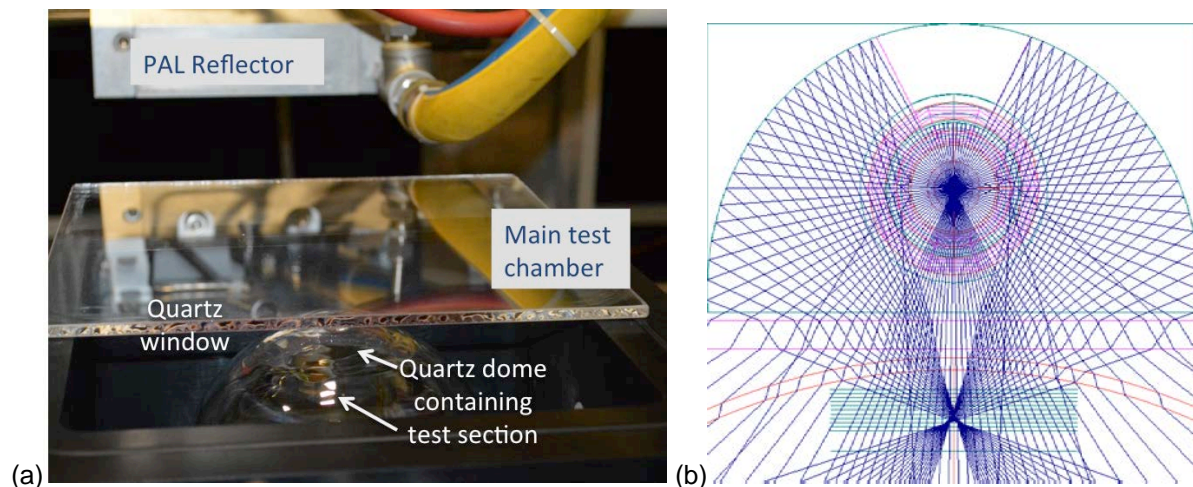


Figure 4. The main configuration components of the PAL experimental setup (PAL reflector, quartz window, and quartz dome): (a) picture of the setup and (b) schematic of ray tracing toward the specimen.

Mattson Technologies provided ORNL with schematics for various reflector shapes simulated (Table 2). The various thicknesses of quartz fixtures (windows, dome or cylinder) used for radiological containment are given in mm in Table 2. It was found that the best case for the current ORNL program is the case in which the test section is contained in a quartz dome. The maximum heat flux that is estimated to be attained for the dome configuration is 12 MW/m². The current activities to upgrade the heat-flux capabilities of the PAL facilities at ORNL are shown in Table 3. The fabrication of the reflector is imminent.

Table 2. Cases simulated to obtain heat flux through the containment chamber onto the specimen surface. The thickness of quartz fixtures are given in mm.

Test configuration	Peak Flux [MW/m ²]	Containment chambers	Applicability
Horizontal tube test section	14	Tube (3mm)	Mockup specimen only
Dome test section	12.3	Dome (3mm)	<i>Best for current setup</i>
Thin quartz window	11.7	Window (7mm)	
Thick quartz window	9.4	Window (25mm)	
Thick quartz and dome	8.3	Window (25mm) Dome (3mm)	To be used only when two containment chambers are needed
Baseline (current uniform reflector)	4	-	

The maximum heat flux from the reflector without containment was estimated to be 21 MW/m².

Table 3. Activities designing, fabrication, and installation of 12 MW/m² reflector on the ORNL PAL

Activity	Responsibility	Progress to date	Planned Completion	Completion
Obtain reflector shape	Mattson	completed	10/15/16	10/30/16
Component drawings	Mattson	completed	12/1/16	12/15/16
Pyrometer placement, reflector holes	Mattson, ORNL	completed	12/1/16	12/15/16
Structural support of reflector	Mattson, ORNL	completed	12/30/16	1/10/17
Design of test section to allow the use of new reflector	ORNL	completed	1/13/17	1/13/17
Fabrication of new test section components	ORNL	ongoing	2/17/17	
Assembly of new test section at ORNL	ORNL	scheduled	2/28/17	
Fabrication quotes for reflector components	Mattson	completed	12/30/16	1/10/17
Coating and polishing quotes for reflector surfaces	Mattson	ongoing	12/30/16	
Assembly of new reflector at ORNL	ORNL	scheduled	2/28/17	

5. MAGNETIC AND DIAGNOSTIC SYSTEM MATERIALS

No contributions this reporting period.

6. FUSION CORROSION AND COMPATIBILITY SCIENCE

6.1 CHARACTERIZATION OF FeCrAlMo AFTER EXPOSURE TO FLOWING Pb-LI AT 500°-600°C– B. A. Pint and J. Jun (Oak Ridge National Laboratory, USA)

OBJECTIVE

This task is investigating the possibility of increasing the Pb-Li temperature in the dual coolant lead-lithium (DCLL) blanket concept in order to improve the overall system efficiency. Alloys based on FeCrAl are a potential candidate and monometallic thermal convection loops of a commercial FeCrAl alloy are being built and operated to establish a maximum operating temperature for operation in flowing eutectic Pb-Li.

SUMMARY

The second monometallic thermal convection loop (TCL) using Kanthal FeCrAlMo alloy APMT tubing and specimens completed 1000 h using commercial purity eutectic Pb-Li with a peak temperature of 600°C. Characterization of the oxide surface morphologies after exposure based on the pre-oxidation conditions suggests that the oxide formed in PbLi is the most adherent. The tensile properties of selected hot and cold leg specimens have been measured at room temperature and no significant degradation occurred between 515°-600°C in the second loop.

PROGRESS AND STATUS

Introduction

The DCLL blanket concept (eutectic Pb-17 at.%Li and He coolants) is the leading U.S. design for a test blanket module (TBM) for ITER and for a DEMO-type fusion reactor[1]. With reduced activation ferritic-martensitic (FM) steel as the structural material, the DCLL is limited to ~475°C metal temperature because Fe and Cr readily dissolve in Pb-Li above 500°C and Eurofer 97 plugged a Pb-Li loop at 550°C.[2-3] With the addition of Al to Fe-Cr alloys, isothermal compatibility tests have shown low mass losses at up to 800°C [4-7]. Thermodynamic evaluations [8,9] indicated that Al₂O₃ should be stable in Pb-Li and inhibit dissolution by forming at the alloy surface, however, capsule studies found that a preformed α -Al₂O₃ surface layer transformed to LiAlO₂ during exposures at 600°-800°C [4,10]. To further evaluate the Pb-Li compatibility of FeCrAl-type, exposures in flowing Pb-Li are needed where changes in solubility with temperature can drive mass transfer [2,11]. In 2014, a monometallic thermal convection loop (TCL) was operated for 1000 h with a peak temperature of 550°C using commercial Fe-21Cr-5Al-3Mo alloy (Kanthal APMT) tubing and specimens in the hot and cold legs [12-15]. This was the first time that Pb-Li was flowed at 550°C without plugging flow and only small mass losses were noted after the exposure. In 2016, a second monometallic FeCrAlMo TCL was operated for 1000 h with a peak temperature of 600°C [16]. The FeCrAlMo specimens from the second loop are being characterized while the third FeCrAlMo loop is being assembled for operation at a peak temperature of 650°C.

Experimental Procedure

The details of the TCL construction and operation have been previously described in detail [12-14,16]. The TCL was ~1 m tall and 0.5 m wide and heated on one side by resistively heated furnaces (i.e. the hot leg). The loop contained two specimen chains of 20 SS-3 type (25 x 4 x 0.9 mm) APMT specimens connected with APMT wire. One in the hot leg and one in the cold leg. Most of the specimens were heated treated for 8 h at 1050°C in air to form an α -Al₂O₃ surface layer or scale. Two specimens in each chain had no pre-oxidation treatment, preoxidation for 2 h at 1000°C and preoxidation for 8 h at 1100°C. Rectangular

coupons of unalloyed tungsten were attached at the bottom of each specimen chain to act as a “sinker” to keep the relatively low density specimen chains from floating in the Pb-Li test fluid, and to act as “spacers” to keep the specimen chain centered within the tubing and liquid metal flow path. Commercial purity Pb-17Li was used with impurity levels of 1200ppmw O, 240 ppmw C and <10 ppmw N (average of 6 samples) and no metallic impurities above the detection limit of ~1 ppmw. Six thermocouples in thermowells that protruded about 0.3 cm into the flow path at the top, bottom and middle of each leg monitored the temperature during operation. The temperature data were used to estimate the exposure temperature of each specimen. The temperature gradient in the loop was ~85°C from 515°-600°C and the velocity was measured at 0.6-0.7 m/min by heating a section of the tubing using a gas torch and tracking the temperature spike as the heated liquid moved around the loop. Following 1000 h of operation at 600°C, the Pb-Li was drained into the dump tank at the bottom of the cold leg. After removal, specimens were soaked in cleaning solution (1:1:1 mixture of ethanol, hydrogen peroxide, and acetic acid) while within the loop (as an assembled chain) and again upon removal from the loop (as individual specimens). The SS-3 specimens were tensile tested at room temperature with a 10^{-3} s^{-1} strain rate. Selected specimens were examined using scanning electron microscopy (SEM) equipped with energy dispersive X-ray (EDX) analysis.

Results and Discussion

Prior to tensile testing, the surface oxide morphology was evaluated for the 4 different starting conditions: as-received (without preoxidation) and pre-oxidation at 1000°, 1050° and 1100°C. Figures 1 and 2 show

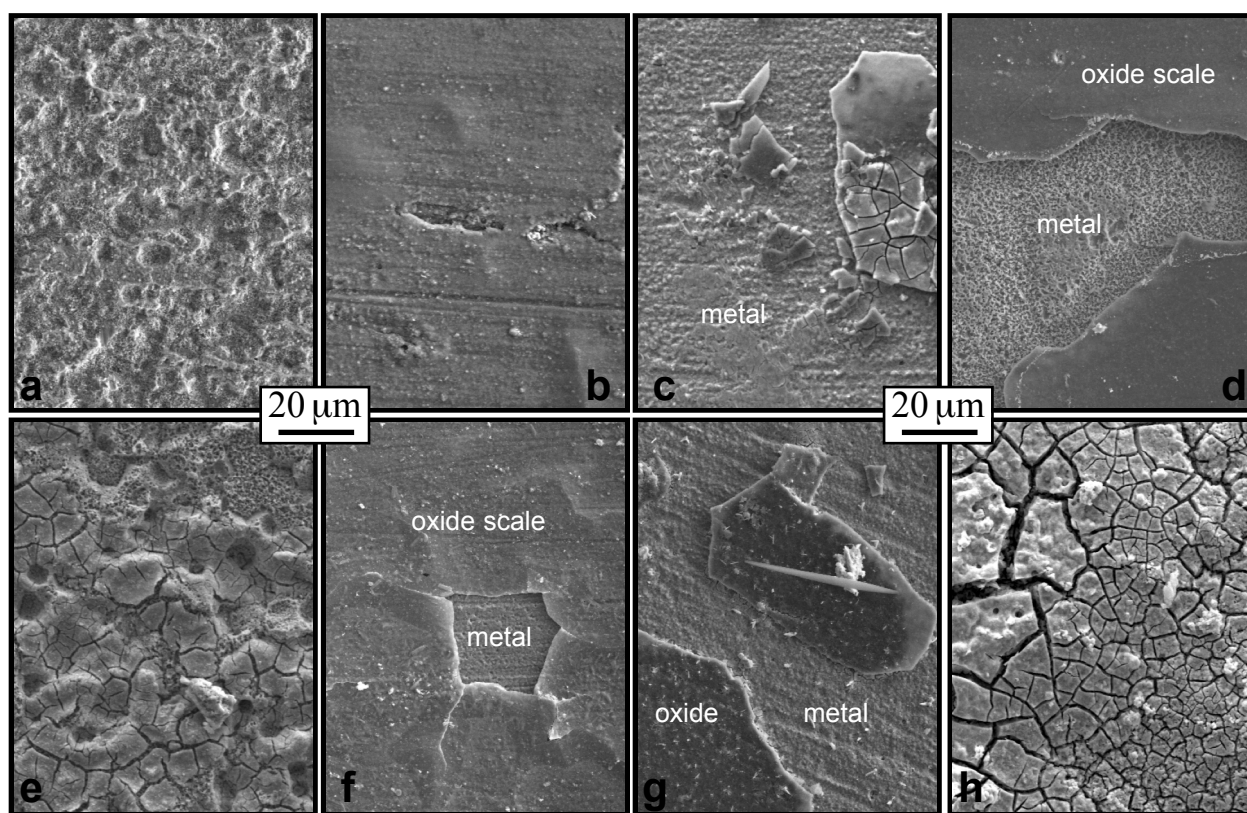


Figure 1. SEM plan view images of the reaction product formed on (a-d) hot leg and (e-h) cold leg specimens, (a,e) as-received (no pre-oxidation) and preoxidation at (b,f) 1000°C, (c,g) 1050°C and (d,h) 1100°C.

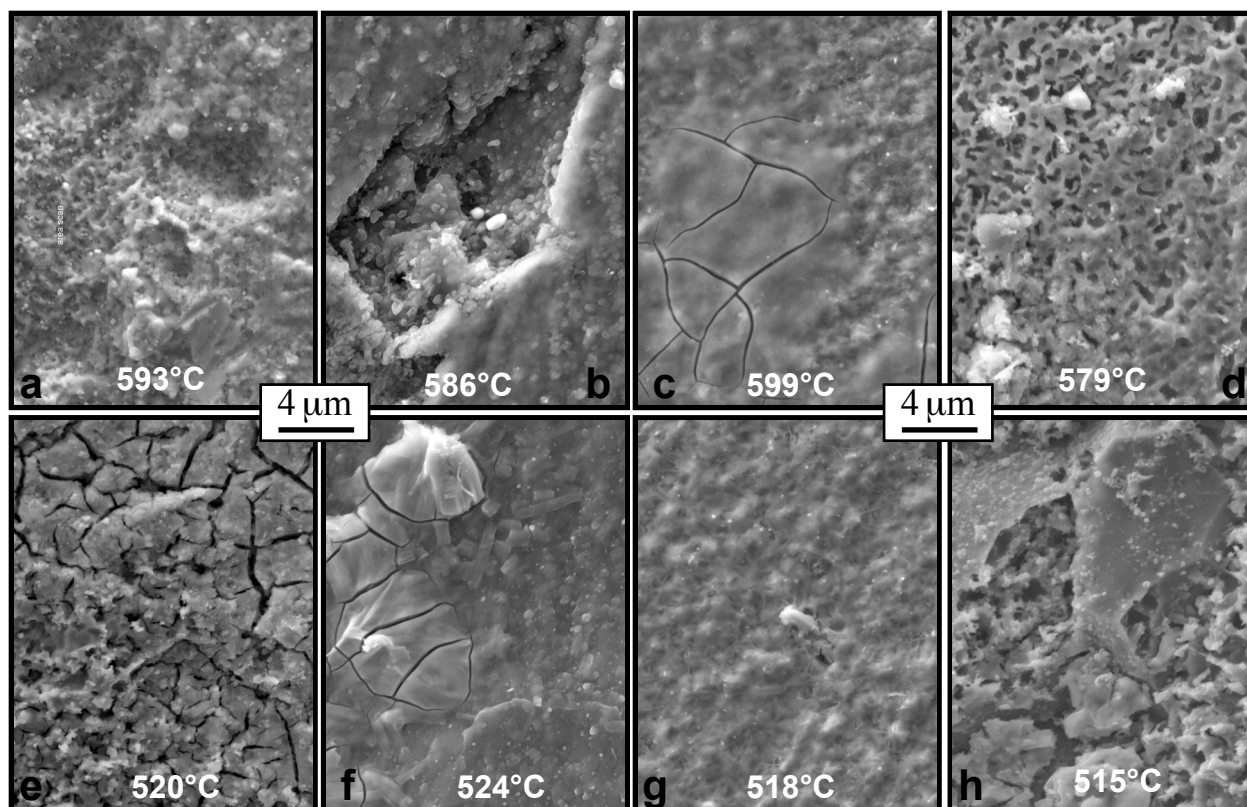


Figure 2. SEM plan view images of the reaction product formed on (a-d) hot leg and (e-h) cold leg specimens, (a,e) as-received (no pre-oxidation) and preoxidation at (b,f) 1000°C, (c,g) 1050°C and (d,h) 1100°C.

the oxide morphologies at two magnifications for the hot and cold legs. The estimated temperature of each specimen is shown in Figure 2. Poor oxide scale adhesion was noted on all of the pre-oxidized specimens despite the variation in pre-oxidation temperature, Figure 1, which changed the thickness of the initial oxide from ~1 μm after 2 h at 1000°C [10] to several microns for 8 h at 1100°C. In prior capsule exposures, it was not uncommon to observe significant scale spallation after 600°C isothermal testing [4]. The scale was more adherent on the specimens that were not pre-oxidized, Figures 2a and 2e. These specimens typically showed significantly higher mass loss, presumably due to dissolution before the oxide could form [16]. X-ray diffraction was used to examine the specimens but the oxide phase could not be positively identified during an initial evaluation. Previous studies determined that the pre-formed α -Al₂O₃ [10] transformed to LiAlO₂ during the exposure [4,10,15].

Figure 3 summarizes the room temperature yield strength (YS) and total plastic elongation measured in both the 550° and 600°C TCLs. The shaded areas denote the range of pre-exposure properties of YS (~640 MPa) and elongation (~24.5%). For the 600°C loop, the exposure temperatures were 515°-600°C and the tensile properties were not strongly affected with some loss in ductility and a slight increase in YS observed. In contrast for the 550°C loop, below ~500°C there was a significant increase in YS and decrease in ductility associated with the formation of α' [15]. This behavior was consistent with the well-known 475°C embrittlement of ferritic steels [17]. In the 600°C TCL, this temperature range was not encountered and no embrittlement was observed. Approximately half of the hot and cold leg specimens were broken at room temperature. Additional tensile testing may be conducted at a higher temperature such as 550°C. The broken specimens are being metallographically sectioned to further study the

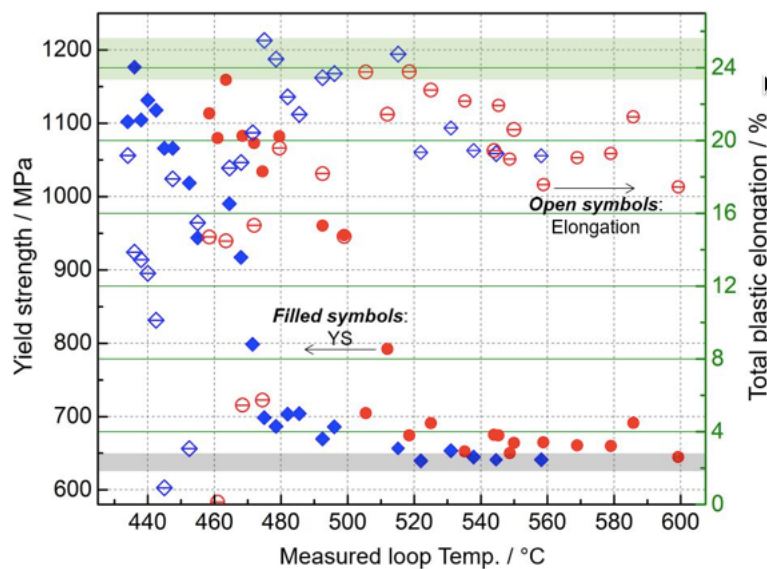


Figure 3. Room temperature tensile properties of FeCrAlMo alloy specimens as a function of exposure temperature in the 550° and 600°C TCLs. Hot leg specimens are red and cold leg specimens are blue.

remaining oxide scale and any composition gradients in the substrate.

References

- [1] M. Abdou, D. Sze, C. Wong, M. Sawan, A. Ying, N. B. Morley and S. Malang, *Fus. Sci. Tech.*, 47 (2005) 475.
- [2] O. K. Chopra, D. L. Smith, P. F. Tortorelli, J. H. DeVan and D. K. Sze, *Fusion Technol.*, 8 (1985) 1956.
- [3] J. Konys, W. Krauss, J. Novotny, H. Steiner, Z. Voss and O. Wedemeyer, *J. Nucl. Mater.* 386-88 (2009) 678.
- [4] B. A. Pint, L. R. Walker and K. A. Unocic, *Mater. High Temp.* 29 (2012) 129.
- [5] K. A. Unocic and B. A. Pint, *J. Nucl. Mater.* 455 (2014) 330.
- [6] B. A. Pint, S. Dryepondt, K. A. Unocic and D. T. Hoelzer, *JOM* 66 (2014) 2458.
- [7] K. A. Unocic, D. T. Hoelzer and B. A. Pint, *Mater. High Temp.* 32 (2015) 123.
- [8] P. Hubberstey, T. Sample and A. Terlain, *Fusion Technol.*, 28 (1995) 1194-9.
- [9] P. Hubberstey, *J. Nucl. Mater.* 247 (1997) 208.
- [10] B. A. Pint and K. L. More, *J. Nucl. Mater.* 376 (2008) 108.
- [11] J. H. DeVan, *J. Nucl. Mat.*, 85-86 (1979) 249.
- [12] S. J. Pawel, DOE-ER-0313/56 (2014) 178.
- [13] S. J. Pawel, DOE-ER-0313/57 (2014) 132.
- [14] S. J. Pawel, DOE-ER-0313/58 (2015) 185.
- [15] S. J. Pawel and K. A. Unocic, *submitted* *J. Nucl. Mater.*
- [16] B. A. Pint and S. J. Pawel, DOE-ER-0313/60 (2016) 137.
- [17] P. J. Grobner, *Metal. Trans.* 4 (1973) 251.

7. MECHANISMS AND ANALYSIS

7.1 THERMAL AND ELECTRICAL PROPERTIES OF MAX PHASES AFTER NEUTRON IRRADIATION—C. Ang*, C. Shih, S.J. Zinkle, C. Silva, C. Parish, N. Cetiner, P. Edmondson, Q. Smith and Y. Katoh (Oak Ridge National Laboratory)

OBJECTIVE

$M_{n+1}AX_n$ (MAX) phase materials are candidate ceramics for advanced reactor technology and continue to be evaluated at Oak Ridge National Laboratory. Three prior publications have concluded that irradiation tolerance improves at temperatures above 600°C, but recovery is incomplete. This small program is currently exploring fundamental understanding of defect evolution by investigation of thermophysical properties. Previous data on unirradiated properties have been reported in DOE/ER-0313/58.

SUMMARY

$M_{n+1}AX_n$ (MAX) phases of “ Ti_3SiC_2 ” and “ Ti_2AlC ” composition were neutron irradiated in HFIR to 2×10^{25} n/m² ($E > 0.1$ MeV) or ~ 2 dpa based on the SiC displacement cross-section (see DOE/ER-0313/58). Compositions were determined to be $\sim 80\%$ MAX phase. During irradiation at $\sim 400^\circ\text{C}$, 5-10 wt% or less decomposed to MX. Swelling was higher in the Al-variant, with a c-axis swelling ($\Delta c/c$) of 3.1% compared to 1.6% for the Si-variant. After irradiation at $\sim 630\text{-}700^\circ\text{C}$, unit cell swelling was not observed, and equibiaxial flexural strength values were within 80-95% of unirradiated values. The prior program under the Unique Materials FOA was able to obtain thermal diffusivity and dilatometry annealing data, but the quantitative determination of activation energies was improved by electrical resistivity annealing. This was obtained in a Nuclear Science User Facilities Rapid Turnaround Experiment in October 2016. Preliminary data suggested differences in defect configurations, and/or concentrations of defects in Ti_3SiC_2 and Ti_2AlC_2 .

PROGRESS AND STATUS

Introduction

The attraction of $M_{n+1}AX_n$ (MAX) phases as engineering ceramics is due to their ability to mitigate catastrophic failure by confining flaws within grains. The “A-layer” metal (Al or Si atoms) alternating between crystalline “MX” ceramic (Ti-C in this case) unit cells appears crucial for not only these mechanical properties, but also for the electronic contribution to thermal conductivity and electrical conductivity. Defects in the A layer likely result in scattering of conduction band electrons. Three methods are currently being used to quantify the defect damage using electrical resistivity annealing and thermal diffusivity data.

Experimental Procedures

The samples used for thermal diffusivity were cylindrical disks 6 x 1.5(t) mm. Thermal diffusivity was measured by ASTM E1461 using a NETZSCH LFA 457 Micro Flash Laser Flash Thermal Diffusivity Apparatus on samples cut from the same block of material. Measurements were done at room temperature and from 100 to 1000°C at 100°C intervals at 10 °C/min and a dwell time of 30 minutes. The electrical resistivity was measured using the four-point probe method following the guidelines of ASTM B193 and F390 using the sheet resistivity method on 6 x 6 x 0.5 mm discs, which was correlated to reference samples with sample dimensions 25 x 2 x 1.5 mm using ASTM C611. The current was generated using a KEITHLEY 2400 Source Meter and the voltage drop across the probes was measured using a KEITHLEY 2192A Nanovoltmeter. For the sheet resistivity technique, three measurements were conducted on four duplicate samples (total of 12 measurements). Samples were heated to the selected annealing temperature and held for 30 minutes, and then after cooling to room temperature electrical resistivity was measured. For further details, see DOE/ER-0313/55 and 58.

Results

X-ray characterization of the compositions included Rietveld analysis of XRD data by GSASTM, TOPASTM v4.2 and CrystalDiffractTM Suite. Therefore, the first method to quantify defect damage is an ad hoc application of the Wiedmann-Franz Law, which indicates that the electronic proportion of thermal conductivity can be calculated from the product of the Lorenz number, the proportionality constant and the electrical conductivity. By quantitative XRD of the phases and using unirradiated electrical conductivity values of the material, the individual contributions from the intermetallic and carbide impurities using values from literature can be subtracted from the total diffusivity (or conductivity) over the annealing temperature. This can correct and determine the actual loss of thermal conductivity in MAX phase materials after neutron irradiation and is currently underway.

The electrical resistivity annealing can be correlated to lattice parameter changes. Figure 1(a) shows the compiled cell volume change of MAX phases from this work and other data from literature. The plot contains cell volume changes from irradiations to >2 dpa and assumes saturation swelling at each irradiation temperature. For both Ti_3SiC_2 and Ti_3AlC_2 , the reduction in cell volume swelling appears linear at irradiation temperatures between 0 and 700°C.

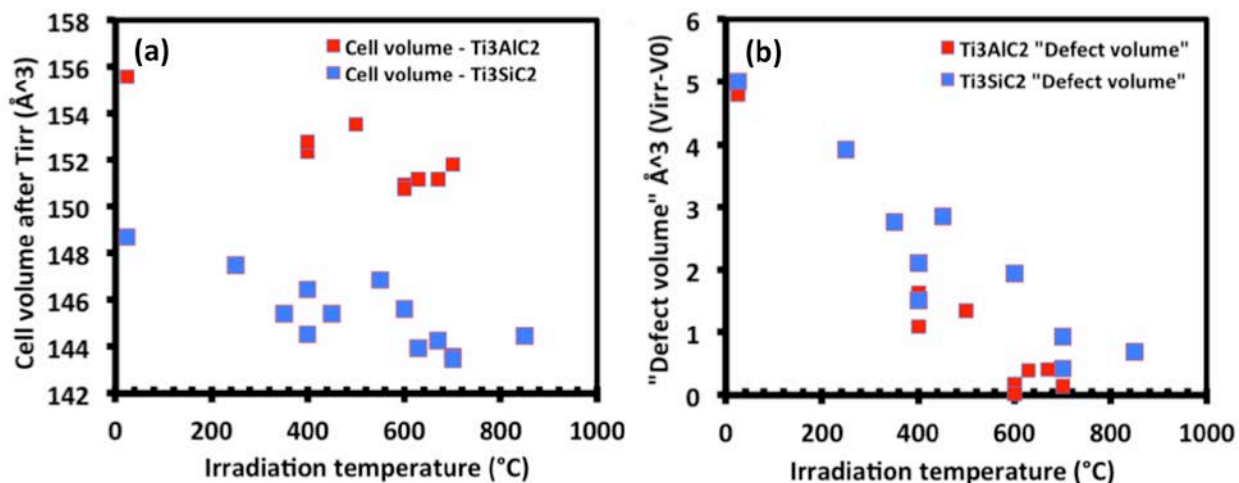


Figure 1. (a) Cell volume of MAX phases after irradiation at selected temperatures, calculated from Ref.[1-3] (b) "Defect volume" calculated from changes in cell-volume after irradiation

Figure 1(b) shows that when the volumetric swelling is subtracted from the original unit cell volumes, the lattice volume of defects in Ti_3SiC_2 is larger than in Ti_3AlC_2 at the same irradiation temperatures. This can be explained by a-axis shrinkage (~1%) in Al- variants, and is minimal (-0.1%) in the Si-variants. This result appears surprising given that the volumetric, macroscopic swelling of Al-variants has thus far been larger than Si-variants. However, it is in agreement with ab initio calculations that suggested that antisite defects would mitigate volume variation in Al-variants compared to Si-variants. TEM imaging of Ti_3AlC_2 after irradiation at ~630°C has indicated antisite defects are still stable. This suggests that surviving defect concentrations are different in the two materials.

The electrical resistivity annealing data from two samples irradiated at ~400°C are shown in Figure 2(a). The electrical resistivity is shown as a function of the thermal annealing temperature, where each data point indicates the electrical resistivity after a 30 minutes hold time at temperature. The electrical resistivity change is significantly larger for the Al-variant and when normalized (not shown), is significantly higher than the Si variant. The resistivity recovers as the annealing temperature is increased, until the defect that is responsible can migrate during annealing, and it no longer degrades the electronic conductivity. However, since conduction electron scattering is proportional to mean free path, this

supports the presumption that surviving defect fractions are higher in the Al- material. Figure 2(b) shows the derivative (by linear approximation) of the resistivity with annealing temperature and indicates that the peak “characteristic” annealing temperature is $\sim 750^\circ\text{C}$.

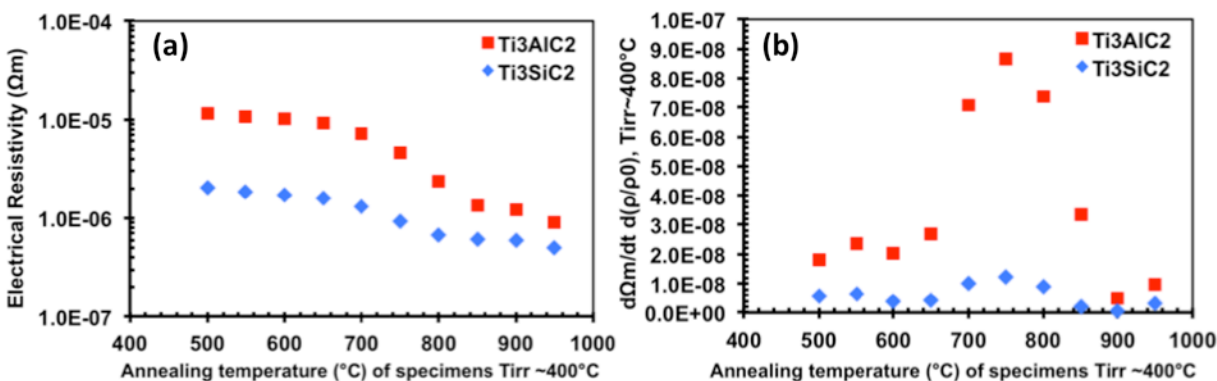


Figure 2. (a) Electrical resistivity annealing of MAX phases after irradiation at $\sim 400^\circ\text{C}$ (b) Linear approximation of change in resistivity with temperature after annealing

Since lattice parameter recovery and resistivity were reportedly identical to unirradiated materials during irradiations at $\sim 695^\circ\text{C}$ [4], this would seem to indicate these are the respective recovery (600°C) and annealing ($700\text{--}750^\circ\text{C}$) temperatures where point-defects annihilate or collapse to form defect clusters (such as dislocation loops). As expected, the thermal annealing temperature is higher than the dynamic recovery temperature, due to the contribution from radiation-enhanced diffusion. Crucially, the characteristic annealing temperature appears to be identical for both MAX phases. This suggests similarities in the migration energy (including the binding contribution) in the defect causing loss of electron-derived electrical conductivity in both materials.

Conclusions and Future Work

The analysis of the data is continuing; (1) the application of Wiedmann-Franz with quantitative XRD, which should show that thermal diffusivity change of the MAX phases (eliminating the MX:MA phases) after irradiation should be similar to the electrical resistivity data after neutron irradiation. (2) The electrical resistivity data can be used to determine the activation energy for the migration of the defect responsible for lattice parameter recovery, mechanical, thermal and electrical properties. The temperature-compensated time data from isothermal annealing is not available, and the experimental data from Figure 2(a) and (b) assumed that each annealing pulse has reached the isothermal asymptote. The resistivity versus annealing temperature, and the resistivity versus neutron flux (exposure curve) are available. A function relating resistivity to the defect concentration has not yet been developed. Finally, (3) the linear-appearing slope of the lattice parameter change versus irradiation temperature could be used to approximate the thermal or electrical properties change over annealing temperature; this may be used to develop a simple relation between defect concentration and resistivity.

Publication

Part of this work was included in a journal paper submitted during the reporting period: C. Ang, C. Shih, C. Parish, C. Silva and Y. Katoh, “Microstructure and mechanical properties of titanium aluminum carbides neutron irradiated at $400\text{--}700^\circ\text{C}$ ”, *Journal of the European Ceramic Society*, In Press

Acknowledgements

The authors would like to thank Patricia Tedder, Brian Eckhart, Bill Comings, Ashli Clark, Jordan Couch, Michael McAlister and Felipe Mora in the LAMDA facility at ORNL. Particular thanks to Kenny Curtis,

Jeremy McKinney and Becky Johnson for contamination control and activated materials handling. This work was sponsored by Office of Fusion Energy Sciences, US Department of Energy, and for capsule irradiation, the Institute for Materials Research, Tohoku University, under contracts DE-AC05-00OR22725 and NFE-13-00416, respectively, with UT-Battelle, LLC. Electrical resistivity annealing studies were funded by the Office of Nuclear Energy under DOE Idaho Operations Office Contract DE-AC07-051D14517 as part of a Nuclear Science User Facilities experiment.

References

- [1] C. Ang, C. Shih, C. Silva, S.J. Zinkle, N. Cetiner, Y. Katoh, Phase stability, swelling, morphology and strength of Ti₃SiC₂-TiC ceramics after low dose neutron irradiation, *J. Nucl. Mater.* 483 (2017) 44-53.
- [2] C. Ang, S. Zinkle, C. Parish, C. Shih, G.W. Chinthaka Silva, P. Edmondson, Y. Katoh, Neutron irradiation of Ti₃AlC₂-Ti₅Al₂C₃ and Ti₃SiC₂ materials - recovery and annealing at elevated temperature, *Materials Science & Technology 2016*, Salt Lake City, UT, USA, 2016.
- [3] C. Ang, C. Silva, C. Shih, T. Koyanagi, Y. Katoh, S.J. Zinkle, Anisotropic swelling and microcracking of neutron irradiated Ti₃AlC₂-Ti₅Al₂C₃ materials, *Scr. Mater.* 114 (2016) 74-78.
- [4] D.J. Tallman, E.N. Hoffman, E.a.N. Caspi, B.L. Garcia-Diaz, G. Kohse, R.L. Sindelar, M.W. Barsoum, Effect of neutron irradiation on select MAX phases, *Acta Mater.* 85(0) (2015) 132-143.

7.2 DAMAGE MECHANISM INTERACTIONS AT THE PLASMA-MATERIALS INTERFACE (Early Career Award)—C. M. Parish, K. Wang (Oak Ridge National Laboratory)

OBJECTIVE

This work intends to develop the fundamental scientific basis for modeling and predicting the behavior of helium bubbles in refractory metals, to provide support for the science and engineering of tokamak plasma-facing components.

SUMMARY

Effort this reporting period emphasized exploration of effects of starting microstructures (hot rolled state vs recrystallized state) on the plasma materials interaction in tungsten using multi-types of electron microscopy characterization. This has included performing tKD analysis on isolated tungsten nanotendrils to understand the growth mechanism of the nanotendrils in low energy helium ions exposure environments.

PROGRESS AND STATUS

Introduction

As the choice for the ITER divertor, and present leading candidate for subsequent tokamak systems, tungsten metal is the current focus of high-flux, high-fluence, and high-temperature plasma-materials interaction (PMI) studies. An adequate fundamental scientific basis for explaining observed PMI behavior (e.g., nanofuzz growth) and predicting long-term behavior (e.g., PMI response in a nuclear environment) is lacking. In this reporting period, we have interrogated plasma-exposed tungsten in order to begin building the understanding and methods for quantitative characterization of defects and crystallography in these materials.

Experimental Procedure

In this summary, data from several sets of experiments are presented. Transmission Kikuchi diffraction (tKD) was performed in a JEOL 6500F SEM using an EDAX EBSD system, with beam parameters 20-30 keV, 3-5 nA. TEM and STEM imaging and microanalysis were performed in the ORNL LAMDA lab using the FEI Talos F200X and JEOL 2100F instruments.

Results

Grain orientations and grain boundaries in tungsten nanotendrils

To understand the underlying growth mechanism of nanofuzz tendrils, transmission Kikuchi diffraction (tKD) experiments were performed on isolated nanofuzz tendrils exposed under the condition of 900 °C, 10^{23} He/m²sec, 4×10^{26} He/m² and 50 eV ion energy. Thirteen tendrils or tendril clusters were interrogated via tKD. Figure 1 shows analysis of a typical individual tendril. The high angle (> 15°) grain boundaries denoted by black lines in Figure 1 (c) were identified in a single tendril. The tendrils are generally only one grain wide, so the given orientation down the tendril axis can be acquired for most grains.

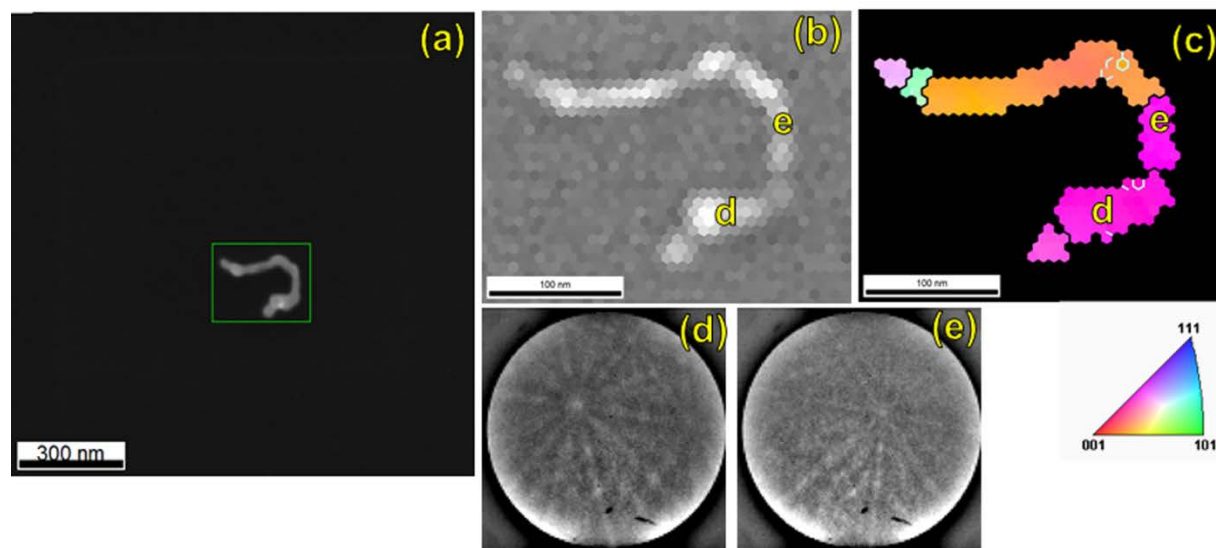


Figure 1: (a) SEM image of an isolated tungsten nanotendrils on a continuous carbon film. The green box denotes the area of tKD mapping. (b) Image quality map. (c) Z-axis (out-of-the-page) inverse pole figure colored map. Coloration is by the inset unit triangle. Black boundaries are high angle, cyan boundaries are low-angle. (d-e) Typical tKD patterns from the marked points. Pixel pitch: 8 nm. Reprinted from [1].

In total, 34 individual grains were measured in the tendrils. The points of tendrils long axis are spread across the unit triangle as shown in Figure 2 (a). It's interesting that no preferred tendrils growth axis is observed, in contrast to the anticipated hypothesis that a given nanotendrils growth axis should be strongly preferred to $\langle 111 \rangle$ direction from the presumed mechanism [2]. Perhaps, surface adatoms produced by loop-punching may have enough time to experience surface diffusion and lose their identity as punched loops, and attach to a convenient new location on the growing tendrils. Besides, we also measured the axis/angle pairs that describe the grain boundaries as indicated in Figure 2 (b) and (c). Figure 2 (c) shows a slight preference at 60° . This is also a surprising point that grain boundaries are not towards low angle. As assumed, if tendrils grew by a continuous extrusion of the underlying grain, a gradual rotation of the crystal lattice might be expected, giving rise to low angle grain boundaries. However, our results imply an occasional nucleation of a new grain with a random orientation rather than a continuous lattice rotation and this question need to be addressed in future work.

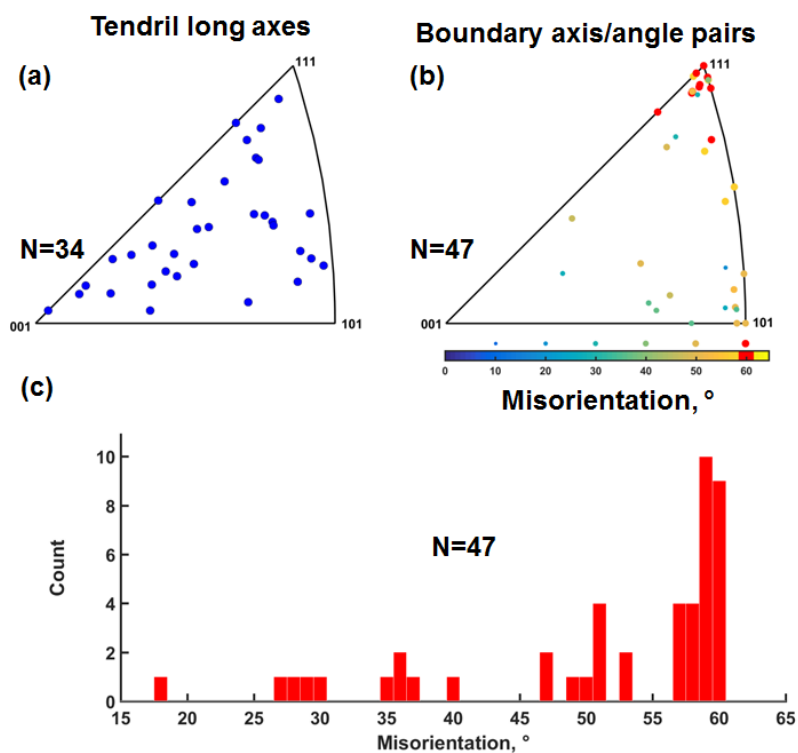


Figure 2: (a) Long axes of the tungsten tendril grains. (b) Axis/angle pairs of the tendril grain boundaries. (c) Histogram of the grain boundary misorientation axes. No grain boundaries $<15^\circ$ analyzed. Reprinted from [1].

In short, no preferred crystallographic direction was found in the grains' long axis along the tendrils' growth directions from the tKD analysis, which perhaps implies that growth is sufficiently fast and non-equilibrium that any preferences from thermodynamics or dislocation slip for a given axis is overwhelmed by the rapid growth, allowing random growth orientations. There is slight preference for certain high-angle axis/angle pairs in the grain boundary distribution, but the underlying interpretation requires further investigation.

Effect of starting microstructure on the helium plasma-materials interaction in tungsten

We explored the influence of the starting microstructure of tungsten, specifically of a hot-rolled state (HR) containing many dislocations and grain boundaries vs. a recrystallized state (RX) with very few of these intrinsic defects, on the development of the surface morphology and the near-surface microstructure. The samples were given a series of helium surface exposures (80 eV, $\sim 10^{20}$ He/m²sec, 2 or 20×10^{23} He/m², 900°C). The initial microstructures of HR and RX tungsten before ions exposure are shown in Figure 3. A very high density of dislocations and many grain boundaries are visible for the HR sample in the plane-view electron channeling contrast images (ECCI) and in TEM images, while large grains and few internal dislocations are seen in the RX material.

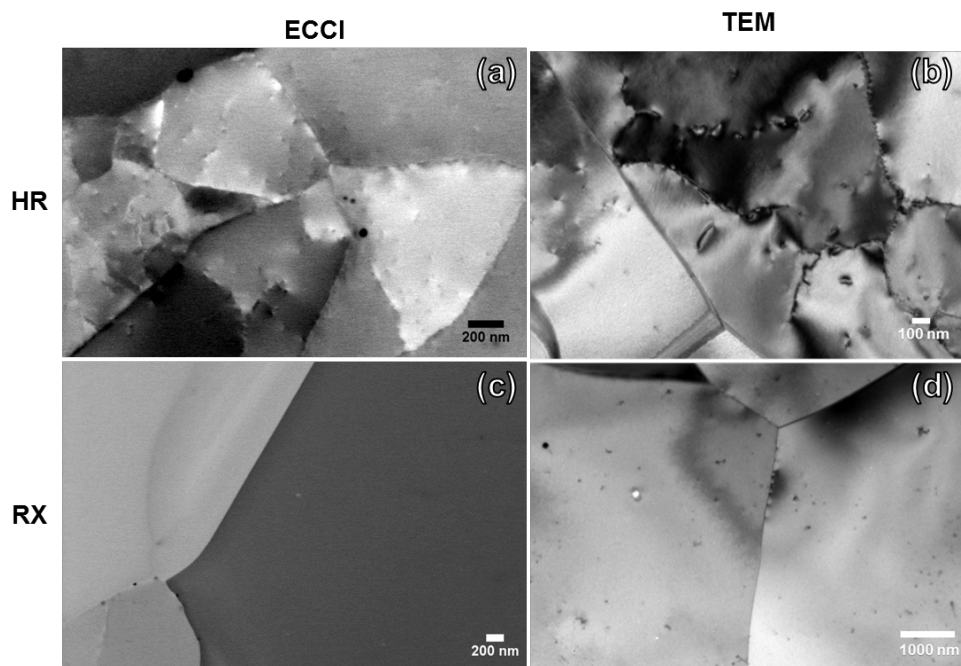


Figure 3: Starting microstructures of the HR and RX tungsten, examined by ECCI and TEM. Reprinted from [3].

Generally, a faceted surface structure is visible at the lower fluence and short but well-developed nanofuzz structure is seen at the higher fluence in both HR and RX samples. Figure 4 shows higher magnification typical surface microstructures after exposure. In particular, the widths of nanofuzz were statistically counted from a number of high resolution SEM images. The average size of the tendrils widths is given in the bottom row of Figure 4, for the HR samples as 27.6 ± 9.1 nm (mean ± 1 standard deviation) tendrils width, and for the RX samples 32.8 ± 9.2 nm.

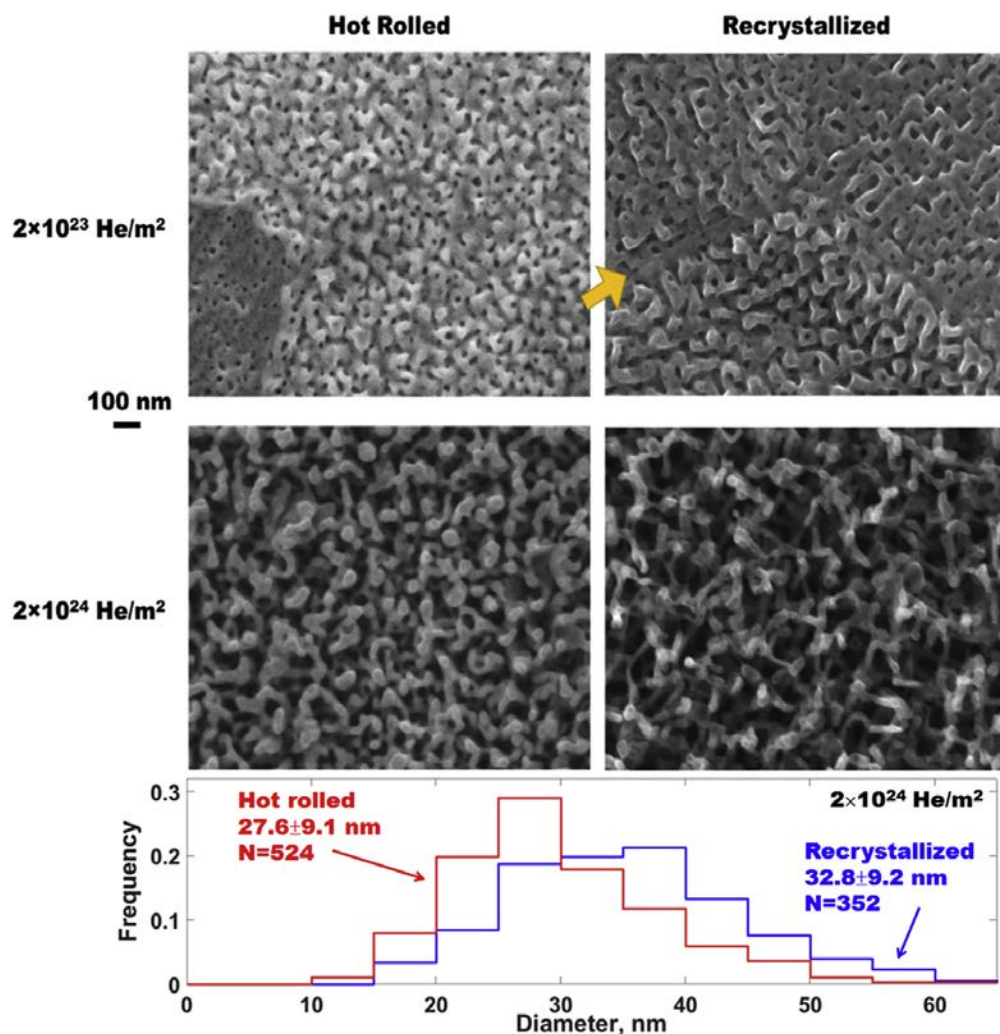


Figure 4: Higher-magnification SEM images showing the relative effects of tungsten microstructure and fluence. Arrow in the top right image denotes suppression of morphology growth at a grain boundary. Histogram (bottom row) is an analysis of multiple grains each of the $20 \times 10^{23} \text{ He/m}^2$ samples' tendril diameters. Reprinted from [3].

Cross-sectional TEM observation indicated little difference in the near-surface regions for the hot-rolled (HR) vs. the recrystallized (RX) at first glance. Bubbles were binned into depths 0-50 nm, 50-100 nm, and >100 nm as denoted in Figure 5 (a). Then the quantitative analysis of helium bubbles in these three different depth regions was performed by the Kolmogorov-Smirnov (K-S) test that can help determine if two datasets are distinct. As shown in Figure 6, the shallow 0-50 nm bubbles at both fluences gives very little distinct distributions, while the distributions in the deeper region (50-100 nm and 100 nm+) appear to be significantly different between the HR and RX states. Specifically, the difference is larger at $2 \times 10^{23} \text{ He/m}^2$ than at $20 \times 10^{23} \text{ He/m}^2$.

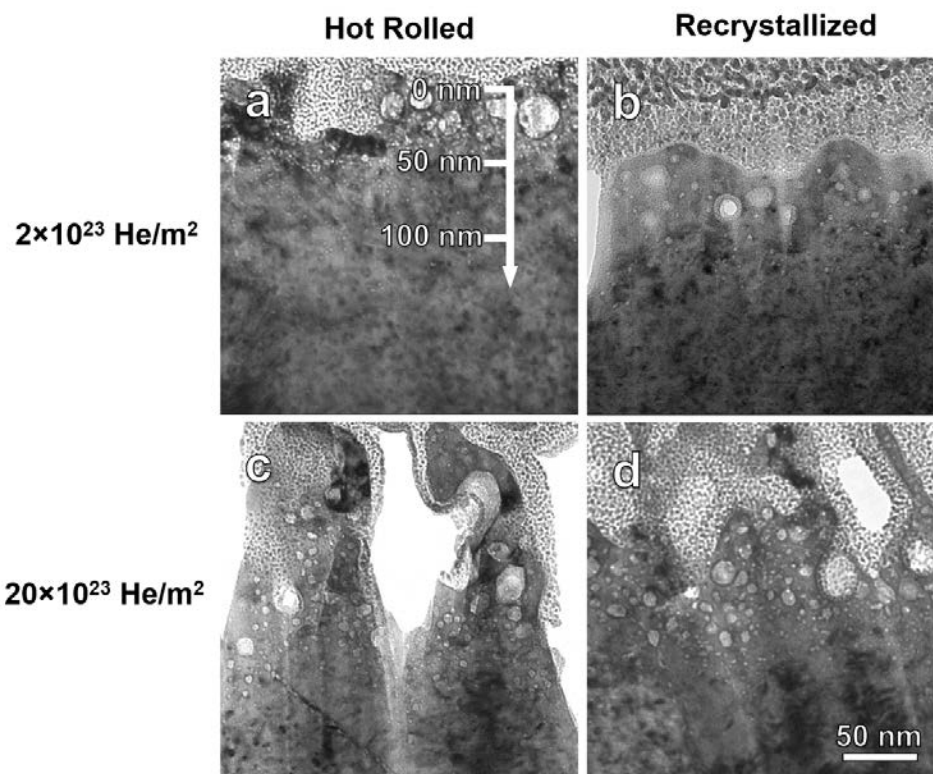


Figure 5: High-magnification TEM images showing the relative effects of tungsten microstructure and fluence. Flux $\sim 10^{20}$ He/m² sec, E=80 eV, T=900°C. Reprinted from [3].

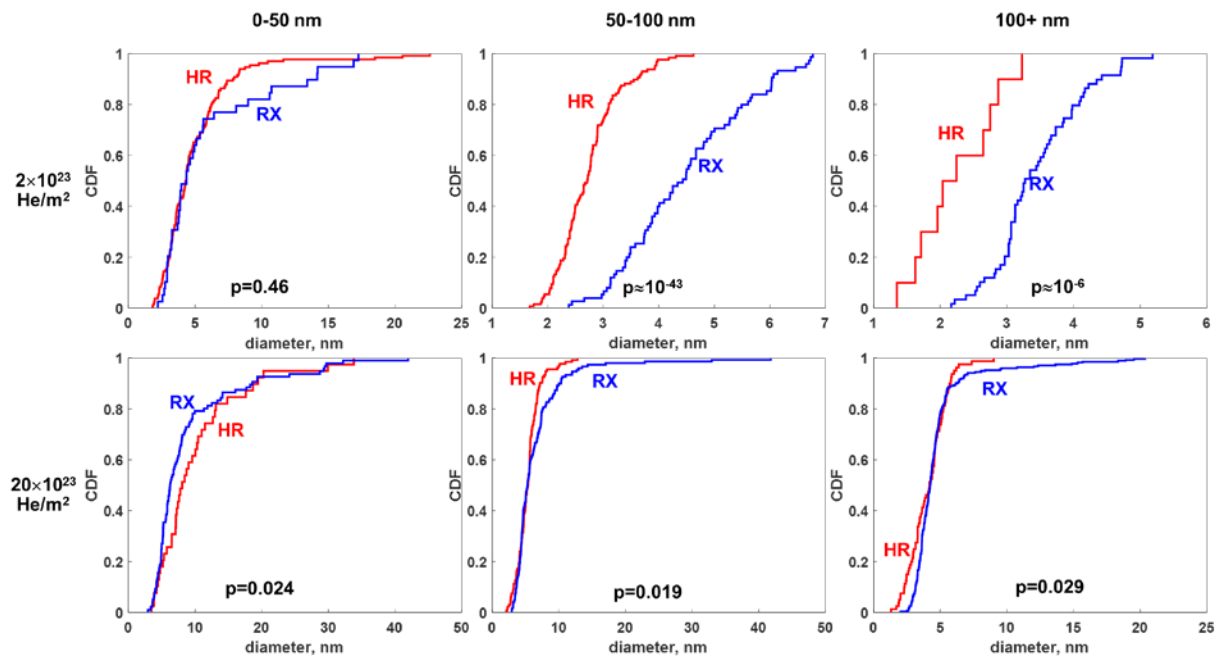


Figure 6: Empirical cumulative distribution functions of helium bubble sizes for the six comparisons. Reprinted from [3].

Based on the analysis of results we acquired from this series of experiments, we hypothesize that due to easy near-surface trap mutation, dislocations and grain boundaries are not very effective in capturing helium in the near-surface region. Deeper in the material the influence of the dislocations and grain boundaries becomes more pronounced.

Summary

We have employed electron microscopy methods to interrogate the damage mechanism of plasma materials interactions. Combining quantitative information of the surface morphology evolution and the bubble distributions in the subsurface, the possible hypothesis has been given to interpret the effect of starting microstructure on the bubbles growth and surface damage. Advanced tKD method has been performed to quantify the crystallography information in the nanotendrils, which helps to realize the growth mechanism of nanotendrils. In the future, the HR and RX tungsten exposed at other flux and fluence conditions will be interrogated by similar electron microscopy methods in order to identify the flux and fluence effects as well as starting microstructure influence on the plasma materials interactions. Using the newly acquired in situ heating holder for the ORNL LAMDA lab transmission electron microscope, we intend to perform heating experiment to capture processes such as bubble nucleation or coalescence while underway.

Acknowledgements

We thank M. Baldwin and R. Doerner, UC-San Diego, and X. Hu, F. W. Meyer and M. E. Bannister, ORNL, for collaborations. Talos F200X STEM instrument provided by the Department of Energy, Office of Nuclear Energy, Fuel Cycle R&D Program and the Nuclear Science User Facilities.

References

- [1] C.M. Parish, K. Wang, R.P. Doerner, M.J. Baldwin, Grain orientations and grain boundaries in tungsten nanotendrils grown under divertor-like conditions, *Scripta Materialia*, 127 (2017) 132-135.
- [2] N. Ohno, Y. Hirahata, M. Yamagiwa, S. Kajita, M. Takagi, N. Yoshida, R. Yoshihara, T. Tokunaga, M. Tokitani, Influence of crystal orientation on damages of tungsten exposed to helium plasma, *Journal of Nuclear Materials*, 438, Supplement (2013) S879-S882.
- [3] K. Wang, M.E. Bannister, F.W. Meyer, C.M. Parish, Effect of starting microstructure on helium plasma-materials interaction in tungsten, *Acta Materialia*, 127 (2017) 132-135.

8. MODELING PROCESSES IN FUSION SYSTEM MATERIALS

8.1 STRENGTHENING DUE TO RADIATION INDUCED OBSTACLES IN Fe AND FERRITIC ALLOYS—Yu. N. Osetskiy (Oak Ridge National Laboratory)

OBJECTIVE

The purpose of this research is to understand atomic level strengthening mechanisms in materials with radiation induced localized microstructural features such as voids, gas-filled bubbles, second phase precipitates and oxide particles. These microstructures work as obstacles to dislocation motion and cause radiation induced hardening and embrittlement. Currently, we are investigating the map of mechanisms depending on the obstacle type and size.

SUMMARY

Irradiation of structural alloys by neutrons and ions lead to formation of a high density of nanoscale features such as second phase precipitates, voids and gas-filled bubbles. These objects are obstacles to dislocation motion and cause wanted or unwanted changes in mechanical properties. In order to predict materials behavior these obstacles must be characterized as well as their individual strength estimated. The only technique that allows this at the scale of nanometers is classical molecular dynamics (MD). In this work we modeled vacancy voids, He-filled bubbles, Cu precipitates and rigid inclusions in a bcc-Fe matrix. At the current stage of the research we investigated $\frac{1}{2}\langle 111 \rangle\{110\}$ edge dislocations. During its motion this dislocation cannot change its glide plane (cannot cross-slip) to avoid interaction with obstacles and therefore produces maximum effect on strengthening. The results obtained in this research will be used to improve theoretical prediction of mechanical property changes.

PROGRESS AND STATUS

Strength of different obstacles

We have finished modeling obstacles up to 8 nm in diameter. This type of modeling demands large modeling crystals, $>8 \times 10^6$ atoms, and long physical time for dislocation-obstacle interaction, up to a few ns. The results for all obstacles studied are presented in Figure 1 as the critical resolved shear stress (CRSS) of different obstacles versus their size. The results obtained with obstacles up to 8 nm have demonstrated that according to the interaction mechanisms all obstacles can be divided in two groups. One group consists of only rigid inclusions that interact with dislocations by the classical Orowan interaction mechanism [1]. The other includes voids, bubbles and precipitates which can be cut by interacting dislocation.

The first group demonstrates much stronger obstacle size dependence of critical resolved shear stress (CRSS) than does the second group. Small rigid inclusions, ≤ 1 nm, can be very weak obstacles, comparable to soft precipitates. Larger rigid inclusions demonstrate maximum strength among all the studied obstacles

Small obstacles of the second group, < 4 nm, show individual mechanisms with different hardness. However, large obstacles, ≥ 4 nm, are strong and have very similar interaction mechanism: before the obstacles are sheared, the dislocation forms a long dipole of screw dislocations, and the mechanism is assumed to be the Orowan-type. However, as our modeling has demonstrated, the classical Orowan mechanism [1] i.e. with formation of a sheared dislocation loops around the obstacle is applicable only to rigid obstacles from the first group.

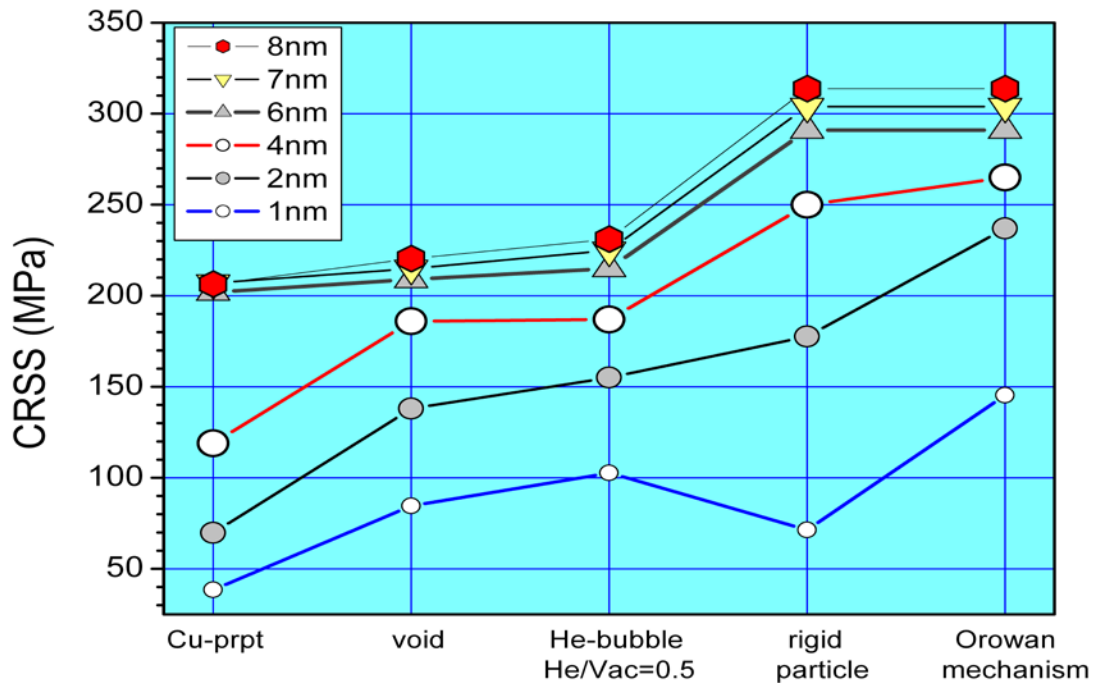


Figure 1. Critical resolved shear stress at 300K for several types of obstacles of different obstacle sizes, obtained by molecular dynamics modeling.

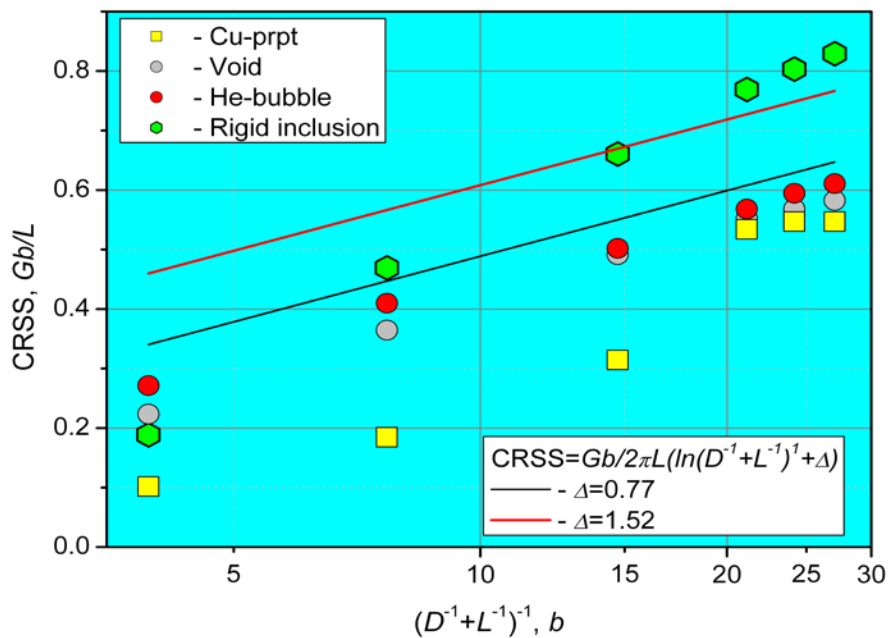


Figure 2. Critical resolved shear stress in reduced units as a function of harmonic mean of an obstacle diameter, D , and spacing between them along the dislocation line. Symbols - rigid inclusions simulated in current work; lines - dependences obtained from dislocation dynamic modeling for Orowan mechanism (black line) and void (red line) in [1,2].

Rigid obstacles are found to be the strongest. The dependence of their strength is also exceptionally strong within the range studied as can be seen in Figure 2 where the comparison of atomistic modeling of rigid obstacles from 1 to 8 nm in diameter at 300 K (symbols) with theoretical estimation from [2,3] (lines) is presented.

Future Studies

Future tasks within this continuing modeling effort will include:

- Finalize modeling of edge dislocation interaction with He-filled bubbles up to 10 nm in diameter and different He-to-vacancy ratios.
- Finalize modeling of temperature and strain rate effects.
- Extend dislocation-obstacle interaction to $\frac{1}{2}\langle 111 \rangle$ screw dislocations.
- Modify the dispersed barrier hardening model by including dislocation obstacle interaction mechanisms revealed in atomic-scale modeling.
- Extend the modeling program to dislocation-type obstacles such as dislocation loops. So far dislocation loops are treated in the same way as inclusions; however their interaction with dislocations is quite different and this must be taken into account.

References

- [1] Orowan E., A type of plastic deformation new in metals, *Nature*, 149 (1942) 643.
- [2] Bacon, D. J., Kocks, U. F., and Scattergood, R. O., *Phil. Mag.*, 28 (1973) 1241.
- [3] Scattergood, R. O., and Bacon, D. J., *Acta metall.*, 30 (1982) 1665.

8.2 DEVELOPMENT OF INTERATOMIC POTENTIALS IN TUNGSTEN-RHENIUM SYSTEMS—W. Setyawan and R. J. Kurtz (Pacific Northwest National Laboratory)

OBJECTIVE

The objective of this research is to develop interatomic potentials for exploring radiation damage in W in the presence of solid transmutant Re and radiation-induced precipitation of W-Re intermetallics.

SUMMARY

Reference data are generated using ab initio methods to fit interatomic potentials for W-Re system. The reference data include single phases of W and Re, strained structures, slabs, systems containing several concentrations of point defects, melt structures, structures in the σ and χ phases, and structures containing several concentrations of solid solutions of Re in bcc W and W in hcp Re. The initial fit of the angular-dependent potential for pure W has been completed. The potential is capable of reproducing the cohesive energy of single phases of W and the equation of states of bcc W. Melting behavior and defect formation energies will be explored in the future.

PROGRESS AND STATUS

In the previous report, ab initio data were calculated using standard pseudopotentials in which only electrons in 6s and 5d states are treated as valence electrons. In this report, these data are updated by including the 5p semicore states as valence states for better accuracy of forces and energies in compressive strains. In addition, preliminary fitting of the W potential is presented.

Updated ab initio data for W

Table 1 summarizes the reference data for pure W. For each system, the number of atoms (N_{atoms}) and the total energy (E_{total}) are given. In Table 1, universal strains refer to the universal linear-independent coupling strains (ULICS) [1]. In general, there are 6 ULICS strain vectors as the following (given in engineering notation):

$$\begin{aligned} u_1 &= [1 \ 2 \ 3 \ 4 \ 5 \ 6] * \text{factor} \\ u_2 &= [-2 \ 1 \ 4 \ -3 \ 6 \ -5] * \text{factor} \\ u_3 &= [3 \ -5 \ -1 \ 6 \ 2 \ -4] * \text{factor} \\ u_4 &= [-4 \ -6 \ 5 \ 1 \ -3 \ 3] * \text{factor} \\ u_5 &= [5 \ 4 \ 6 \ -2 \ -1 \ -3] * \text{factor} \\ u_6 &= [-6 \ 3 \ -2 \ 5 \ -4 \ 1] * \text{factor} \end{aligned}$$

For a given strain vector $u = [e_1 \ e_2 \ e_3 \ e_4 \ e_5 \ e_6]$, the corresponding strain tensor is

$$\varepsilon = \begin{bmatrix} e_1 & e_6/2 & e_5/2 \\ e_6/2 & e_2 & e_4/2 \\ e_5/2 & e_4/2 & e_3 \end{bmatrix}$$

The slab systems are constructed from a bcc conventional cell and include approximately 15 Å of vacuum space. To obtain the melt reference structures, classical molecular dynamics simulations are performed with LAMMPS [2] software using the W potential from Ref. [3]. Three melt structures are then taken and the forces, energies, and stresses are calculated with density functional theory (DFT) simulations. In the DFT, for each melt structure, three different hydrostatic strains of -0.05, 0, and 0.2 are applied for a total of nine melt structures.

Table 1. Ab initio data for pure W. Calculations are performed with plane wave energy cutoff = 300 eV and number of \mathbf{k} -points = $12,000/N_{\text{atoms}}$

System	N_{atoms}	E_{total} (eV)
bcc	54	-699.444
simple cubic	27	-311.189
fcc	108	-1347.038
hcp	48	-597.900
hydrostatic strain in bcc:		
-0.2	54	-82.218
-0.15	54	-411.423
-0.1	54	-591.650
-0.05	54	-676.223
-0.02	54	-694.259
-0.01	54	-698.457
0	54	-699.444
0.01	54	-698.921
0.02	54	-697.027
0.05	54	-684.402
0.1	54	-646.541
0.15	54	-596.289
0.2	54	-540.633
universal strain u_1 , factor = 0.01	54	-699.425
melt structures:		
structure 1, strain = -0.05	128	-1383.412
structure 1, strain = 0	128	-1509.830
structure 1, strain = 0.2	128	-1303.142
structure 2, strain = -0.05	128	-1380.596
structure 2, strain = 0	128	-1509.241
structure 2, strain = 0.2	128	-1305.376
structure 3, strain = -0.05	128	-1372.157
structure 3, strain = 0	128	-1502.498
structure 3, strain = 0.2	128	-1303.882
vacancies in bcc 54-atom cell:		
18 sample 1	36	-410.644
18 sample 2	36	-413.185
18 sample 3	36	-411.974
12 sample 1	42	-505.206
12 sample 2	42	-506.540
12 sample 3	42	-507.580
6 sample 1	48	-601.283
6 sample 2	48	-601.171
6 sample 3	48	-602.079

slab systems:		
{100} 9 layers	81	-1004.035
{100} 10 layers	90	-1120.600
{110} 8 layers	96	-1208.829
{110} 9 layers	108	-1364.315
{111} 15 layers	60	-746.306
{111} 16 layers	64	-798.425

Updated ab initio data for Re

Table 2 summarizes the reference data for pure Re. The universal strains are applied to an hcp structure in an orthorhombic cell. In the orthorhombic cell, the x-axis is along the basal close-packed row direction, the y-axis is perpendicular to x, and the z-axis is parallel to the c-axis of the original hcp unit cell, as shown in Figure 1. The melt reference structures are generated in a similar way as in tungsten using the same ad hoc potential.

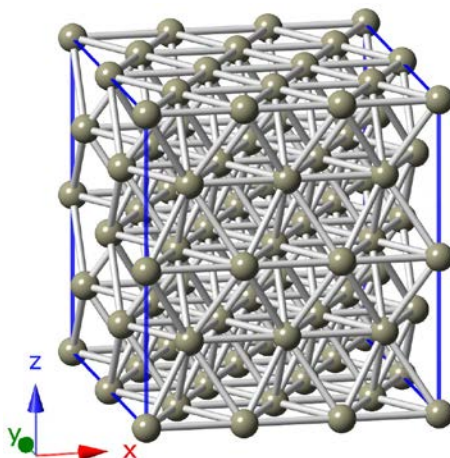


Figure 1. Hexagonal close-packed structure in an orthorhombic 3x2x2 supercell. The close-packed plane stacking is along the z-axis.

Table 2. Ab initio data for pure Re. Calculations are performed with plane wave energy cutoff = 300 eV and number of \mathbf{k} -points = $12,000/N_{\text{atoms}}$

System	N_{atoms}	E_{total} (eV)
bcc	54	-654.030
simple cubic	27	-298.506
fcc	108	-1335.311
hcp	48	-596.465
hydrostatic strain in hcp:		
-0.2	48	55.605
-0.15	48	-296.213
-0.1	48	-485.422
-0.05	48	-572.612
-0.02	48	-592.687
-0.01	48	-595.411

0	48	-596.465
0.01	48	-596.022
0.02	48	-594.238
0.05	48	-582.195
0.1	48	-546.307
0.15	48	-499.304
0.2	48	-448.084
<hr/>		
universal strain u_1 , factor = 0.01	48	-596.461
universal strain u_2 , factor = 0.01	48	-596.444
universal strain u_3 , factor = 0.01	48	-596.381
<hr/>		
melt structures:		
structure 1, strain = -0.05	144	-668.402
structure 1, strain = 0	144	-737.084
structure 1, strain = 0.2	144	-613.292
structure 2, strain = -0.05	144	-633.563
structure 2, strain = 0	144	-716.408
structure 2, strain = 0.2	144	-619.716
structure 3, strain = -0.05	144	-653.538
structure 3, strain = 0	144	-727.758
structure 3, strain = 0.2	144	-614.746
<hr/>		
vacancies in hcp 48-atom cell:		
18 sample 1	30	-330.800
18 sample 2	30	-327.560
18 sample 3	30	-328.795
12 sample 1	36	-413.509
12 sample 2	36	-413.343
12 sample 3	36	-414.120
6 sample 1	42	-503.515
6 sample 2	42	-502.763
6 sample 3	42	-503.388
<hr/>		
slab systems:		
{0001} 8 layers	96	-1167.134
{0001} 9 layers	108	-1315.874
{11-20} 13 layers	104	-1259.138
{11-20} 14 layers	112	-1358.550
{10-10} 14 layers	90	-1086.657
{10-10} 16 layers	96	-1166.073

Updated ab initio data for W-Re

Table 3 summarizes the reference data for W-Re systems. For each system, the number of W atoms (N_W) and Re atoms (N_{Re}) are presented. The crystal structure of the σ and χ phases are taken from [4]. In the σ phase, there are five unique sites labeled A, B, C, D, and E. In the χ phase, there are four sites: A,

B, C, and D. In Table 3, a system in the σ phase that is labeled as WWR_WRe indicates for this system the sites from A to E are occupied by W, W, Re, W, and Re, respectively.

Table 3. Ab initio data for W-Re. Calculations are performed with plane wave energy cutoff = 300 eV and number of \mathbf{k} -points = 12,000/ N_{atoms}

System	N_W	N_{Re}	N_{atoms}	$N_{\text{Re}}/N_{\text{atoms}}$	E_{total} (eV)
σ phase:					
dir1 WWWW	60	0	60	0	-766.816
dir2 WWWWRe	44	16	60	0.267	-758.793
dir3 WWRReW	44	16	60	0.267	-765.278
dir4 WWRReRe	28	32	60	0.533	-756.692
dir5 WWRReWW	44	16	60	0.267	-759.760
dir6 WWRReWRe	28	32	60	0.533	-751.853
dir7 WWRReReW	28	32	60	0.533	-756.380
dir8 WWRReReRe	12	48	60	0.8	-746.782
dir9 WReWWW	52	8	60	0.133	-761.367
dir10 WReWWRe	36	24	60	0.4	-754.021
dir11 WReWReW	36	24	60	0.4	-759.983
dir12 WReWReRe	20	40	60	0.667	-751.583
dir13 WReReWW	36	24	60	0.4	-754.068
dir14 WReReWRe	20	40	60	0.667	-746.087
dir15 WReReReW	20	40	60	0.667	-750.416
dir16 WReReReRe	4	56	60	0.933	-740.831
dir17 ReWWW	56	4	60	0.067	-766.566
dir18 ReWWWRe	40	20	60	0.333	-758.567
dir19 ReWWRReW	40	20	60	0.333	-764.875
dir20 ReWWRReRe	24	36	60	0.6	-755.827
dir21 ReWRReWW	40	20	60	0.333	-759.581
dir22 ReWRReWRe	24	36	60	0.6	-751.392
dir23 ReWRReReW	24	36	60	0.6	-755.810
dir24 ReWRReReRe	8	52	60	0.867	-745.599
dir25 ReReWWW	48	12	60	0.2	-760.863
dir26 ReReWWRe	32	28	60	0.467	-753.341
dir27 ReReWReW	32	28	60	0.467	-759.377
dir28 ReReWReRe	16	44	60	0.733	-750.481
dir29 ReReReWW	32	28	60	0.467	-753.662
dir30 ReReReWRe	16	44	60	0.733	-745.361
dir31 ReReReReW	16	44	60	0.733	-749.643
dir32 ReReReReRe	0	60	60	1	-739.637
χ phase:					
dir101 WWWW	58	0	58	0	-734.631
dir102 WWWWRe	34	24	58	0.414	-735.211

dir103 WReW	34	24	58	0.414	-730.479
dir104 WReRe	10	48	58	0.826	-726.046
dir105 WReWW	50	8	58	0.138	-728.704
dir106 WReWRe	26	32	58	0.552	-728.943
dir107 WReReW	26	32	58	0.552	-722.497
dir108 WReReRe	2	56	58	0.966	-719.365
dir109 ReWWW	56	2	58	0.0345	-732.948
dir110 ReWRe	32	26	58	0.449	-733.800
dir111 ReWReW	32	26	58	0.448	-728.522
dir112 ReWReRe	8	50	58	0.862	-724.484
dir113 ReReWW	48	10	58	0.172	-726.754
dir114 ReReWRe	24	34	58	0.586	-727.106
dir115 ReReReW	24	34	58	0.586	-720.320
dir116 ReReReRe	0	58	58	1	-717.559
Re solid solution in bcc W:					
dir201	51	3	54	0.0556	-697.200
dir202	49	5	54	0.093	-695.705
dir203	40	14	54	0.259	-688.875
dir204	27	27	54	0.5	-678.885
dir205	14	40	54	0.741	-669.249
W solid solution in hcp Re:					
dir251	2	46	48	0.958	-596.520
dir252	5	43	48	0.896	-596.602
dir253	12	36	48	0.75	-596.895
dir254	24	24	48	0.5	-597.311
dir255	36	12	48	0.25	-612.980

Parameterization

We seek to utilize the angular-dependent potential (ADP) formulation [5]. ADP extends the embedded-atom method (EAM) formulation [6] with three angular terms. The total energy in ADP is expressed as

$$E = \frac{1}{2} \sum_{i,j(j \neq i)} \phi_{s_i s_j}(r_{ij}) + \sum_i F_{s_i}(\bar{\rho}_i) + \frac{1}{2} \sum_{i,\alpha} (\mu_{i\alpha})^2 + \frac{1}{2} \sum_{i,\alpha,\beta} (\lambda_{i\alpha\beta})^2 - \frac{1}{6} \sum_i v_i^2 \quad (1)$$

Where indices i and j enumerate atoms, while $\alpha, \beta = x, y, z$ are the Cartesian coordinate components. $\phi_{s_i s_j}$ is the pair interaction that depends on the type s_i of atom- i and type s_j of atom- j and the distance between the atoms r_{ij} . The functional F_{s_i} is the embedding energy, which is a function of the electron density $\bar{\rho}_i$ at the location of atom- i induced by all other atoms. The electron density $\bar{\rho}_i$ is given by

$$\bar{\rho}_i = \sum_{j \neq i} \rho_{s_j}(r_{ij}) \quad (2)$$

where ρ_{s_j} is the atomic electron density function of atom- j . The last three terms in Eq. (1) contain the angular characters, i.e. non-central, of the bonding through the vectors

$$\mu_{i\alpha} = \sum_{j \neq i} u_{s_i s_j}(r_{ij}) r_{ij\alpha} \quad (3)$$

and tensors

$$\lambda_{i\alpha\beta} = \sum_{j \neq i} w_{s_i s_j}(r_{ij}) r_{ij\alpha} r_{ij\beta} \quad (4)$$

with v_i is the trace of λ :

$$v_i = \sum_{\alpha} \lambda_{i\alpha\alpha} \quad (5)$$

The pair interaction is parameterized with a polynomial and a smoothing cutoff function as follows:

$$\phi(r) = \psi\left(\frac{r-r_c}{h_1}\right) \sum_{n=0}^5 a_n (r-r_0)^n \quad (6)$$

where the cutoff function ψ is given by

$$\psi(x) = \frac{x^4}{1+x^4} \quad (7)$$

The embedding energy is parameterized with the following polynomial that ensures F is zero when the electron density vanishes. The atomic electron density is parameterized with a screened Coulomb function multiplied with a smoothing cutoff function:

$$F(\bar{\rho}) = \sum_{n=1}^5 b_n \bar{\rho}^n \quad (8)$$

$$\rho(r) = \psi\left(\frac{r-r_c}{h_2}\right) \frac{c_1}{r} e^{-c_2 r} \quad (9)$$

The functions u and w in the angular terms are parameterized also as screened Coulomb functions:

$$u(r) = \psi\left(\frac{r-r_c}{h_3}\right) \frac{d_1}{r} e^{-d_2 r} \quad (10)$$

$$w(r) = \psi\left(\frac{r-r_c}{h_4}\right) \frac{f_1}{r} e^{-f_2 r} \quad (11)$$

Fitting of the W Potential

The energy per atom in the reference (Table 1) is shifted by the same amount so that the energy per atom in the bcc phase is equal to -8.9 eV based on the experimental cohesive energy of W. The fitting is performed with the software POTFIT [7] based on the force-matching framework [8]. In this framework, the energies, forces, and stresses in the reference data obtained from the ab initio calculations are used to fit the potential parameters. Firstly, the pair interaction is fitted. Next, the atomic electron density and the embedding energy are fitted while the pair interaction is fixed. Then, the ρ , F , and ϕ are all allowed to relax and are re-optimized. Next, with the fitted ρ , F , and ϕ , the angular terms are fitted. In the final stage, all ρ , F , ϕ , u , and w are re-optimized. The fitted parameters are presented in Table 4. The RMS errors of the forces, energies, and stresses are 0.582 eV/Å, 0.193 eV, and 0.327 MPa, respectively. The potential

is capable of reproducing the cohesive energy of single phases of W and the equation of states of bcc W reasonably well. The melting behavior and the defect formation energies will be explored in the future.

Table 4. Fitted parameters of the ADP potential for pure W. Energies are in eV and distances are in Å.

Parameters	Values
r_c	6.6
a_0	-23.68505
a_1	-1.18950
a_2	8.56144
a_3	7.98912
a_4	-4.49762
a_5	-10.39484
r_0	3.50644
h_1	8.11175
b_1	-5.09856
b_2	4.54812
b_3	-1.47838
b_4	0.27400
b_5	-0.01957
c_1	6.61199
c_2	1.03695
h_2	0.10532
d_1	26.57458
d_2	9.61441
h_3	10.0
f_1	19.42935
f_2	2.35622
h_4	0.02081

Acknowledgement

This research has been supported by the U.S. Department of Energy, Office of Science, Office of Fusion Energy Sciences (DE-AC06-76RL0-1830).

References

- [1] R. Yu, et al., *Computer Physics Communications* 181 (2010) 671.
- [2] S. Plimpton, *Journal of Computational Physics* 117 (1995) 1.
- [3] N. Juslin, B. D. Wirth, *Journal of Nuclear Materials* 432 (2013) 61.
- [4] J. C. Crivello, J. M. Joubert, *Journal of Physics Condensed Matter* 22 (2010) 035402.
- [5] Y. Mishin, et al., *Acta Materialia* 53 (2005) 4029.
- [6] M. S. Daw and M. L. Baskes, *Physical Review Letters* 50 (1983) 1285.
- [7] B. Peter and G. H. Franz, *Modeling and Simulation in Materials Science and Engineering* 15 (2007) 295.
- [8] F. Ercolessi and J. B. Adams, *Europhysics Letters* 26 (1994) 583.

8.3 STRUCTURES AND TRANSITIONS IN TUNGSTEN GRAIN BOUNDARIES—Timofey Frolov (Lawrence Livermore National Laboratory), Qiang Zhu (University of Nevada Las Vegas), Jaime Marian (University of California Los Angeles) and Robert E. Rudd (Lawrence Livermore National Laboratory)

OBJECTIVE

The objective of this study is to develop a computational methodology to predict structure, energies of tungsten grain boundaries as a function of misorientation and inclination. The energies and the mobilities are the necessary input for thermomechanical model of recrystallization of tungsten for magnetic fusion applications being developed by the Marian Group at UCLA.

SUMMARY

Recrystallization determines the upper extent of the operating temperature of tungsten as a divertor or first-wall material. At temperatures above the onset of recrystallization, migrating grain boundaries sweep out defects that contribute to hardening, making the material brittle. Thermomechanical models to predict recrystallization and its effect on mechanical properties have to be informed of the mechanisms of grain boundary migration, their structure and kinetic properties at tokamak operating temperatures. In this work grain boundary structures and energies as a function of misorientation and inclination were generated using atomistic simulations with several empirical potentials and compared with the available DFT calculations. We find new ground states of previously studied boundaries by performing grand canonical optimization of the structure. The finding of the true ground states of grain boundaries at temperatures relevant to tokamak operation has important consequences for recrystallization and embrittlement.

BACKGROUND

Tungsten has been identified as the divertor material in ITER and is a leading candidate for the plasma-facing components in DEMO and subsequent magnetic fusion energy systems because of its high mechanical strength, high thermal conductivity, high melting point and low yield for sputtering by hydrogen isotopes. While tungsten has a number of favorable properties it is also intrinsically brittle even at relatively high temperatures especially after recrystallization. As materials are subjected to harsh conditions, their microstructure changes, leading to changes in materials properties. The need to understand materials under these conditions motivates the development of computational models and simulations that can predict mechanical and kinetic properties of tungsten grain boundaries. Accumulating computational studies demonstrate that finding the ground state of grain boundaries is a challenging task that requires advanced grand canonical sampling [1, 2, 3, 4, 5, 6]. In addition, recent experimental and computational studies demonstrated that elevated temperatures and changes in chemical composition could lead to structural transformations at grain boundaries that result in discontinuous changes in materials properties [7, 8, 9, 10, 11, 12]. Experimental studies linked these transitions to abnormal grain growth and embrittlement in metallic and ceramic systems [13, 14, 15]. We use atomistic simulations to predict grain boundary structures and structural transitions and investigate their effect on embrittlement and mobility in the context of recrystallization.

PROGRESS AND STATUS

Methods

Tungsten grain boundaries were modeled using four different potentials, three of which are the embedded-atom method (EAM) potentials EAM1 [16], EAM2 [17], EAM3 [18, 19] and one is the bond-order potential (BOP) [20]. The predictions of the different models were benchmarked against the existing DFT calculations [21, 22]. Grain boundary structure and energy calculations were performed for two different sets of grain boundaries. The first set contained 246 [001] tilt boundaries with misorientation angle θ ranging from 0 to $\pi/2$ degrees and the inclination angle φ ranging from $-\pi/4$ to $\pi/4$ degrees. While the distinct grain boundary structures can be found within angular domain $0^\circ < \theta < \pi/4$ and $0^\circ < \varphi < \pi/4$,

we simulated grain boundary structures in the extended domain for future mobility calculations. The boundaries were obtained by rotating upper and lower grains around the common [001] axis by the angles $\theta/2$ and $-\theta/2$, respectively and then rotating each grain by the same angle φ . Figure 1a illustrates (θ, φ) map describing the misorientation and inclination angles of the grain boundaries studied in the work. The boundaries were chosen such as to minimize the grain boundary area for the computational efficiency, while evenly covering the entire angle range so that the spacing between the neighboring points is not larger than five degrees. On the plot the data points with $\varphi = 0^\circ$ represent symmetrical tilt boundaries. All other boundaries are asymmetrical. The second set contained fifty-seven [110] symmetrical tilt boundaries, with the misorientation angle ranging from 0° to π . This set of boundaries was generated to compare grain boundary structures and energies to the results of previous DFT calculations [21, 22]. Grain boundary structures and energies were calculated using the γ surface approach as well as by grand canonical sampling (GCS) technique.

The γ surface approach is a common method of constructing grain boundaries. In this approach two misoriented crystals are shifted relative to each other by a certain translation vector parallel to the future grain boundary plane. The translation is followed by a local relaxation of atoms that minimizes the energy of the system. Periodic boundary conditions are applied in the direction parallel to the boundary. This approach produces several different metastable states corresponding to different translation vectors. The configuration with the lowest grain boundary energy is assumed to be the ground state. It has been recognized that the surface method may not always find the ground state configuration. The first limitation is a lack of sampling: during the energy minimization atoms in the grain boundary region simply fall into the local energy minima, which means that other possible grain boundary configurations are not observed. The second limitation is that the sampling needs to be grand canonical: otherwise, the constant number of atoms in the system and periodic boundary conditions impose an unphysical constraint on possible grain boundary configurations. Despite these limitations the γ surface approach often yields ground states. It is computationally efficient and remains the standard method of grain boundary construction.

To validate the ground states predicted by the γ surface method we performed a full grand canonical sampling on a subset of boundaries at 0K. Motivated by recent studies on grain boundary phase transitions in Cu we selected $\Sigma 5(310)[001]$ and $\Sigma 5(210)[001]$ which are the typical high-angle high-energy boundaries with misorientation angles of 36.87° and 53.13° degrees, respectively. We also selected six [110] symmetrical tilt boundaries: $\Sigma 33(118)[110]$ (20.1°), $\Sigma 19(116)[110]$ (26.5°), $\Sigma 3(112)[110]$ (70.5°), $\Sigma(111)[110]$ (109.5°), $\Sigma 3(332)[110]$ (129.5°) and $\Sigma 27(552)[110]$ (148.4°). These boundaries sample the entire misorientation range and have been investigated recently by DFT calculations. The GCS calculations are more computationally demanding compared to the simple γ surface approach, so the calculations were performed using only two out of four model potentials that we studied. The choice of potentials from Refs. [17, 16] was motivated by their better agreement with the DFT calculations [21, 22].

To validate the ground state structures calculated at 0K, we performed molecular dynamic simulations at high temperatures with grain boundaries terminated at open surfaces following the methodology proposed in Ref. [11]. Surfaces provide a source and sink for atoms and effectively introduces grand canonical environment in the grain boundary region. The simulations were performed in the temperature range from 1000K to 3000K. The initial states for the high temperature anneal were taken from both the surface construction as well as the CGS calculations to ensure that the final grain boundary state is independent of the initial conditions.

Grain boundary structures and energies from the γ surface approach

[100] tilt boundaries

The grain boundary energy of 246 [100]-tilt boundaries covering the entire misorientation and inclination range was calculated using four different potentials. The energy surface has several deep cusps. Figure 1

illustrates GB energy as a function of misorientation and inclination for angles $\varphi=0$, $\theta = 36.87^\circ$ and $\theta = 53.13^\circ$, respectively. Figure 1 illustrates grain boundary energy of symmetrical tilt boundaries as a function of misorientation. The two deep energy cusps on the plot correspond to $\Sigma 5(310)[001]$ and $\Sigma 5(210)[001]$ boundaries. The structure of these boundaries illustrated in Figure 2 is well known and composed of kite-shaped structural units. The left-hand side panel of the figure shows grain boundary structure with the tilt axis normal to plane of the figure, while in the right-hand side panel the tilt axis is parallel to the plane of the figure. While all four potentials predict similar shape of the energy curve, the magnitude of the grain boundary energy shows significant difference. The EAM1 potential due to Marinica et al. from Ref. [16] shows an excellent agreement with the DFT calculations of $\Sigma 5(210)[001]$ boundary from Refs [21, 22]. These two boundaries are also energy cusps as a function of inclination as illustrated in Figures 1 c) and d). In addition to the difference in the magnitude of grain boundary energy, EAM1 and EAM2 potentials predict noticeably stronger anisotropy with changing inclination compared to the EAM3 and BOP potentials. Vicinal boundaries are expected to form steps because of the strong anisotropy, while more isotropic models predict homogeneous grain boundary structures. The presence of deep grain boundary energy cusps has consequences for grain boundary motion because vicinal boundaries may move by flow of steps. Therefore, the mobility of such boundaries is controlled by the mobility of steps.

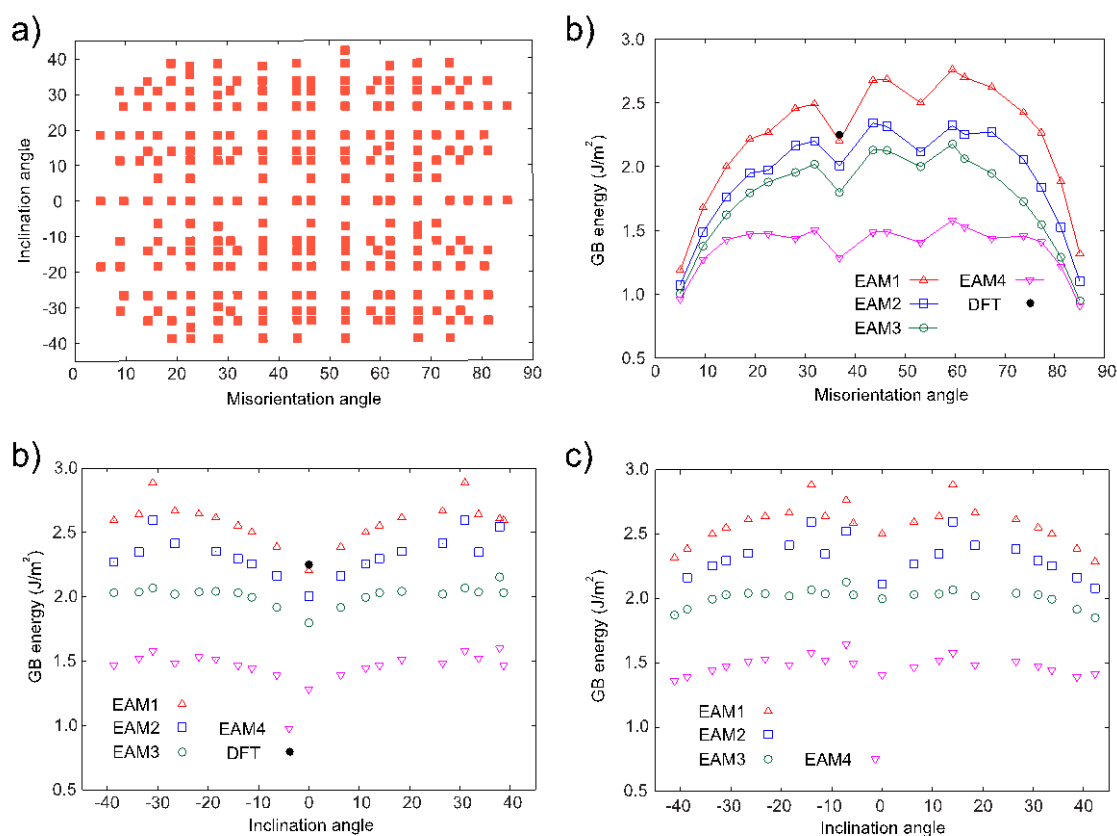


Figure 1. a) Studied 246 [001] tilt boundaries with misorientation angle ranging from 0° to 90° degrees and the inclination angle ranging from -45° to 45° degrees. b) Energy of symmetrical tilt boundaries calculated using four different potentials using γ surface construction. Energy of $\Sigma 5(310)[001]$ calculated with DFT. c) and d) GB energies as functions of inclination angle for misorientations of 36° and 53.13° degrees. Zero inclinations represent $\Sigma 5(310)[001]$ and $\Sigma 5(210)[001]$ symmetrical tilt boundaries, respectively.

Figure 1d) indicates for a given misorientation that the low energy configurations correspond to inclinations of $\varphi = 0^\circ$ and $\theta \pm 45^\circ$. The strong inclination anisotropy suggests that the boundaries with the intermediate inclinations should form facets composed of $\Sigma 5(310)[001]$ and $\Sigma 5(210)[001]$ symmetrical tilt boundaries. This faceting has been observed in bcc Fe by electron microscopy and molecular dynamic simulations [23]. Faceting has strong influence on grain boundary mobility as well. Increasing temperature is expected to decrease the grain boundary anisotropy, so the faceting may disappear as the melting temperature is approached. The exact temperature at which the defaceting occurs must be determined from separate atomistic simulations.

[110] Symmetrical tilt boundaries

The magnitude of the grain boundary energy and the inclination anisotropy determines the driving force for coarsening and the mechanism of grain boundary motion which in turn influences the mobility. Since the different potentials studied here demonstrated very different predictions for both the magnitude and the degree of anisotropy, these predictions have to be checked against the existing DFT calculations. For this comparison, we calculated grain boundary energies for the second set of [110] symmetrical tilt boundaries for which grain boundary energy was calculated for a large misorientation range using first principles methods [21, 22].

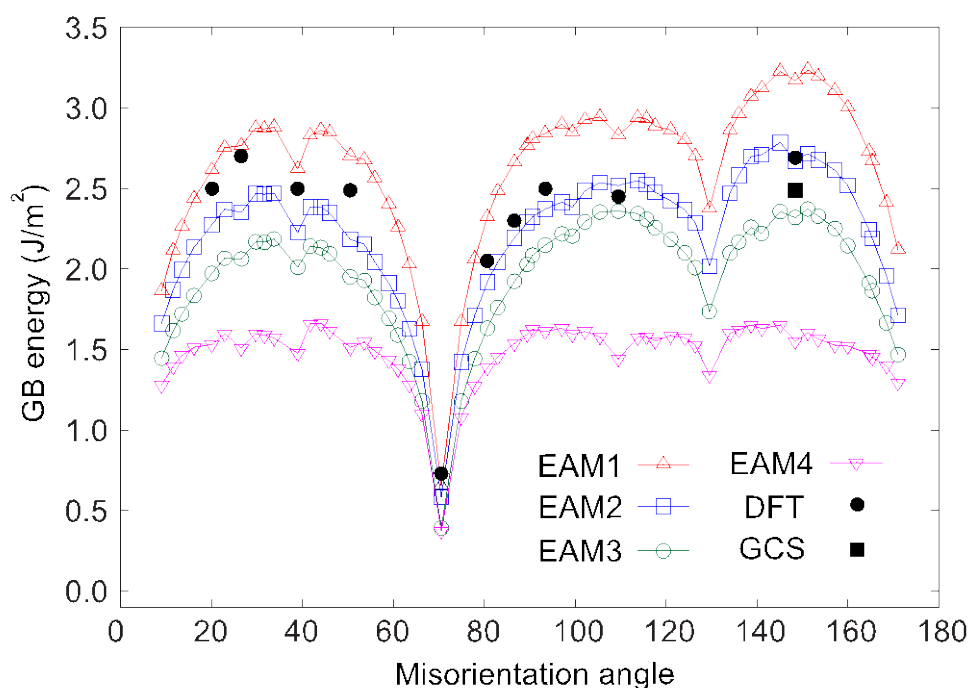


Figure 2. GB energy as a function of misorientation angle for [110] symmetrical tilt boundaries.

Figure 2 illustrates grain boundary energy as a function of misorientation calculated for [110] symmetrical tilt boundaries calculated using four different interatomic potentials. The plot also contains the DFT data from Refs. [21, 22]. The energies of the fifty-seven boundaries were obtained using the γ surface approach. It is evident from the figure that the different potentials predict similar trends, but provide significantly different magnitudes of the grain boundary energies. The grain boundary energy function has two deep cusps at 70.5° and 129.5° misorientation angles. The deepest energy cusp corresponds to $\Sigma 3(112)[110]$ boundary. The structure of this boundary is illustrated in Figure 3c).

Despite the sim

in some cases the different potentials predict very different grain boundary structures for the same misorientation angle. For example Figures 7a) and b) illustrates two different structures of the $\Sigma 33(118)[110]$ (20.1°) boundary predicted by EAM1 and EAM2 potentials, respectively. The EAM1 structure agrees with the DFT calculations. At the same time EAM1 overestimates and EAM2 underestimates the DFT value by about the same amount. While EAM1 perfectly matches the grain boundary energy values for some boundaries, the EAM2 performs better on average for a number of $[110]$ symmetrical tilt boundaries. These discrepancies motivate us to check whether the γ surface approach actually finds the ground states.

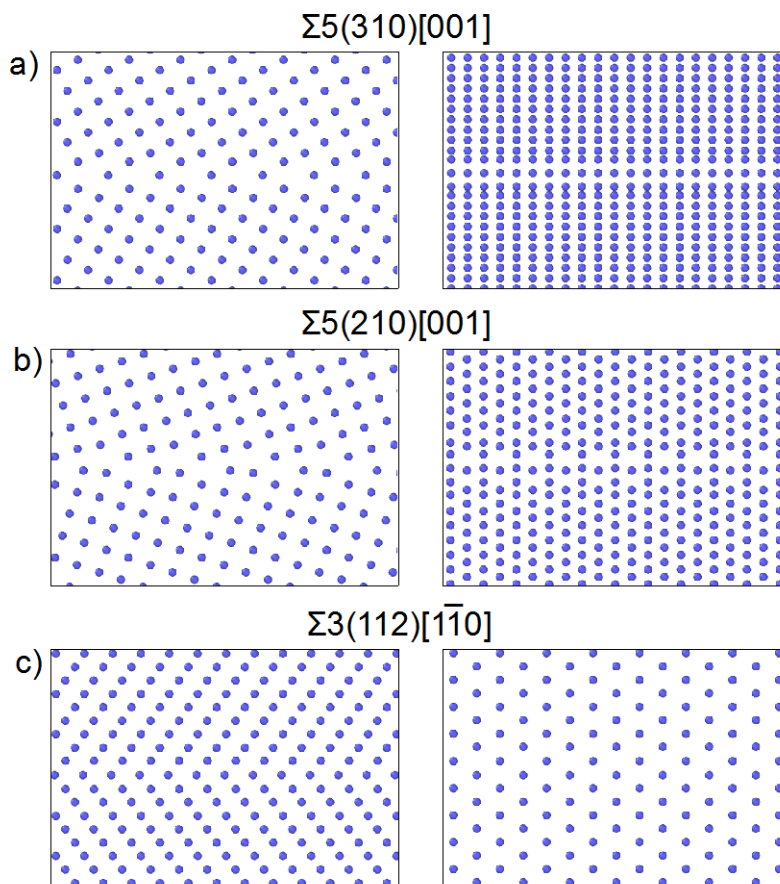


Figure 3. Examples of ground states of high angle $[001]$ and $[110]$ symmetrical tilt boundaries obtained by γ surface construction and GCS methods.

Grand Canonical Sampling (GCS) of grain boundary structure

We performed the grand canonical search for a subset of eight grain boundaries taken from a wide range of misorientation angles. In GCS approach, in addition to the rigid translations of the grains relative to each other, we change the atomic density at the boundary and sample different structures by displacing atoms in the grain boundary region from their ideal lattice positions. The calculations demonstrated that GCS yields the same ground states as the γ surface approach for $\Sigma 5(210)[001]$, $\Sigma 5(310)[001]$, $\Sigma 3(112)[110]$ and $\Sigma (111)[110]$ boundaries. These boundaries correspond to energy cusps for $[100]$ and $[110]$ symmetrical tilt boundaries. Although atomically ordered states with higher atomic grain boundary density were observed upon loading of interstitials into $\Sigma 5(210)[001]$ grain boundary in bcc Mo [24], the energy of those states were found to be much higher than the energy of the ground state. The

$\Sigma 3(112)[110]$ boundary is very ordered and is the deepest energy cusp, so perhaps it is not surprising that it was found to be the ground state.

On the other hand, GCS applied to other four $[110]$ boundaries yielded structures that were significantly different from the γ surface generated configurations. These boundaries were selected to cover a wide range of misorientations away from the energy cusps located at 70.5 and 129.5.

In the range $0^\circ < \theta < 70.5^\circ$ we selected the 20.1° and 26.5° misorientations. As discussed earlier, the γ surface approach configurations generated using EAM1 and EAM2 potentials are illustrated in Figures 7 a) and b), respectively. At an extra atomic fraction of 1/3 of the $[118]$ plane, GCS predicts different grain boundary configurations with energies $\gamma_{GB} = 2.615 \text{ J/m}^2$ and $\gamma_{GB} = 2.226 \text{ J/m}^2$ for EAM1 and EAM2 potentials, respectively. These values are nearly degenerate with ones generated by the γ surface approach which yields $\gamma_{GB} = 2.611 \text{ J/m}^2$ and $\gamma_{GB} = 2.257 \text{ J/m}^2$ for these two potentials. The GCS generated structures are illustrated in Figures 7 c) and d). The GCS configurations are 1 x 3 reconstructions, which means that they have larger area compare to the γ surface constructed boundary. Differently from the configuration in Figure 7a) and b), grain boundary atoms occupy positions between the $[110]$ planes, while the planes of the two different grains are still aligned. This arrangement is analogous to structures of high temperature grain boundary phases found in previous work in Cu [7]. While the γ surface approach yields very different structures for EAM1 and EAM2, the GCS states are still not identical but remarkably similar. In fact, GCS predicts a large number of grain boundary configurations of the type illustrated in Figures 7 c) and d) with nearly identical energies but slightly different arrangement of atoms along the tilt axis. This multiplicity of structures may contribute to the configurational entropy making these structures favorable at finite temperature.

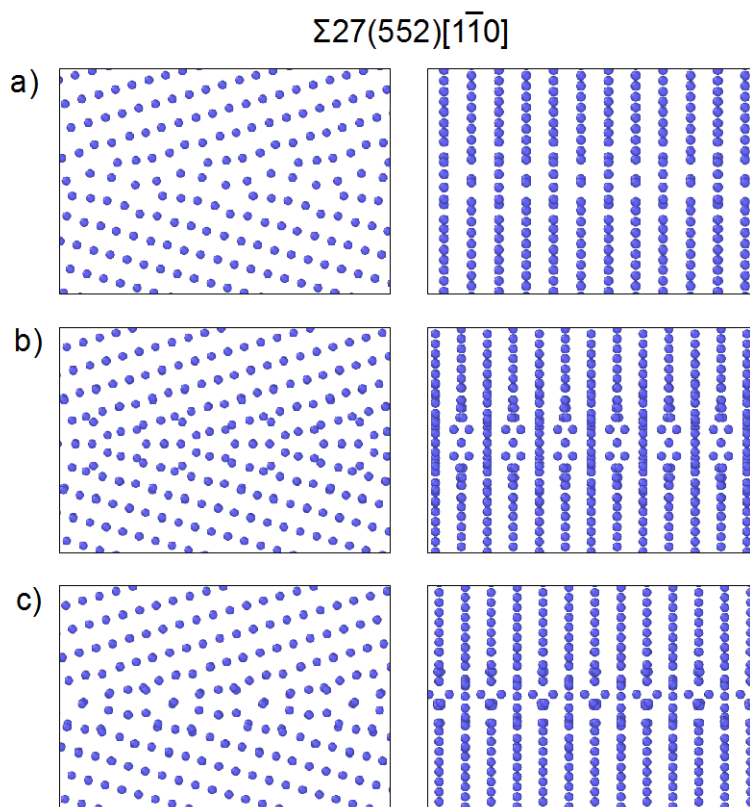


Figure 4. Multiple structures of $\Sigma 27(552)[110]$ grain boundary. a) The best configuration predicted by the traditional approach of γ surface construction with GB energy $\gamma_{GB} = 2.67 \text{ J/m}^2$ b) and c) Grain boundary structures obtained by GCS with atomic fractions 0 and 0.5 and energies $\gamma_{GB} = 2.495 \text{ J/m}^2$ and $\gamma_{GB} = 2.493 \text{ J/m}^2$, respectively.

In the angle range $129.5^\circ < \theta < 180^\circ$ we examined the $\Sigma 27(552)[110]$ boundary with a misorientation angle of 148° . Figure 4 illustrates multiple structures of this grain boundary predicted by EAM2 potential. Figure 4a) shows the best configuration predicted by the traditional approach of γ surface construction with GB energy $\gamma_{GB} = 2.67 \text{ J/m}^2$, while b) and c) correspond to grain boundary structures obtained by GCS with atomic fractions 0 and 0.5 and energies $\gamma_{GB} = 2.495 \text{ J/m}^2$ and $\gamma_{GB} = 2.493 \text{ J/m}^2$, respectively. Notice that the configuration in Figure 4b) has much lower energy even though no atoms are added or removed from the grain boundary core just like in the γ surface approach. This example emphasizes the importance of sampling. Similar to the 20.5° and 26° boundaries discussed earlier, the GCS configurations of this boundary are 1×3 reconstructions with the grain boundary atoms also occupying positions between the $[110]$ planes.

The GCS for other two boundaries with misorientations of 26.5° and 109.5° degrees demonstrated similar trends.

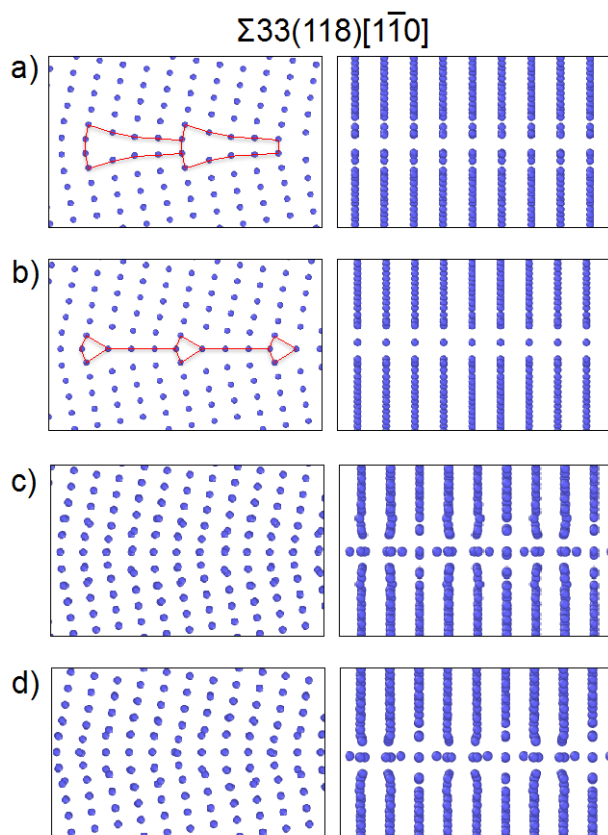


Figure 5. Structures of $\Sigma 33(118)[110]$ grain boundary (20.1°). a) Lowest energy state with $\gamma_{GB} = 2.611$ J/m^2 generated with the γ surface approach using EAM1 potential, same structure as γ surface approach with DFT [22, 21] b) γ surface approach with EAM2, $\gamma_{GB} = 2.257$ J/m^2 c) Grain boundary structures obtained by GCS using EAM1 with atomic fraction 0.333 and energy $\gamma_{GB} = 2.615$ J/m^2 . d) Grain boundary structures obtained by GCS using EAM2 with the same atomic fraction of 0.333 and energy $\gamma_{GB} = 2.226$ J/m^2 .

High temperature simulations

To validate the grain boundary structures generated at 0K by the GCS approach we annealed the bicrystals at high temperature following the simulation methodology proposed in our previous work [11]. In this approach, instead of using periodic boundary conditions a grain boundary is terminated at an open surface. The surface acts as source and sink of atoms. During the simulation the atomic density of the boundary can adjust by the diffusion of atoms to and from the surface. The transport of atoms along the grain boundary is limited by diffusion, as a result, the system has to be annealed at a relatively high temperature for tens of nanoseconds. To make sure that the final grain boundary structure is independent of the initial configuration we performed simulations with the initial structure taken from both the γ surface approach and GCS calculations.

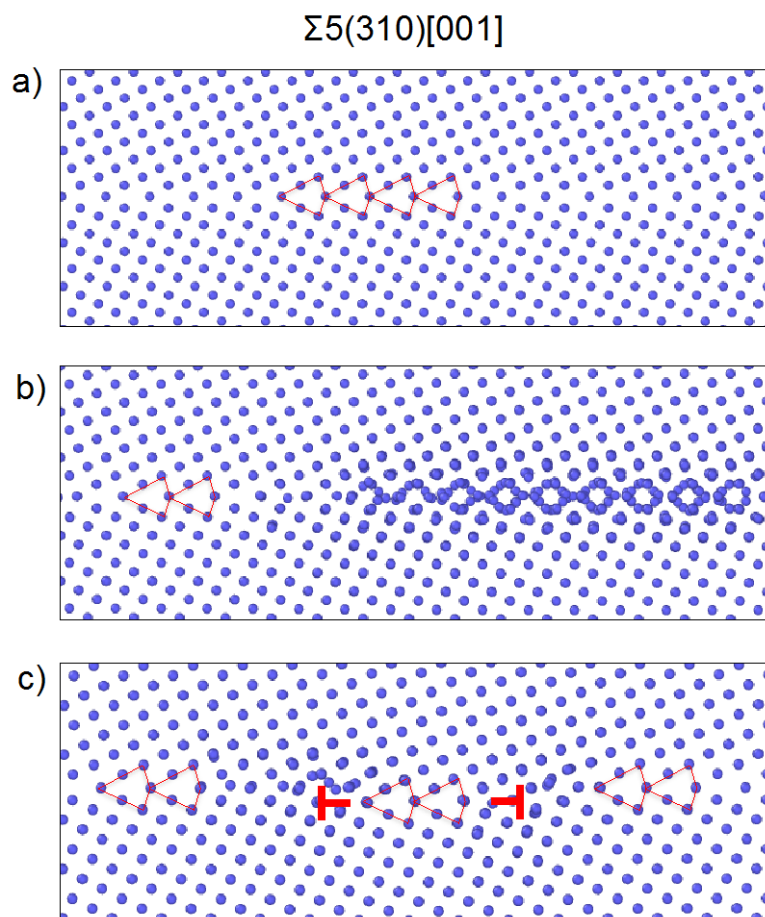


Figure 6. a) Interstitials are introduced into a bicrystal with perfect $\Sigma 5(310)[001]$ grain boundary. The grain boundary kite-shaped structural units are outlined in red. b) The atoms diffuse to the boundary and get absorbed by locally forming a metastable ordered grain boundary structure with higher energy. c) Metastable grain boundary segment transforms into an interstitial loop at the grain boundary.

Isothermal anneals of the $\Sigma 5(310)[001]$ with an open surfaces confirmed that the 0K calculated structure was also stable at high temperature. To observe the metastable states with higher atomic density, we introduced interstitials into the bulk lattice just above the grain boundary plane and annealed the simulation blocks at 2000K and 2500K. In these simulations, periodic boundary conditions were applied parallel to the grain boundary plane to eliminate sinks for the interstitial atoms. At both temperatures we first observed a formation of an ordered grain boundary structure that absorbed the interstitials. Figure 6b) illustrates the two different states of the boundary, which are similar to structures observed by Novoselov and Yuniikin in Mo [24]. This new metastable configuration exists for almost 100ns at 2000K and tens of nanoseconds at 2500K before it transforms into an interstitial loop at the boundary. The final state of the boundary is illustrated in Figure 6c). The grain boundary segment confined between the two grain boundary dislocations is composed of perfect kite shaped structural units. These units appeared out of the metastable configuration with interstitials demonstrating that the kite structure of this boundary is very stable. The relatively long life of the metastable high energy state is probably due to a large barrier of transformation that involves nucleation of the dislocations. The energy analysis at 0K and the simulations at high temperature demonstrate that the γ surface approach predicts the ground state for these boundaries.

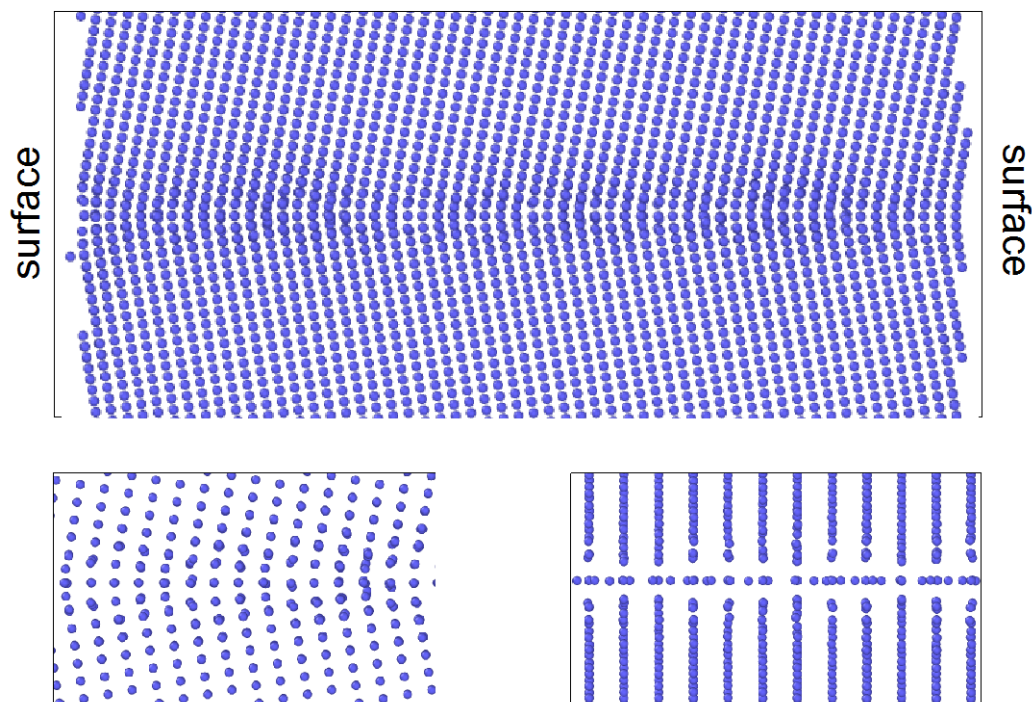


Figure 7. Validation and comparison of grain boundary structures found at 0K with grain boundary structures at finite temperature. Bicrystal with $\Sigma 33(118)[110]$ grain boundary terminated at an open surface and annealed at 2500K for several nanoseconds. The open surface enables variation of atomic density. The bottom panels show the zoomed in views of the equilibrated boundary structure. The high temperature GB structure is different from γ surface constructed boundary, but matches the prediction of GCS calculations.

Very different behavior, but consistent with the 0K calculations, was found for the $[110]$ boundaries. Figure 8 illustrates the bicrystal with the $\Sigma 27(552)[110]$ grain boundary modeled with EAM1 potential that was annealed at 2500 K for 100 ns. The initial configuration was taken from the γ surface approach. After the anneal the structure of the grain boundary is ordered and uniform throughout the bicrystal. Figures 8b) and c) illustrate the closer views of the structure with the tilt axis normal and parallel to the plane of the figure, respectively. Notice that the atoms in the grain boundary region occupy space in between the $[110]$ atomic planes. The grain boundary structure matches the configuration obtained using GSC illustrated in Figure 4c). This grain boundary structure has 50% extra atoms as a fraction of the (552) plane relative to the initial configuration obtained using the γ surface approach, which means that the extra atoms diffused inside the grain boundary from the open surface during the simulation. In addition to changes in the grain boundary structure, the surface triple junction on the left-hand side of the figure shows a chevron reconstruction. Similar reconstructions were previously observed experimentally electron microscopy in Au [25, 26]. The atoms inside the triangular region have bcc structure. The two boundaries that form the chevron are the $\Sigma 3(112)[110]$ (70.5) boundaries. Notice that the other surface triple junction does not undergo a similar reconstruction.

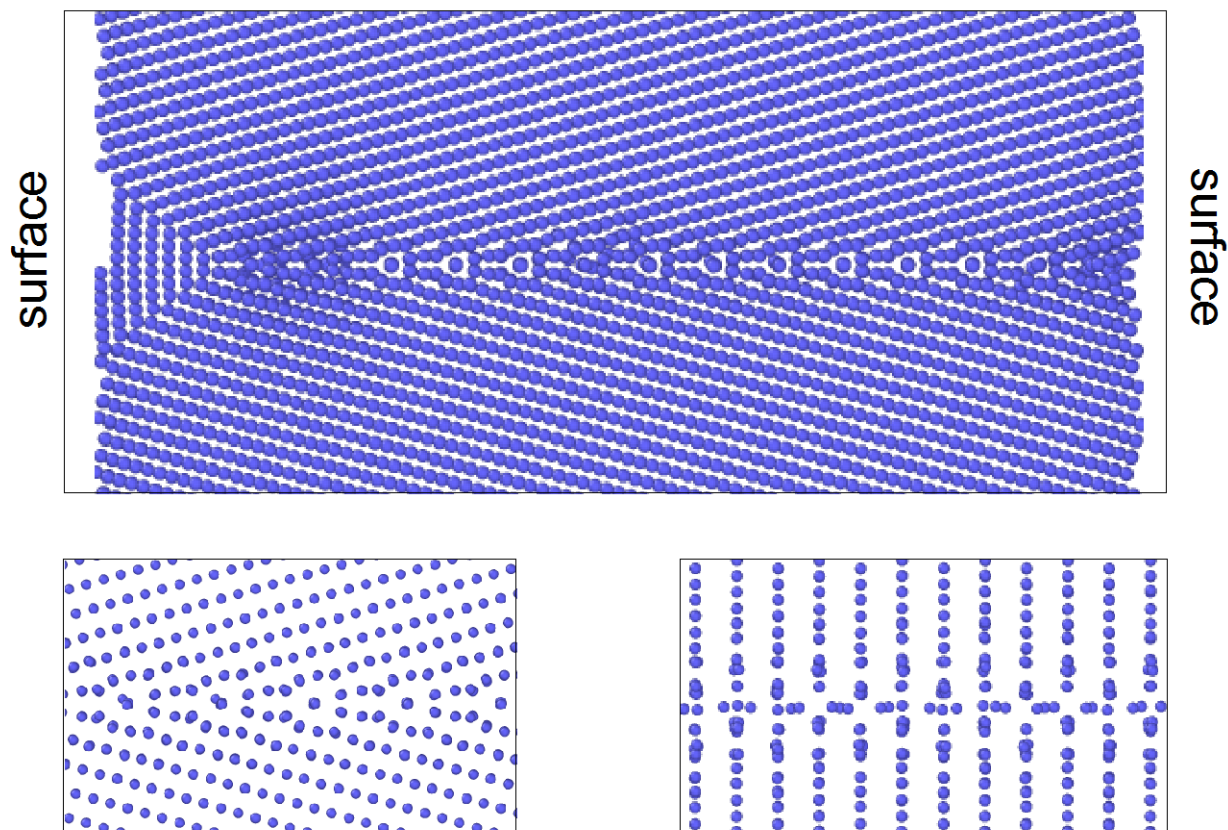


Figure 8: Validation and comparison of grain boundary structures found at 0K with grain boundary structures at finite temperature. Bicrystal with $\Sigma 27(552)[110]$ grain boundary terminated at an open surface and annealed at 2500K for tens of nanoseconds. The open surface enables variation of atomic density. The bottom panels show the zoomed in views of the equilibrated boundary structure. The high temperature GB structure is different from γ surface constructed boundary, but matches the prediction of GCS calculations.

For the majority of the [110] symmetrical tilt boundaries with the exception of the two structures that correspond to energy cusps, the γ surface approach is insufficient to predict grain boundary configurations at 0K and finite temperatures. On the other hand, the GCS calculations predict new grain boundary ground states at 0K that remain to be the stable configurations at high temperature.

Acknowledgments

This work was performed under the auspices of the U.S. Department of Energy by Lawrence Livermore National Laboratory under Contract No. DE-AC52-07NA27344. We acknowledge the use of Livermore Computing supercomputer resources. LLNL-TR-722088.

References

- [1] S. R. Phillpot and J. M. Rickman, *The Journal of Chemical Physics* 97, 2651 (1992).
- [2] S. R. Phillpot, *Phys. Rev. B* 49, 7639 (1994).
- [3] S. von Alfthan, P. D. Haynes, K. Kashi, and A. P. Sutton, *Phys. Rev. Lett.* 96, 055505 (2006).
- [4] S. von Alfthan, K. Kaski, and A. P. Sutton, *Phys. Rev. B* 76, 245317 (2007).

- [5] A. L. S. Chua, N. A. Benedek, L. Chen, M. W. Finnis, and A. P. Sutton, *Nature Mater.* 9, 418 (2010).
- [6] J. Zhang, C.-Z. Wang, and K.-M. Ho, *Phys. Rev. B* 80, 174102 (2009).
- [7] T. Frolov, M. Asta, and Y. Mishin, *Current Opinion in Solid State and Materials Science* 20, 308 (2016).
- [8] P. R. Cantwell, M. Tang, S. J. Dillon, J. Luo, G. S. Rohrer, and M. P. Harmer, *Acta Materialia* 62, 1 (2014).
- [9] T. Frolov, M. Asta, and Y. Mishin, *Phys. Rev. B* 92, 020103 (2015).
- [10] T. Frolov, S. V. Divinski, M. Asta, and Y. Mishin, *Phys. Rev. Lett.* 110, 255502 (2013).
- [11] T. Frolov, D. L. Olmsted, M. Asta, and Y. Mishin, *Nat. Commun.* 4, 1899 (2013).
- [12] T. Frolov, *Applied Physics Letters* 104, 211905 (2014).
- [13] S. J. Dillon and M. P. Harmer, *Acta Materialia* 55, 5247 (2007).
- [14] J. Luo, H. Wang, and Y.-M. Chiang, *Journal of the American Ceramic Society* 82, 916 (1999).
- [15] J. Luo, H. Cheng, K. M. Asl, C. J. Kiely, and M. P. Harmer, *Science* 333, 1730 (2011).
- [16] M. C. Marinica, L. Ventelon, M. R. Gilbert, L. Proville, S. L. Dudarev, J. Marian, G. Bencteux, and F. Willaime, *Journal of Physics: Condensed Matter* 25, 395502 (2013).
- [17] X. Zhou, H. Wadley, R. Johnson, D. Larson, N. Tabat, A. Cerezo, A. Petford-Long, G. Smith, P. Clifton, R. Martens, and T. Kelly, *Acta Materialia* 49, 4005 (2001).
- [18] G. J. Ackland and R. Thetford, *Philosophical Magazine A* 56, 15 (1987).
- [19] N. Juslin and B. Wirth, *Journal of Nuclear Materials* 432, 61 (2013).
- [20] N. Juslin, P. Erhart, P. Traskelin, J. Nord, K. O. E. Henriksson, K. Nordlund, E. Salonen, and K. Albe, *Journal of Applied Physics* 98, 123520 (2005).
- [21] W. Setyawan and R. J. Kurtz, *Journal of Physics: Condensed Matter* 26, 135004 (2014).
- [22] D. Scheiber, R. Pippin, P. Puschnig, and L. Romaner, *Modelling and Simulation in Materials Science and Engineering* 24, 035013 (2016).
- [23] D. Medlin, K. Hattar, J. Zimmerman, F. Abdeljawad, and S. Foiles, *Acta Materialia* 124, 383 (2017).
- [24] I. Novoselov and A. Yanilkin, *Computational Materials Science* 112, Part A, 276 (2016).
- [25] F. Lançon, T. Radetic, and U. Dahmen, *Phys. Rev. B* 69, 172102 (2004).
- [26] T. Radetic, F. Lançon, and U. Dahmen, *Phys. Rev. Lett.* 89, 085502 (2002).

8.4 MODELING DUCTILE-PHASE TOUGHENED TUNGSTEN FOR PLASMA-FACING MATERIALS: PROGRESS IN DAMAGE FINITE ELEMENT ANALYSIS OF THE TUNGSTEN-COPPER BEND BAR TESTS—B. N. Nguyen, C. H. Henager, Jr., R. J. Kurtz (Pacific Northwest National Laboratory)

OBJECTIVE

The objective of this study is to investigate the deformation behavior of ductile phase toughened W-composites such as W-Cu and W-Ni-Fe by means of a multiscale finite element model that involves a microstructural dual-phase model where the constituent phases (i.e., W, Cu, Ni-Fe) are finely discretized and are described by a continuum damage model. Such a model is suitable for modeling deformation, cracking, and crack bridging for W-Cu, W-Ni-Fe, and other ductile phase toughened W-composites, or more generally, any multi-phase composite structure where two or more phases undergo cooperative deformation in a composite system. Our current work focuses on simulating the response and damage development of the W-Cu specimen subjected to three-point bending.

SUMMARY

A promising approach to increasing fracture toughness and decreasing the ductile-brittle transition temperature (DBTT) of a W-alloy is by ductile-phase toughening (DPT) [1-3]. In this method, a ductile phase is included in a brittle matrix to prevent fracture propagation by crack bridging or crack deflection. Liquid-phase sintered W-Ni-Fe alloys and hot-pressed and sintered W-Cu composites are two examples of such materials that PNNL and University of California at Santa Barbara are investigating. However, there is a need for improved mechanical property models of such composite systems in order to begin to optimize these structural materials with regard to strength and fracture toughness. This report describes such a model that has recently been developed at PNNL.

PROGRESS AND STATUS

Background

Tungsten (W) and W-alloys are the solid materials of choice for plasma-facing components (PFCs) of future fusion reactors, such as the International Thermonuclear Experimental Reactor (ITER) and Demonstration Power Plant (DEMO), due to their high melting point, strength at high temperatures, high thermal conductivity, low coefficient of thermal expansion, and low sputtering yield [4-6]. However, W and most W-alloys exhibit low fracture toughness and a high DBTT that would render them as brittle materials during reactor operations [4, 6, 7]. The DBTT for unirradiated W-alloys typically ranges from 573K to 1273K (300 to 1000°C), and in a reactor environment radiation hardening would further elevate this range [6, 8, 9]. W-alloys toughened by engineered reinforcement architectures, such as ductile-phase toughening (DPT), are strong candidates for PFCs. In DPT, a ductile phase is included in a brittle matrix to prevent fracture propagation. The principles of DPT are illustrated in Figure 1, which shows an actual and schematic illustration of ductile bridging ligaments stretching across an open crack in a brittle matrix material, such as W [10].

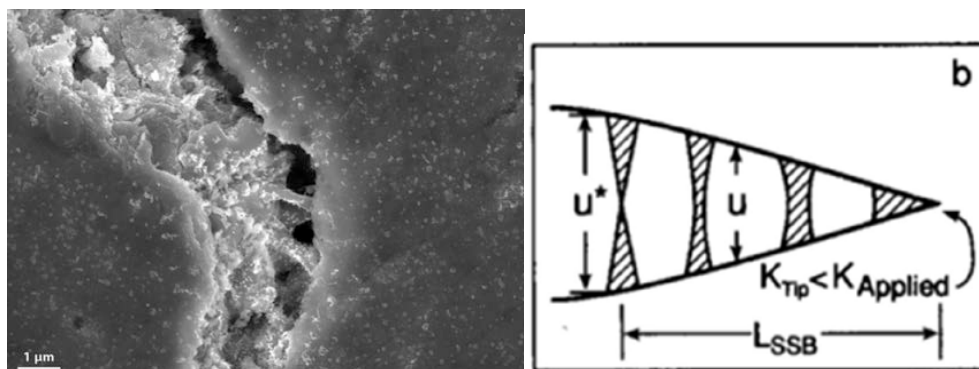


Figure 1. a) SEM image of W-Cu fracture where the ductile phase (Cu) is effectively bridging the crack. b) A steady-state bridging zone shown schematically in 2D [10].

Model Development

The approach is to create homogenized, meshed regions alongside the dual-phase meshed region shown in Figure 2a to create a fully meshed model of a bend bar that corresponds to the physical dimensions of our 3-point or 4-point bend samples. The as-created FE mesh shown in Figure 2a for the bending specimen possesses three regions: the dual phase W-Cu microstructural region containing the notch, and two adjacent continuum homogenized Cu-W regions.

First, the microstructural region is created from a digital image of an actual microstructure using the public domain software OOF2¹ that creates multiple mesh domains with high-resolution elements at phase boundaries. Several digital images of actual microstructures were also used to achieve various FE meshes of the actual microstructures for examinations. Figure 2b shows a magnified view of the microstructural meshed region where the Cu elements (colored in yellow) are embedded in the W elements (colored in dark green). The OOF2 software allows the user to specify mechanical properties for each meshed domain and generates an input file containing FE mesh information and material assignments for ABAQUS®. In this work, an elastic-plastic damage model is subsequently used to describe the behaviors of Cu and of W. Plastic deformation and damage are allowed only in the microstructural dual phase region.

Next, a FORTRAN script was written and used to mesh the homogenized Cu-W elastic regions that are connected to the microstructural region to achieve the meshing for the whole specimen. The elastic properties of the homogenized Cu-W regions were computed using EMTA [11] considering the same volume fraction of W (50%) as for the microstructural region. Finally, to complete the FE model for the W-Cu single-edge-notched bend (SENB) bar, meshing for the supports and loading pin is performed considering their actual dimension (diameter = 3.1 mm) and support span ($L=13$ mm).

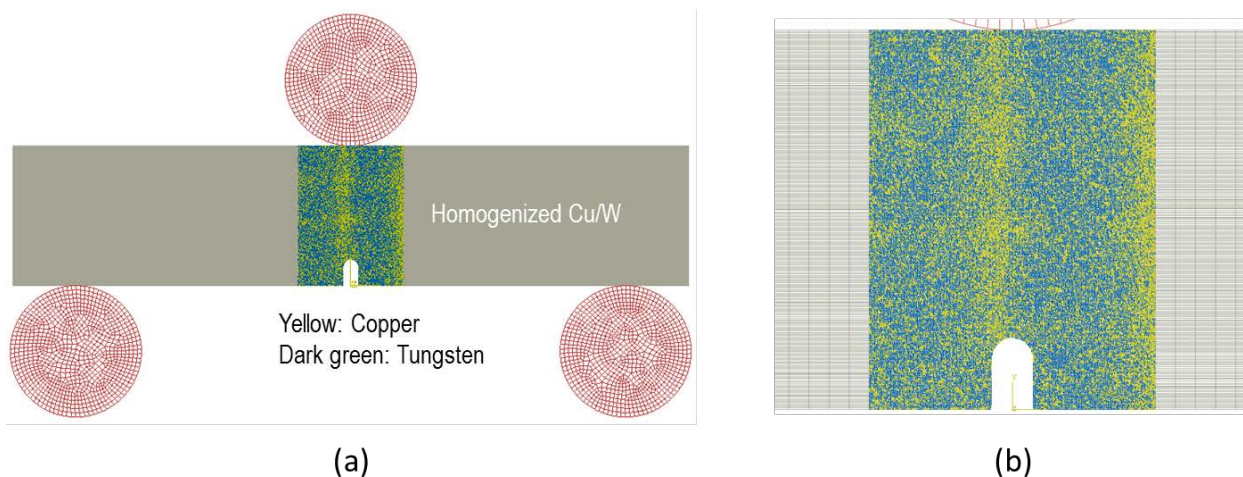


Figure 2. (a) The FE mesh of the W-Cu single-edge-notched bend (SENB) bar that is 3.3 x 1.6 x 16 mm in size. This mesh contains 218654 2D plane-strain elements including 91000 elements in the microstructural zone. (b) A magnified view with the constituent phases identified by color.

A three-dimensional (3D) FE model of the W-Cu SENB bar was also developed by extruding the nodes of the 2D mesh along the specimen thickness direction to generate the nodes in that direction. In this work, considering the symmetry of the specimen with respect to the XY plane (Figure 3) and assuming the symmetry of the microstructure with respect to this plane, a 3D FE mesh was created achieving the specimen's half thickness (0.8 mm). Figure 3 shows the 3D FE model developed for our study containing 554709 3D elements. Such a model is simply *geometrically* three-dimensional and has a simple 3D representation of the actual 3D microstructure in the dual phase region. For computational efficiency, the 2D plane-strain model has been explored at this time of the report.

¹ OOF2 was developed at the National Institute of Standards and Technology (NIST). See <http://www.ctcms.nist.gov/oof/oof2/>.

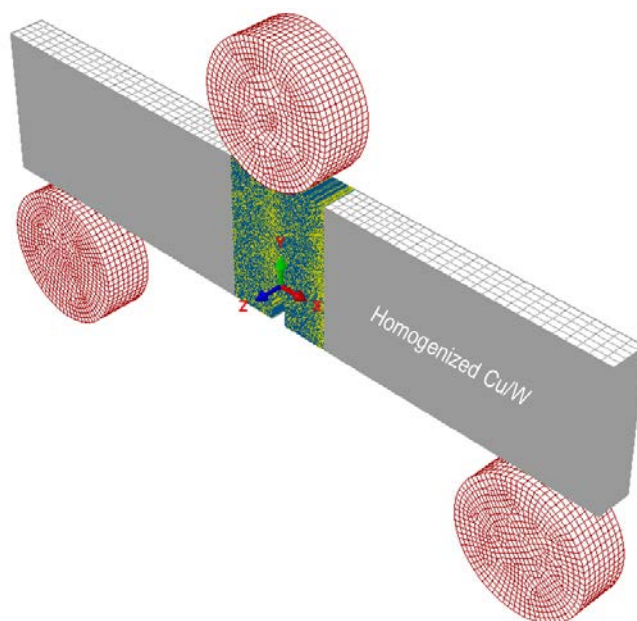


Figure 3. A 3D FE model for the W-Cu SENB specimen generated from 2D mesh shown in Fig. 2a.

The elastic-plastic damage behaviors of W and of Cu considered in the analyses are depicted in the true stress-strain responses shown in Figure 4. While the stress/strain behavior of the polycrystal Cu is generally well-known (e.g., Sandström & Hallgren [12]) and can be used to approximate the constitutive behavior of Cu in the W/Cu composite, the same kind of elastic plastic response of the polycrystal W in the composite is not known and has therefore been a subject of our investigation. The assumed stress/strain curve for W used in our current analysis of the W/Cu SENB bar is given in Figure 4. Cu has much lower elastic modulus and strength than W but has substantially greater ductility.

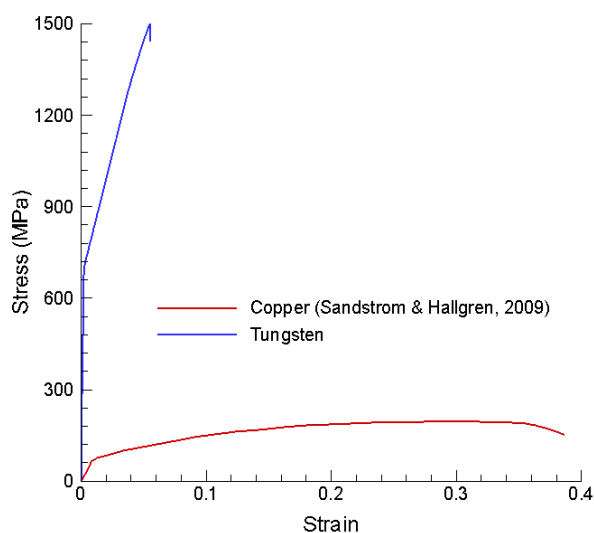


Figure 4. Stress/strain behaviors considered for each of the two phases.

Results

The FE model for the Cu-W SENB specimen subjected to three-point bending was analyzed by ABAQUS®. Figure 5a shows the deformed configuration of the specimen at 2.2-mm applied displacement. Figure 5a also shows the predicted damage distribution in the dual phase region at this loading level. Damage is quantified by a failure indicator that varies from 0 to 1. Total failure (or fracture) occurs if the failure indicator is equal to 1. Cracks are predicted to initiate and mainly propagate from the notch and also develop at some extent from the top surface of the specimen in contact with the loading pin. Figure 5b presents a magnified view of damage and fracture in the dual phase region. In addition to the notch area and top surface that experience cracking, predicted diffuse damage and microcracks are also observed surrounding these areas. We also find linking-up of cracks along the left side of the dual phase region. The occurrence of cracks at this location is believed to be due to a boundary effect that prevents damage to develop outside the dual phase region. Using a significantly wider dual phase region should resolve this problem. Figure 5c shows the cracked region observed in the experiment at room temperature. Comparing Figure 5b to Figure 5c shows that there is a good agreement between the predicted and experimental crack propagation directions. However, a more advanced macrocrack was found in the experiment at about the same applied displacement. Using a significantly wider dual phase region and further adjusting the W behavior would improve the numerical prediction.

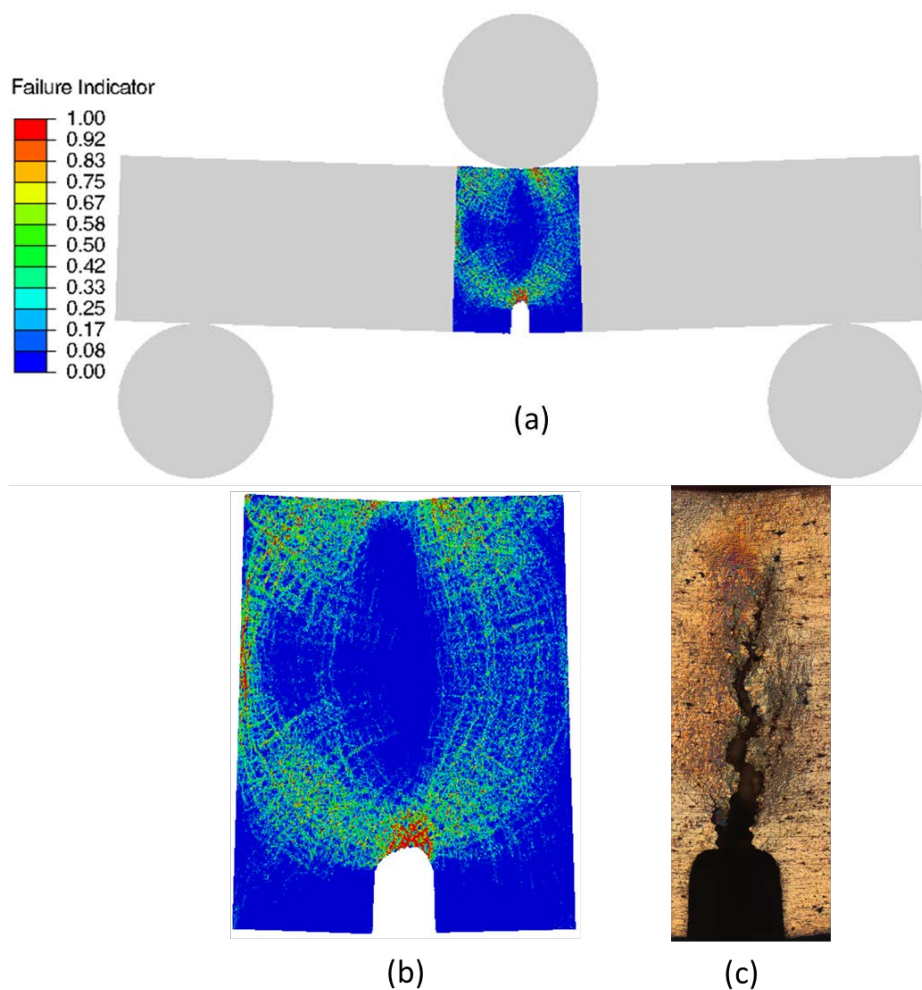


Figure 5. (a) Predicted deformed configuration and damage distribution in the W-Cu SENB specimen for 0.22-mm applied displacement, (b) a magnified view showing damage and fracture in the dual phase region, and (c) an experimental crack pattern observed after RT test.

To determine the extent of crack bridging, we illustrate in Figure 6a damage and fracture distributions in the notch region as well as the contour of equivalent plastic strains in this region (Figure 6b). Figure 6a is simply a magnified view of Figure 5b but it helps elucidate the bridging mechanism perceived in Figure 6b. In the areas where the elements (W or Cu) failed, the equivalent plastic strains are very large and exceed 0.4. These cracked areas are surrounded by Cu elements (light blue or green in the contour) that can still deform plastically as clearly shown in Figure 5b.

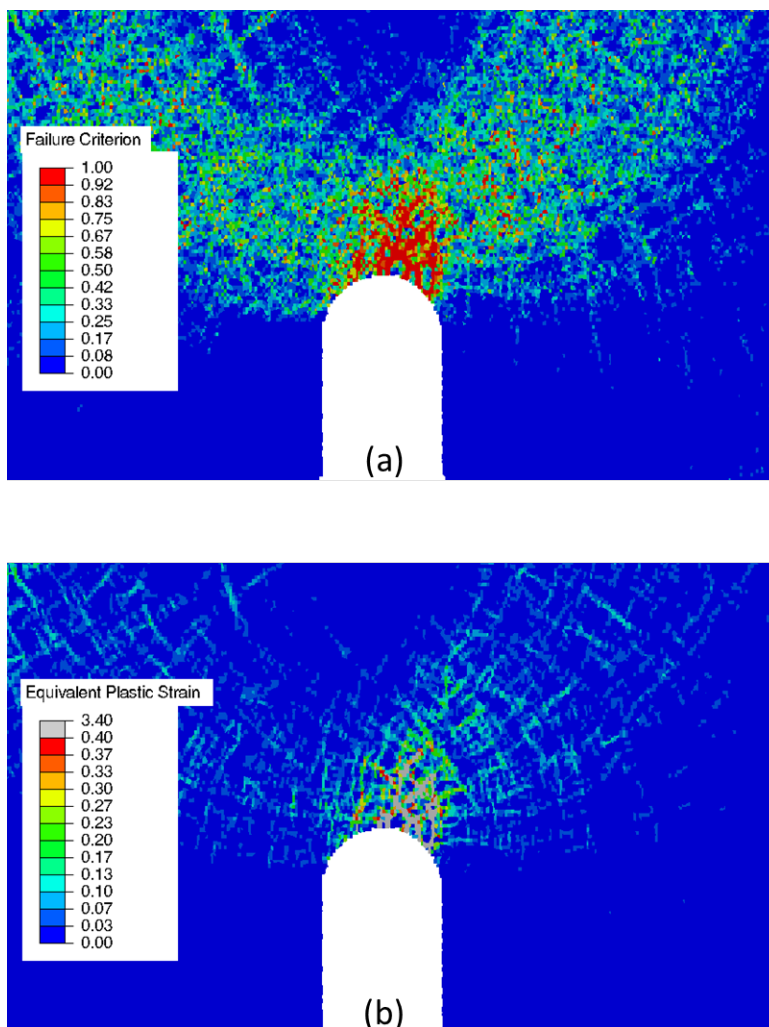


Figure 6. (a) a magnified view showing damage and fracture in notch region, and (b) Equivalent plastic strain in this region.

The predicted load-displacement response reported in Figure 7 agrees reasonably with the experimental data presented on the same figure. At this time, rate-independent plasticity has been used in our model. The predicted load-displacement curve agrees rather better with the experimental ones obtained at high strain rates. However, as mentioned previously, we are working on improving damage and failure prediction by using a significantly larger dual phase region and further assessing the constitutive behavior of W. Combined, that would allow a better prediction for the crack advance and result in better agreement between the prediction and experimental data.

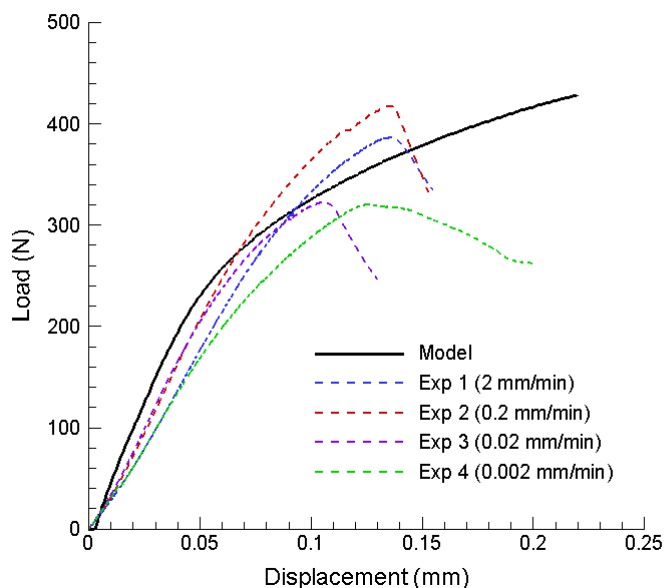


Figure 7. Predicted load-displacement response compared to the experimental results for the Cu-W SENB bar.

Conclusions

Our developed approach appears to be robust and an improvement over the dynamic bridging model previously developed and discussed to describe the amount of load sharing observed in the bend sample that increased with increasing temperature [13]. The current model predictions show reasonable agreement with our experimental data with respect to load-displacement curves and to the distributed cracking and damage in the W-Cu composite. The model can effectively capture the bridging mechanism responsible for preventing crack propagation.

Future Work

We will create FE models for the Cu-W SENB bar containing significantly larger dual-phase microstructural regions for better damage and fracture predictions. Additional bending tests will be conducted and the data including damage and fracture patterns will be collected for the model validation.

Acknowledgements

This research was supported by Office of Fusion Energy Sciences, U.S. Department of Energy (DOE) under Contract DE-AC05-76RL01830.

References

- [1] Deve, H.E., A.G. Evans, G.R. Odette, R. Mehrabian, M.L. Emiliani, and R.J. Hecht, *Acta metallurgica et materialia*, 1990. 38(8): p. 1491-502.
- [2] Erdogan, F. and P.F. Joseph, *J. Am. Ceram. Soc.*, 1989. 72(2): p. 262-270.
- [3] Sigl, L.S., P.A. Mataga, B.J. Dalgleish, R.M. McMeeking, and A.G. Evans, *Acta Metall.*, 1988. 36(4): p. 945-953.

- [4] Rieth, M., J.L. Boutard, S.L. Dudarev, T. Ahlgren, S. Antusch, N. Baluc, M.F. Barthe, C.S. Becquart, L. Ciupinski, J.B. Correia, C. Domain, J. Fikar, E. Fortuna, C.C. Fu, E. Gaganidze, T.L. Galan, C. Garcia-Rosales, B. Gludovatz, H. Greuner, K. Heinola, N. Holstein, N. Juslin, F. Koch, W. Krauss, K.J. Kurzydowski, J. Linke, C. Linsmeier, N. Luzginova, H. Maier, M.S. Martinez, J.M. Missiaen, M. Muhammed, A. Munoz, M. Muzyk, K. Nordlund, D. Nguyen-Manh, P. Norajitra, J. Opschoor, G. Pintsuk, R. Pippan, G. Ritz, L. Romaner, D. Rupp, R. Schaublin, J. Schlosser, I. Uytendhouwen, J.G. Van Der Laan, L. Veleva, L. Ventelon, S. Wahlberg, F. Willaime, S. Wurster, and M.A. Yar, *J. Nucl. Mater.*, 2011. 417: p. 463-467.
- [5] Pitts, R.A., A. Kukushkin, A. Loarte, A. Martin, M. Merola, C.E. Kessel, V. Komarov, and M. Shimada, *Physica Scripta Volume T*, 2009. 2009(T138): p. 014001 (10 pp.).
- [6] Mertens, P., T. Hirai, M. Knaup, O. Neubauer, V. Philipps, J. Rapp, V. Riccardo, S. Sadakov, B. Schweer, A. Terra, I. Uytendhouwen, and U. Samm, *Fusion Eng. Des.*, 2009. 84(7-11): p. 1289-93.
- [7] Mertens, P., V. Philipps, G. Pintsuk, V. Riccardo, U. Samm, V. Thompson, and I. Uytendhouwen, *Physica Scripta Volume T*, 2009. 2009(T138): p. 014032 (5 pp.).
- [8] Gludovatz, B., S. Wurster, A. Hoffmann, and R. Pippan, *Int. J. Refract. Met. Hard Mater.*, 2010. 28(6): p. 674-8.
- [9] Zinkle, S.J. and N.M. Ghoniem, *Fusion Eng. Des.*, 2000. 51-52: p. 55-71.
- [10] Odette, G.R., B.L. Chao, J.W. Sheckherd, and G.E. Lucas, *Acta metallurgica et materialia*, 1992. 40(9): p. 2381-9.
- [11] Nguyen, B.N., *EMTA User's Guide*. Pacific Northwest National Laboratory, Richland, WA, 2010, PNNL-19997.
- [12] Sandstrom, R. and Hallgren, *Stress strain flow curves for Cu-OFP*, Royal Institute of Technology, Swedish Nuclear Fuel and Waste Management Co, 2009, R-09-14.
- [13] Cunningham, K.H., K. Fields, D. Gragg, F.W. Zok, J. C. H. Henager, R.J. Kurtz, and T. Roosendaal, in *DOE/ER-0313/54 - Volume 54, Semiannual Progress Report, June 30, 2013*, Vol. 54, F. Wiffen, R. Godfrey, and B. Waddell, Editors. 2013, US DOE: ORNL, TN. p. 95-107.

8.5 OKMC STUDY OF COMPARISON OF CASCADE ANNEALING IN TUNGSTEN, MOLYBDENUM AND CHROMIUM—G. Nandipati, A. Pattanayak, W. Setyawan, R. J. Kurtz (Pacific Northwest National Laboratory) A. Shelby and B. D. Wirth (University of Tennessee)

OBJECTIVE

The objective of this work is to understand the difference in cascade annealing kinetics for tungsten, molybdenum and chromium cascades, which were obtained using molecular dynamics simulations, using the object kinetic Monte Carlo (OKMC) method.

SUMMARY

Results are obtained and discussed using the object kinetic Monte Carlo (OKMC) code KSOME [1] to simulate annealing of primary cascade damage in bulk tungsten (W), molybdenum (Mo) and chromium (Cr) for primary knock-on atom (PKA) energies of 7.5 keV and 15 keV at 300 K. Differences in defect mobility and, perhaps, cascade defect structures appear to be able to account for the observed annealing differences, but more work is required to fully understand the observations.

PROGRESS AND STATUS

Simulation Details

Simulations were performed using a non-cubic box with dimensions (300a x 304a x 306a, where a is the lattice constants of the materials studied), with each axis parallel to a <100> direction of the crystal. Each defect hops to one of eight body-centered cubic nearest neighbor lattice sites at $a/2(111)$. An isolated cascade is placed in the center of the simulation with absorbing boundary conditions, i.e. when a defect diffuses out of the box it is no longer tracked and it is removed from the simulation. Defects that cross the boundary are considered to have moved far enough from the cascade region that they can be regarded as spatially uncorrelated with the original cascade. The values of the migration barriers of defects for W are taken from Ref. [3], for Mo they were taken from Ref. [4, 5] and for Cr from Ref. [6]. The numerical values are given in Table 1.

Table 1. Migration barriers (in eV) for self-interstitial cluster (SIA) and vacancy clusters

Element	SIA	Vacancy
W	0.0013	1.66
Mo	0.05	1.30
Cr	0.1	0.95

In the present simulations, SIA clusters larger than size five were constrained to diffuse in 1D along one of four <111> directions. SIA clusters up to size five were allowed to change their direction of 1D motion via rotation and thereby to perform a mixed 1D/3D motion. The activation barrier for changing direction from one <111> direction to another in tungsten is 0.38 eV, and we have used the same rotation barrier for the materials. However, the probability for the rotation to occur even for a mono-SIA is negligible at 300 K. The direction of 1D motion was assigned randomly to the SIAs at the start of a simulation, and interstitial clusters of all sizes are assumed to be glissile. The migration rates of SIA clusters decrease with increasing cluster size (n) per $v_0 n^{-1.0}$ ($v_0 = 6 \times 10^{12} \text{ s}^{-1}$) while the migration barrier is taken to be independent of cluster size. In the case of vacancy clusters, sizes larger than five are assumed to migrate in 3D. Their diffusion rates decrease with cluster size (n) according to $v_0 (q^{-1})^{n-1}$ ($v_0 = 6 \times 10^{12} \text{ s}^{-1}$, $q = 1000$) [3]. The dissociation of either SIAs or vacancy clusters is not considered since the probability for dissociation at 300 K is negligible. We have assumed that defect clusters of all sizes and types are spherical objects and can coalesce or recombine if the capture radii of two defects overlap.

Results

Table 1 shows the number of Frenkel pairs in the cascades produced by PKA energies of 7.5 keV and 15 keV at 300 K obtained using molecular dynamics simulations. The number of Frenkel pairs is expected to decrease with increasing mass of the atom, while increasing with increasing PKA energy. The masses (M) of W, Mo and Cr are $M_W > M_{Mo} > M_{Cr}$. As expected, and one can see from Table 1, the number of Frenkel pairs increases with PKA energy while decreasing with atomic mass.

Table 2. Number of Frenkel pairs in the W, Mo and Cr cascades produced by a PKA energies of 7.5 keV and 15 keV at 300 K

Element	PKA Energy	
	7.5 keV	15 keV
W	9.70	15.0
Mo	12.0	21.5
Cr	25.0	45.6

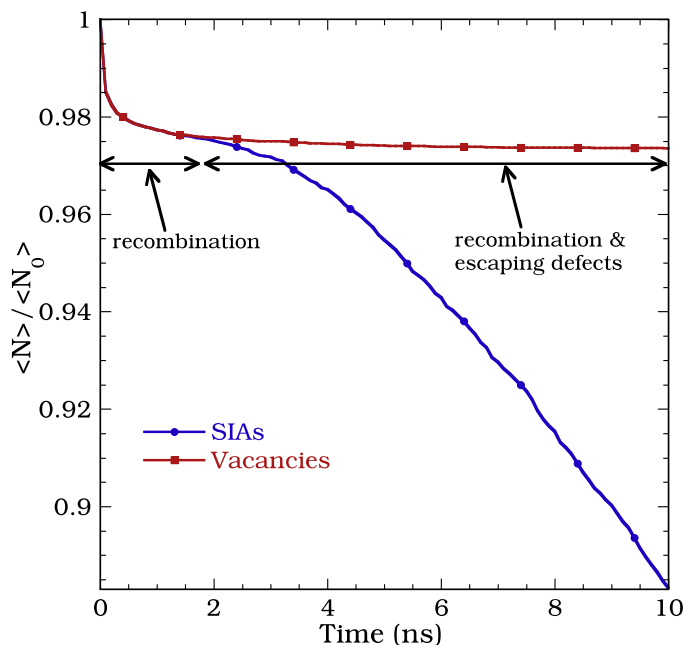


Figure 1. Surviving fraction of SIAs and vacancies as a function of time (Illustration).

At time $t=0$, the total number of vacancies and SIAs are equal. As annealing proceeds, the number of surviving defects initially drops due to recombination only (the surviving fraction of SIAs and vacancies are equal), and this occurs in the very first few ns of simulated time. The behavior can be visualized as shown in Figure 1, a plot of the surviving defect fraction ($n_d = \sum n S_d$, n = number of defect clusters of size S_d) of all SIAs and vacancy-type defects as a function of time. Beyond the recombination phase, the fraction of surviving SIAs continually drops as they diffuse beyond the boundary of the simulation box, resulting in the total number of SIAs no longer being equal to the number of vacancy-type defects. Even at 300 K, the interstitials migrate very fast, and they very quickly diffuse away from the primary damage region while the vacancy migration rate is so low that the vacancies are effectively immobile during the time-scale of the simulation. This plot shows common features of defect evolution across all the materials and PKA energies.

Figure 2 shows the surviving fraction of defects during cascade annealing up to 10 ns for PKA energies of 7.5 keV and 15 keV at 300 K. Note that the surviving fraction of SIAs and vacancies are plotted on different plots to see the differences in the cascade annealing behavior in W, Mo and Cr; otherwise the general behavior of cascade annealing in W and Mo with time is similar. SIAs both in Mo and W start to leave the simulation cell at almost the same time. This can be explained based on their very similar SIA migration barriers. However, the fraction of surviving defects increases with PKA energy while it decreases in Mo, which could be due to differences in the size and spatial distributions of defect clusters in the original cascade. In the case of Cr, cascade annealing is still in the recombination phase because the number of SIAs and vacancy-type defects are equal, and they appear to show a decreasing trend even at 10 ns. Also, no SIA cluster has escaped the simulation box, which is due to Cr having the highest migration barrier for SIA clusters among the three materials.

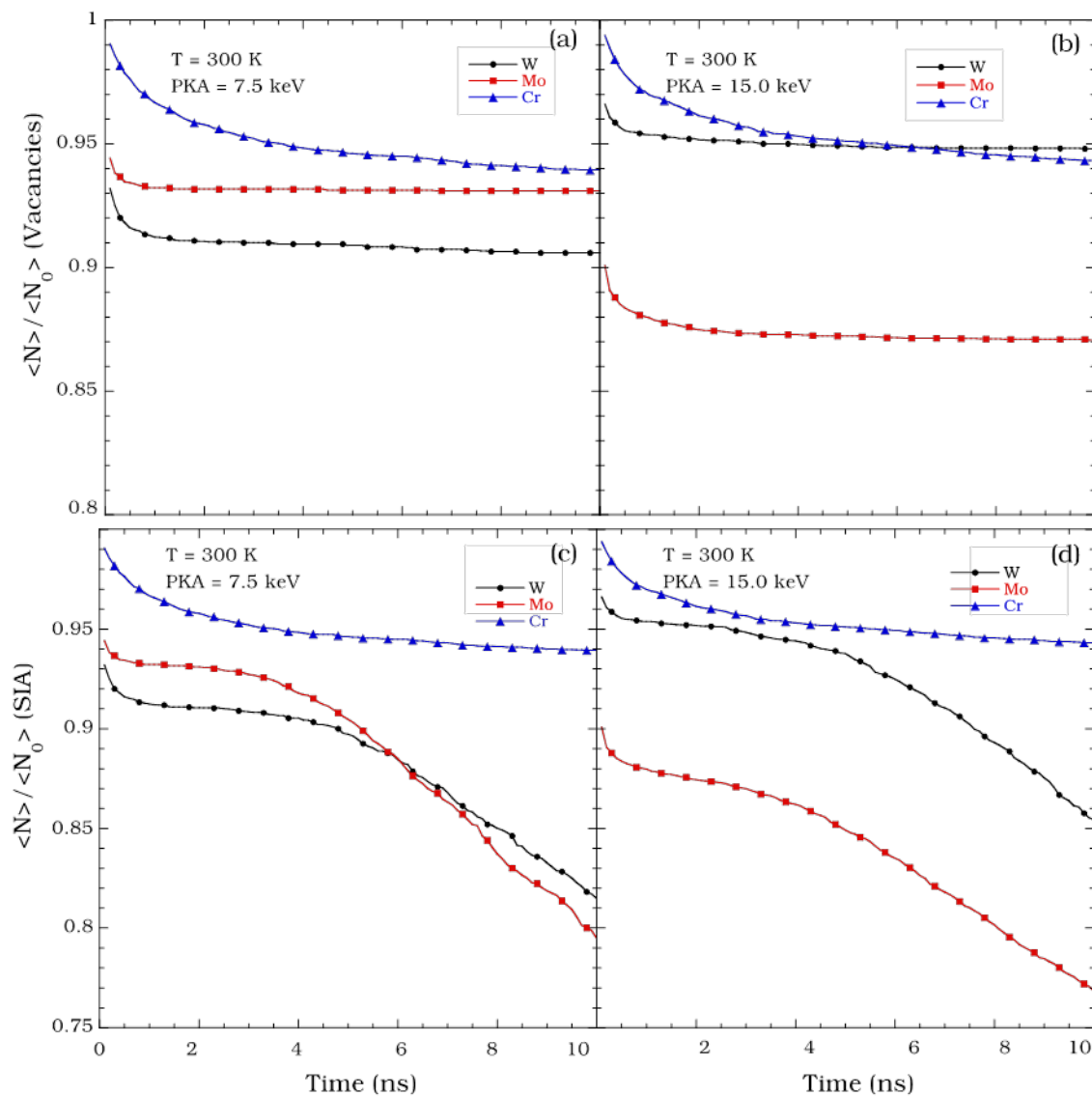


Figure 2. Surviving fraction of SIAs (c-d) and vacancies (a-b) as a function of time for PKA energies of 7.5 keV and 15.0 keV at 300 K.

Future Work

A complete understanding of annealing behavior also requires analyzing the differences in the size and spatial distributions of defect clusters in these materials as a function of PKA energy and temperature. Therefore, we plan to study those differences in these materials and carry out additional cascade annealing simulations using KSOME.

Acknowledgement

These simulations were performed OLYMPUS cluster at PNNL's PIC systems. This research was supported by Office of Fusion Energy Sciences, U.S. Department of Energy (DOE) under Contract DE-AC05-76RL01830.

References

- [1] G. Nandipati *et al.* Semiannual Progress Report DOE/ER-0313/54, June 2013, 179-183.
- [2] G. Nandipati *et al.* J. Nucl. Mater., 463 (2015) 338-344.
- [3] C. S. Becquart *et al.* J. Nucl. Mater., 403 (2010) 75.
- [4] T. T. Mattsson *et al.* Phys. Rev B, 80 (2009) 224104.
- [5] S. Han *et al.* Phys. B, 66 (2002) 220101(R).
- [6] D. Nguyen-Manh *et al.* J. Nucl Mater., 367-370 (2007) 257-262.

9. FUSION SYSTEM DESIGN

9.1 PREPARATION FOR MATERIAL STANDARDIZATION OF ALLOY F82H—H. Sakasegawa, H. Tanigawa, T. Miyazawa, T. Hirose (National Institutes for Quantum and Radiological Science and Technology, Japan), R.K. Nanstad and Y. Katoh (Oak Ridge National Laboratory)

OBJECTIVE

The objective of this work is to prepare for the material standardization activity. The material standardization is an important step required for the use of F82H as the structural material of fusion reactor blanket modules. This work is part of the U.S. Department of Energy – National Institutes for Quantum and Radiological Science and Technology fusion materials collaboration.

SUMMARY

Existing codes such as RCC-MR and ASME define the required material data for the qualification of a new material. The result of gap analyses referring to these codes indicated that we now have adequate F82H material data to meet most requirements, but there are still some missing material data. It is necessary to continue some tests to comply with the requirements. We plan to integrate the material databases, to qualify F82H within the ASTM system.

PROGRESS AND STATUS

Introduction

Material standardization is generally required for new material applications complying with codes. Existing codes such as RCC-MR, RCC-MRx, ASME and JSME each have their own guidance and requirements for new material qualification. In the case of RCC-MRx 2015 edition, the European reduced activation ferritic/martensitic steel, Eurofer, is already qualified as X10CrWVTa9-1 for alloy steel plates 1 to 50 mm thick, though it is still in probationary phase rules. F82H has also reached maturity and is ready to be qualified, since the F82H material database is equivalent to Eurofer [1]. In this work we report the results of gap analyses referring to existing codes, together with the results of assessment of the material database. In addition, the latest results of creep rupture test are given as an example of continuing activity integrating the material database for the material standardization.

Experimental

Gap analyses were conducted with reference to the commercial heat resistant ferritic/martensitic steel, Mod. 9Cr-1Mo, in RCC-MR 2007 edition and ASME B&PV. For the creep properties, creep rupture tests were performed on F82H BA07 heat (as NT) in air from 500 to 650°C at intervals of 50°C.

Results and discussion

Tables 1 and 2 show the gap analysis results for mechanical properties and physical properties, respectively [2]. In Table 1, most materials data have been already obtained meeting requirements in these codes, but the data on tensile properties at temperatures lower than room temperature are missing and creep property data below 450°C is also needed to define the negligible creep temperature. However, it might not be necessary to obtain all the missing data for the ASME code case, because the operation temperature will be higher than 285°C. In Table 2, there appears to be some missing data such as linear expansion coefficient, thermal conductivity, thermal diffusivity and longitudinal elastic modulus, compared to the Mod.9Cr-1Mo. These physical property data have to be obtained in further work. We plan to qualify F82H in ASTM Committee A01 on Steel, Stainless Steel and Related Alloys first, integrating the material database that meets the ASTM requirements.

Figure 1 shows the latest creep rupture test results for F82H BA07 heat (in the NT condition) [3], as an example of continuing activity to integrate the material database. The results were summarized using the Larson Miller parameter (LMP). Table 3 shows the results of chemical analysis and heat treatment conditions of the tested F82Hs. The table gives only the compositions of major elements correlating with mechanical properties of F82H. Undesirable impurities in terms of long-term activation have been studied [4] and specifications for these elements will be developed through further work. The open

symbols show the result from BA07 heat (as NT). The closed symbols and cross marks show the data of BA07 heat (as NNT) and IEA heat (as NT), respectively. The creep properties of BA07 heat (as NT) were comparable or possibly superior to that of the other conditions. First, the difference of heat treatment condition possibly affected the creep properties between as NT and as NNT of BA07 heat. BA07 heat (as NNT) has finer grain sizes due to the second normalizing. In general, the finer grains become, the more easily grain boundary sliding and microstructural recovery occur. Though the refinement in grain sizes contributed to the improvement of material toughness of BA07 heat (as NNT) [5], the creep properties of that heat was likely degraded. Second, the application of Electro Slag Remelting (ESR) possibly affected the creep properties in the comparison of BA07 heat and IEA heat. The added tantalum appropriately contributed to the precipitation of TaX (X: carbon and/or nitrogen) without forming any other coarse complex oxides in BA07 heat produced by the ESR process [6], though the IEA heat melted without ESR contained less TaX precipitates and most of the added tantalum formed coarse complex oxides. MX (M: Metal) such as TaX is known to occur as fine precipitates, a few tenth nanometers in size, that effectively improve the creep properties of ferritic/martensitic steels. The material database of F82H will be integrated including these latest results.

It is also necessary to evaluate welds, tubes and pipes made from F82H, since most of the presently available data were obtained from plate products. It is also indispensable to consider irradiation effects on material properties. In particular, significant irradiation embrittlement accompanying irradiation hardening has been observed with irradiation to a few dpa at 573 K. This issue should be the focus of future work.

Table 1. Gap analysis (Chemical composition and mechanical properties) [2]

Material	Mod. 9Cr-1Mo		F82H	
	RCC-MR 2007 edition	ASME B&PV Code 2013	Status	Missing data and comments
Chemical composition Ladle & Product	Defined	Defined	Prepared	OK
Tensile strength	20 to 600 °C	-30 to 525 °C	20 to 700 °C	<ul style="list-style-type: none"> -30 to 20 °C 25 °C interval data from 300 to 525°C
0.2% proof stress	20 to 600 °C	-30 to 525 °C	20 to 700 °C	<ul style="list-style-type: none"> -30 to 20 °C 25 °C interval data over 100 °C
Elongation	-	RT	20 to 700 °C	-
Max. elongation of stress-strain curve	1.2 %	2.2 %	Analyzed	-
Reduction of area	-	-	20 to 700 °C	-
Creep rupture	425 to 675 °C	700 to 1200 °F (371 to 649 °C)	450 to 750°C	<ul style="list-style-type: none"> 371 to 450 °C 25°C interval data
Su	20 to 600 °C	-30 to 525 °C	20 to 700 °C	<ul style="list-style-type: none"> -30 to 20 °C 25 °C interval data from 300 to 525°C
Yield strength, Sy	20 to 600 °C	-30 to 525 °C	20 to 700 °C	<ul style="list-style-type: none"> -30 to 20 °C 25 °C interval data over 100 °C
The lowest stress intensity Sm	20 to 600 °C	-30 to 375°C	20 to 700°C	<ul style="list-style-type: none"> -30 to 20 °C 25°C interval data from 100 to 150°C 25°C interval data from 300 to 375 °C

Table 2. Gap analysis (Physical properties) [2]

Material	Mod. 9Cr-1Mo		F82H	
	RCC-MR 2007 edition	ASME B&PV Code 2013	Status	Missing data and comments
Linear expansion coefficient	20 to 600 °C	20 to 825 °C	300 to 1200 °C	• 20 to 300 °C
Thermal conductivity	20 to 600 °C	20 to 750 °C	300 to 1200 °C	• 20 to 300 °C
Thermal diffusivity	20 to 600 °C	20 to 825 °C	-	• Can be calculated
Longitudinal elastic modulus	20 to 600 °C	-200 to 700 °C	300 to 1200 °C	• -200 to 300 °C

Table 3. Chemical analysis and heat treatment

Element (wt%)	Heat	
	IEA	BA07
C	0.09	0.088-0.090
Si	0.07-0.11	0.16-0.17
Mn	0.10-0.16	0.45-0.46
P	0.002-0.003	0.008-0.009
S	0.001-0.002	0.002-0.003
Cr	7.64-7.89	7.97-8.02
W	1.95-2.00	1.88
V	0.16-0.19	0.19
Ta	0.02-0.04	0.03-0.04
B	0.0002	0.002
Ti	0.004-0.01	<0.003
O	-	0.001-0.002
N	0.005-0.008	0.015-0.019
Total Al	-	-
Sol. Al*	0.001-0.003	0.007
Fe	Bal.**	Bal.**
Heat treatment	IEA	BA07
1 st normalizing	1040 °C for 40 min	1040 °C for 40 min
2 nd normalizing ***	-	960 °C for 30 min
Tempering	750 °C for 60 min	750 °C for 60 min

*Sol.: Solved

**Bal: Balance

*** 2nd normalizing was performed to obtain a finer grain structure for some BA07 plates.

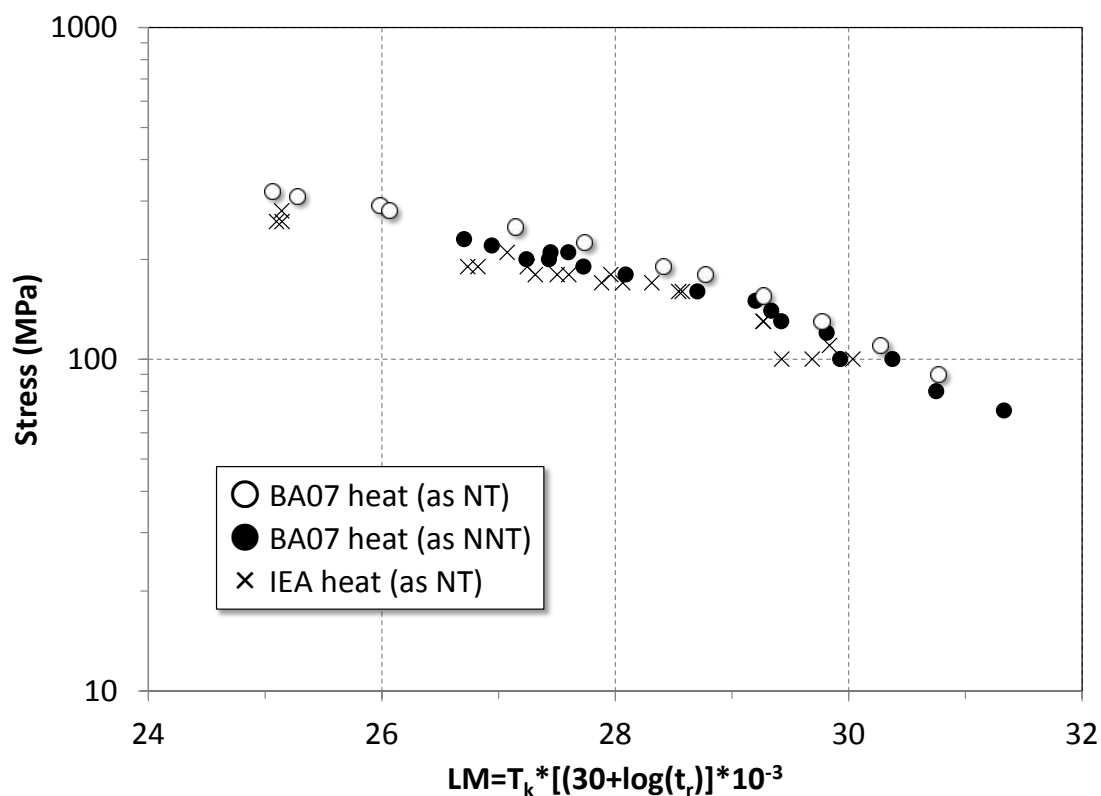


Figure 1. Creep rupture property summarized by Larson-Miller parameter [3].

Acknowledgements

This research was partly sponsored by the National Institutes for Quantum and Radiological Science and Technology (Japan Atomic Energy Research Institute) and the Office of Fusion Energy Sciences, U.S. Department of Energy, under contracts NFE-10-02779 and DE-AC05-00OR22725, respectively, with UT-Battelle, LLC.

References

- [1] F. Tavassoli, Eurofer Steel, Development to Full Code Qualification, *Procedia Engineering* 55 (2013), 300-308.
- [2] H. Tanigawa et al., Assessment of F82H development status toward DEMO application with respect to the existing design code, 29th SOFT, Prague, Czech, 5-9 September (2016).
- [3] ITER BA activity annual report 2016.
- [4] H. Tanigawa et al., Radiological assessment of the limits and potential of reduced activation ferritic/martensitic steels, *Fusion Engineering and Design* 89 (2014), 1573-1578.
- [5] ITER BA activity annual report 2011.
- [6] H. Sakasegawa et al., Precipitation behavior in F82H during heat treatments of blanket fabrication, *Fusion Engineering and Design* 86 (2011), 2541-2544.

10. IRRADIATION METHODS, EXPERIMENTS AND SCHEDULES

10.1 THE MFE-RB-19J HFIR IRRADIATION EXPERIMENT—J.L. McDuffee, J.W. Geringer (Oak Ridge National Laboratory)

OBJECTIVE

The HFIR MFE-RB-19J irradiation experiment is a collaborative effort between the US and Japan Fusion Materials programs to research tungsten for plasma facing components under divertor conditions and to evaluate blanket structural materials for DEMO and other fusion reactors. The objective of this experiment is to irradiate tungsten and RAFM steel specimens at controlled temperatures of 300, 500, 800 and 1200°C in a gadolinium-shielded capsule in a Removable Beryllium (RB) position of the High Flux Isotope Reactor (HFIR).

SUMMARY

The HFIR RB-19J experiment used a new design with a gadolinium metal cylinder thermal neutron shield to modify the fast/thermal neutron ratio over the life of the experiment. The experiment contains six cylindrical holders (four temperature zones) which houses ~1300 tungsten and steel specimens. Assembly of the RB19J capsule was completed in May 2016 and installed in HFIR in June 2016. The first irradiation cycle, number 466, started June 14 2016. Starting temperatures stabilized within design ranges for the 500°C and the 800°C holders. The 1200°C and the 300°C were lower and higher than designed by about 50°C and 100°C respectively. The fourth and last irradiation cycle was completed in December 2016. It was decided to complete at four cycles instead of six due to concerns with possible gadolinium burn-out and risk of excessive tungsten to rhenium and osmium transmutation.

PROGRESS AND STATUS

Experiment Description

The capsule has a gadolinium shield inside the capsule housing to reduce thermal neutron flux and thus reduce transmutation rates in specimen materials. The expected radiation damage levels for the steel and tungsten specimens for the originally planned six cycles of HFIR operation were ~2.5 to 3 dpa and ~1.0 to 1.5 dpa respectively.

The HFIR RB-19J irradiation experiment contains six cylindrical holders (four temperature zones) which houses ~1300 tungsten and steel specimens. The capsule assembly was completed in May 2016 and installed in HFIR in June 2016. The first irradiation cycle, 466, started June 14 2016. Starting temperatures stabilized within design ranges for the 500°C and the 800°C holders. The 1200°C and the 300°C were lower and higher than designed by about 50°C and 100°C respectively.

Experiment Design and Specimen Matrices

Thermal and Neutronics Analysis and Mechanical Design of the RB-19J experiment have been reported in detail in the Fusion Materials Semiannual Progress Report for the Period Ending June 30, 2016, report DOE-ER-0313/60, available in pages 205-214 in: (http://web.ornl.gov/sci/physical_sciences_directorate/mst/fusionreactor/Vol60.shtml).

The Specimen Matrices for the experiment are documented in the same Semiannual Progress Report in pages 215-233.

Operating History

The capsule completed four irradiation cycles, three in FY16, cycle 466, 467 and 468 and a fourth in FY17, cycle 469. It remained inserted in the HFIR since its installation in May 2016. Due to malfunction of the thermocouples during the first three cycles, temperature control for the fourth cycle was exercised by replicating the recorded data of earlier gas concentrations to maintain design temperatures.

Due to the trending data observed from cycle length reduction a detailed neutronics calculation was performed to evaluate gadolinium burnout effects. It was determined that transmutation of W to Re, Os must remain less than 1% for the experiment to meet the objectives. The analysis indicated that during the originally planned fifth cycle a rapid increase in Re, Os will start to occur. Based on this results it was decided to remove the capsule after the fourth cycle.

The capsule is now in safe pool storage until it can be transferred to ORNL Building 3525 hot cell facilities for disassembly.

Future Plans

The next steps for the RB-19J experiment are to calculate the isotope inventory generated by irradiation of the experiment. This will enable the shipping procedures to be developed and determine the amount of rigor required. At this time it is foreseen that a standard loop-cask will be used to transfer the capsule from HFIR to Building 3525 by May 2017. The experiment will then be disassembles, subcapsules or specimen holders distributed to appropriate hot cells for eventual specimen recovery and ultimately for post irradiation examination (PIE).

10.2 NEUTRON FLUENCE MEASUREMENTS AND RADIATION DAMAGE CALCULATIONS FOR THE JP30 AND JP31 EXPERIMENTS IN HFIR—L. R. Greenwood, B. D. Pierson, M. G. Cantaloub and T. Trang-Le (Pacific Northwest National Laboratory)

OBJECTIVE

Measure the neutron fluence and energy spectra during irradiations in HFIR and calculate fundamental radiation damage parameters including dpa and gas production.

SUMMARY

The JP30 and JP31 experiments were irradiated in target positions E2 and B4, respectively, of HFIR in cycles 439 starting November 21, 2011 through cycle 449 ending August 24, 2013 for a total exposure of 276.13 EFPD (effective full power days) at a nominal power level of 85 MW for a total exposure of 23471.28 MWD (megawatt days). Neutron dosimetry monitors fabricated by PNNL were inserted in the JP30 and JP31 experimental assemblies at various elevations. After the irradiation, the neutron fluence monitors were recovered and sent to PNNL for analysis. The activated monitor wires were analyzed to determine activation rates that were used to adjust the neutron fluence spectrum at each irradiation position. The adjusted neutron fluence spectra were then used to calculate radiation damage parameters.

PROGRESS AND STATUS

Neutron dosimetry monitors were fabricated by PNNL for insertion in the JP30 and JP31 irradiation assemblies. The vanadium monitors measure 0.050" in diameter by 0.340" long. Each monitor has a 2-digit code stamped on the bottom. The monitors were filled with small wire segments of Fe, Ti, Nb, Cu, and 1% Co-V and were electron beam welded to maintain integrity throughout the irradiation. The irradiated monitors were received at PNNL for analysis in June 2016 following irradiation. The monitors from the JP30 and JP31 irradiations were received in the same containers that had the monitors from the JP28 and JP29 experiments which will be reported separately. The monitors were identified, when possible, using the 2-digit ID stamp on the bottom. The monitors were also weighed after irradiation so that the mass values could be compared with the fabrication records in cases where the 2-digit code could not be determined due to damage. Table 1 provides a list of all of the monitors that were initially inserted along with the monitors that were recovered and analyzed for this report.

Table 1 – List of neutron fluence monitors and recovery status

JP30			JP31		
Monitor	Height, cm	Status	Monitor	Height, cm	Status
ZB	20.39	Recovered	BF	19.68	Recovered
XB	16.50	Recovered	Z8	16.04	Lost
5C	5.70	Lost	B5	-3.31	Recovered
EL	-8.49	Recovered	H5	-9.11	Recovered
DI	-25.20	Recovered	5J	-25.52	Recovered

All of the monitors were gamma counted as received. The monitors were then opened and the individual wires were gamma counted separately to avoid any possible interference as well as to detect weaker nuclides that could not be detected in the whole monitor counts due to the ^{60}Co activity. The nuclear reactions and activation products that were detected are listed in Table 2. The "90% neutron energy range" represents the energy range of the neutrons that produced 90% of the listed reaction; 5% of the activity was produced by neutrons with energies below the lower energy and 5% above the higher

energy. The “90% neutron energy ranges” listed in Table 2 represent the maximum spread from all eight dosimetry monitors. The different energy ranges for the four threshold reactions are very useful in defining the neutron spectrum, as discussed later in this report.

Table 2 – Nuclear reactions with half-lives and energy sensitivity ranges

Nuclear Reaction	Half-life	90% Neutron Energy Range, MeV
$^{63}\text{Cu}(n,a)^{60}\text{Co}$	5.27 a	4.5 to 12.0
$^{54}\text{Fe}(n,p)^{54}\text{Mn}$	312 d	2.0 to 7.4
$^{46}\text{Ti}(n,p)^{46}\text{Sc}$	83.8 d	3.7 to 10.0
$^{93}\text{Nb}(n,n')^{93\text{m}}\text{Nb}$	16.1 a	0.78 to 5.5
$^{59}\text{Co}(n,g)^{60}\text{Co}$	5.27 a	Thermal/Epithermal
$^{93}\text{Nb}(n,g)^{94}\text{Nb}$	20,300 a	Thermal/Epithermal

The gamma detectors are calibrated using NIST traceable standards obtained from Eckert and Zeigler. Control counts are performed every day that a detector is used to check the continuing calibration of the energy, efficiency, and resolution. All nuclear data was adopted from the Nudat 2 database at the National Nuclear Data Center at Brookhaven National Laboratory[1]. The weights of the individual wires were measured during fabrication and all results are reported as activity per gram of the elements with natural abundances using the before irradiation masses. The measured activities corrected back to the end of irradiation time are provided in Table 3. The activities were not corrected for nuclear burnup or gamma absorption because these corrections are applied to the reaction rates using the SigPhi calculator from the STAYSL_PNNL software suite [2].

Table 3 – Measured activities in Bq/g for the JP30 and JP31 irradiations; uncertainties are $\pm 2\%$. Results are corrected to the end of irradiation time of August 24, 2013.

ID	Height,cm	^{54}Mn	$^{93\text{m}}\text{Nb}$	^{94}Nb	$^{60}\text{Co}(\text{Co})$	^{46}Sc	$^{60}\text{Co}(\text{Cu})$
JP30		Bq/g					
D1	-25.20	3.91e+9	1.04e+10	1.52E+8	1.81E+11	1.28E+9	8.06E+7
EL	-8.49	8.57E+9	2.20E+10	2.22E+8	2.44E+11	3.49E+9	1.69E+8
XB	16.50	7.77E+9	1.94E+10	2.29E+8	2.35E+11		1.65E+8
ZB	20.39	5.93E+9	1.37E+10	2.00E+8	2.23E+11	2.28E+9	1.14E+8
JP30		Bq/g					
5J	-25.52	3.11E+9	7.73E+9	1.51E+8	1.86E+11		6.54E+7
B5	-3.31	9.48E+9	2.01E+10	2.43E+8	2.59E+11	2.14E+9	1.76E+8
H5	-9.11	8.74E+9	1.83E+10	2.43E+8	2.45E+11	3.13E+9	1.66E+8
BF	16.04	5.70E+9	1.26E+10	1.97E+8	2.38E+11	1.97E+9	1.06E+8

The $^{93\text{m}}\text{Nb}$ activities were determined by x-ray counting of the 16.6 and 18.6 keV x-rays using a low energy photon spectrometer (LEPS) detector. The high purity niobium wires were dissolved in a mixture of nitric and hydrofluoric acid using small Teflon beakers. A small aliquot (about 0.5%) of the solution was accurately weighed and dried on thin filter paper covered by 0.25 mil Mylar for LEPS counting. The very small mass and thin cover nearly eliminated concerns over x-ray absorption, backscatter, and fluorescence as discussed in ASTM practice E1297 [3].

The saturated reaction rates are calculated from the measured activities in Table 3 by applying corrections for decay during irradiation, gamma absorption, and nuclear burnup of the target and product nuclides. These corrections are included with the BCF and SIG-PHI Calculator modules of the STAYSL_PNNL computer suite. (2) The irradiation history was provided by ORNL and is described briefly in the Summary section of this report. The BCF program breaks the irradiation up into periods of nearly constant reactor power and calculates the growth and decay of each activation product (see page 47 [2]). The resultant correction factor corrects for decay during the irradiation and normalizes to 276.13 EFPD at full reactor power using the nominal value of 85 MW. Gamma absorption in the small wire segments is based on the XCOM database (see ref. [4]) as described Section 7.3 of ref [2]. Neutron burnup corrections for thermal neutron reactions use an iterative procedure using a ratio of the burnup reaction rates for the target and product nuclides. The uncorrected reaction rate is used to determine a correction and this procedure is iterated until convergence is achieved. The resulting thermal reaction rates are then used as the basis for calculating the burnup corrections for the threshold nuclear reactions using known thermal neutron cross sections and resonance integrals. For complete details regarding the iterative neutron burnup correction see Figure 28 of ref. [2]. The calculated saturated reaction rates are listed in Table 4.

Table 4 – Saturated reaction rates in product atoms/(target atom – second) for the JP30 and JP31 experiments. Uncertainties are $\pm 2\%$ except for ^{93m}Nb which are estimated at $\pm 5\%$. Data with an asterisk were not used in the final fluence analysis due to failure to recover the complete wire.

ID	Height	^{60}Co	^{60}Co	^{54}Mn	^{94}Nb	^{46}Sc	^{93m}Nb
JP30	cm	atom/atom-sec⁻¹					
ZB	20.39	3.96 E-8	2.13 E-13	3.14 E-11	1.63 E-9	4.48 E-12	6.97 E-11
XB	16.50	4.37 E-8	3.09 E-13	4.15 E-11	1.93 E-9		9.93 E-11
EL	-8.49	4.71 E-8	3.21 E-13	4.66 E-11	1.84 E-9	6.95 E-12	1.13 E-10
D1	-25.20	2.81 E-8	1.47 E-13	2.01 E-11	1.12 E-9	2.48 E-12*	5.24 E-11
JP30	cm	atom/atom-sec⁻¹					
BF	19.68	4.50 E-8	2.01 E-13	3.10 E-11	1.56 E-9	3.93 E-12	6.41 E-11
B5	-3.31	5.36 E-8	3.39 E-13	5.24 E-11	2.11 E-9		1.04 E-10
H5	-9.11	5.15 E-8	3.44 E-13	5.09 E-11	2.33 E-9	6.88 E-12	1.03 E-10
5J	-25.52	2.93 E-8	1.20 E-13	1.60 E-11	1.11 E-9		3.90 E-11

The saturated reaction rates are equal to the integral of the neutron activation cross section times the neutron flux over all neutron energies. At each irradiation position we thus have at most 6 integral equations that are solved simultaneously using a generalized least-squares procedure in the STAYSL PNNL computer suite. The neutron activation cross sections were adopted from the IRDFF database compiled by the Nuclear Data Section of the International Atomic Energy Agency [5]. The input neutron spectrum was provided by Joel McDuffee at ORNL (see Figure1, blue) [6]. The input to STAYSL PNNL consisted of the measured saturated reaction rates, the input neutron spectrum, the irradiation length, and the IRDFF neutron activation cross sections including all known uncertainties and covariances. Matrix inversion was then used to determine the adjusted neutron flux spectrum and uncertainties including the complete cross-section covariance matrices and a Gaussian formalism based flux covariance matrix. The results are presented in Table 5 and a typical neutron spectral adjustment is shown in Figures 1 and 2.

Table 5 – Neutron fluences for the JP30 and JP31 irradiations

ID	Height	Thermal		Epithermal		> 0.11 MeV		> 1 MeV	
		< 0.5 eV	±%	0.5 eV to 110 keV	±%		±%		±%
JP30	cm								
ZB	20.39	2.85E+22	12	1.99E+22	25	1.58E+22	6	7.98E+21	5
XB	16.50	3.06E+22	13	2.70E+22	24	2.15E+22	6	1.08E+22	5
EL	-8.49	3.40E+22	12	2.45E+22	26	2.39E+22	6	1.22E+22	5
D1	-25.20	2.04E+22	12	1.32E+22	26	1.12E+22	6	5.57E+21	5
JP31	cm								
BF	19.68	3.33E+22	12	1.53E+22	28	1.51E+22	6	7.64E+21	5
B5	-3.31	3.88E+22	12	2.80E+22	26	2.51E+22	6	1.26E+22	5
H5	-9.11	3.26E+22	13	3.01E+22	24	2.23E+22	6	1.12E+22	5
5J	-25.52	2.15E+22	12	1.11E+22	26	8.85E+21	6	4.35E+21	5

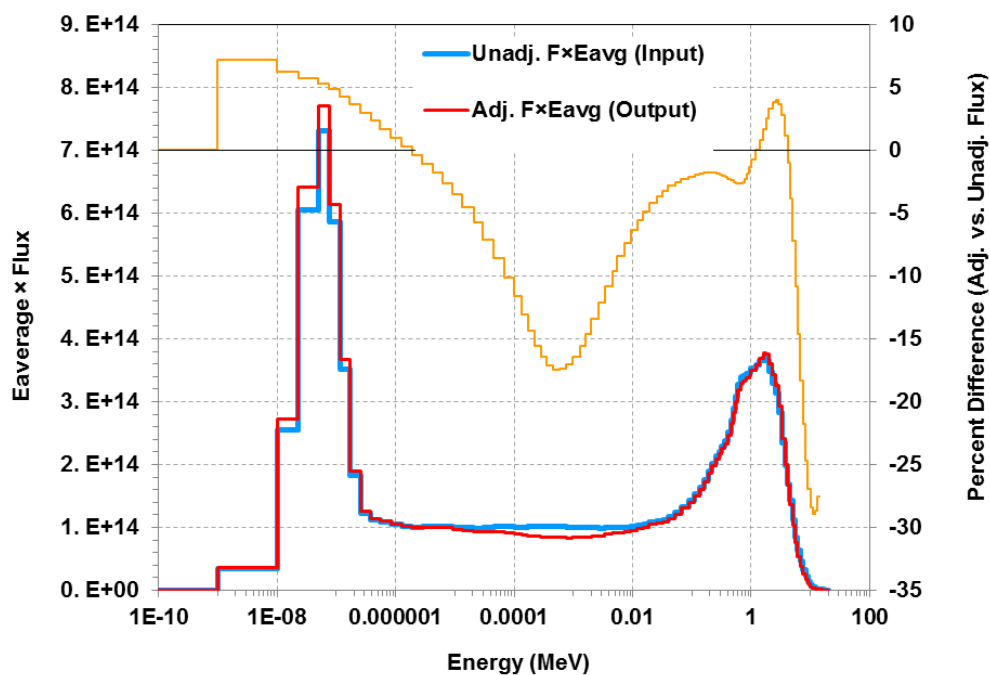


Figure 1 – Neutron spectral adjustment with STAYSL PNNL for the JP30 B5 position at -3.3 cm. Flux per lethargy is shown both before and after adjustment. The top curve shows the size of the adjustment using the percent difference scale on the right side.

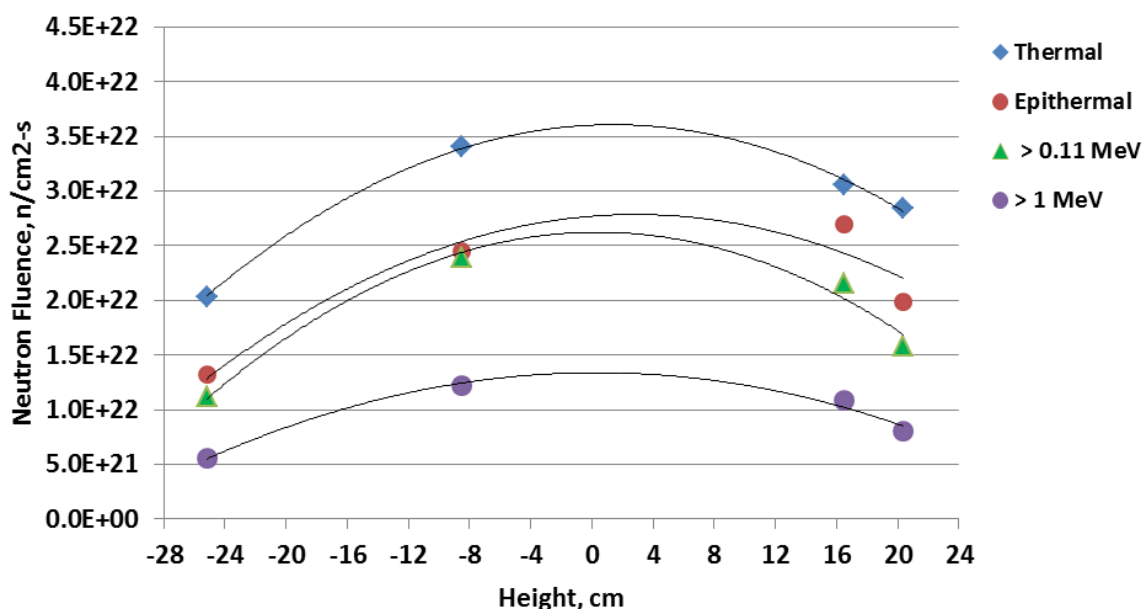


Figure 2 – Neutron fluence values are plotted vs. height in the HFIR JP30 experiment. The solid lines are trend lines used as eye guides. The epithermal fluence has a higher uncertainty than the thermal and fast fluences. The higher uncertainty is most visibly apparent near +20 cm on the x-axis.

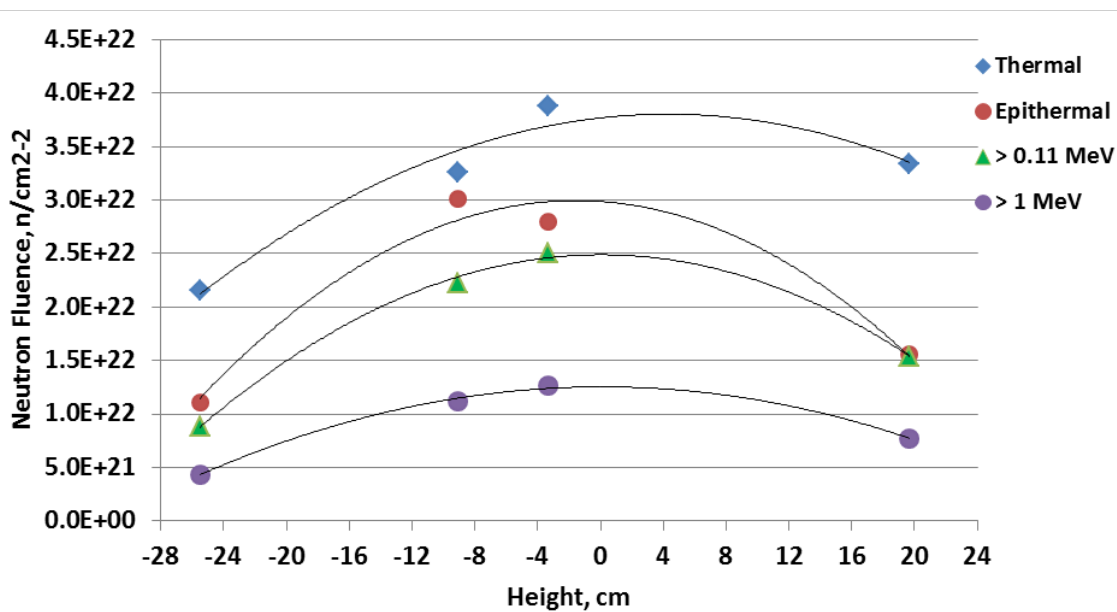


Figure 3 – Neutron fluence values are plotted vs. height in the HFIR JP31 experiment. The solid lines are trend lines used as eye guides. The epithermal fluence has a higher uncertainty than the thermal and fast fluences. In the case of monitor H5, the thermal/epithermal ratio was difficult to deconvolute precisely.

Radiation Damage Calculations

The adjusted neutron spectrum determined at each position in the irradiation assemblies was used to calculate the dpa and helium production in various elements and alloys using the SPECTER computer code [7] and the damage parameters are listed in Table 6 and plotted in Figures 4 and 5. The radiation damage calculations do not take into account the significant transmutation that occurs during irradiation. In most cases the transmutation does not significantly change the dpa or helium production but may lead to changes in the alloy composition. The tungsten in the alloy F82H was converted by more than 90% to Re and Os, as discussed in ref. [8].

Table 6 – Radiation damage parameters for the JP30 and JP31 experiments

ID	Height	F82H		Fe		Ni	
		dpa	He,appm	dpa	He,appm	dpa	He,appm
JP30	cm	dpa	He,appm	dpa	He,appm	dpa	He,appm
ZB	20.39	11.25	3.24	11.3	3.40	22.65	5770.2
XB	16.50	15.24	4.66	15.3	4.88	28.00	6415.5
EL	-8.49	17.03	4.91	17.1	5.15	31.50	7299.4
D1	-25.20	7.82	2.23	7.85	2.33	14.82	3492.0
JP31	cm	dpa	He,appm	dpa	He,appm	dpa	He,appm
BF	19.68	10.86	3.01	10.9	3.15	24.75	7083.5
B5	-3.31	17.83	5.16	17.9	5.41	34.92	8688.0
H5	-9.11	15.84	4.70	15.9	4.93	29.80	7008.9
5J	-25.52	6.22	1.82	6.24	1.91	30.92	3787.9

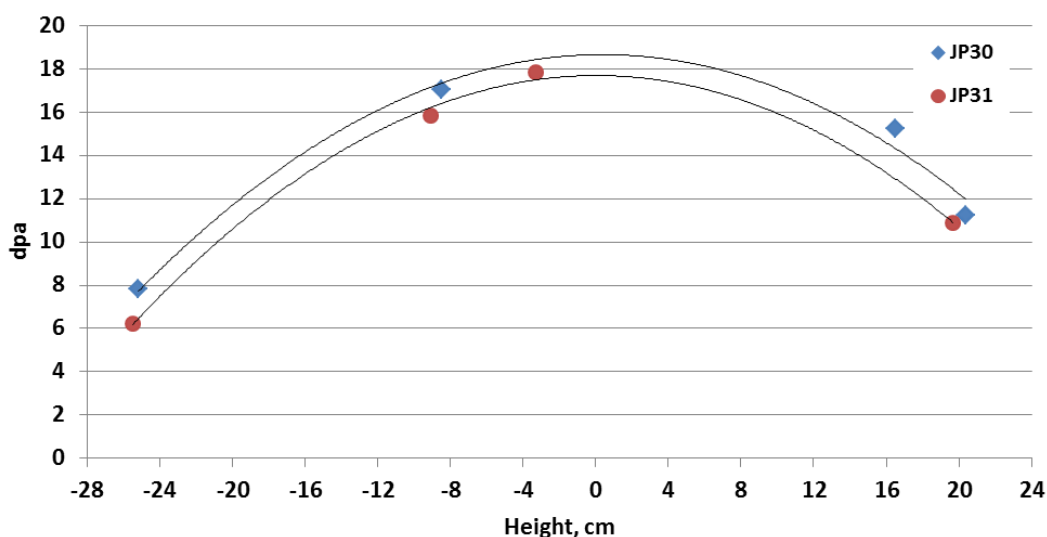


Figure 4 – F82H dpa for the JP30 and JP31 experiments. The solid lines are polynomial fits to the data, as described in the text and Table 7.

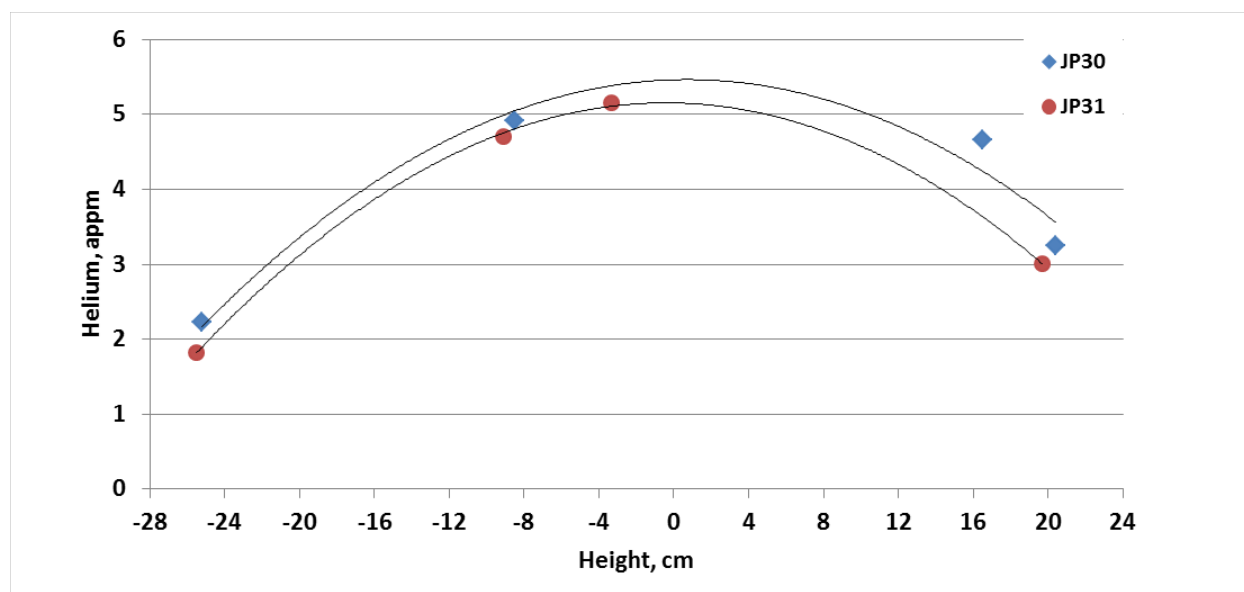


Figure 5 – Helium production (appm) in F82H for the JP30 and JP31 experiments. The solid lines are polynomial fits to the data, as described in the text and Table 7.

The neutron fluence and radiation damage parameters can be well described by a polynomial function as shown by the trend lines on the plots. The form of the polynomial is given as equation (1) below where a is the maximum value, and b is the quadratic parameter. The flux, dpa, and helium (appm) values at any location in the assembly can then be determined using the height, z in cm, and the coefficients listed in Table 7. The functions are symmetric about core midplane.

$$F(z) = a \cdot (1 + b \cdot z^2) \quad (1)$$

Table 7 – Polynomial coefficients for Equation 1 to calculate neutron fluence and damage parameters

JP30	a	b
Thermal	3.669E+22	-6.507E-04
Epithermal	2.886E+22	-7.683E-04
>0.1 MeV	2.640E+22	-9.020E-04
> 1 MeV	1.345E+22	-9.169E-04
F82H dpa	18.79	-9.093E-04
F82H He,appm	5.54	-9.212E-04
JP31	a	b
Thermal	3.7754E+22	-5.790E-04
Epithermal	2.9819E+22	-1.021E-03
>0.1 MeV	2.4881E+22	-9.916E-04
> 1 MeV	1.2528E+22	-1.003E-03
F82H dpa	17.69	-9.989E-04
F82H He,appm	5.15	-1.014E-03

Future Plans

Work is in progress on measuring the neutron fluence and damage parameters for the HFIR JP28 and JP29 irradiations.

References

- [1] A. A. Sonzogni, "Nudat 2.0: Nuclear structure and decay data on the internet," in *AIP Conference Proceedings*, 2005, vol. 769, p. 574.
- [2] L. R. Greenwood and C. D. Johnson, "User Guide for the Staysl Pnnl Suite of Software Tools," Pacific Northwest National Laboratory (PNNL), Richland, WA (US), PNNL-22253, Feb. 2013.
- [3] ASTM E-1297-08 Standard Test method for Measuring Fast-Neutron Reaction Rates by Radioactivation of Niobium (reapproved in 2013).
- [4] M. J. Berger *et al.*, "XCOM: Photon Cross Section Database (version 1.5)(2010)," *Natl. Inst. Stand. Technol. Gaithersburg MD*, 2013.
- [5] R. Capote, K. Zolotarev, V. Pronyaev, and A. Trkov, "Updating and Extending the IRDF-2002 Dosimetry Library," *Updat. Extending IRDF-2002 Dosim. Libr.*, 2012.
- [6] T. Daly and J. L. McDuffee, Experimental and Computational Study of the Flux Spectrum in Materials Irradiation Facilities of the High Flux Isotope Reactor, PHYSOR 2012, Advances in Reactor Physics Linking Research, Industry, and Education, Knoxville, TN, April 2012.
- [7] LR Greenwood and RK Smither, SPECTER: Neutron Damage Calculations for Materials Irradiations, ANL/FPP/TM-197, January 1985.
- [8] L. R. Greenwood and F. A. Garner, Transmutation of Mo, Re, W, Hf, and V in Various Irradiation Test Facilities and STARFIRE, *Journal of Nuclear Materials* 212-215 (1994)635-639.

10.3 HFIR IRRADIATION EXPERIMENTS—J.P. Robertson (Oak Ridge National Laboratory)**PROGRESS AND STATUS****Status of the Reactor**

The HFIR completed 3.3 cycles during the second half of 2016. Cycle 466 ended on July 7, 2016, accumulating 1970.95 MWD. Cycle 467 began on July 26 and ended on August 18, 2016 (2003.84 MWD), Cycle 468 began on September 6 and ended on September 30, 2016 (2036.29 MWD), and Cycle 469 began on November 15 and ended on December 8, 2016 (1990.19 MWD).

SUMMARY**Summary of Recent, Current and Planned Fusion Materials Program Experiments**

Experiment Designation	Primary Materials	Specimen Types*	Irradiation Temperature (°C)	Max Exposure (dpa)	Number of Reactor Cycles	Irradiation Period (month/year)		
<i>Beryllium reflector (RB) irradiation positions</i>								
RB-15J	F82H	T, F, FT	300, 400	6	10	6/08	–	12/09
RB-19J	W alloys and F82H	various	300, 500, 800, 1200	1.5	4	6/16		12/16
<i>Target zone full-length capsules</i>								
JP-25	F82H	T, FT	300, 500	20	10	2/99	–	1/01
JP-26	F82H	T, FT	300,400,500	9	5	12/03	–	11/04
JP-27	F82H	T, FT	300, 400	21	13	12/03	–	1/08
JP-28	F82H	T, FT	300,400,500	80	46	4/05	–	7/13
JP-29	F82H	T, FT	300,400,500	80	46	1/05	–	7/13
12-DCT	F82H	DCT	50	1.6	1	8/11	–	8/11
JP-30	F82H	T, FT	300,400,650	20	~10	11/11	–	8/13
JP-31	F82H	T, FT	300,400,650	20	~10	11/11	–	8/13
<i>Target zone rabbit capsules (DOE-JAEA)</i>								
F8A1	F82H	T, FT	300	50	29	2/09	–	7/13
F8A2	“	“	“	“	“	“	–	“
F8B1	“	“	“	“	“	“	–	“
F8B2	“	“	“	“	“	“	–	“
JCR-1	SiC/SiC	Bend bars	800	30	15	10/04	–	1/09
JCR-2	“	“	“	“	“	“	–	“
JCR-3	“	“	“	“	“	“	–	“
JCR-4	“	“	“	“	“	“	–	“
JCR-5	“	“	“	>50	>25	10/04	–	2/11
JCR-6	“	“	“	“	“	“	–	“
JCR-7	“	“	“	“	“	“	–	“
JCR-8	“	“	“	“	“	“	–	“

Target zone rabbit capsules (DOE-JAEA) - Continued

Experiment Designation	Primary Materials	Specimen Types*	Irradiation Temperature (°C)	Max Exposure (dpa)	Number of Reactor Cycles	Irradiation Period (month/year)		
JCR-9	“	“	500	30	15	10/04	–	1/09
JCR-10	“	“	“	“	“	“	–	“
JCR-11	“	“	“	“	“	“	–	“
JCR-12	“	“	“	“	“	“	–	“
F11A3	F82H	T, FT	300	20	12	5/11	–	2/13
F11A4	“	“	“	“	“	“	–	“
F11B3	“	“	“	“	“	“	–	“
M4-TEN	F82H	DCT	50	1.6	1	8/11	–	8/11
JCR11-01	SiC/SiC	Bend bars	950	50	25	11/12	–	
JCR11-02	SiC/SiC	Bend bars	950	10	5	10/12	–	8/13
JCR11-03	SiC/SiC	Bend bars	950	30	15	5/13	–	8/15
JCR11-04	SiC/SiC	Bend bars	950	30	15	5/13	–	8/15
JCR11-05	SiC/SiC	Bend bars	950	50	25	10/12	–	
JCR11-06	SiC/SiC	Bend bars	950	10	5	10/12	–	7/13
JCR11-07	SiC/SiC	Bend bars	950	100	50	10/12	–	
JCR11-08	SiC/SiC	Bend bars	950	100	50	10/12	–	
JCR11-09	SiC/SiC	UDMC	950	4	2	6/13	–	11/13
JCR11-10	SiC/SiC	UDMC	950	10	8	6/13	–	8/14
JCR11-11	SiC/SiC	UDMC	950	30	15	6/13	–	8/15
JCR11-12	SiC/SiC	UDMC	950	100	50	6/13	–	
F13A5	F82H	T, FT	300	10	9	1/14	–	3/15
F13A6	F82H	T, FT	300	50	28	1/14	–	
F13B4	F82H	T, FT	300	10	9	1/14	–	3/15
F13B5	F82H	T, FT	300	20	18	1/14	–	
SCF6	SiC/SiC	Bend bars	600	10	6	11/14	–	10/15
SCF7	SiC/SiC	Bend bars	600	30	14	11/14	–	
SCF8	SiC/SiC	Bend bars	600	100	45	11/14	–	
SCF9	SiC/SiC	Bend bars	600	200	90	11/14	–	
SCF10	SiC/SiC	Bend bars	950	10	5	1/15	–	10/15
SCF11	SiC/SiC	Bend bars	950	30	14	1/15	–	
SCF12	SiC/SiC	Bend bars	950	100	45	1/15	–	
Target zone rabbit capsules (DOE-NIFS)								
T8A1	SiC	BSR	300	0.01	HT**	10/09	–	10/09
T8A2	SiC	BSR	300	0.1	HT	10/09	–	10/09
T8B1	SiC	BSR	500	0.01	HT	10/09	–	10/09
T8B2	SiC	BSR	500	0.1	HT	10/09	–	10/09
T8C1	SiC	BSR	500	~1	1	5/09	–	6/09
T8D1	SiC	BSR	800	0.1	HT	3/11	–	10/09
T8E1	SiC	BSR	800	~1	1	8/09	–	8/09
T8F1	SiC	BSR	1200	~1	1	8/09	–	8/09
T9A1	W, Ni	Discs	90	0.1	HT	1/09	–	10/09
T9A2	W, Ni	Discs	90	1.2	1	1/09	–	1/09
T9C1	Steels	T, MC	500	5.5	3	11/09	–	2/10
T9C2	Steels	T, MC	500	9.6	5	11/09	–	6/10
T9G1	Steels	T, MC	300	1.2	1	6/09	–	8/09
T9G2	Steels	T, MC	300	9.6	8	6/09	–	8/11

Target zone rabbit capsules (DOE-NIFS) - Continued

Experiment Designation	Primary Materials	Specimen Types*	Irradiation Temperature (°C)	Max Exposure (dpa)	Number of Reactor Cycles	Irradiation Period (month/year)		
MTTN01	Steels	T, MC	300	4.8	4	1/12	–	8/11
300-LD-1	Steels	SSJ, MC	300	2	1	5/12	–	6/12
300-HD-1	Steels	SSJ, MC	300	12	6	5/12	–	2/13
500-LD-1	Steels	SSJ, MC	500	2	1	5/12	–	6/12
500-HD-1	Steels	SSJ, MC	500	12	6	5/12	–	2/13
500-HD-2	Steels	SSJ, MC	500	12	6	5/12	–	2/13
500-HD-3	Steels	SSJ, MC	500	12	6	5/12	–	2/13
650-LD-1	Steels	SSJ, MC	650	2	1	5/12	–	6/12
650-LD-2	Steels	SSJ, MC	650	2	1	5/12	–	6/12
650-HD-1	Steels	SSJ, MC	650	12	6	5/12	–	2/13
650-HD-2	Steels	SSJ, MC	650	12	6	5/12	–	2/13
300-LD-2	Steels, W	SSJ, MC	300	2	2	7/12	–	8/12
300-MD-1	Steels, W	SSJ, MC	300	7	4	7/12	–	2/13
500-LD-2	Steels, W	SSJ, MC	500	2	2	1/13	–	7/13
300-LD-3	Steels, W	SSJ, MC	300	2	2	7/12	–	11/12
300-HD-2	Steels, W	SSJ, MC	300	12	8	7/12	–	2/14
500-LD-3	Steels, W	SSJ, MC	500	2	1	7/12	–	8/12
500-HD-4	Steels, W	SSJ, MC	500	12	6	7/12	–	7/13
650-LD-3	Steels, W	SSJ, MC	650	2	2	10/12	–	7/13
650-HD-3	Steels, W	SSJ, MC	650	12	8	7/12	–	11/13
PC1	Various	SSJ, MC	80/100	0.02	HT	6/12	–	6/12
PC1A	Various	SSJ, MC	80/100	0.02	HT	6/12	–	6/12
PC2	Various	SSJ, MC	80/100	0.1	HT	6/12	–	6/12
PC2A	Various	SSJ, MC	80/100	0.1	HT	6/12	–	6/12
PC3	Various	SSJ, MC	80/100	0.5	HT	6/12	–	7/12
PC3A	Various	SSJ, MC	80/100	0.5	HT	6/12	–	7/12
PC4	Various	SSJ, MC	80/100	2	1	6/12	–	7/12
PC4A	Various	SSJ, MC	80/100	2	1	6/12	–	7/12
PC5	Various	SSJ, MC	80/100	20	9	6/12	–	11/13
TB-300-1	Steels, W	SSJ, MC	300	0.02	HT	8/12	–	8/12
TB-300-2	Steels, W	SSJ, MC	300	0.1	HT	8/12	–	8/12
TB-300-3	Steels, W	SSJ, MC	300	0.5	HT	8/12	–	8/12
TB-300-4	Steels, W	SSJ, MC	300	7	5	7/12	–	6/13
TB-500-1	Steels, W	SSJ, MC	500	0.1	HT	8/12	–	8/12
TB-500-2	Steels, W	SSJ, MC	500	0.5	HT	8/12	–	8/12
TB-500-3	Steels, W	SSJ, MC	500	7	4	7/12	–	2/13
TB-650-1	Steels, W	SSJ, MC	650	0.1	HT	8/12	–	8/12
TB-650-2	Steels, W	SSJ, MC	650	0.5	HT	8/12	–	8/12
TB-650-3	Steels, W	SSJ, MC	650	7	5	7/12	–	6/13
TB-650-4	Steels, W	SSJ, MC	650	20	11	7/12	–	7/14
TTN09	SiC	Joint	500	3.4	2	8/11	–	11/11
TTN10	SiC	Joint	500	4.1	2	8/11	–	11/11
TTN11	SiC	Joint	800	4	2	3/12	–	5/12
TTN01	SiC	BSR	300	1	1	2/11	–	3/11
TTN02	SiC	BSR	300	10	6	2/11	–	12/11
TTN03	SiC	BSR	300	20	11	2/11	–	8/13
TTN04	SiC	BSR	500	10	6	5/11	–	4/12
TTN05	SiC	BSR	500	20	11	5/11	–	8/13

Target zone rabbit capsules (DOE-NIFS) - Continued

Experiment Designation	Primary Materials	Specimen Types*	Irradiation Temperature (°C)	Max Exposure (dpa)	Number of Reactor Cycles	Irradiation Period (month/year)	
TTN06	SiC	BSR	800	10	6	5/11	– 4/12
TTN07	SiC	BSR	800	20	11	5/11	– 8/13
TTN08	SiC	BSR	1200	10	6	5/11	– 8/12
TTN16	SiC	Fiber BSR	500	1	1	11/11	– 12/11
TTN17	SiC	Fiber BSR	500	10	6	8/11	– 6/12
TTN18	SiC	Fiber BSR	500	20	11	8/11	– 8/13
TTN19	SiC	Fiber BSR	1200	1	1	3/12	– 4/12
TTN20	SiC	Fiber BSR	1200	10	6	3/12	– 11/12
PXW1	W	Discs	800	2	1		–
PXW2	W	Discs	800	2	1	1/15	– 2/15
PXW3	W	Discs	800	6	3		–
PXW4	W	Discs	1100	2	1		–
PXW5	W	Discs	1100	2	1	1/15	– 2/15
PXW8	W	Discs	1100	6	3		–

Target zone rabbit capsules (US-NIFS-JAEA)

T11-01J	V-4Cr-4Ti	BTC	425	2	1	11/12	– 12/12
T11-02J	V-4Cr-4Ti	BTC	425	6	3	1/13	– 7/13
T11-03J	V-4Cr-4Ti	BTC	425	2	1	11/12	– 12/12
T11-04J	V-4Cr-4Ti	BTC	425	6	3	1/13	– 7/13
T11-05J	SiC	BTC	600	2	1	11/12	– 12/12
T11-06J	SiC	BTC	600	6	3	1/13	– 7/13
T11-08J	SiC	BTC	600	6	3	1/13	– 7/13
T11-09J	SiC	BTC	600	2	1	11/12	– 12/12
T11-11J	SiC	BTC	600	2	1	11/12	– 12/12
T11-13J	Graphite	BTC	600	2	1	11/12	– 12/12
T11-14J	Graphite	BTC	600	6	3	1/13	– 7/13
J12-01	F82H	BTC	300	1.5	1	1/13	– 2/13
J12-02	F82H	BTC	300	6	3	5/13	– 7/13
J12-03	F82H	BTC	300	1.5	1	5/13	– 2/13
J12-04	F82H	BTC	300	6	3	1/13	– 6/13
J12-05	F82H	BTC	300	1.5	1	1/13	– 2/13
J12-06	F82H	BTC	300	6	3	5/13	– 6/13

Target zone rabbit capsules (US-IMR)

MX-1	Ceramics	Various	400	2	1	7/13	– 8/13
MX-2	Ceramics	Various	400	6	3	7/13	– 3/14
MX-3	Ceramics	Various	400	10	6	7/13	– 7/14
MX-4	Ceramics	Various	700	2	1	7/13	– 8/13
MX-5	Ceramics	Various	700	6	3	7/13	– 2/14
MX-6	Ceramics	Various	700	10	5	7/13	– 5/14
MX-7	Ceramics	Various	1000	2	1	7/13	– 8/13
MX-8	Ceramics	Various	1000	6	3	7/13	– 3/14
MX-9	Ceramics	Various	1000	10	5	7/13	– 5/14
IMR2	Various	Various	200	2	1	6/15	– 7/15
IMR3	Various	Various	200	2	1	6/15	– 7/15

Target zone rabbit capsules (US-IMR) - Continued

Experiment Designation	Primary Materials	Specimen Types*	Irradiation Temperature (°C)	Max Exposure (dpa)	Number of Reactor Cycles	Irradiation Period (month/year)		
IMR4	Various	Various	200	2	1	6/16	–	7/16
IMR6	Various	Various	600	2	1	6/16	–	7/16
IMR7	Various	Various	600	6	3	6/16	–	9/30
IMR8	Various	Various	600	10	5	6/16	–	7/16
IMR9	Various	Various	1000	2	1	6/16	–	7/16
IMR10	Various	Various	1000	10	5	6/16	–	1/17
IMR11	Various	Various	1000	10	5	6/16	–	1/17
Target zone rabbit capsules (US)								
SCJ2-10	Ceramics	Joint	500	3	2	5/14	–	7/14
SCJ2-11	Ceramics	Joint	500	>10	12	5/14	–	8/16
SCJ2-12	Ceramics	Joint	500	3	2	5/14	–	7/14
SCJ2-16	Ceramics	Joint	1000	3	2	6/14	–	8/14
SCJ2-17	Ceramics	Joint	1000	3	2	6/14	–	8/14

*T = Tensile, F = Fatigue, FT = Fracture Toughness, MC = Multipurpose Coupon, BSR = Bend Stress Relaxation Creep, DCT = Disc Compact Tension, BTC: Bellows-loaded Tensile Creep, UDMC: Uni-directional Mini-composite. Most experiments also contain TEM disks, other special purpose specimens, and monitors occupying small spaces.

**Hydraulic tube – fractional cycle exposures.